Chapter 5

Propagation and Scattering in a Spherical-Stratified Refracting Medium

5.1 Introduction

We extend the Mie scattering treatment of Chapter 3 to the case of a scattering spherical surface embedded in a refracting medium that is laminar but otherwise spherical symmetric. Figure 5-1 depicts this scenario. At the boundary, n or one of its derivatives may be discontinuous with a refraction profile $n^+(r)$ in the overlying medium and $n^-(r)$ inside the sphere. The angle α_L is the refractive bending angle at the low Earth orbiting (LEO) spacecraft. The angle $\tilde{\alpha}$ is the cumulative bending angle along the ray. A thin phase screen approach to this problem is discussed in Chapter 2. There the scalar diffraction integral, which is a convolution integral over the vertical continuum of emitters in a thin screen model, is used to calculate the phase and amplitude of the emitted wave at a point some distance from the thin screen. In that essentially wave/optics approach, the thin screen serves as a surrogate for the actual atmosphere. The radiation field from the emitters in the screen mimics the phase and amplitude effects on the electromagnetic wave resulting from propagating through the actual atmosphere, including the effects from the refractive gradient and from the embedded scattering surface. Fresnel diffraction, interference, shadowing, caustics, etc., all can be evaluated using the thin phase screen approach combined with the scalar diffraction integral.

A wave theory approach is based on solutions to Maxwell's equations applied to a spherical atmosphere. A convolution integral also appears in wave theory, but it is over spectral number instead of thin screen altitude. The wave theory approach can be considered more accurate, albeit computationally more expensive. In both approaches, thin-screen/scalar diffraction theory and wave

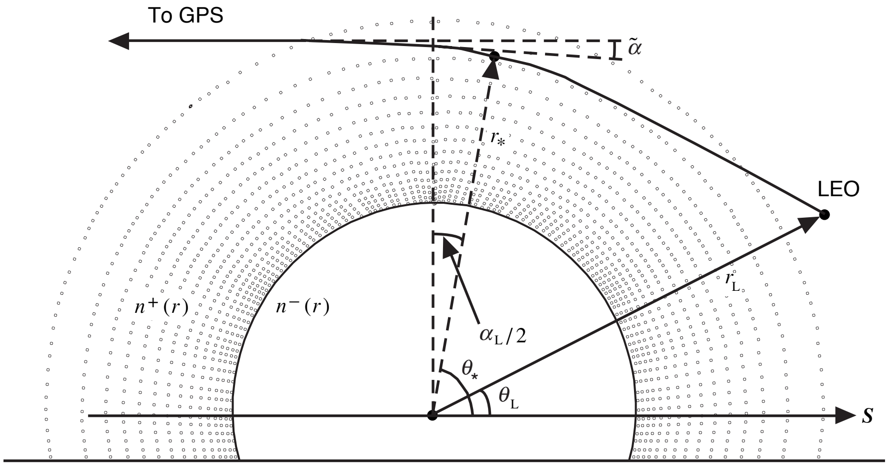

Fig. 5-1. Ray path geometry for a scattering sphere embedded in a stratified medium. The profiles for the index of refraction are given by $n^-(r)$ inside the sphere and by $n^+(r)$ outside the sphere.

theory, one ends up with a prediction of the observed phase and amplitude of the wave at some point as a result of its passing through an intervening atmosphere and perhaps encountering an embedded scattering surface. One question addressed here is the level of agreement between these two approaches, and how that level depends on the adversity of the wave propagation conditions in the atmosphere.

One concludes from a review of wave propagation literature that scattering theory in a sphere is potentially a very complicated problem. For example, see the survey article by Chapman and Orcutt [1] on wave propagation problems in seismology. There one finds refracted rays reflecting from multiple surfaces, Rayleigh and Love waves skittering along boundaries, super-refracted waves with multiple reflections ducted along between layers, and so on. Here we specifically rule out ducting, evanescence, or other confounding propagation effects, except for the effects resulting from the class of discontinuities under study here, which would include interference, shadow zones, caustics, diffraction, and super-refractivity. We assume that embedded in and co-centered with this refracting medium is a single large spherical scattering surface. Across this surface a discontinuity in the refractivity model is assumed to exist. This discontinuity can take different forms, ranging from a discontinuity in *n* itself, or in its gradient, or to a discontinuity merely in one of its higher derivatives. We must account for the effects of the refractive gradient in the overlying medium surrounding the sphere on the phase and amplitude of the electromagnetic wave. Therefore, scattering in this context includes external reflection from the scattering sphere, transmission through and refraction by the scattering sphere, including the possibility that the scattered wave has undergone one or more reflections inside the scattering sphere, and finally the refractive bending of the scattered ray from the overlying medium.

For the purpose of comparing results from the full-wave theory approach with the scalar diffraction/thin phase screen approach, we assume that the local gradient of the refractivity is sufficiently small throughout the medium surrounding the scattering sphere so that the "thin atmosphere" conditions [see Section 2.2, Eqs. (2.2-8) and (2.2-9)] apply. Where rapid changes in refractivity are encountered—for example, at the boundary of a super-refracting water vapor layer—we assume that such changes are sufficiently localized that ray optics is still valid, i.e., rays do exist that pass through such a barrier, for at least a certain range of tangency points.

The wave theory approach followed here is derived from Mie scattering theory, but it is adapted to a medium with a continuously changing refractivity. The original formulation of Mie scattering theory [2] deals with a single spherical scattering surface in an otherwise homogeneous medium. Numerical wave theory approaches involve approximations to the solutions of Maxwell's equations in one form or another. In this chapter, we use an osculating parameter technique for dealing with the spectral integrals associated with wave theory. The accuracy of such a technique and its range of applicability are important questions that need to be addressed. The accuracy and range of applicability depend on the choice of basis functions used in the osculating parameter technique. For example, in a Cartesian-stratified medium, the use of sinusoids as the basis functions results in an osculating parameter solution that is identical to the Wentzel–Kramer–Brillouin (WKB) solution. The conditions for attaining a given accuracy and ascertaining its range of applicability are well established for WKB solutions. There also is a wealth of literature on the connection problem in WKB solutions across the transition zone between the oscillatory and exponential-decaying branches, important for quantum tunneling processes and other applications. Fortunately, we are concerned with the electromagnetic field away from turning points; therefore, asymptotic forms applicable to the oscillatory branch play an important role here. For a different choice of basis functions, the osculating parameter solutions do not reduce to the WKB forms and have a different range of applicability. Here the favored basis functions are the spherical Bessel functions or their Airy function surrogates, which are asymptotically equivalent when the radius of the scattering surface is very large compared to the wavelength of the electromagnetic wave. These particular basis functions offer a wide range of applicability for the osculating parameter solutions. Even at a turning point, a bête noir for wave theory, these basis functions provide a useful, if not completely successful, approach.

The question arises concerning the many sections to follow as to which parts are essential to this wave theory approach. Sections 5.2 and 5.3 provide a brief review of the basic general concepts in classical electrodynamics involving harmonic waves: Maxwell's equations, scalar potentials for generating the electromagnetic field vectors, and series solutions using the separation of variables technique. These series involve spherical harmonic functions, which apply for spherical symmetry, but special functions are needed for the radial component. For the homogeneous case, these radial solutions become the spherical Bessel functions, but in general the radial functions depend on the refractivity profile of the medium. It is here that techniques like the WKB method or the osculating parameter technique arise.

Section 5.4 briefly summarizes the asymptotic approximations that are used in this chapter. A fuller account is found in Section 3.8. This section is referred to frequently in the later text.

Section 5.5 begins the adaptation of Mie scattering theory from a single large spherical surface to a concatenated series of concentric layers that in their limiting form approach a medium with a continuously varying refractivity. This section introduces a spectral density function for the phase delay induced by the refractive gradient in the medium. This quantity (defined as $G[\rho,\nu]$ in that section) essentially accounts for the extra phase delay at the radial position ρ experienced by a radial wave component of integer spectral number $l = \nu - 1/2$, which results from the refractive gradient of the medium. In a homogeneous medium, $G[\rho,\nu] \equiv 0$. We consider there the propagation of an incident wave that asymptotically is planar at large approaching distances relative to the scattering sphere. The adjustments to account for a spherical approaching wave (when the emitting Global Positioning System (GPS) satellite is placed only a finite distance away) are noted.

Section 5.6 reviews several important concepts from geometric optics that are needed later when correspondences are established between these concepts and certain properties from wave theory when the spectral number assumes a stationary phase value. Geometric optics is discussed in Appendix A, but here, in addition to discussing the stationary phase property of a ray and its bending angle and phase delay, this section also introduces the concept of a cumulative bending angle along the ray, which mainly arises when evaluating the electromagnetic field within the refractive medium. This section also discusses Bouguer's law and the impact parameter of a ray, the geometric optics equivalent of the conservation of angular momentum in a conservative force field. This section also covers defocusing and the first Fresnel zone. Limitations in second-order geometric optics, which arise in association with caustics or when two or more rays have impact parameter separations that are less than the first Fresnel zone, are discussed in Section 5.12.

Section 5.7 develops more asymptotic forms needed later. The ratio of the radius of curvature of the stratified surface to the wavelength of the incident wave, r_o / λ, is sufficiently large that asymptotic forms for the Bessel functions apply. Also, because only spectral numbers that are of the same order of magnitude as r_o / λ contribute significantly to the spectral integrals representing the field, we also can use the asymptotic forms for the harmonic functions that apply for large spectral number. Section 5.7 shows the close correspondence between certain geometric optics quantities—for example, the cumulative bending angle of a ray with an impact parameter value, ν, and evaluated at a radial position, ρ, and a certain spectral quantity from wave theory, $\partial G[\rho,\nu] / \partial \nu$. The issue of a breakdown in accuracy of the osculating parameter technique near a turning point $\nu = \rho$ also is addressed here. The behavior of the WKB solutions near a turning point is used to provide guidance in dealing with this breakdown. An asymptotic matching technique is developed to set the value of $G[\rho,\nu]$ for the regime $\nu > \rho$.

Section 5.8 begins the representation of the electromagnetic field in terms of the spectral integrals involving the spectral components of the radial osculating parameter functions and the harmonic functions for the angle coordinates.

This discussion is continued in Section 5.9, where a phasor representation for the integrands in these spectral integrals is introduced. The stationary phase technique also is introduced here. It is used to determine spectral number points that yield stationary values of the phasor, thereby aiding the numerical evaluation of the spectral integrals.

Section 5.10 compares results from wave theory with results from a thin phase screen model combined with the scalar diffraction integral. Correspondences between stationary phase values of certain wave theoretic quantities and their analogs in geometric optics are discussed.

Section 5.11 deals with the turning point problem using an Airy layer.

Section 5.12 discusses caustics and multipath from a wave theoretic point of view in a spectral number framework. It also discusses caustics and multipath in a second-order geometric optics framework, including its shortcomings near caustics or in dealing with ray pairs with nearly merged impact parameters. Third-order stationary phase theory is introduced to develop a ray theory that can accurately deal with these situations. Beginning in Section 5.12, numerical solutions for the spectral representation of the field at the LEO are presented. Here the numerical integrations have been aided by the stationary phase technique to identify contributing neighborhoods in spectral number, greatly improving the efficiency of the technique.

Section 5.13 deals with a spherical scattering surface embedded in an overlying refracting medium.

Finally, Section 5.14 discusses the perfectly reflecting sphere that is embedded in an overlying refracting medium. This section also discusses the correspondence between geometric optics quantities and wave theory quantities when stationary phase values are used in each system. For example, at a LEO position sufficiently away from the shadow boundary of the reflecting sphere, the stationary phase values in spectral number in wave theory closely correspond to ray path impact parameter values that satisfy the law of reflection.

5.2 Maxwell's Equations in a Stratified Linear Medium

We follow closely the development given in Section 3.2 for the homogeneous case; the relevant symbols are defined in that section (see also the Glossary). Here Gaussian units are used. A harmonic electromagnetic wave may be written in the form

$$\left.\begin{aligned}\boldsymbol{E} &= \boldsymbol{E}(\boldsymbol{r})\exp(-i\omega t)\\ \boldsymbol{H} &= \boldsymbol{H}(\boldsymbol{r})\exp(-i\omega t)\end{aligned}\right\} \tag{5.2-1}$$

Maxwell's equations for the time-independent components in a linear medium, free of charge and current densities, are given by

$$\nabla\times\boldsymbol{E} = ik\mu\boldsymbol{H} \tag{5.2-2a}$$

$$\nabla\times\boldsymbol{H} = -ik\varepsilon\boldsymbol{E} \tag{5.2-2b}$$

$$\nabla\cdot(\varepsilon\boldsymbol{E}) = 0 \tag{5.2-2c}$$

$$\nabla\cdot(\mu\boldsymbol{H}) = 0 \tag{5.2-2d}$$

Here ε is the electrical permittivity of the propagation medium, μ is its magnetic permeability, and $k = 2\pi/\lambda$; k is the wave number of the harmonic wave in a vacuum, $\omega = kc$, where c is the velocity of light. These equations in Eq. (5.2-2) may be recast through successive vector calculus operations into separate vector wave equations that $\boldsymbol{E}$ and $\boldsymbol{H}$ must individually satisfy [3]. These are given by

$$\nabla^2\boldsymbol{E} + \mu\varepsilon k^2\boldsymbol{E} + \nabla(\log\mu)\times(\nabla\times\boldsymbol{E}) + \nabla\left[\boldsymbol{E}\cdot(\nabla(\log\varepsilon)\right] = 0 \tag{5.2-3a}$$

$$\nabla^2\boldsymbol{H} + \mu\varepsilon k^2\boldsymbol{H} + \nabla(\log\varepsilon)\times(\nabla\times\boldsymbol{H}) + \nabla\left[\boldsymbol{H}\cdot(\nabla(\log\mu)\right] = 0 \tag{5.2-3b}$$

Here the identity $\nabla\times\nabla\times\boldsymbol{A} = \nabla(\nabla\cdot\boldsymbol{A}) - \nabla^2\boldsymbol{A}$ is used. These are the modified wave equations that the time-invariant component of a harmonic wave must satisfy in a linear medium.

We assume now that the medium is spherical stratified. In this case, the index of refraction is a function of only the radial coordinate,

$$n(r) = \sqrt{\mu(r)\varepsilon(r)} \tag{5.2-4}$$

It follows for this case that the gradient vectors of $\varepsilon(r)$ and $\mu(r)$ are radial directed, which simplifies Eq. (5.2-3).

For the special case where $\mu \equiv 1$ throughout the medium, which is essentially the case for L-band radio signals in the neutral atmosphere, Eq. (5.2-3) is further simplified. In the special case where $\boldsymbol{E}$ is perpendicular or transverse to $\boldsymbol{r}$, which is the so-called transverse electric (TE) wave, then $\nabla\varepsilon \cdot \boldsymbol{E}_{\mathrm{TE}} \equiv 0$ and Eq. (5.2-3a) becomes

$$\nabla^2 \boldsymbol{E}_{\mathrm{TE}} + n^2 k^2 \boldsymbol{E}_{\mathrm{TE}} = 0 \tag{5.2-5}$$

Equation (5.2-5) is nearly the Helmholtz equation [see Section 3.2, Eq. (3.2-1c)] except for the radial dependency of $n(r)$. This variation of $n(r)$ will be very slight in our case of a thin atmosphere, except possibly at a boundary. But, because r_o / λ is so large, even a small variation, δn, results in a significant change, $k\delta n$, in the gradient of the phase accumulation of the wave.

5.2.1 Scalar Potential Functions

Following the approach in Section 3.2 for Mie scattering theory, we use the scalar potential functions for the electromagnetic field in a stratified medium expressed as a series summed over integer spectral number. It is convenient to express the electromagnetic field vectors in terms of vector calculus operations on a pair of scalar potentials, ${}^{\mathrm{e}}\Pi(r,\theta,\phi)$ and ${}^{\mathrm{m}}\Pi(r,\theta,\phi)$. In Section 3.2, it is shown [3] for the case where ε and μ are constant that these two scalar potentials are linearly independent solutions to the Helmholtz equation:

$$\nabla^2 \Pi + k^2 n^2 \Pi = 0 \tag{5.2-6}$$

where, in Section 3.2, n is a constant. Each solution for a homogeneous medium can be represented using the technique of separation of variables in spherical coordinates as a series expansion. The series is expressed in terms of spherical Bessel functions of integer order l, which are a function of the radial coordinate $\rho = nkr$, and the spherical harmonic functions of degree m and order l, which are functions of the angular coordinates θ and ϕ. Here θ is the angle between $\boldsymbol{r}$ and the z-axis. The latter is the axis of propagation [the asymptotic direction of the Poynting vector $\boldsymbol{S}$ (Fig. 5-1)] for the approaching wave. Also, ϕ is the azimuth angle about the z-axis. See Fig. 4-10 for the definition of the coordinate frame.

The electromagnetic field vectors for the homogeneous medium are obtained from a particular vector form for the scalar potentials (first introduced by Hertz). These are given by

$$\left.\begin{aligned} \boldsymbol{E} &= \nabla\times\nabla\times\left({}^{\mathrm{e}}\Pi\boldsymbol{r}\right)+ik\mu\nabla\times\left({}^{\mathrm{m}}\Pi\boldsymbol{r}\right) \\ \boldsymbol{H} &= \nabla\times\nabla\times\left({}^{\mathrm{m}}\Pi\boldsymbol{r}\right)-ik\varepsilon\nabla\times\left({}^{\mathrm{e}}\Pi\boldsymbol{r}\right) \end{aligned}\right\} \tag{5.2-7}$$

In the electrodynamics literature, the TE and transverse magnetic (TM) waves are generated from linearly independent solutions to the Helmholtz equation in Eq. (5.2-6). In Eq. (5.2-7), the term $ik\mu\nabla\times\left[{}^{\mathrm{m}}\Pi\boldsymbol{r}\right]$ generates the electric field $\boldsymbol{E}_{\mathrm{TE}}$, which is perpendicular to $\boldsymbol{r}$, that is, a transverse electric field; this wave is known in the literature as the TE wave. Similarly, the term $-ik\varepsilon\nabla\times\left[{}^{\mathrm{e}}\Pi\boldsymbol{r}\right]$ generates a transverse magnetic field $\boldsymbol{H}_{\mathrm{TM}}$, or the TM wave. One can readily show (see Appendix I) that these expressions in Eq. (5.2-7) yield field vectors that satisfy Maxwell's equations in Eq. (5.2-2) when ε and μ are constant.

For the stratified medium with $n=n(r)$, the scalar potentials are solutions to a modified Helmholtz equation. In classical electrodynamics, there is a certain degree of arbitrariness in the definition of the scalar electric potential Φ and the vector magnetic potential $\boldsymbol{A}$ from which $\boldsymbol{E}$ and $\boldsymbol{H}$ are derived. Specifically, the electromagnetic field remains invariant if Φ and $\boldsymbol{A}$ are transformed together to some other pair of functions through a so-called gauge transformation; that is, the transformation is effected while Φ and $\boldsymbol{A}$ are constrained to satisfy a gauge condition such as that provided by the Lorentz condition [4]. The electromagnetic field is called gauge invariant. It is rooted in the symmetries in the electrodynamics equations when they are expressed in the space-time framework of Special Relativity. There, the form of the electrodynamics equations for the 4-vector $(\Phi,\boldsymbol{A})$ remains invariant under a Lorentz transformation; the 4-vector $(\Phi,\boldsymbol{A})$ is called covariant in a relativistic framework.

Similarly, the scalar potentials for the stratified medium have some degree of freedom in their definition. For the case where $n=n(r)$, it is shown in Appendix I that the electromagnetic field can be expressed through vector calculus operations on the modified scalar potentials, $\left[{}^{\mathrm{e}}\Pi\varepsilon^{1/2}\boldsymbol{r}\right]$ and $\left[{}^{\mathrm{m}}\Pi\mu^{1/2}\boldsymbol{r}\right]$. These expressions are given by

$$\left.\begin{aligned} \boldsymbol{E} &= \varepsilon^{-1}\nabla\times\nabla\times\left[{}^{\mathrm{e}}\Pi\varepsilon^{1/2}\boldsymbol{r}\right]+ik\nabla\times\left[{}^{\mathrm{m}}\Pi\mu^{1/2}\boldsymbol{r}\right] \\ \boldsymbol{H} &= \mu^{-1}\nabla\times\nabla\times\left[{}^{\mathrm{m}}\Pi\mu^{1/2}\boldsymbol{r}\right]-ik\nabla\times\left[{}^{\mathrm{e}}\Pi\varepsilon^{1/2}\boldsymbol{r}\right] \end{aligned}\right\} \tag{5.2-8}$$

The factors $\varepsilon^{1/2}$ and $\mu^{1/2}$ have been inserted into the potential terms in Eq. (5.2-8) to simplify the resulting modified Helmholtz equation that each of the scalar potentials must satisfy. These scalar potentials must satisfy modified Helmholtz equations, which are given by

$$\left.\begin{aligned} \nabla^2\,{}^{\mathrm{e}}\Pi + k^2\tilde{n}_{\mathrm{TM}}^2\,{}^{\mathrm{e}}\Pi = 0 \\ \nabla^2\,{}^{\mathrm{m}}\Pi + k^2\tilde{n}_{\mathrm{TE}}^2\,{}^{\mathrm{m}}\Pi = 0 \end{aligned}\right\} \tag{5.2-9}$$

Here the modified indices of refraction are

$$\left.\begin{aligned} \tilde{n}_{\mathrm{TM}}^2 = n^2\left[1 - \frac{r^2\varepsilon^{1/2}}{k^2n^2}\frac{d}{dr}\left(\frac{1}{r^2}\frac{d}{dr}\left(\frac{1}{\varepsilon^{1/2}}\right)\right)\right] \\ \tilde{n}_{\mathrm{TE}}^2 = n^2\left[1 - \frac{r^2\mu^{1/2}}{k^2n^2}\frac{d}{dr}\left(\frac{1}{r^2}\frac{d}{dr}\left(\frac{1}{\mu^{1/2}}\right)\right)\right] \end{aligned}\right\} \tag{5.2-10}$$

For the case where $\mu(r) \equiv 1$ throughout the medium, we note from Eq. (5.2-10) that the modified index of refraction for the TE wave reduces to the regular index of refraction. When the conditions $|\nabla n| << 1$ and $kr_o >> 1$ apply, which do apply for L-band propagation in the Earth's thin neutral atmosphere, it follows that $\tilde{n}(r)$ differs from $n(r)$ by a small amount of the order of n'' / k^2; for L-band signals in dry air, this translates into a fractional difference in refractivity of roughly parts in 10^{11}. So, for computations in neutral atmosphere conditions, we may simply use $n(r)$ in the modified Helmholtz wave equation. Therefore, we herewith drop the distinction between $\tilde{n}_{\mathrm{TE}}$ or $\tilde{n}_{\mathrm{TM}}$ and $n(r)$, and simply use $n(r)$ in the modified Helmholtz equation in the following discussion. For the ionosphere, these differences may be more significant.

5.3 Modified Spherical Bessel Functions

We assume now that our stratified medium satisfies the asymptotic condition $n(r) \to 1$ as $r \to \infty$, so that the scalar potential series solutions for the homogeneous medium in Section 3.2 can be used as asymptotic boundary conditions for the stratified case. For the stratified medium, we again seek solutions to the modified Helmholtz equation using the technique of separation of variables of the form

$$\Pi = R(r)\Theta(\theta)\Phi(\phi) \tag{5.3-1}$$

where $\Pi(r,\theta,\phi)$ may be taken as any spectral component of a scalar potential. For large values of r, where $n(r) \to 1$, we know that these solutions must approach the forms given in Chapter 3 for the homogeneous case. We also conclude because of the spherical symmetry of the propagation medium that spherical harmonic functions will be applicable; that is, the $\Theta(\theta)$ functions will be the same associated Legendre polynomials $\mathrm{P}_l^m(\cos\theta)$ of order l and degree m, and the $\Phi(\phi)$ functions will be sinusoids of the form $\exp(\pm im\phi)$. For an electromagnetic vector field, the m values are restricted to $m=\pm1$. This follows from Bauer's identity, applicable to a plane wave in a homogeneous medium (see, for example, Chapter 3, Eq. (3.2-3)), and also [3]. Referring to Fig. 1-6, Bauer's identity is obtained from the multipole expansion [4] for a spherical wave centered at the point G and evaluated at the point L. The amplitude and phase of the time-independent part of the spherical wave is given by $\exp(inkr_{\mathrm{LG}})/(nkr_{\mathrm{LG}})$. Its expansion in terms of spherical Bessel and spherical harmonic functions of the transmitter and receiver coordinates is given by

$$\left.\begin{aligned}&\frac{\exp(i\rho_{\mathrm{LG}})}{\rho_{\mathrm{LG}}}=i\sum_{l=0}^{\infty}(2l+1)\frac{\psi_l(\rho_{\mathrm{L}})}{\rho_{\mathrm{L}}}\frac{\xi_l^+(\rho_{\mathrm{G}})}{\rho_{\mathrm{G}}}\mathrm{P}_l\big(\cos(\theta_{\mathrm{G}}-\theta_{\mathrm{L}})\big),\\&\rho_{\mathrm{L}}<\rho_{\mathrm{G}},\ \rho=nkr\end{aligned}\right\} \tag{5.3-2}$$

which is obtained by applying the addition theorem for spherical harmonic functions. If we now let $\rho_{\mathrm{G}}\to\infty$ and $\theta_{\mathrm{G}}=\pi$, then $\rho_{\mathrm{LG}}\to\rho_{\mathrm{G}}+\rho_{\mathrm{L}}\cos\theta_{\mathrm{L}}$ and we can replace $\xi_l^+(\rho_{\mathrm{G}})$ with its asymptotic form for large $\rho_{\mathrm{G}}>>l$, $\xi_l^+(\rho_{\mathrm{G}})\to(-i)^{l+1}\exp(i\rho_{\mathrm{G}})$. We substitute these forms into the above expansion for the spherical wave, cancel terms, and note that $\mathrm{P}_l(-x)=(-1)^l\,\mathrm{P}_l(x)$. It follows that, for a plane harmonic wave traveling along the z-axis in a homogeneous medium, the time-independent component is given by $\exp(i\rho\cos\theta)$ and that Bauer's identity is given by

$$\exp(i\rho\cos\theta)=\sum_{l=0}^{\infty}i^l(2l+1)\frac{\psi_l(\rho)}{\rho}\mathrm{P}_l(\cos\theta),\ \rho=nkr \tag{5.3-3}$$

The vector version (for a plane wave with its electric field vector directed along the x-axis in Fig.4-10) is given by multiplying Eq. (5.3-3) by $(\hat{\boldsymbol{r}}\sin\theta\cos\phi+\hat{\boldsymbol{\theta}}\cos\theta\cos\phi-\hat{\boldsymbol{\phi}}\sin\phi)$. When the coefficients of the basis functions $R(r,l)\mathrm{P}_l^m(\cos\theta)\exp(\pm im\phi)$ in the series solution to Eq. (5.2-6) for a given vector component of the field are matched on a term-by-term basis with the corresponding coefficients in the Bauer series for the same vector component (and using the property $\partial\mathrm{P}_l/\partial\theta=-\mathrm{P}_l^1$), one finds that m is indeed restricted to $m=\pm1$. This restriction is perpetuated to the scattered field by the continuity conditions in electrodynamics that apply to the field components across a scattering boundary.[1] The form of the series solutions in this case must approach, as $r \to \infty$, the same form as that given in Chapter 3, Eq. (3.2-4). Only the $R(r)$ functions will differ from the spherical Bessel functions that apply to the homogeneous case, and these modified functions will approach the Bessel function form as $r \to \infty$. Thus, we have

$$rR = \tilde{\xi}_l^{\pm}(kr) \tag{5.3-4}$$

where $\tilde{\xi}_l^{\pm}$ is related to the spherical Hankel functions of the first (+) and second (–) kind, but modified for the stratified medium. These functions must satisfy the modified differential equation for spherical Bessel functions, which is given by

$$\tilde{\xi}_l^{\pm\prime\prime} + \left(n(r)^2 - \frac{l(l+1)}{u^2} \right) \tilde{\xi}_l^{\pm} = 0 \tag{5.3-5}$$

Here, $u = kr$ and $(*)' = d(*)/du$. See Section 3.2, Eq. (3.2-8), for the definition of these spherical Hankel functions in the case of a homogenous medium in terms of the integer Bessel functions of the first and second kind. In particular, the relationships between the modified spherical Bessel functions of the first and second kind, $\tilde{\psi}_l(u)$ and $\tilde{\chi}_l(u)$, for the stratified medium and the modified spherical Hankel functions are given by

$$\left. \begin{aligned} \tilde{\xi}_l^{+}(u) &= \tilde{\psi}_l(u) + i\tilde{\chi}_l(u) \\ \tilde{\xi}_l^{-}(u) &= \tilde{\psi}_l(u) - i\tilde{\chi}_l(u) \\ \tilde{\psi}_l(u) &= \frac{1}{2}\tilde{\xi}_l^{+}(u) + \frac{1}{2}\tilde{\xi}_l^{-}(u) \\ \tilde{\chi}_l(u) &= \frac{1}{2i}\tilde{\xi}_l^{+}(u) - \frac{1}{2i}\tilde{\xi}_l^{-}(u) \end{aligned} \right\} \tag{5.3-6}$$

For $u \to 0$, $\tilde{\psi}_l(u) \to 0$ and $\tilde{\chi}_l(u) \to \infty$.

The form of the modified spherical Hankel functions $\tilde{\xi}_l^{\pm}$ will depend on the functional form of $n(r)$. For example, let the special function for the index of refraction be given by

$$n^2 = 1 + \eta + \beta \left(\frac{r_o}{r} \right)^2 \tag{5.3-7}$$

---

[1] The quantum mechanical analog of this restriction in *m* values for a photon is that its angular momentum vector is restricted to a unit value times Planck's constant parallel or anti-parallel to $\boldsymbol{S}$, the Poynting vector.

where η and β are constants. This was introduced in [5]. From Eq. (5.3-5), it can be shown that this form offsets the spherical Hankel function in argument and spectral number:

$$\left.\begin{aligned} \tilde{\xi}_l^{\pm}(u) &= \xi_{\tilde{l}}^{\pm}(\tilde{u}) \\ \tilde{u} &= u\sqrt{1+\eta} \\ \tilde{l}^2+\tilde{l} &= l^2+l+\beta u_o^2 \end{aligned}\right\} \tag{5.3-8}$$

For a thin atmosphere, $\eta+\beta \approx 0$; these parameters may be individually chosen to match the index of refraction and its gradient at $u=u_o$. For example, for dry air at the Earth's surface, $\eta+\beta \approx 1/4\times 10^{-3}$ and $\beta \doteq -r_o n' \approx 0.2$. On the other hand, Eq. (5.3-7) does not satisfy our asymptotic boundary condition of $n(r)\to 1$ as $r\to\infty$. This form for $n(r)$ in Eq. (5.3-7) is useful for regional applications or over thin layers with boundaries on the top and bottom sides, and it has been used to study ducting, tunneling, super-refractivity, and other propagation effects in a strongly refracting medium.

Another technique, applicable when $n(r)$ assumes a general form, uses the WKB method to obtain an approximate expression for $\tilde{\xi}_l^{\pm}(u)$. We define $f_l(u)$ by

$$f_l = \frac{n^2u^2 - l(l+1)}{u^2} \tag{5.3-9}$$

The WKB approximate solution, $W_l^{\pm}(u) \doteq \tilde{\xi}_l^{\pm}(u)$, to Eq. (5.3-5) is given by [6]

$$W_l^{\pm}(u) = \left(f_l\right)^{-(1/4)} \exp\left(\pm i\int_{u_o}^{u} \sqrt{f_l}\,du\right) \tag{5.3-10}$$

Depending on the sign of $f_l(u)$, $W_l^{\pm}(u)$ has either an exponential form or a sinusoidal form. The WKB method has very widespread applicability. For examples in seismology, see Chapman and Orcutt's review [1]. It also has been mentioned in Chapter 4 in regard to wave propagation through a Cartesian-stratified medium.

We will use an osculating parameter technique here. When $n(r)$ is variable, we may write

$$\left.\begin{aligned} \tilde{\xi}_l^{\pm}(u) &= a_l^{\pm}(\rho)\xi_l^{\pm}(\rho) \\ \rho &= krn(r) \\ u &= kr \end{aligned}\right\} \tag{5.3-11}$$

where $a_l^{\pm}(\rho)$ is a so-called osculating parameter. It carries the deviation in amplitude and phase of $\tilde{\xi}_l^{\pm}(u)$ from these quantities in $\xi_l^{\pm}(\rho)$ due to the variability of $n(r)$.

The general series solution for the scalar potentials in a spherical stratified medium using this osculating parameter approach is given by

$$\left.\begin{aligned}\Pi^{\pm}(r,\theta,\phi) &= \sum_{l=0}^{\infty}\left(a_l^{\pm}(\rho)\cos\phi + b_l^{\pm}(\rho)\sin\phi\right)\frac{\xi_l^{\pm}(\rho)}{\rho}\mathrm{P}_l^1(\cos\theta)\\ \rho &= krn(r)\end{aligned}\right\} \quad (5.3\text{-}12)$$

In a homogeneous medium, these spectral coefficients $a_l^{\pm}$ and $b_l^{\pm}$ are functions only of the spectral number, and their form depends on the asymptotic boundary conditions for the waveform; see Eqs. (3.2-4) through (3.2-6). In the inhomogeneous but spherical symmetric medium, these spectral coefficients $a_l^{\pm}(\rho)$ and $b_l^{\pm}(\rho)$ vary also with ρ. The technique for obtaining their variability with ρ is rather similar to one of the parabolic equation techniques [7], but here their variability with ρ is due only to the gradient of the refractivity; the geometric component of the delay is retained by the $\xi_l^{\pm}(\rho)$ functions. Our task is to determine the form of these osculating spectral coefficients in a refracting medium in which a discontinuity also may be embedded, and to evaluate the series solutions for the electromagnetic field.

5.4 Asymptotic Forms

Because the spherical Bessel functions will be used extensively in later sections, we will need their asymptotic forms in terms of the Airy functions that are applicable for very large values of $\rho = knr$ and l. These have already been presented in Chapter 3, Section 3.8. There we established that the principal contributions to the spectral coefficients come from spectral number values in the vicinity of $l = \rho$. Therefore, asymptotic forms that exploit the relatively small value of $|l-\rho|/\rho$ but the large value of ρ are appropriate. All of the asymptotic forms presented in Section 3.8 carry over to the stratified case here with the transformation $x = kr \to \rho = nkr$ in the argument of the Bessel functions, and with $y \to \hat{y}$ in the argument of the Airy functions. The argument $\hat{y}$ is a function of $\rho = knr(r)$ and ν. We have placed the caret over y to indicate its dependence on n through ρ. The key asymptotic forms used later are summarized here.

From Eqs. (3.2-8) and (3.8-9), we have for the spherical Hankel functions when $l \approx \rho$:[2]

$$\left.\begin{aligned} \xi_l^{\pm}(\rho) &\sim \sqrt{\pi K_\rho}\left(1-K_\rho^{-2}\frac{\hat{y}}{15}+\mathrm{O}\left[\rho^{-5/3}\right]\right)\left(\mathrm{Ai}[\hat{y}]\mp i\,\mathrm{Bi}[\hat{y}]\right)\\ \xi_l^{\pm\,\prime}(\rho) &\sim -\sqrt{\frac{\pi}{K_\rho}}\left(1+K_\rho^{-2}\frac{\hat{y}}{15}+\mathrm{O}\left[\rho^{-5/3}\right]\right)\left(\mathrm{Ai}'[\hat{y}]\mp i\,\mathrm{Bi}'[\hat{y}]\right) \end{aligned}\right\},\ l \approx \rho \tag{5.4-1}$$

where $\rho = knr(r)$ and $\nu = l + 1/2$, and where $\mathrm{Ai}[\hat{y}]$ and $\mathrm{Bi}[\hat{y}]$ are the Airy functions of the first and second kind, respectively. See also [8]. For convenience we will use the spectral number l and $\nu = l + 1/2$ more or less interchangeably. The distinction between them is inconsequential because of the enormity of their values in the stationary phase neighborhoods. The argument $\hat{y}$ is given by

$$\hat{y} = \nu^{2/3}\zeta\left(\frac{\nu}{\rho}\right) \tag{5.4-2}$$

Here the auxiliary function $\zeta(\mu)$, $\mu = \nu/\rho$, and it series expansions in powers of $\left[\left(\rho^2-\nu^2\right)/\nu^2\right]$ and in powers of $[(\rho-\nu)/\nu]$ are defined in Eqs. (3.8-4) and (3.8-5) for both regimes $\mu \geq 1$ and $\mu \leq 1$. Using these expansions, we summarize the key relationships between $\hat{y}$ and ρ and ν:

$$\left.\begin{aligned} &\hat{y} = \frac{1}{4K_\nu^4}\left(\nu^2-\rho^2\right)\left[1+\frac{2}{5}\frac{\nu^2-\rho^2}{\nu^2}+\cdots\right]\\ &\hat{y} = \frac{1}{K_\rho}(\nu-\rho)\left(1-\frac{\nu-\rho}{60K_\rho^3}+\cdots\right)\\ &\nu = \rho + K_\rho\hat{y}\left(1+\frac{\hat{y}}{60K_\rho^2}+\cdots\right),\quad K_\nu = \left(\frac{\nu}{2}\right)^{1/3},\quad K_\rho = \left(\frac{\rho}{2}\right)^{1/3} \end{aligned}\right\} \tag{5.4-3}$$

These truncated series expansions for $\hat{y}$ and ν are very accurate for large values of ρ with $\nu \approx \rho$. For most stationary phase neighborhoods, the value of $\hat{y}$ will be small compared to K_ρ. Therefore, the term $K_\rho^{-2}\hat{y}/15$ in Eq. (5.4-1) can be dropped in the applications here. For GPS wavelengths, $K_\rho^{-2}/15 \approx 3\times 10^{-7}$.

---

[2] When $\rho >> l$, Eq. (5.4-1) is not appropriate. Starting from Eq. (3.8-10), it follows that $\xi_l^{\pm}(\rho) \to \mp i\,\exp(\pm i\mathrm{X})$, and $\mathrm{X} = (\rho^2-\nu^2)^{1/2} - \nu\cos^{-1}(\nu/\rho) + \pi/4 \to \rho - l\pi/2$. Hence, $\xi_l^{\pm}(\rho) \to (\mp i)^{l+1}\exp(\pm i\rho)$ for $\rho >> l$.

The quantity $K_\rho = (\pi n r/\lambda)^{1/3}$, a quasi-constant, appears frequently throughout this monograph. For GPS wavelengths at sea level, $K_\rho \approx 500$ and $2K_\rho/k \approx 30\ \mathrm{m}$. The latter turns out to be the spatial distance over which the Airy functions asymptotically transform from exponential functions to sinusoidal functions.

We also will need the asymptotic forms for the Airy functions. See [8] for a comprehensive discussion. They also are given in Chapter 3, Eq. (3.8-7), for negative values of $\hat{y}$ and by Eq. (3.8-8) for positive values.

5.5 Modified Mie Scattering in a Spherical Stratified Medium

The central task in this section is to derive the spectral density function for the phase delay incurred by the lth spectral component of the wave as a result of the refractive gradient of the medium. This function $G[\rho,\nu]$, with $\nu = l+1/2$, accounts for the extra phase delay in the lth spectral coefficient induced by only the refractive gradient of the medium. The geometric component of the phase delay is carried by the spherical Hankel function.

To follow a Mie scattering approach, we use the scalar potentials for the approaching, transmitted, and scattered wave. Electric and magnetic scalar potentials, ${}^{\mathrm{e}}\Pi^{(i)}$ and ${}^{\mathrm{m}}\Pi^{(i)}$, were discussed in Chapter 3 and also in Section 5.2. An incoming planar harmonic wave with in-plane polarization and with zero phase at $\theta = \pi/2$ can be represented by series solutions in terms of spherical Bessel functions and spherical harmonic functions. For a non-conducting homogeneous medium, these representations are given by

$$\left.\begin{aligned}
{}^{\mathrm{e}}\Pi_l &= \frac{E_0}{nk} i^{l-1} \frac{(2l+1)}{l(l+1)} \frac{\psi_l(nu)}{nu} \mathrm{P}_l^1(\cos\theta)\cos\phi \\
{}^{\mathrm{m}}\Pi_l &= \frac{H_0}{nk} i^{l-1} \frac{(2l+1)}{l(l+1)} \frac{\psi_l(nu)}{nu} \mathrm{P}_l^1(\cos\theta)\sin\phi \\
E_0\sqrt{\varepsilon} &= H_0\sqrt{\mu}; \quad u = kr, \quad n = \text{constant}
\end{aligned}\right\} \tag{5.5-1}$$

Here ${}^{\mathrm{e}}\Pi_l$ and ${}^{\mathrm{m}}\Pi_l$ are the lth spectral components of the electric and magnetic scalar potentials, respectively.

To obtain the electromagnetic field from these scalar potentials, one uses the vector curl operations on their vector form given in Eq. (5.2-7). This vector form, $(\Pi_l \boldsymbol{r})$, is known as the Hertz potential. Here E_o is the amplitude of the electric field vector that lies in the plane defined by $\phi = 0$, that is, along the $\hat{\boldsymbol{x}}$

direction in Fig. 4-10. Similarly, H_o is the amplitude of the magnetic field vector, which points in the $\hat{y}$ direction. From Maxwell's equations, it follows that $E_o\sqrt{\varepsilon} = H_o\sqrt{\mu}$.

Following that treatment for the homogeneous case, we obtain the series expansion solutions for the scalar potentials of the incoming wave in the spherical symmetric stratified medium with an index of refraction $n(u)$. Here the scalar potentials are given by

$$\left.\begin{aligned} {}^{\mathrm{e}}\tilde{\Pi} &= \frac{E_o}{nk}\sum_{l=1}^{\infty} {}^{e}a_l(nu)\frac{\psi_l(nu)}{nu}\mathrm{P}_l^1(\cos\theta)\cos\phi \\ {}^{\mathrm{m}}\tilde{\Pi} &= \frac{H_o}{nk}\sum_{l=1}^{\infty} {}^{m}a_l(nu)\frac{\psi_l(nu)}{nu}\mathrm{P}_l^1(\cos\theta)\sin\phi \\ E_o\sqrt{\varepsilon} &= H_o\sqrt{\mu}, \qquad u = kr \end{aligned}\right\} \tag{5.5-2}$$

The main difference from the homogeneous case is that we have introduced the spectral coefficients $a_l(nu)$, which are now variable with u, to account for the effects of the variability in $n(r)$. Each spectral component of these series satisfies the modified Helmholtz equation in Eq. (5.2-8); thus, the product $a_l(nu)\psi_l(nu)$ constitutes a formal solution to the modified spherical Bessel equation in Eq. (5.3-3). For each integer value of l, $a_l(nu)$ is an osculating parameter. The osculating parameter technique already has been discussed in Section 4.8 for a Cartesian-stratified medium. This technique is useful for solving certain ordinary differential equations where the rapidly varying component is carried by the basis function, $\psi_l(nu)$ in this case, and the more slowly (sometimes) varying component is carried by $a_l(nu)$.

We will need the asymptotic form for $a_l(nu)$ corresponding to an incoming wave well outside the atmosphere and its refractivity or scattering effects. The asymptotic form depends on where we place the emitting GPS satellite, either a finite or an infinite distance away, but always in the direction $\theta = \pi$. For the infinite case, the incoming waves are planar, and it follows from Eq. (5.5-1) that $a_l(nu)$ has the limit

$$a_l(nu) \underset{u\to\infty,\ n\to 1}{\longrightarrow} i^{l-1}\frac{2l+1}{l(l+1)} \tag{5.5-3a}$$

This form satisfies the asymptotic boundary condition that the approaching wave must be planar at large distances and traveling in the direction of the positive z-axis (see Eq. (4.11-1) and Fig. 4-10). The form of the approaching wave is $\exp(iu_{\mathrm{L}}\cos\theta_{\mathrm{L}})$. This is referenced to the phase on the line $\theta = \pi/2$.

For the case of the GPS satellite at a finite distance, we have to account for the arrival of a spherical wave, with its center at the transmitting GPS satellite instead of a planar or collimated wave. Referring to Fig. A-3 in Appendix A, this spherical wave is given by $\exp(iu_{\mathrm{LG}})/u_{\mathrm{LG}}$. In this case, the asymptotic form for $a_l(nu)$ is more complicated than that given in Eq. (5.5-3a) because it must correspond to the spectral component of the spherical waveform, which explicitly includes the location of the transmitter. From Section 5.3, where Bauer's identity is derived from the multipole expansion for a spherical wave, one can work out the correct asymptotic form for the spherical case. It is given by[3]

$$a_l(nu) \to Ai^{l-1}\frac{2l+1}{l(l+1)}\left(i^{l+1}\frac{\xi_l^+(u_{\mathrm{G}})}{u_{\mathrm{G}}}\right) \tag{5.5-3b}$$

---

[3] Equation (5.5-3b) follows from the homogeneous case, $n \equiv 1$, by first noting that

$$\frac{i}{u_{\mathrm{L}}}\frac{\partial}{\partial\theta_{\mathrm{L}}}\left(\frac{\exp[iu_{\mathrm{LG}}]}{u_{\mathrm{LG}}}\right) = \left(\frac{\exp[iu_{\mathrm{LG}}]}{u_{\mathrm{LG}}}\right)\left(1+\frac{i}{u_{\mathrm{LG}}}\right)\sin(\theta_{\mathrm{L}}-\chi_{\mathrm{G}})$$

where χ_{G} is the deflection angle of the straight line between the transmitting GPS satellite and the LEO (see Fig. A-3). The GPS satellite is located at $(r_{\mathrm{G}},\theta_{\mathrm{G}})$, but always in the direction $\theta_{\mathrm{G}} = \pi$. The radial component of the electric field at the LEO from the spherical wave centered at $(r_{\mathrm{G}},\theta_{\mathrm{G}})$ is given by

$$E_r(r_{\mathrm{L}},\theta_{\mathrm{L}}) = \left(\frac{\exp[iu_{\mathrm{LG}}]}{u_{\mathrm{LG}}}\right)\sin(\theta_{\mathrm{L}}-\chi_{\mathrm{G}})$$

Dropping the i/u_{LG} term, it follows that

$$E_r(r_{\mathrm{L}},\theta_{\mathrm{L}}) \doteq \frac{i}{u_{\mathrm{L}}}\frac{\partial}{\partial\theta}\left(\frac{\exp[iu_{\mathrm{LG}}]}{u_{\mathrm{LG}}}\right) = \sum_{l=0}^{\infty}(-1)^l(2l+1)\frac{\psi_l(u_{\mathrm{L}})}{u_{\mathrm{L}}^2}\frac{\xi_l^+(u_{\mathrm{G}})}{u_{\mathrm{G}}}\mathrm{P}_l^1(\cos\theta_{\mathrm{L}})$$

The right-hand side (RHS) of this equation comes from the multipole expansion for $(\exp[iu_{\mathrm{LG}}]/u_{\mathrm{LG}})$ given in Eq. (5.3-2). Equating this series form for $E_r(r_{\mathrm{L}},\theta_{\mathrm{L}})$ to the form obtained from the corresponding vector calculus operations on the trial scalar potential series [see Eqs. (5.5-7) and (5.5-8)] yields the asymptotic form for the spectral coefficients given Eq. (5.5-3b). Getting the coefficients for one component of the field, $E_r(r_{\mathrm{L}},\theta_{\mathrm{L}})$ in this case, is sufficient.

Here the phase in this asymptotic form is now referenced to the position r_{G} of the transmitting GPS satellite.[4] The amplitude A is a constant. For example, if we renormalize the amplitude by setting $A = u_{\mathrm{LG}}$, then in the limit as $r_{\mathrm{G}}, r_{\mathrm{LG}} \to \infty$, the asymptotic form for $a_l(nu)$ in Eq. (5.5-3b), but referenced to the $\theta = \pi/2$ line, approaches the form given in Eq. (5.5-3a) for the collimated wave. In any case, we will assume the collimated form in Eq. (5.5-3a) subsequently. The correction for the case of an incident spherical wave appears straightforward, and it is noted in Section 5.10 and Chapter 6.

To develop a functional form for $a_l(nu)$, we first will obtain the change in $a_l(nu)$ that results from a change in the index of refraction across a spherical boundary, which is embedded in an *otherwise homogeneous* medium and located at $r = r_o$. By applying the continuity conditions from Maxwell's equations, the spectral coefficients for the transmitted and reflected waves are expressed in terms of the spectral coefficients of the incident wave at the boundary and the change in refractivity. After obtaining the changes in the spectral coefficients that apply across a boundary, we will use a limiting procedure to obtain a continuous version for these spectral coefficients.

The change in $a_l(nu)$ obtained in this manner is characterized by a first-order differential equation. On the other hand, Maxwell's equations comprise a second-order system for this essentially two-dimensional problem. (See Section 4.11.) Therefore, this approach involves an approximation, the accuracy of which we will establish. We saw in the Cartesian case discussed in Sections 4.8 and 4.9 that this approximation works well for points sufficiently distant from a turning point and when thin atmosphere conditions apply. The same conclusions hold here, although the concept of a turning point in a wave theory approach has to be expressed in terms of both the radial coordinate ρ and the spectral number l.

Chapter 3, Sections 3.3 and 3.5, and also Chapter 4, Section 4.6 for the Cartesian case, discuss the formalism for treating standing electromagnetic waves in terms of a spectral composition of incoming and outgoing waves. In Chapter 3, the spherical Bessel function was bifurcated into the spherical

---

[4] We can use the asymptotic form

$$i^{l+1}\xi_l^{+}(u_{\mathrm{G}}) \to \left(u_{\mathrm{G}}^2/(u_{\mathrm{G}}^2-\nu^2)\right)^{1/4}\exp\left[i\left(\sqrt{u_{\mathrm{G}}^2-\nu^2}+\nu\sin^{-1}(\nu/u_{\mathrm{G}})\right)\right],\ \ \nu = l+1/2$$

in Eq. (5.5-3b) because u_{G} will be very much larger than the range of spectral numbers yielding stationary values for the spectral series. If the phase terms here are added to the spectral density function for the phase delay through the atmosphere given from the collimated case, we have the correct form for the phase for the case where the incident wave is spherical. See Section 5.10, Eq. (5.10-12). The term $\left(u_{\mathrm{G}}^2/(u_{\mathrm{G}}^2-\nu^2)\right)^{1/4}$ is related to the reduced limb distance used to convert the geometry with u_{G} finite to an equivalent geometry with u_{G} infinite.

Hankel function of the first kind to represent outgoing waves, and into its equally weighted complex conjugate, the spherical Hankel function of the second kind, to represent incoming waves. Specifically, the spherical Hankel functions of the first (+) and second (−) kinds, $\xi_l^{\pm}$, are defined by $\xi_l^{\pm} = \psi_l \pm i\chi_l$, where $\psi_l(x) = (\pi x/2)^{1/2} J_{l+1/2}(x)$ and $\chi_l(x) = (\pi x/2)^{1/2} Y_{l+1/2}(x)$, where $J_l(x)$ and $Y_l(x)$ are the integer Bessel functions of the first and second kinds, respectively. Using the asymptotic forms for the Bessel functions applicable when $x >> l$, one can readily show that ξ_l^{+} assumes the form that describes an outgoing spherical wave, and that ξ_l^{-} describes an incoming spherical wave. In a homogeneous medium, outgoing waves interior to the scattering boundary are generated from incoming waves that reflect around the origin, which the scattering coefficients b_l show as $r \to 0$. This formalism was necessary to treat internal reflections at the boundary of the scattering sphere and to isolate the scattering coefficients for an emerging wave that has undergone a specific number of internal reflections.

We adopt the same formalism here. Thus, the electric field at any point will be treated as a spectral composition of radial incoming and radial outgoing wavelets, which are combined in a weighted summation over all spectral numbers. They also are combined in such a way as to eliminate the singularity at the origin arising from the Bessel function of the second kind.

5.5.1 Incoming Waves

Let us first consider an incoming incident wave. Here the scalar potentials [see Eq. (5.5-1)] that generate $\boldsymbol{E}^{(i)}$ and $\boldsymbol{H}^{(i)}$ are given by

$$\left.\begin{aligned} {}^{\mathrm{e}}\Pi^{(i)} &= \frac{E_o}{2n_1 k} \sum_{l=1}^{\infty} {}^{\mathrm{e}}a_l^{(i)} \frac{\xi_l^{-}(n_1 u)}{n_1 u} \mathrm{P}_l^1(\cos\theta)\cos\phi \\ {}^{\mathrm{m}}\Pi^{(i)} &= \frac{H_o}{2n_1 k} \sum_{l=1}^{\infty} {}^{\mathrm{m}}a_l^{(i)} \frac{\xi_l^{-}(n_1 u)}{n_1 u} \mathrm{P}_l^1(\cos\theta)\sin\phi \end{aligned}\right\} \tag{5.5-4}$$

Here $u = kr$ is the radial coordinate expressed in phase units. The scattering boundary is located at u_o; ε_1 and μ_1 are constants that define the index of refraction [see Eq. (5.2-4)] in the homogeneous medium on the incident side of the boundary where $u \ge u_o$; $a_l^{(i)}$ is the spectral coefficient for the incoming incident wave. Because $\boldsymbol{E}^{(i)}$ and $\boldsymbol{H}^{(i)}$ are the fields for an incoming wave at the boundary, we must use the spherical Hankel functions of the second kind,

$\xi_l^- / 2$, for the radial function instead of ψ_l for determining the spectral coefficients at the boundary.[5]

Similarly, the scalar potentials for the scattered or reflected wave are given in terms of the scattering coefficients b_l by

$$\left.\begin{aligned} {}^{\mathrm{e}}\Pi^{(S)} &= \frac{E_o}{n_1 k}\sum_{l=1}^{\infty} {}^{\mathrm{e}}b_l \frac{\xi_l^+(n_1 u)}{n_1 u} \mathrm{P}_l^1(\cos\theta)\cos\phi \\ {}^{\mathrm{m}}\Pi^{(S)} &= \frac{H_o}{n_1 k}\sum_{l=1}^{\infty} {}^{\mathrm{m}}b_l \frac{\xi_l^+(n_1 u)}{n_1 u} \mathrm{P}_l^1(\cos\theta)\sin\phi \end{aligned}\right\} \tag{5.5-5}$$

Because the scattered wave is outgoing, we must use the spherical Hankel functions of the first kind, ξ_l^+, in this representation in order to match the asymptotic boundary condition as $r \to \infty$, which requires a spherical wave front from a scattering surface (and which the ξ_l^+ function indeed provides in its asymptotic form for large r). Finally, the scalar potentials for the transmitted wave, which is incoming, are given by

$$\left.\begin{aligned} {}^{\mathrm{e}}\Pi^{(T)} &= \frac{E_o}{2 n_2 k}\sum_{l=1}^{\infty} {}^{\mathrm{e}}a_l^T \frac{\xi_l^-(n_2 u)}{n_2 u} \mathrm{P}_l^1(\cos\theta)\cos\phi \\ {}^{\mathrm{m}}\Pi^{(T)} &= \frac{H_o}{2 n_2 k}\sum_{l=1}^{\infty} {}^{\mathrm{m}}a_l^T \frac{\xi_l^-(n_2 u)}{n_2 u} \mathrm{P}_l^1(\cos\theta)\sin\phi \end{aligned}\right\} \tag{5.5-6}$$

Here $a_l^{(T)}$ is the spectral coefficient for the wave transmitted across the boundary located at u_o; ε_2 and μ_2 are constants that define the index of refraction on the transmitted side of the boundary where $u \le u_o$.

To obtain the continuity conditions, consider first the electromagnetic field generated by the scalar potential ${}^{\mathrm{e}}\Pi(r,\theta,\phi)$, which generates the TM wave. From Eq. (5.2-7) and using the identity $\nabla\times\nabla\times\mathbf{A} = \nabla(\nabla\cdot\mathbf{A}) - \nabla^2\mathbf{A}$, one obtains

---

[5] Recall that $\psi_l = (\xi_l^+ + \xi_l^-)/2$. If we did use ψ_l in the scalar potential series for the incoming incident wave, we would find upon applying the continuity conditions at the boundary that the scattering coefficients $b_l(nu)$ would carry an extra "–1" term that would exactly cancel the $\xi_l^+ / 2$ part of ψ_l, effectively leaving only the $\xi_l^- / 2$ part to represent the entire field, incident plus scattered. For this case where ψ_l is used in the incident series, as $(n_2 - n_1)u \to 0$, $b_l(nu) \to -a_l^{(i)}(nu)/2$.

$$\left.\begin{aligned} \boldsymbol{E}_{\mathrm{TM}} &= (2+\boldsymbol{r}\cdot\nabla)\nabla\left({}^{\mathrm{e}}\Pi\right) - \boldsymbol{r}\nabla^2\left({}^{\mathrm{e}}\Pi\right) \\ \boldsymbol{H}_{\mathrm{TM}} &= -ik\varepsilon\nabla\left({}^{\mathrm{e}}\Pi\right)\times\boldsymbol{r} \end{aligned}\right\} \tag{5.5-7}$$

For example, using Eq. (5.5-4) for the incident wave (and using the differential equation for the spherical Bessel function, $d^2\xi_l / d\rho^2 + \left(1 - l(l+1)/\rho^2\right)\xi_l = 0$, for E_r), the field components in Eq. (5.5-7) become

$$\left.\begin{aligned}
\left[E_r^{(i)}\right]_{\mathrm{TM}} &= \left(\frac{\partial^2}{\partial r^2}\left({}^{\mathrm{e}}\Pi^{(i)}r\right) + n_1^2 k^2\,{}^{\mathrm{e}}\Pi^{(i)}r\right) \\
&= \frac{E_o^{(i)}}{n_1 u}\sum_{l=1}^{\infty} l(l+1)\,{}^{\mathrm{e}}a_l^{(i)}\,\frac{\xi_l^-(n_1u)}{2n_1u}\,\mathrm{P}_l^1\cos\phi \\
\left[E_\theta^{(i)}\right]_{\mathrm{TM}} &= \frac{1}{r}\frac{\partial^2}{\partial r\partial\theta}\left({}^{\mathrm{e}}\Pi^{(i)}r\right) = E_o^{(i)}\sum_{l=1}^{\infty}{}^{\mathrm{e}}a_l^{(i)}\,\frac{\xi_l^{\prime -}(n_1u)}{2n_1u}\frac{d\,\mathrm{P}_l^1}{d\theta}\cos\phi \\
\left[E_\phi^{(i)}\right]_{\mathrm{TM}} &= \frac{1}{r}\frac{\partial^2}{\partial r\partial\phi}\left({}^{\mathrm{e}}\Pi^{(i)}r\right) = -E_o^{(i)}\sum_{l=1}^{\infty}{}^{\mathrm{e}}a_l^{(i)}\,\frac{\xi_l^{\prime -}(n_1u)}{2n_1u}\,\mathrm{P}_l^1\sin\phi \\
\left[H_r^{(i)}\right]_{\mathrm{TM}} &\equiv 0 \\
\left[H_\theta^{(i)}\right]_{\mathrm{TM}} &= \frac{k\varepsilon}{ir}\frac{\partial}{\partial\phi}\left({}^{\mathrm{e}}\Pi^{(i)}r\right) = \frac{iH_o^{(i)}}{\sin\theta}\sum_{l=1}^{\infty}{}^{\mathrm{e}}a_l^{(i)}\,\frac{\xi_l^-(n_1u)}{2n_1u}\,\mathrm{P}_l^1\sin\phi \\
\left[H_\phi^{(i)}\right]_{\mathrm{TM}} &= \frac{ik\varepsilon}{r}\frac{\partial}{\partial\theta}\left({}^{\mathrm{e}}\Pi^{(i)}r\right) = iH_o^{(i)}\sum_{l=1}^{\infty}{}^{\mathrm{e}}a_l^{(i)}\,\frac{\xi_l^-(n_1u)}{2n_1u}\frac{d\,\mathrm{P}_l^1}{d\theta}\cos\phi \\
E_o^{(i)}\sqrt{\varepsilon_1} &= H_o^{(i)}\sqrt{\mu_1},\quad \mathrm{P}_l^1 = \mathrm{P}_l^1(\cos\theta)
\end{aligned}\right\} \tag{5.5-8}$$

We can write a set of expressions of a similar form for the scattered fields, $\boldsymbol{E}^{(S)}$ and $\boldsymbol{H}^{(S)}$, and for the transmitted fields, $\boldsymbol{E}^{(T)}$ and $\boldsymbol{H}^{(T)}$. Using the symmetry properties of the electromagnetic field discussed in Section 3.2, one also can readily develop a set of expressions from ${}^{\mathrm{m}}\Pi$ for the TE wave. The complete field is given by the sum of these TM and TE expressions.

To obtain the required relationships between the spectral coefficients, we use the continuity conditions from Maxwell's equations that the various field components must satisfy. Across a boundary with neither surface charges nor surface currents, Maxwell's equations require the components of the electromagnetic field to satisfy the following continuity conditions:

$$\left.\begin{aligned}\boldsymbol{E}_{\text{tang}}^{(i)}+\boldsymbol{E}_{\text{tang}}^{(S)}=\boldsymbol{E}_{\text{tang}}^{(T)},\quad \varepsilon_1\left(\boldsymbol{E}_r^{(i)}+\boldsymbol{E}_r^{(S)}\right)=\varepsilon_2\boldsymbol{E}_r^{(T)}\\ \boldsymbol{H}_{\text{tang}}^{(i)}+\boldsymbol{H}_{\text{tang}}^{(S)}=\boldsymbol{H}_{\text{tang}}^{(T)},\quad \mu_1\left(\boldsymbol{H}_r^{(i)}+\boldsymbol{H}_r^{(S)}\right)=\mu_2\boldsymbol{H}_r^{(T)}\end{aligned}\right\}\tag{5.5-9a}$$

Here ε_1 and μ_1 apply to the incident side of the boundary; ε_2 and μ_2 apply to the transmitted side.

We apply these continuity conditions to the vector fields generated from the scalar potentials in Eqs. (5.5-4) through (5.5-6) for a boundary located at $r=r_o$. The electromagnetic field for the incident TM wave is shown in Eq. (5.5-8), but because they are all similar, we forego writing the other five sets for the scattered and transmitted TM waves and for all TE modes. Applying the continuity conditions in Eq. (5.5-9a) to these waves at all applicable points on the boundary of the sphere located at $r=r_o$, we obtain an equivalent set of continuity conditions that involve only the individual spectral coefficients and their Hankel functions. These conditions written in matrix form become

$$\left.\begin{aligned}\begin{pmatrix}\dfrac{\xi_l^-(n_2u_o)}{\mu_2} & \dfrac{-\xi_l^+(n_1u_o)}{\mu_1}\\[2ex] \dfrac{\xi_l^{-\prime}(n_2u_o)}{n_2} & \dfrac{-\xi_l^{+\prime}(n_1u_o)}{n_1}\end{pmatrix}\begin{pmatrix}{}^{\text{e}}a_l^{(T)}\\ 2^{\text{e}}b_l\end{pmatrix}=\begin{pmatrix}\dfrac{\xi_l^-(n_1u_o)}{\mu_1}\\[2ex] \dfrac{\xi_l^{-\prime}(n_1u_o)}{n_1}\end{pmatrix}{}^{\text{e}}a_l^{(i)}\\ \begin{pmatrix}\dfrac{\xi_l^-(n_2u_o)}{n_2} & \dfrac{-\xi_l^+(n_1u_o)}{n_1}\\[2ex] \dfrac{\xi_l^{-\prime}(n_2u_o)}{\mu_2} & \dfrac{-\xi_l^{+\prime}(n_1u_o)}{\mu_1}\end{pmatrix}\begin{pmatrix}{}^{\text{m}}a_l^{(T)}\\ 2^{\text{m}}b_l\end{pmatrix}=\begin{pmatrix}\dfrac{\xi_l^-(n_1u_o)}{n_1}\\[2ex] \dfrac{\xi_l^{-\prime}(n_1u_o)}{\mu_1}\end{pmatrix}{}^{\text{m}}a_l^{(i)}\end{aligned}\right\},\quad l=1,2,\cdots\tag{5.5-9b}$$

Solving the linear system of equations in Eq. (5.5-9b) for the transmission and scattering coefficients in terms of the incident coefficients, we obtain

$$\left.\begin{aligned}{}^{\text{e}}a_l^{(T)}=\left[\frac{-2i}{n_1\mu_1{}^{\text{e}}\mathcal{W}_\ell}\right]{}^{\text{e}}a_l^{(i)},\quad 2^{\text{e}}b_l=-\left[\frac{{}^{\text{e}}\mathcal{W}_\ell^-}{{}^{\text{e}}\mathcal{W}_\ell}\right]{}^{\text{e}}a_l^{(i)}\\ {}^{\text{m}}a_l^{(T)}=\left[\frac{-2i}{n_1\mu_1{}^{\text{m}}\mathcal{W}_\ell}\right]{}^{\text{m}}a_l^{(i)},\quad 2^{\text{m}}b_l=-\left[\frac{{}^{\text{m}}\mathcal{W}_\ell^-}{{}^{\text{m}}\mathcal{W}_\ell}\right]{}^{\text{m}}a_l^{(i)}\end{aligned}\right\},\quad l=1,2,\cdots\tag{5.5-10}$$

where

$$\left.\begin{aligned}
{}^{\mathrm{e}}\mathcal{W}_{\ell} &= \frac{\xi_l^{+}(n_1u_o)\xi_l^{-\prime}(n_2u_o)}{n_2\mu_1} - \frac{\xi_l^{+\prime}(n_1u_o)\xi_l^{-}(n_2u_o)}{n_1\mu_2} \\
{}^{\mathrm{e}}\mathcal{W}_{\ell}^{\pm} &= \frac{\xi_l^{\pm}(n_1u_o)\xi_l^{\pm\prime}(n_2u_o)}{n_2\mu_1} - \frac{\xi_l^{\pm\prime}(n_1u_o)\xi_l^{\pm}(n_2u_o)}{n_1\mu_2} \\
{}^{\mathrm{m}}\mathcal{W}_{\ell} &= \frac{\xi_l^{+}(n_1u_o)\xi_l^{-\prime}(n_2u_o)}{n_1\mu_2} - \frac{\xi_l^{+\prime}(n_1u_o)\xi_l^{-}(n_2u_o)}{n_2\mu_1} \\
{}^{\mathrm{m}}\mathcal{W}_{\ell}^{\pm} &= \frac{\xi_l^{\pm}(n_1u_o)\xi_l^{\pm\prime}(n_2u_o)}{n_1\mu_2} - \frac{\xi_l^{\pm\prime}(n_1u_o)\xi_l^{\pm}(n_2u_o)}{n_2\mu_1}
\end{aligned}\right\}, \quad l = 1, 2, \cdots \tag{5.5-11}$$

The Wronskian of the spherical Hankel functions,

$$\mathscr{W}\left[\xi_l^{+}(z), \xi_l^{-}(z)\right] = \xi_l^{+}\xi_l^{-\prime} - \xi_l^{+\prime}\xi_l^{-} = -2i \tag{5.5-12}$$

has been used in Eq. (5.5-9b) to obtain the transmission coefficients in Eq. (5.5-10).

The "electric" coefficients $({}^{\mathrm{e}}a_l, {}^{\mathrm{e}}b_l)$ and the "magnetic" coefficients $({}^{\mathrm{m}}a_l, {}^{\mathrm{m}}b_l)$ differ from their counterparts by a small quantity of the order $N = n - 1$. Because we have assumed a thin atmosphere, $N(r) << 1$; we will ignore this difference herewith and, in the interest of simplifying the notation, we will suppress the superscripts "e" and "m" on the scattering coefficients and retain only the electric coefficients in the following. These small differences can readily be reconstituted to obtain the scattered wave from the vector calculus operations on both the electric and magnetic scalar potentials. Also, for the case where $\boldsymbol{E}$ lies in the plane $\phi = 0$, one can show that for large spectral numbers the magnetic coefficients provide a negligible contribution to the field. This follows from noting that the magnetic coefficients involve $\mathrm{P}_l^1(\cos\theta)$, whereas the electric coefficients involve $d\mathrm{P}_l^1/d\theta$. However, $\mathrm{P}_l^1/(d\mathrm{P}_l^1/d\theta) \sim l^{-1} << 1$.

We note that the GPS signals are principally right-hand circular polarized; therefore, to study polarization effects from the refracting sphere, we would need to retain the cross-plane polarization ($\phi = \pi/2$) scattering terms also, which are appropriately offset in phase to secure the proper elliptical or circular polarization. However, for $N << 1$, the scattering for the two linear polarization modes differs by an amount of the order N. Also, because of the previously mentioned relativistic covariance of the electrodynamics equations, we can exploit that symmetry to convert the solution for $\boldsymbol{H}^{(S)}$ for the in-plane polarized case discussed here directly into a solution for $\boldsymbol{E}^{(S)}$ for the cross-plane polarization case.

For outgoing waves—for example, for waves that have passed through the scattering sphere or, in a geometric optics context, rays that have passed their point of tangency with an arbitrary spherical boundary at radius $r = r_*$—one would obtain a system of transfer equations analogous to those given in Eq. (5.5-10). The only difference is that the scalar potential series for the incident and transmitted waves would each carry the $\xi_l^+ / 2$ functions instead of the $\xi_l^- / 2$ functions because they are outgoing. Also, the scalar potential series for the waves reflected from the inner side of the boundary would carry the $\xi_l^- / 2$ functions because they are incoming after being reflected.

5.5.2 Evaluating the Spectral Coefficients in a Stratified Medium

We now set $\mu(r) \equiv 1$ in the following discussion, which further simplifies the notation, albeit at the price of losing the symmetries in Eqs. (5.5-10) and (5.5-11).

Next, we treat the continuously varying refractivity in the medium as a series of concentric shells. Within each spherical shell the refractivity is a constant, but it changes discontinuously across the boundary of each shell. So, the refractivity varies in the radial direction in a stepwise manner. This is the thin-film model, or one version of the so-called onionskin model. Across each boundary, the transition equations for the spectral coefficients in Eq. (5.5-10) apply. After obtaining these spectral coefficients across the boundary of each shell, we will let the number of shells grow infinite while requiring their individual widths to become infinitesimal in such a way that the ensemble spans the appropriate physical space or range.

At the boundary located at $u_o = kr_o$, we let $n_1 = n - \Delta n / 2$ and $n_2 = n + \Delta n / 2$, where Δn is sufficiently small that $u\Delta n$ can be considered as an infinitesimal. Expanding $n_1 n_2 \mathcal{W}_\ell$ and $n_1 n_2 \mathcal{W}_\ell^{\pm}$ in powers of $u\Delta n$, we obtain

$$\left.\begin{aligned} n\mathcal{W}_\ell &= -2i - \frac{\Delta n}{2n}\Big[nu\Big(2\xi_l^{+\prime}\xi_l^{-\prime} - \xi_l^{-}\xi_l^{+\prime\prime} - \xi_l^{+}\xi_l^{-\prime\prime} \Big) \\ &\qquad + \xi_l^{+\prime}\xi_l^{-} + \xi_l^{+}\xi_l^{-\prime} \Big]_{nu_o} + \mathrm{O}\big[(u\Delta n)^2\big] \\ n\mathcal{W}_\ell^{\pm} &= -\frac{\Delta n}{n}\Big[nu\Big(\xi_l^{\pm\prime}\xi_l^{\pm\prime} - \xi_l^{\pm}\xi_l^{\pm\prime\prime} \Big) + \xi_l^{\pm\prime}\xi_l^{\pm} \Big]_{nu_o} + \mathrm{O}\big[(u\Delta n)^2\big] \end{aligned}\right\} \qquad (5.5\text{-}13)$$

It follows that as $\Delta n \to 0$, $\mathcal{W}_\ell^{\pm} \to 0$, but $n\mathcal{W}_\ell \to -2i$. From Eq. (5.5-11), it follows that $b_l \to 0$ and that $a_l^{(T)} \to a_l^{(i)}$ when $\Delta n \to 0$.

For a series of concatenated shells, multiple internal reflections should be considered. For example, outward-reflected rays from inner shell boundaries again will be reflected inward at the boundary of interest. We already have discussed this in Section 4.8 for Cartesian layers, and Fig. 4-8 in that section applies here as well. Specifically, we can use the discussion in Section 4.12 to transform our spherical geometry here into an equivalent Cartesian-stratified geometry involving Airy layers. By this means, conclusions drawn from the Cartesian case can be applied here. In Section 4.8, we showed that the ensemble of doubly reflected rays that adds to the incident wave each involves a factor of the order of Δn^2 (here Δn is the average change in index of refraction from layer to layer). Moreover, the phase of these secondary rays (at the right-hand boundary of the *j*th layer in Fig. 4-8) will be distributed randomly when the span Δr of the layers is such that $\Delta r >> \lambda$. It can be shown by vector summing up the contributions from all of these reflected rays with a second reflection from the left-hand boundary of the *j*th layer that the ratio of their combined contributions to the main ray contribution is given by $n'\lambda$, which is negligible for a thin atmosphere. Therefore, in calculating the spectral coefficients for the transmitted wave through a transparent medium, we can neglect secondary and higher-order reflections in our shell model when thin-atmosphere conditions apply and provided that we avoid turning points.

The incident field at the *j* + 1st boundary can be considered as the product of the transmission coefficients from the previous *j* layers. If we then expand that product and retain only the first-order terms, we can obtain a first-order differential equation for the spectral coefficients. The range of validity of this linear truncation is essentially the same as that found for the truncation of the characteristic matrix to linear terms given in Section 4.4. There we found for a thin atmosphere that the accuracy of this truncation was satisfactory provided that we stay clear of turning points.

Let us define $(a_l^-)_j$ to be the lth spectral coefficient of an incoming transmitted wave for the *j*th layer. The superscript "–" on a_l^- denotes an incoming wave. We drop herewith the superscripts "*i*" and "*T*". Then, using Eqs. (5.5-10) and (5.5-13), it follows that

$$\left(a_l^-\right)_{j+1} \doteq \left(a_l^-\right)_j \left[\frac{1+\Delta n/2n}{1-ig_l\Delta n/n}\right]_j \tag{5.5-14}$$

where $g_l(\rho_j)$ is a function of the spherical Hankel functions obtained from Eq. (5.5-13), which is defined in Eq. (5.5-19) and will be discussed shortly. Here we define $\rho = un(r) = krn(r)$. For a series of layers, it follows from Eq. (5.5-14) that

$$\left(a_l^-\right)_{k+1} \doteq \left(a_l^-\right)_1 \prod_{j=1}^{k} \left(\frac{1+\dfrac{\Delta n_j}{2n_j}}{1-ig_l\left(\rho_j\right)\dfrac{\Delta n_j}{n_j}} \right) \tag{5.5-15}$$

To evaluate Eq. (5.5-15), we note that $\log\left[\prod(*)_j\right]=\sum\left[\log(*)\right]_j$. When $g_l \Delta n_j << 1$, we can expand $\log\left[1-ig_l\left(\rho_j\right)\left(\Delta n_j / n_j\right)\right]$, retaining only first-order terms in Δn_j. Thus, Eq. (5.5-15) becomes

$$\log\left(\frac{\left(a_l^-\right)_{k+1}}{\left(a_l^-\right)_1}\right) \doteq \sum_{j=1}^{k}\left(\left(\frac{1}{2}+ig_l\left(\rho_j\right)\right)\frac{\Delta n_j}{n_j}\right) \tag{5.5-16}$$

We set[6] $\Delta n=(dn/d\rho)\Delta\rho$. Also, we define $\Delta n_j = n_{j+1}-n_j$ to be the change in the index of refraction across the *j*th boundary (Fig. 4-8), and we define $\Delta\rho_j=\rho_{j+1}-\rho_j$ to be the optical thickness of the *j*th layer. From Eq. (5.5-16), it follows that in the limit as $\Delta\rho \to 0$, we obtain

$$\frac{1}{a_l^-}\frac{da_l^-}{d\rho}=\left(\frac{1}{2}+ig_l(\rho)\right)\frac{d\log n}{d\rho} \tag{5.5-17}$$

Here $g_l(\rho)$ is defined by

$$g_l(\rho)=\left[\frac{\rho}{2}\left(\xi_l^{\pm\prime}\xi_l^{\mp\prime}-\xi_l^{\pm}\xi_l^{\mp\prime\prime}\right)+\frac{1}{4}\left(\xi_l^{+}\xi_l^{-\prime}+\xi_l^{+\prime}\xi_l^{-}\right)\right]_{\rho=un} \tag{5.5-18}$$

Bessel's equation in Eq. (5.3-3) has implicitly been used in Eq. (5.5-18). The enormity of $\rho \sim 10^8$ allows us to ignore the second term, $(\xi_l^{+}\xi_l^{-\prime}+\xi_l^{+\prime}\xi_l^{-})/4$. Using Bessel's equation to replace $\xi_l^{\pm\prime\prime}$ and dropping the relatively small term in Eq. (5.5-18), one obtains

---

[6] Note that $d\log n/d\rho=(n+udn/du)^{-1}d\log n/du$. Also, $\rho(d\log n/d\rho)=u(d\log n/du)/(1+u(d\log n/du))$. The quantity $u\,|\,d\log n/du\,|$ is the ratio of the radius of curvature (r) of the spherical boundary to the local radius of curvature of the ray ($n/|\,dn/du\,|$). It is the parameter β defined in Chapter 2, Eq. (2.2-9), which is small for a thin atmosphere (for dry air in the Earth's atmosphere at sea level this ratio is about 0.2). In a super-refracting medium, occasionally caused by a water vapor layer in the lower troposphere, $d\rho/du<0$. Across a boundary, $d\rho/du=0$, which requires reverting to the variable u in Eq. (5.5-17).

$$g_l(\rho) \doteq \frac{\rho}{2}\left(\xi_l^{+\prime} \xi_l^{-\prime} + \left(1 - \frac{l(l+1)}{\rho^2}\right)\xi_l^{+} \xi_l^{-} \right) \tag{5.5-19}$$

Figure 5-2 shows $g_l(\rho)$ versus $\hat{y}$, including its asymptotic forms. Here $\hat{y}$ is the argument of the Airy functions. The relationship between $\hat{y}$, l, and $\rho = un$ was discussed earlier in Section 5.4, Eqs. (5.4-2) and (5.4-3). It suffices here to note that $\nu = l + 1/2 \doteq \rho + \hat{y}(\rho/2)^{1/3}$ to very high accuracy when ρ is large and $\hat{y}$ is relatively small. For $\hat{y}$ values greater than about +2, $g_l(\rho)$ is dominated by the spherical Bessel function of the second kind, and it breaks sharply to very large negative values.

The derivation for $da_l^- / d\rho$ fails for this regime, $\hat{y} > 0$, because the basic assumption that $g_l \Delta n_j << 1$ in Eq. (5.5-16) is invalid when $g_l(\rho) \to \infty$ for increasing $\nu > \rho$. In fact, the correct form for $g_l(\rho)$ rapidly approaches zero for $\nu > \rho$, rather than blowing up, as the form for $g_l(\rho)$ given in Eq. (5.5-19) does. The modified Mie scattering derivation that we have used did not account for curvature terms, and it assumes that $g_l(\rho)\Delta n$ can be made a small quantity, which is not valid below a turning point. We return to this issue in Section 5.7, after a discussion of asymptotic forms. There we present one method for asymptotic matching of the $g_l(\rho)$ function given in Eq. (5.5-19) with a version that does hold for $\hat{y} > 0$.

In general the initial condition for a_l^- in Eq. (5.5-17) depends on the boundary conditions for the electromagnetic field. In a geometric optics context, the initial condition for a_l^- is a ray-specific quantity; that is, it depends

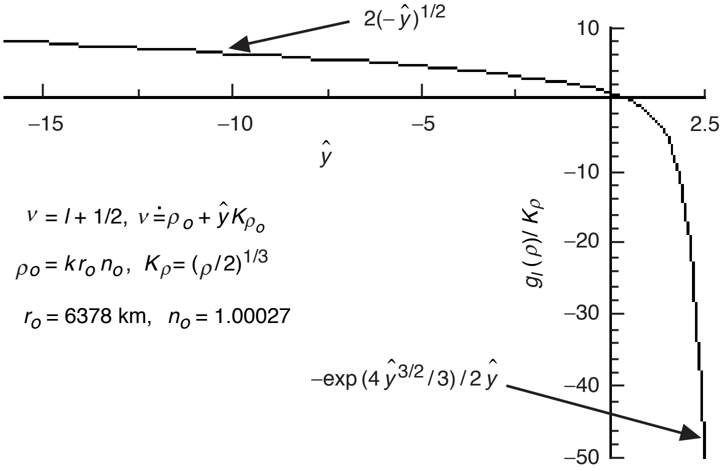

Fig. 5-2. Phase rate term $g_l(\rho)$ for spectral numbers near ρ.

at least in part on the impact parameter of the ray (or cophasal normal path) associated with the wave as it propagates through the medium. Therefore, the constant of integration obtained from integrating Eq. (5.5-17) will depend on ray-specific boundary conditions. However, in the special case where the approaching rays are collimated before encountering the medium, they all have the same asymptotic boundary condition as $u \to \infty$; in this case, the constant of integration will be invariant with impact parameter. For departing waves, this symmetry is spoiled[7] by the intervening refracting medium, and the asymptotic boundary conditions as $u \to \infty$ will vary with the impact parameter of the approaching ray.

We define the functional $G[\rho, v]$ by

$$G[\rho, v] = \int_\rho^\infty \left(\frac{d \log n}{d\rho'} \right) g_l(\rho') d\rho' \tag{5.5-20}$$

For convenience in this and in the following sections, we use the spectral number l and the parameter $v = l + 1/2$ interchangeably. The distinction between them is inconsequential because of the enormity of their values in their stationary phase neighborhoods. It is understood here that the form for $g_l(\rho)$ given in Eq. (5.5-19) must be modified so that $g_l(\rho) \to 0$ for increasing $v > \rho$.

Using the asymptotic boundary condition for $a_l^-(\rho)$ given in Eq. (5.5-3a) and noting that $\rho \to u = kr$ asymptotically with large r, the solution $a_l^-(\rho)$ can be obtained by integrating Eq. (5.5-17), and it can be written as

$$a_l^-(\rho) = n^{1/2} i^{l-1} \frac{2l+1}{l(l+1)} \exp\left(-iG[\rho, v]\right) \tag{5.5-21}$$

Thus, $-G[\rho, v]$ is the phase retardation induced by the refractive gradient in the lth spectral component of an incoming wave, which results from traveling through a transparent, spherical symmetric, refracting medium from infinity down to a radial distance r. Initially, as $r \to \infty$, the incoming wave is planar, and its spectral coefficient is given by Eq. (5.5-3a). For a homogeneous medium, $G[\rho, v] \equiv 0$.

---

[7] We could, however, form a symmetric problem merely by forcing the electromagnetic wave to be planar along the line $\theta = \pi / 2$. The boundary conditions for this case are $a_l^\pm |_{\theta=\pi/2} = i^{l-1}(2l+1)/l(l+1)$, and $a_l^\pm$ at (ρ, θ) is

$$a_l^\pm(\rho, \theta, \rho_*) = i^{l-1}(2l+1)/l/(l+1)(\exp[\mp i(G[\rho_*, v] - G[\rho, v])]),$$

where $\rho_* = \rho_*(\rho, \theta)$ from Eq. (5.6-3), which is Bouguer's law.

For thin atmospheres, the term $n^{1/2}$ in Eq. (5.5-21) is essentially unity, and it will be ignored in subsequent discussions.

5.5.3 Outgoing Waves

We have a similar expression for a radial outgoing wave. In this case, we let $\Delta a_l^+ = a_l^{(T)} - a_l^{(i)}$, where $a_l^{(i)}$ is the spectral coefficient of spectral number l for the outward traveling wave incident on the inner side of the boundary, and $a_l^{(T)}$ is the coefficient for the outward-directed transmitted wave. The scalar potential series for both of these waves uses the ξ_l^+ functions because they are outgoing waves. Also, in Eq. (5.5-9b) we must change the ξ_l^- functions to ξ_l^+ functions because $a_l^{(i)}$ and $a_l^{(T)}$ are now the spectral coefficients for outgoing waves; similarly, we must change from ξ_l^+ to ξ_l^- for b_l because the reflected wave is incoming. Working through the same boundary conditions applicable to an outgoing wave and applying the same limit procedures that held for the inward case [see Eqs. (5.5-8) through-(5.5-17)], one obtains a differential equation for the spectral coefficients of the outward-directed wave:

$$\frac{1}{a_l^+}\frac{da_l^+}{d\rho} = -i\frac{d\log n}{d\rho} g_l(\rho) \tag{5.5-22}$$

Comparing Eq. (5.5-22) with Eq. (5.5-17) (and dropping the $n^{1/2}$ term), we see that the gradients of a_l^- and a_l^+ have opposite polarities. In other words, the spatial derivative of the spectral coefficient along the radial direction of propagation is invariant to whether the wave is incoming or outgoing. This must be true from a physical consideration: the rate of phase accumulation at a given site should be the same for the radial-traveling incoming and outgoing wavelets.

We see upon integrating Eq. (5.5-22) that a_l^+ will depend on the adopted value of a constant of integration. Let us fix that constant at $r = r_*$. We write a_l^+ in the form $a_l^+[\rho,\rho_*]$ to express this dual dependency; here $\rho_* = kr_*n(\rho_*)$. Integrating Eq. (5.5-22) and using Eq. (5.5-20), we obtain

$$a_l^+[\rho,\rho_*] = a_l^+[\rho_*,\rho_*]\exp\left[-i\left(G[\rho_*,\nu] - G[\rho,\nu]\right)\right] \tag{5.5-23}$$

If we let $r \to \infty$, which would be appropriate when observing the refracted wave from outside the refracting medium, such as the neutral atmosphere observed from a LEO, then $G[\rho,\nu] \to 0$ and one obtains

$$a_l^+[\infty,\rho_*] = a_l^+[\rho_*,\rho_*]\exp\left(-iG[\rho_*,\nu]\right) \tag{5.5-24}$$

The phase retardation incurred by the νth wavelet in traveling outward from r_* to infinity is $-G[\rho,\nu]$, which is the same retardation incurred by the inward traveling wavelet from infinity down to r_*.

The actual value(s) of $a_l^+[\rho_*,\rho_*]$ will depend in part on the physical properties assumed for the refracting and perhaps scattering atmosphere, and also in part on the impact parameter(s) associated with the ray(s). For example, if $dn/dr \equiv 0$ for $r < r_o$, then Eqs. (5.5-17) and (5.5-22) show that both a_l^- and a_l^+ will be constant in that region. They also must be equal there to avoid the Hankel function singularity at the origin. (Recall the definition of the spherical Bessel function of the first kind, $\psi_l = (\xi_l^+ + \xi_l^-)/2$, which is well-behaved at the origin.) It follows in this case that $a_l^+[\rho_o,\rho_o] = a_l^-(\rho_o)$, where $a_l^-(\rho_o)$ is given from Eq. (5.5-21) and it is the applicable spectral coefficient for an incoming wave that was initially planar. At the LEO, in this case we would have

$$a_l^+[\infty,\rho_o] = i^{l-1}\frac{2l+1}{l(l+1)}\exp\left(-i2G[\rho_o,\nu]\right) \tag{5.5-25}$$

Thus, $-2G[\rho_o,\nu]$ is the total phase delay incurred by the lth spectral coefficient of an initial plane wave with an impact parameter ρ_o as a result of the wave passing completely through an intervening medium. We will return to this topic in a later section, where specific refracting and scattering models are discussed. We also will discuss later the accuracy of this particular spectral representation in terms of osculating parameters.

5.5.4 Correspondence between Cartesian and Spherical-Stratified Phase Quantities

In Chapter 4, we applied the thin-film concepts to a Cartesian-stratified medium to solve the wave equations expressed in terms of the unitary state transition matrix $\boldsymbol{M}[x_2,x_1]$. Central quantities in that presentation, which are given in Eq. (4.4-13), are the phase accumulation $\mathscr{A}(x,x_o)$ and its rate $\varpi(x)$ (with $\mu \equiv 1$) that results from the profile $n(x)$ in that Cartesian-stratified medium. These are

$$\left.\begin{aligned} &\mathscr{A}(x,x_o) = k\int_{x_o}^{x} \varpi(x')dx', \\ &\varpi(x) = \left(n^2(x) - n_o^2\right)^{1/2}, \ \ n_o = n(x_o) \end{aligned}\right\} \tag{5.5-26}$$

Note that $\mathscr{A}(x,x_o)$ provides the total phase accumulation of the wave along the x-axis, perpendicular to the plane of stratification, from the turning point at

x_o up to the altitude at x. It is an implicit function of the refractivity profile and the "angle of incidence" φ of the wave through the value of n_o, which is a constant for a particular wave (generalized Snell's law, $n_o = n\sin\varphi$), analogous to the impact parameter ρ_* for the spherical geometry. Thus, both $\mathscr{A}(x,x_o)$ and $\varpi(x)$ depend on the angle of incidence of the wave. Defining $\rho = kxn(x)$ for the Cartesian-stratified case, it follows from Eq. (5.5-26) that $\mathscr{A}$ may be rewritten in the form

$$\mathscr{A}(\rho,\rho_o) = \int_{\rho_o}^{\rho} \frac{\varpi}{n} d\rho' - \int_{\rho_o}^{\rho} \frac{d\log n}{d\rho'} \frac{\varpi\rho'}{n} d\rho' \tag{5.5-27}$$

The first integral provides the "geometric" phase delay ($\varpi / n = \cos\varphi$), and the second integral provides the additional phase delay resulting from the gradient of the refractivity over the interval ρ_o to ρ. The correspondence between the spectral quantities derived in this section for spherical stratification, $g_l(\rho)$ and $G[\rho,\nu]$, and their counterparts in Cartesian stratification should be clear. It is

$$\left.\begin{array}{l} G[\rho_o,\nu] - G[\rho,\nu] \Leftrightarrow \mathscr{A}(\rho,\rho_o) - \displaystyle\int_{\rho_o}^{\rho} \frac{\varpi}{n} d\rho' \\ g_l(\rho) \Leftrightarrow \dfrac{\rho\varpi(\rho,\rho_o)}{n(\rho)} \Rightarrow \rho\cos\varphi, \quad \sin^{-1}\left(\dfrac{\nu}{\rho}\right) \Leftrightarrow \varphi \end{array}\right\} \tag{5.5-28}$$

Note that this correspondence applies only for $\rho > \nu$. Here the angle of incidence φ in the Cartesian frame is related to the spectral number l in the spherical frame through the relation given in Eq. (4.12-8).

5.5.5 Absorption

The modified Mie scattering approach used here lends itself easily to a medium with mild absorption. Here the index of refraction has the form $\hat{n} = n(1+i\kappa)$, where $n(r)$ is the real component and $n\kappa$ is the imaginary component; κ is the extinction coefficient, and it is real. Because the refracting sphere is so large, κ must be a very small quantity or else the penetrating waves will be completely damped before escaping from the sphere. In any case, it follows from Eq. (5.5-17) that, when $\kappa \neq 0$, $a_l^-(\rho)$ will have an exponentially damping component in addition to a phase delay. In this case, the constant E_o, which is the amplitude of the incident wave, must be treated more carefully to account for the actual absorption through the medium. Also, in the case where the emitting GPS satellite is located at a finite distance away, ρ_{LG}, then E_o must account for the space loss in amplitude that the spherical wave emitted from the GPS satellite incurs in traveling to the LEO.

5.6 More Geometric Optics: Cumulative Bending Angle, Bouguer's Law, and Defocusing

We need a few more concepts from geometric optics for incoming and outgoing waves in order to interpret these wave theory results using the stationary phase technique. Appendix A briefly discusses deriving the ray path in geometric optics from Fermat's principle and the Calculus of Variations. We know that the path integral for the phase delay along the ray from the observed GPS satellite to the LEO, $\int n ds$, is stationary with respect to the path followed by the signal. That is, the actual path provides a stationary value for the phase delay compared with the phase delay that would be obtained by following any neighboring path with the same end points. Here s is path length. If one applies the Calculus of Variations to this phase delay integral, then one obtains Euler's equation, which is a second-order differential equation. This equation provides a necessary condition that the path must satisfy to yield a stationary value for the phase delay path integral. When the path integral is expressed in polar coordinates with r as the independent variable, then $ds = \left(1 + r^2\theta'^2\right)^{1/2} dr$, and Euler's equation becomes

$$\frac{d}{dr}\left(\frac{\partial}{\partial\theta'}\left(n\sqrt{1+r^2\theta'^2}\right)\right) - \frac{\partial}{\partial\theta}\left(n\sqrt{1+r^2\theta'^2}\right) = 0 \tag{5.6-1a}$$

Provided that n is a function only of r, this equation may be integrated once to obtain a constant of integration:

$$\frac{nr^2\theta'}{\sqrt{1+r^2\theta'^2}} = n_* r_*, \quad \theta' = \frac{d\theta}{dr}, \quad n_* = n(r_*), \quad \frac{r\theta'}{\sqrt{1+r^2\theta'^2}} = \sin\gamma \tag{5.6-1b}$$

Here θ' is related to the slope of the ray at the point (r,θ), and γ is the angle between the radius vector and the tangent vector of the ray. For planar approaching waves, i.e., for the case where the occulted GPS satellite is set infinitely far away in the $\theta = \pi$ direction, then $\gamma = \tilde{\alpha} + \theta$. Here $\tilde{\alpha}$ is the cumulative bending angle up to the point (r,θ) incurred by the ray relative to its original direction $(\theta = 0)$ as an approaching planar wave. In Appendix A, Fig. A-1, a positive value for $\tilde{\alpha}$ corresponds to a clockwise rotation of the tangent vector of the ray relative to the line $\theta = 0$. Along a ray path satisfying Euler's equation, the impact parameter $\rho_* = kn_* r_*$ must be constant when n is not a function of θ. From geometric optics, the differential bending angle $d\tilde{\alpha}$ over an infinitesimal length ds along the ray path expressed in polar coordinates is given by $d\tilde{\alpha} = (dn / dr)\sin\gamma ds$. Upon applying Eq. (5.6-1b) and integrating

$d\tilde{\alpha}$ along the ray path from the GPS satellite (assumed to be at infinity) to an approaching point (r,θ), one obtains

$$\left.\begin{aligned}&\tilde{\alpha}[r,\theta]=\tilde{\alpha}(\rho,\rho_*)=-\rho_*\int_{\rho}^{\infty}\frac{d\log n}{d\rho'}\frac{d\rho'}{\sqrt{\rho'^2-\rho_*^2}}\\&\rho=krn(r),\ \theta_*<\theta<\pi\end{aligned}\right\}\tag{5.6-2}$$

Here θ_* marks the angular coordinate of the tangency or turning point for a particular ray with an impact parameter value of ρ_*. See Fig. A-1. We note that $\theta_*=\theta_*(\rho_*)$, and also $\tilde{\alpha}$ at any approaching point (r,θ) may be considered to be a function of $\rho=rn(r)$ and the impact parameter ρ_* for the ray passing through that point. Thus, $\tilde{\alpha}=\tilde{\alpha}(\rho,\rho_*)$ and also $\tilde{\alpha}=\tilde{\alpha}[r,\theta]$. From Eqs. (5.6-1) and (5.6-2), it follows that the impact parameter $\rho_*=kr_*n(r_*)$ is given in terms of (r,θ) and $\tilde{\alpha}$ by

$$\left.\begin{aligned}&\text{Incoming: }\pi>\theta\geq\theta_*:\quad\rho_*=\rho\sin\left[\theta+\tilde{\alpha}(\rho,\rho_*)\right]\\&\text{Outgoing: }\theta_*\geq\theta>0:\quad\rho_*=\rho\sin\left[\theta+2\tilde{\alpha}(\rho_*,\rho_*)-\tilde{\alpha}(\rho,\rho_*)\right]\\&\theta_*=\frac{\pi}{2}-\tilde{\alpha}(\rho_*,\rho_*);\ \rho=krn(r)\end{aligned}\right\}\tag{5.6-3}$$

This is a version of Bouguer's law, which has been expressed for both an incoming ray ($\pi>\theta\geq\theta_*$) and for an outgoing ray ($\theta_*\geq\theta>0$). By symmetry, the bending angle for an outgoing ray is $2\tilde{\alpha}(\rho_*,\rho_*)-\tilde{\alpha}(\rho,\rho_*)$, where $\tilde{\alpha}(\rho_*,\rho_*)$ is the cumulative bending up to the turning point. The constant value of ρ_* along a given ray path is the geometric optics analog of the conservation of angular momentum in a classical mechanical system with spherical symmetry in its force field. One can solve Eqs. (5.6-2) and (5.6-3) simultaneously to obtain the values of both ρ_* and $\tilde{\alpha}(\rho,\rho_*)$ for a given position (r,θ) [which may or may not be uniquely determined, depending on the profile of $n(r)$].

We denote the coordinates (with the radial coordinate in phase units) of the LEO by $(\rho_{\mathrm{L}},\theta_{\mathrm{L}})$. When the LEO is outside of the atmosphere where $n\equiv 1$, $\tilde{\alpha}(\rho,\rho_*)\rightarrow 0$ as $\rho\rightarrow\infty$. Therefore, Bouguer's law becomes

$$\rho_{\mathrm{L}}\sin(\theta_{\mathrm{L}}+\alpha_{\mathrm{L}})=\rho_*=\text{constant},\quad\alpha_{\mathrm{L}}=2\tilde{\alpha}(\rho_*,\rho_*)\tag{5.6-4}$$

Here $\alpha_{\mathrm{L}}(\rho_*)$ is the total refractive bending angle observed by the LEO. Thus, for a given LEO position $(\rho_{\mathrm{L}},\theta_{\mathrm{L}})$, there is a one-to-one correspondence (when spherical symmetry applies) between $\alpha_{\rm L}$ and the impact parameter $\rho_* = kr_*n_*$. These relations are given by

$$\left.\begin{aligned} &\rho_* = \rho_{\rm L}\sin\left(\theta_{\rm L} + \alpha_{\rm L}(\rho_*)\right) \\ &\alpha_{\rm L}(\rho_*) = 2\tilde{\alpha}[\rho_*, \theta_*] = 2\tilde{\alpha}(\rho_*, \rho_*) = -2\rho_* \int_{\rho_*}^{\infty} \frac{d\log n}{d\rho} \frac{d\rho}{\sqrt{\rho^2 - \rho_*^2}} \end{aligned}\right\} \tag{5.6-5}$$

where (r_*, θ_*) is the turning point for a ray with an impact parameter value of ρ_*. Given a position $(\rho_{\rm L}, \theta_{\rm L})$ for the LEO, Eqs. (5.6-4) and (5.6-5) yield the values ρ_* and $\alpha_{\rm L}(\rho_*)$ that must follow in order for the LEO to observe the ray (or rays if ρ_* and $\alpha_{\rm L}$ are not uniquely determined at that position) from the GPS satellite that has been deflected as a result of refractive bending. The point of tangency of the ray on the boundary is located at an angular position $\theta = \pi/2 - \alpha_{\rm L}/2$ (for an infinitely distant GPS) and at a radial position of $r = r_*$.

Figure 5-3 shows an example of the solution to Eq. (5.6-5) for an exponential refractivity profile. In this case, the bending angle decreases monotonically with increasing impact parameter so that the solution is unique. If the refractivity profile causes the bending angle to exhibit reversals in slope, then there may be multiple solutions for a certain range of impact parameter values. We will discuss the question of uniqueness of the impact parameter and

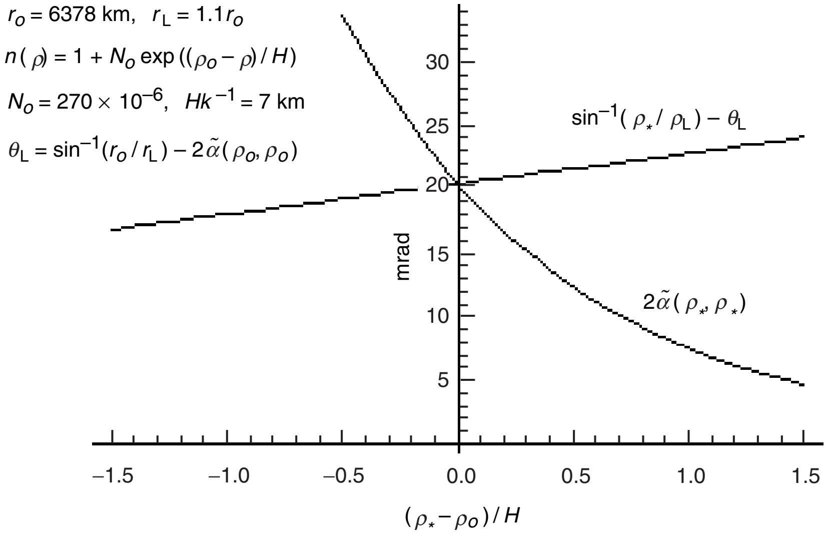

Fig. 5-3. Solution for refractive bending angle and impact parameter at the intersection of curves. Because $2\tilde{\alpha}$ is monotonic, the solution is unique.

total bending angle for a given LEO position $(\rho_{\mathrm{L}}, \theta_{\mathrm{L}})$ in Section 5.12, which also addresses multipath and ray caustics.

5.6.1 Defocusing

Because defocusing will arise when we apply the stationary phase technique in wave theory, we review it here in somewhat more detail than given in Appendix A. Defocusing arises because of dispersive refraction. Incoming rays, which were collimated prior to encountering the atmosphere, are dispersed or spread out after entering the atmosphere because of the refractive gradient. To obtain a measure of the defocusing at a given point (r, θ), we compute the ratio of the signal flux density of an incoming wave prior to encountering the atmosphere with the signal flux density at the point (r, θ). This ratio is readily obtained from Bouguer's law and by invoking the principle of conservation of energy. Let $\Delta\sigma$ be the perpendicular displacement in phase units between two rays (Fig. A-1) in the neighborhood of the point (r, θ) that results from changing the impact parameter by an amount $\Delta\rho_*$. Conservation of energy requires (assuming complete transparency) that the power through a cross section of width $\Delta\rho_*$ in the collimated beam prior to atmospheric entry must equal the power through the cross section of width $\Delta\sigma$ at the point (r, θ) after atmospheric entry. Thus, the ratio $\zeta = \Delta\rho_* / \Delta\sigma$ gives us the defocusing, and its square root gives the ratio of the signal amplitudes: the amplitude of the wave at (r, θ) divided by the amplitude of the collimated wave prior to atmospheric entry.

Upon differentiating Bouguer's law given in Eq. (5.6-3) with respect to ρ_*, and defining $\gamma = \theta + \tilde{\alpha}$, one obtains

$$\left.\begin{aligned}
&\text{Incoming: } \pi > \gamma \geq \pi/2\text{: } \Delta\rho_* = \\
&\Delta r(n + \rho n'/n)\sin\gamma + \big(\Delta\theta + \Delta\tilde{\alpha}(\rho, \rho_*)\big)\cos\gamma, \\
&\text{Outgoing: } 0 < \gamma \leq \pi/2\text{: } \Delta\rho_* = \\
&\Delta r(n + \rho n'/n)\sin\gamma + \big(\Delta\theta + 2\Delta\tilde{\alpha}(\rho_*, \rho_*) - \Delta\tilde{\alpha}(\rho, \rho_*)\big)\rho\cos\gamma
\end{aligned}\right\} \quad (5.6\text{-}6)$$

Here

$$\left.\begin{aligned}
&\Delta\tilde{\alpha}(\rho, \rho_*) = \partial\tilde{\alpha}/\partial\rho_*\Delta\rho_* + \partial\tilde{\alpha}/\partial\rho\Delta\rho, \\
&\Delta\tilde{\alpha}(\rho_*, \rho_*) = d\tilde{\alpha}/d\rho_*\Delta\rho_*, \\
&\Delta\rho = k(n + rn')\Delta r,\ \ n' = \frac{dn}{dr},\ \ k\frac{dn}{d\rho} = \frac{n'}{n + rn'},\ \ \gamma = \theta + \tilde{\alpha}
\end{aligned}\right\} \quad (5.6\text{-}7)$$

From Eq. (5.6-2), it follows that

$$\left.\begin{aligned}\frac{\partial\tilde{\alpha}}{\partial\rho_*} &= -\int_\rho^\infty \frac{\rho'}{n}\frac{dn}{d\rho'}\frac{\rho' d\rho'}{\left(\rho'^2-\rho_*^2\right)^{3/2}} = \\ &-\frac{\rho}{n}\frac{dn}{d\rho}\frac{1}{\left(\rho^2-\rho_*^2\right)^{1/2}} - \int_\rho^\infty \frac{d}{d\rho'}\left(\frac{\rho'}{n}\frac{dn}{d\rho'}\right)\frac{d\rho'}{\left(\rho'^2-\rho_*^2\right)^{1/2}}\end{aligned}\right\} \tag{5.6-8}$$

and

$$\frac{\partial\tilde{\alpha}}{\partial\rho} = \frac{\rho_*}{n}\frac{dn}{d\rho}\frac{1}{\left(\rho^2-\rho_*^2\right)^{1/2}} \tag{5.6-9}$$

On the lower line of Eq. (5.6-8) the integral is well-behaved and bounded as $\rho_* \to \rho$. For an exponential refractivity profile, this integral is very closely equal to $-\tilde{\alpha}(\rho,\rho_*)/H$. But Eqs. (5.6-8) and (5.6-9) show that $\partial\tilde{\alpha}/\partial\rho_*$ and $\partial\tilde{\alpha}/\partial\rho$ have a $(\rho^2-\rho_*^2)^{-1/2}$ singularity at $\rho=\rho_*$. In the defocusing expression, these partial derivatives are multiplied by D, which is given by

$$D = \rho\cos\gamma = \pm\left(\rho^2-\rho_*^2\right)^{1/2} \tag{5.6-10}$$

D is essentially the optical distance between the point (r,θ) and the tangency point on the circle of radius ρ_*. Here the plus sign is used for an outgoing ray and the minus sign for an incoming ray. Multiplying the expressions in Eq. (5.6-8) or Eq. (5.6-9) by D removes the singularity.

In Eq. (5.6-6), Δr and $r\Delta\theta$ are constrained to follow a displacement direction at (r,θ) that is perpendicular to the ray. From Fig. A-1, it follows that

$$\left.\begin{aligned} k\Delta r &= \Delta\sigma\sin\gamma \\ kr\Delta\theta &= \Delta\sigma\cos\gamma \end{aligned}\right\} \tag{5.6-11}$$

If these quantities in Eqs. (5.6-8) through (5.6-11) are substituted into Eq. (5.6-6) and Bouguer's law is used, one can show that the defocusing ratios are given by

$$\left.\begin{aligned}&\text{Incoming: } \pi > \gamma \geq \frac{\pi}{2}:\\&\quad n\frac{d\sigma}{d\rho_*} = 1 - \frac{\partial\tilde{\alpha}(\rho,\rho_*)}{\partial\rho_*}\rho\cos\gamma\\&\text{Outgoing: } 0 < \gamma \leq \frac{\pi}{2}:\\&\quad n\frac{d\sigma}{d\rho_*} = 1 - \left(2\frac{d\tilde{\alpha}(\rho_*,\rho_*)}{d\rho_*} - \frac{\partial\tilde{\alpha}(\rho,\rho_*)}{\partial\rho_*}\right)\rho\cos\gamma\end{aligned}\right\} \tag{5.6-12}$$

For a point located at the LEO outside of the atmosphere, $\tilde{\alpha}(\rho,\rho_*) \to 0$ as $\rho \to \infty$, and the outgoing form in Eq. (5.6-12) becomes

$$\left.\begin{aligned}\frac{d\sigma}{d\rho_*} &= 1 - 2D\frac{d\tilde{\alpha}}{d\rho_*}\\\tilde{\alpha} &= \tilde{\alpha}(\rho_*,\rho_*)\end{aligned}\right\} \tag{5.6-13}$$

Here D becomes the distance (in phase units) of the LEO from the Earth's limb minus $\rho_*\alpha_{\mathrm{L}}(\rho_*)$. In practice a GPS satellites is not infinitely distant; its orbit radius is only about 4 Earth radii. To compensate for the wave-front curvature resulting from this finite distance, it is customary to use the "reduced distance" in Eq. (5.6-13), which is defined in the same way as the "reduced mass" in two-body dynamical systems. This is given by

$$D^{-1} = D_{\mathrm{L}}^{-1} + D_{\mathrm{G}}^{-1} \tag{5.6-14}$$

This definition for D follows directly from the Fresnel approximation in the thin phase screen theory (see Section 5.11). This form for D gives a slightly more accurate measure of defocusing. It also is very useful in thin phase screen analyses for diffraction and multipath.

For a circular LEO orbit, it follows from Fig. A-1 that $\Delta\sigma = D\Delta\theta_{\mathrm{L}}$, where $\Delta\theta_{\mathrm{L}}$ is the displacement in orbital position of the LEO required to intercept two nearby rays separated in impact parameter by $\Delta\rho_*$. In this case of a circular orbit for the LEO, the defocusing equation in Eq. (5.6-13) can be written as

$$\zeta^{-1} = \frac{d\sigma}{d\rho_*} = D\frac{d\theta_{\mathrm{L}}}{d\rho_*} = 1 - 2D\frac{d\tilde{\alpha}}{d\rho_*} \tag{5.6-13$'$}$$

From Eq. (5.6-2) it follows that

$$\begin{aligned}\frac{d\tilde{\alpha}(\rho_*,\rho_*)}{d\rho_*} &= \frac{\tilde{\alpha}}{\rho_*} - \rho_*^2 \int_{\rho_*}^{\infty} \frac{d}{d\rho}\left(\frac{1}{\rho}\frac{d\log n}{d\rho}\right)\frac{d\rho}{\sqrt{\rho^2-\rho_*^2}} \\ &\doteq -\rho_* \int_{\rho_*}^{\infty} \frac{1}{n}\frac{d^2 n}{d\rho^2}\frac{d\rho}{\left(\rho^2-\rho_*^2\right)^{1/2}}, \quad \rho_* >> 0\end{aligned} \tag{5.6-15}$$

For an exponential refractivity profile, $d^2 n / d\rho^2 = -H^{-1} dn / d\rho$, and it follows that $d\tilde{\alpha} / d\rho_* \doteq -\tilde{\alpha} / H$. In this case, the defocusing is related to the deflection $2\tilde{\alpha}D$ at the LEO expressed as the number of scale heights $2\tilde{\alpha}D / H$ that refractive bending induces.

At a turning point, $\gamma = \theta + \tilde{\alpha} \to \pi / 2$. One could naïvely conclude that the defocusing factor would reduce to $1/(n_* + r_* n_*')$, which is the reciprocal of the derivative of the impact parameter ρ_* with respect to the radial coordinate kr at the turning point (r_*, θ_*). Equations (5.6-8) and (5.6-10) show that the singularity in $\partial\tilde{\alpha}(\rho,\rho_*)/\partial\rho_*$ as $\rho \to \rho_*$ yields a finite contribution to the defocusing ratio at a turning point. From Eqs. (5.6-8) and (5.6-10), Eq. (5.6-12) becomes at a turning point

$$n_* \frac{d\sigma}{d\rho_*} = 1 - \frac{\rho_*}{n_*}\left.\frac{dn}{d\rho}\right|_{\rho_*} = \frac{n_*}{n_* + r_* n_*'} \tag{5.6-16}$$

thus, confirming our intuition.

5.7 More Asymptotic Forms

We will need asymptotic forms for the functions $g_l(\rho)$ and $G[\rho, \nu]$, defined in Eqs. (5.5-19) and (5.5-20). We also must complete the unfinished business of fixing that form for $g_l(\rho)$. The derivation obtained in Section 5.5 based on modified Mie scattering fails when $\rho < \rho^{\dagger}(\nu)$. We know from Chapter 3 that the principal contributions to the scattering integrals come from spectral coefficients with wavenumber values in the near vicinity of $l = \rho_*$. Here asymptotic forms that exploit the relatively small value of $| l - \rho_* | / \rho_*$ but the large value of ρ_* are appropriate. Therefore, we use the asymptotic forms for the spherical Hankel functions in terms of the Airy functions of the first and second kind that have been given in Eq. (5.4-1).

It then follows upon replacing the spherical Hankel functions with their Airy function asymptotic forms that for $g_l(\rho)$ one obtains the following from Eq. (5.5-19):

$$\begin{gathered} g_l(\rho) \to g(\hat{y}) = \\ \pi K_\nu^2 \left(\mathrm{Ai}'[\hat{y}]^2 + \mathrm{Bi}'[\hat{y}]^2 \right) - \hat{y} \left(\mathrm{Ai}[\hat{y}]^2 + \mathrm{Bi}[\hat{y}]^2 \right) \left(1 - \frac{\hat{y}}{5K_\nu^2} + \cdots \right) \end{gathered} \tag{5.7-1}$$

Here $\nu = l + 1/2$. The quantities $\hat{y}$ and K_ν are defined in Eq. (5.4-3) in terms of ν and ρ. When $\nu \approx \rho$, we can drop the $\hat{y}/K_\nu^2$ term in Eq. (5.7-1) because of the enormity of ρ_*.

It follows from Eq. (5.5-20) that the applicable asymptotic form for $G[\rho, \nu]$ is given by

$$G[\rho, \nu] \doteq \int_\rho^\infty \left(\frac{d \log n}{d\rho'} \right) g(\hat{y}') d\rho', \;\; \hat{y}' = \zeta\left(\frac{\nu}{\rho'} \right), \;\; \rho > \rho^\dagger(\nu) \tag{5.7-2}$$

Here $\hat{y}'$ and ρ' are integration variables, and they are connected through the expression for $\hat{y}$ given in Eq. (5.4-3).

If one uses the asymptotic forms applicable to negative arguments for the Airy functions given by Eq. (3.8-7), it follows from Eq. (5.7-1) that

$$g(\hat{y}) = \left(\rho^2 - \nu^2 \right)^{1/2} \left(1 + 1 / \left(16 \hat{y}^3 \right) + \cdots \right), \;\; \nu < \rho \tag{5.7-3}$$

Similarly, from Eq. (5.7-2) it follows for negative arguments that

$$G[\rho, \nu] \doteq \int_\rho^\infty \frac{d \log n}{d\rho'} \sqrt{\rho'^2 - \nu^2} d\rho', \;\; \nu < \rho \tag{5.7-4}$$

Even at $\nu = \rho$ this asymptotic form for $G[\rho, \nu]$ is very accurate. The difference between the values of $G[\rho, \nu]$ from Eqs. (5.7-2) and (5.7-4) is roughly $0.2\beta/(1-\beta)$, yielding a relative accuracy in most conditions of a few parts in 10^5. A super-refractive region (where $\beta \geq 1$ requires special treatment; see Sections 5.8 and 6.4.

From the cumulative bending angle given by Eq. (5.6-2), we have upon integrating on ρ_*

$$\begin{aligned} \int_\nu^\rho \tilde{\alpha}(\rho, \nu') d\nu' &= \int_\rho^\infty \frac{d \log n}{d\rho'} \left[\sqrt{\rho'^2 - \rho^2} - \sqrt{\rho'^2 - \nu^2} \right] d\rho' \\ &= -\int_\rho^\infty \tilde{\alpha}(\rho', \rho') d\rho' - \int_\rho^\infty \frac{d \log n}{d\rho'} \sqrt{\rho'^2 - \nu^2} d\rho' \end{aligned} \tag{5.7-5}$$

From Eqs. (5.7-4) and (5.7-5), it follows that

$$G[\rho,\nu] \doteq -\int_{\nu}^{\rho} \tilde{\alpha}(\rho,\omega)d\omega - \int_{\rho}^{\infty} \tilde{\alpha}(\omega,\omega)d\omega, \quad \nu < \rho \tag{5.7-6}$$

We recall that $-G[\rho,\nu]$ is the phase delay induced by the spherical symmetric atmosphere upon a radial wavelet of wavenumber ν at the radial position $\rho = krn$. Equation (5.7-6) provides a physical interpretation for these integrals of the bending angle. This is similar in form to the stationary phase condition that we found for the thin-screen model in Chapter 2. We note from Eq. (5.7-6) that $-2G[\rho,\rho]$ corresponds to the thin-screen phase profile $\varphi(h)$ given in Eq. (2.5-1).

Differentiating $G[\rho,\nu]$ given in Eq. (5.7-2) with respect to ν and using the defining differential equation for the Airy functions, $\mathrm{Ai}'' = \hat{y}\,\mathrm{Ai}, \mathrm{Bi}'' = \hat{y}\,\mathrm{Bi}$, [and the near-linear relationship between $\hat{y}$ and ν given in Eq. (5.4-3)], one obtains

$$\frac{\partial G}{\partial \nu} = \int_{\rho}^{\infty} \left(\frac{d\log n}{d\rho'} \right) \frac{dg}{d\hat{y}} \frac{\partial \hat{y}}{\partial \nu} d\rho' \doteq -\pi K_{\nu} \int_{\rho}^{\infty} \left(\frac{d\log n}{d\rho'} \right) \left(\mathrm{Ai}[\hat{y}']^2 + \mathrm{Bi}[\hat{y}']^2 \right) d\rho' \tag{5.7-7}$$

For negative arguments of $\hat{y}$, we can use the negative asymptotic forms for the Airy functions; Eq. (5.7-7) becomes [alternatively, one can take the partial derivative of Eq. (5.7-4)]

$$\frac{\partial G}{\partial \nu} \doteq -\nu \int_{\rho}^{\infty} \frac{d\log n}{d\rho'} \frac{1}{\sqrt{\rho'^2 - \nu^2}} d\rho' = \tilde{\alpha}(\rho,\nu), \quad \nu < \rho \tag{5.7-8}$$

Comparing Eqs. (5.6-2) and (5.7-8), we conclude that, for negative values of $\hat{y}$, that is, for $\nu < \rho$, $\partial G[\rho,\nu]/\partial \nu$ *may be interpreted as the cumulative bending angle* $\tilde{\alpha}(\rho,\nu)$ *of an incoming ray at the radial position* r *(*$\rho = krn$*) and with an impact parameter value* ν. The accuracy of this correspondence deteriorates only when ν lies in the immediate vicinity of ρ, that is, near a turning point (r_*, θ_*) where $\theta_* = \pi/2 - \tilde{\alpha}(\rho_*, \rho_*)$.

Figure 5-4 shows the level of this agreement in the vicinity of a turning point for an exponential refractivity profile that decreases with altitude. It roughly corresponds to the dry air refractivity profile for the Earth near sea level. Only for spectral numbers in the range $\nu > \rho - \sim 2K_{\nu}$ does the agreement deteriorate. Note that $\tilde{\alpha}(\rho,\nu)$ is not defined for $\nu > \rho$ $(\hat{y} > 0)$ and that $\partial \tilde{\alpha}(\rho,\nu)/\partial \nu \to \infty$ as $\nu \to \rho^-$, whereas $G[\rho,\nu]$ and its derivatives are well-behaved in this neighborhood. However, the form for $G[\rho,\nu]$ derived in Section 5.5 and its asymptotic form, given in Eqs. (5.7-1) and (5.7-2), change rapidly with increasing $\nu > \rho$ because of the behavior of the Airy function of

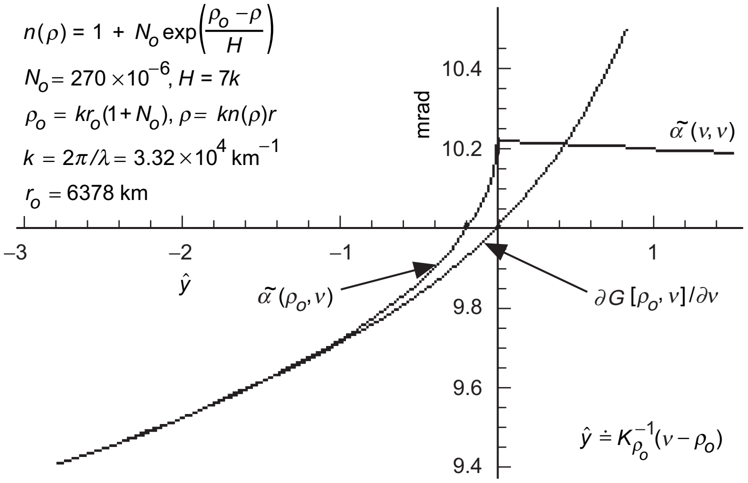

Fig. 5-4. Comparison of the gradient of the wave theory phase function $\partial G[\rho,\nu]/\partial \nu$ with the cumulative refractive bending angle $\tilde{\alpha}$ from geometric optics, in the vicinity of a turning point.

the second kind. This form fails for $\nu > \rho$. In fact, we show later that $g(\hat{y}) \to 0$ for increasing $\hat{y} > 0$, and that $G[\rho,\nu]$ approaches a constant value. The small discrepancies near the turning point result from the deviations of the Airy functions from their asymptotic forms for negative arguments, and also from the breakdown in accuracy of the spectral coefficients near a turning point when they are derived from Eq. (5.5-21). Figure 5-5 compares $\partial^2 G / \partial \nu^2$, a defocusing quantity from wave theory, with the analogous quantity $\partial \tilde{\alpha} / \partial \nu$ from geometric optics.

That there should be this very close, although not perfect, agreement between ray quantities and spectral coefficients from wave theory when the latter are evaluated at their stationary phase values should not be too surprising. In wave theory, the stationary phase process, which is discussed later, is effected over spectral number. The value $\nu = \rho_*$, which we will show to be very close to a stationary phase point in wave theory, also provides an equivalent ray in geometric optics between the GPS satellite and the point (r,θ), and with an impact parameter value of ρ_*. The ray path from geometric optics is in fact a path of stationary phase. Using geometric optics, we may vary the impact parameter over impact parameter space for a ray with constrained end points. The path has a stationary value of the phase delay when the impact parameter takes on the value $\rho_* = \nu$. Any other path with the same end points in the neighborhood of the actual ray path would present the observer at (r,θ) with a phase delay that differed from the observed phase delay by an amount that has only a second-order dependency on the coordinate and slope deviations

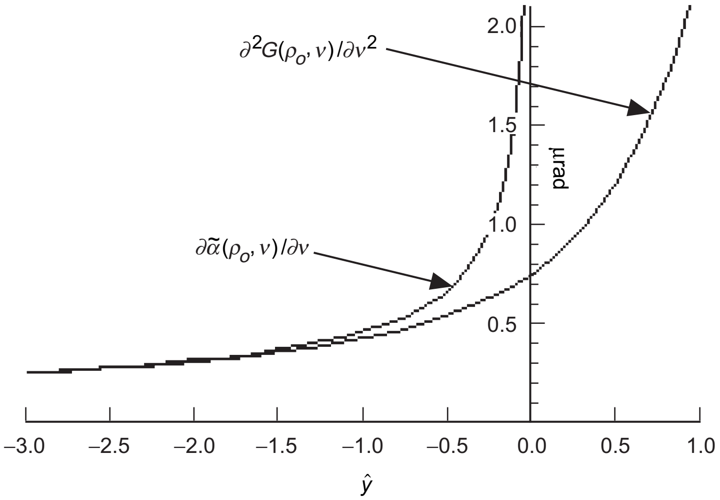

Fig. 5-5. Comparison of defocusing quantity $\partial^2 G/\partial v^2$ from wave theory with the analogous quantity $\partial\tilde{\alpha}/\partial v$ from geometric optics, in the vicinity of a turning point.

of the alternate path. This second-order variation would be due to a deviation in the value of the impact parameter. We will show that, when stationary values are assumed by the spectral number in wave theory and by the impact parameter in geometric optics, a close correspondence results.

Consider next the variability of $G[\rho, v_o]$ with r for a fixed value of the wavenumber v_o. At a point (r, θ) on the approaching side at large distances where $n \to 1$, we set $kr\sin\theta = v_o$; that is, v_o becomes the impact parameter for the ray passing through the point (r, θ). Figure 5-6 shows an example of $G[\rho, v_o]$ versus ρ in the vicinity of $\rho = v_o$. Here an exponential refractivity profile decreasing with altitude is used, but the altitude range shown in the figure is very narrow, $\sim 7K_{v_o}/k$, or about 100 meters for the parameter values shown. This is a small fraction of the refractivity scale height H (7 km) adopted in the figure. On the left side of the figure where $\hat{y} < 0$, that is, where $\rho > v_o$, the $g(\hat{y})$ function is slowly decreasing with increasing $\hat{y}$ (decreasing ρ) (see Fig. 5-2), and $G[\rho, v_o]$ decreases with increasing $\hat{y}$ because the gradient of the refractivity is negative. On the right side where $\hat{y} > 0$, $g(\hat{y})$ breaks sharply negative because of the rapid growth of the Airy function of the second kind in this region. Therefore, $G[\rho, v]$, according to the (erroneous) form given in Eq. (5.7-2), rapidly increases with increasing $\hat{y}$ because the refractivity gradient is negative in the example shown in Fig. 5-6. Therefore, $G[\rho, v]$ has a stationary value at the zero crossing of $g(\hat{y})$ near $\rho = v_o$. The correct form for $G[\rho, v]$ approaches a constant for increasing $\hat{y} > 0$. This point

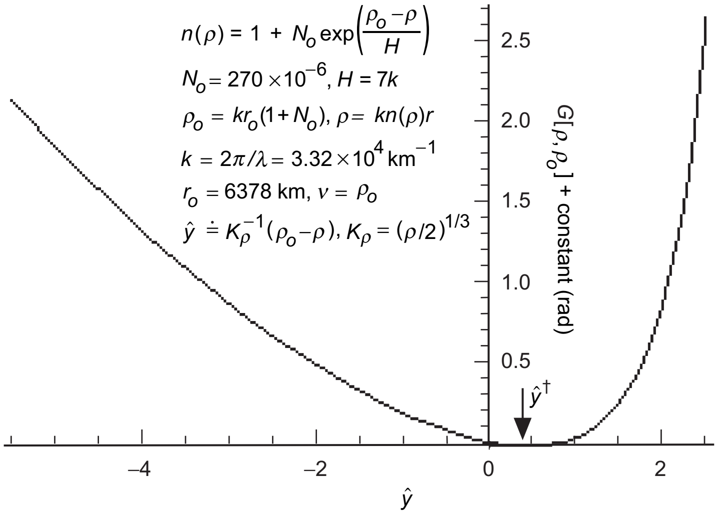

Fig. 5-6. Variation of $G[\rho, \nu_o]$ with ρ near $\rho = \nu_o = \rho_o$ obtained from Eqs. (5.7-1) and (5.7-2). This form is invalid for increasing $\hat{y} > \hat{y}^\dagger$.

where $g(\hat{y}) = 0$ marks a stationary phase point for $a_l^-(\rho)$ (with $l = \nu_o + 1/2$). It also is a stationary point for $a_l^+(\rho)$. Later, we will set $a_l^+ = a_l^-$ at this point to ensure no singularity at the origin from the spherical Hankel function.

For other refractivity profiles, there may be other stationary points for $G[\rho, \nu]$, but their occurrence and location are dependent on the functional form of the index of refraction. However, there is always one near $\rho = \nu_o$ (unless $dn/d\rho \equiv 0$), reflecting the "deepest penetration" by the corresponding ray into the sphere. This region ($\hat{y} > 0$) corresponds to refractivity features lying *below* the impact parameter, or the point of closest approach of the associated ray. Such features lying below the point of closest approach are not "felt" by the ray. Refractivity features lying near or above the point of closest approach ($\hat{y} \le 0$) are "felt" twice by the ray, incoming and outgoing; these can have a prominent effect on the shape of $G[\rho, \nu]$, depending on the actual refractivity profile.

From the definition of $G[\rho, \nu]$ in Eq. (5.7-2) and the asymptotic form for $g_l(\rho) \to g(\hat{y})$ in Eq. (5.7-1), it follows that

$$\begin{aligned}\frac{\partial G}{\partial \rho} &= -\frac{d \log n}{d\rho} g(\hat{y}) \\ &\doteq -\pi K_\nu^2 \frac{d \log n}{d\rho}\left(\mathrm{Ai}'[\hat{y}]^2 + \mathrm{Bi}'[\hat{y}]^2 - \hat{y}\left(\mathrm{Ai}[\hat{y}]^2 + \mathrm{Bi}[\hat{y}]^2\right)\right)\end{aligned} \tag{5.7-9}$$

Upon setting $\partial G/\partial\rho = 0$, it follows that either $g(\hat{y}) = 0$, or $dn/d\rho = 0$, or both are zero. Consider first $g(\hat{y}) = 0$ in Eq. (5.7-9). This yields a stationary point for $\hat{y}$ that is given by

$$\hat{y}^{\dagger} = \frac{\mathrm{Ai}'\left[\hat{y}^{\dagger}\right]^2 + \mathrm{Bi}'\left[\hat{y}^{\dagger}\right]^2}{\mathrm{Ai}\left[\hat{y}^{\dagger}\right]^2 + \mathrm{Bi}\left[\hat{y}^{\dagger}\right]^2} = 0.44133\cdots \tag{5.7-10}$$

From the properties of the Airy functions, it can be shown that this value of $\hat{y}^{\dagger}$ is unique. We have seen this quantity before in Section 4.6 in regard to turning points for waves traveling in a Cartesian-stratified Airy medium.

Upon using Eq. (5.4-3), Eq. (5.7-9) yields a stationary phase point $\rho = \rho^{\dagger}$ that is a function of ν_o and which is given by

$$\left.\begin{aligned} \rho^{\dagger} &\doteq \nu_o - K_{\rho^{\dagger}}\hat{y}^{\dagger} \\ K_{\rho^{\dagger}} &= \left(\frac{\rho^{\dagger}}{2}\right)^{1/3} \end{aligned}\right\} \tag{5.7-11}$$

Thus, $|\rho^{\dagger} - \nu_o|/\nu_o = y^{\dagger}/2K_{\rho^{\dagger}}^2 \sim 10^{-6}$ for $\nu_o \sim 10^8$.

Continuing to the second derivative, $\partial^2 G/\partial\rho^2$, and evaluating it at $\rho = \rho^{\dagger}(\nu_o)$, it follows that

$$\left.\frac{\partial^2 G}{\partial\rho^2}\right|_{\rho^{\dagger}} \doteq -\pi K_{\nu}\left.\frac{d\log n}{d\rho}\right|_{\rho^{\dagger}}\left(\mathrm{Ai}\left[\hat{y}^{\dagger}\right]^2 + \mathrm{Bi}\left[\hat{y}^{\dagger}\right]^2\right) \tag{5.7-12}$$

Setting ν_o equal to $kr_o n(r_o)$, adopting the Earth's dry air conditions at sea level, and using 19 cm for the GPS wavelength, $\partial^2 G/\partial\rho^2|_{\rho^{\dagger}} \sim 10^{-6}$ rad. It follows that G will vary from its stationary phase value by the order of 1 radian when $G|\rho - \rho^{\dagger}|/\rho^{\dagger} \sim 10^{-5}$; in other words, the stationary phase neighborhood about $\rho = \rho^{\dagger}$ is very narrow (a few dekameters) when $\rho^{\dagger}$ is so large ($\sim 2\times 10^8$).

In stationary phase theory (to be discussed in a later section), we will use $\partial^2 G[\rho,\nu]/\partial\nu^2$, which is related to defocusing. A comparison of this second derivative with $\partial\tilde{\alpha}(\rho,\nu)/\partial\nu$, also used in geometric optics for defocusing, is shown in Fig. 5-5 for the same conditions given in Fig. 5-4. These also agree closely except near a turning point. Accordingly, we expect the accuracy of the amplitude predicted by the osculating parameter technique to degrade for $\hat{y} > -2$. Numerical results verify this threshold. At a turning point, the correct value for the defocusing in a refracting medium without scattering is given by Eq. (5.6-16). At a turning point, the stationary phase value in spectral number using the osculating parameter approach is equivalent to $\hat{y} \approx 0$; it predicts unity there for the defocusing.

5.7.1 Equating $dG\left[\rho^{\dagger}(\nu),\nu\right]/d\nu$ to $\tilde{\alpha}(\nu,\nu)$ and $d^2G\left[\rho^{\dagger}(\nu),\nu\right]/d\nu^2$ to $d\tilde{\alpha}(\nu,\nu)/d\nu$

We note in Fig. 5-4 at the turning point that the value of $\partial G[\rho_o,\nu]/\partial\nu$ at $\nu = \nu^{\dagger} = \rho_o + K_{\rho_o}\hat{y}^{\dagger}$ is very close to the value of $\tilde{\alpha}(\rho_o,\rho_o)$. In fact, the actual numbers for Fig. 5-4 are 10.114 mrad for $\tilde{\alpha}(\rho_o,\rho_o)$ and 10.115 mrad for $\partial G[\rho_o,\nu]/\partial\nu$. Since $\rho = \rho^{\dagger}(\nu)$ marks a stationary point for $G[\rho,\nu]$ where $\partial G/\partial\rho = 0$, it follows that

$$\frac{dG^{\dagger}(\nu)}{d\nu} \equiv \frac{dG\left[\rho^{\dagger}(\nu),\nu\right]}{d\nu} = \left(\frac{\partial G[\rho,\nu]}{\partial\nu}\right)_{\rho=\rho^{\dagger}} \tag{5.7-13}$$

Hence, $dG^{\dagger}(\nu)/d\nu$ also will be very close in value to $\tilde{\alpha}(\nu,\nu)$. We show in Appendix J that

$$\left.\begin{aligned} &\frac{dG^{\dagger}(\nu)}{d\nu} = \tilde{\alpha}(\nu,\nu) + \mathrm{O}\left[\rho\frac{d^2n}{d\rho^2}\right] \\ &G^{\dagger}(\nu) = G\left[\rho^{\dagger}(\nu),\nu\right] \end{aligned}\right\} \tag{5.7-14}$$

Therefore, the difference between $dG^{\dagger}(\nu)/d\nu$ and $\tilde{\alpha}(\nu,\nu)$ depends on the curvature in the refractivity profile. For the thin-atmosphere conditions shown in Fig. 5-4, it can be shown that $\rho_o\left(d^2n/d\rho^2\right) \approx 10^{-3}$ mrad, which we can ignore. The difference becomes significant when near-super-refractivity conditions are encountered. See Appendix J.

Similarly, it can be shown that

$$\begin{aligned} \frac{d^2G^{\dagger}(\nu)}{d\nu^2} &\equiv \frac{d^2G\left[\rho^{\dagger}(\nu),\nu\right]}{d\nu^2} \doteq \left(-\frac{\partial^2G[\rho,\nu]}{\partial\rho^2} + \frac{\partial^2G[\rho,\nu]}{\partial\nu^2}\right)_{\rho=\rho^{\dagger}} \\ &= \frac{d\tilde{\alpha}(\nu,\nu)}{d\nu} + \mathrm{O}\left[\frac{d^2n}{d\rho^2}\right] \end{aligned} \tag{5.7-15}$$

For thin-atmosphere conditions, the curvature term here also can be dropped. Equations (5.7-14) and (5.7-15) will play key roles when we apply the stationary phase technique in wave theory to outgoing waves. Equation (5.7-14) is related to the ray bending angle, and Eq. (5.7-15) is related to defocusing.

Regarding the near-equivalence of $dG[\rho^{\dagger}(\nu),\nu]/d\nu$ and $\tilde{\alpha}(\nu,\nu)$, we note a property of Bauer's identity. It is given in cylindrical coordinates in Eq. (4.10-9). We can transform $\theta \to \theta+\alpha$ to obtain

$$\exp\left[i\rho\cos(\theta+\alpha)\right] = \sum_{l=-\infty}^{l=\infty} i^l J_l(\rho)\exp\left[il(\theta+\alpha)\right] \qquad (5.7\text{-}16)$$

Noting that $G[\rho_o,\nu]$ shows up in the exponential term in the spectral series representations for the electromagnetic field, its variability with spectral number will be related to the angle α above. Thus, we would expect $\partial G[\rho_o,\nu]/\partial\nu$ to be closely related to an angle, which turns out to be the bending angle.

5.7.2 Fixing the Form for $g(\hat{y})$ when $\hat{y}>0$ by Asymptotic Matching

We have noted the failure of the modified Mie scattering approach to secure the correct form for $g(\hat{y})$ when $\hat{y} >\sim 0$. Equation (5.7-1) predicts that $g(\hat{y}) \to \infty$ for increasing $\hat{y}>0$; in fact, $g(\hat{y})$ should approach zero. We can use the form for $g(\hat{y})$ obtained from an Airy layer as guidance. In an Airy layer with a boundary at $r=r_0$, the profile for the index of refraction is given by $n^2 = n_0^2 + 2n_0 n'(r-r_0)$, where n_0 and n' are constants. The quadratic term $(n' r_0)^2((r-r_0/r_0))^2$ is negligible.

In Chapter 4, Section 4.12, we showed that the solutions to the wave equations in a spherical Airy layer are given by the Airy functions. Let $U^{\pm}(\tilde{y})$ be a solution for the scalar field, with the top sign for an outgoing wave and the bottom sign for an incoming wave. When $\beta<1$, from Eq. (4.10-3) and Eqs. (4.12-4) through-(4.12-6) we have

$$U^{\pm}(\tilde{y}) = c^{\pm}\left(\mathrm{Ai}[\tilde{y}] \mp i\,\mathrm{Bi}[\tilde{y}]\right) \qquad (5.7\text{-}17)$$

where $c^{\pm}$ are complex constants obtained from matching this Airy function solution and its derivative at the boundary $r=r_0$ with the incoming and outgoing wave forms applicable on the other side of the boundary. The argument of the Airy functions is given by

$$\left.\begin{aligned}\tilde{y} &= \frac{1}{K_{\rho_0}|1-\beta|^{2/3}}\big((\beta-1)(\tilde{\rho}-\tilde{\rho}_0)+l-\tilde{\rho}_0\big)\\ \beta &= -\frac{n' r_0}{n_0}\\ \tilde{\rho} &= k n_0 r\end{aligned}\right\} \tag{5.7-18}$$

These forms also apply in a super-refracting medium where $\beta > 1$. Also, it is easily shown that in an Airy layer

$$\begin{aligned}\rho = krn(r) &= \rho_0 + k\big(n_0 + n' r_0\big)\big(r-r_0\big) + kn'\big(r-r_0\big)^2\\ &\doteq \tilde{\rho}_0 + (1-\beta)\big(\tilde{\rho}-\tilde{\rho}_0\big) - \beta\big(\tilde{\rho}-\tilde{\rho}_0\big)^2/\tilde{\rho}_0\end{aligned} \tag{5.7-19}$$

The quadratic term is negligible, and it is dropped. Note that $\rho_0 = \tilde{\rho}_0$. It follows that the arguments of the Airy functions are related by

$$\hat{y} \doteq \frac{1}{K_{\rho_0}}\big(l-\rho\big) = \tilde{y}|1-\beta|^{2/3} \tag{5.7-20}$$

From Eq. (5.7-17), it follows that the phase $\psi_l^{A^-}$ of the incoming Airy function solution (for $\beta < 1$) is given by

$$\psi_l^{A^-} = \tan^{-1}\left(\frac{\mathrm{Bi}[\tilde{y}]}{\mathrm{Ai}[\tilde{y}]}\right) + \text{constant} \tag{5.7-21}$$

Similarly, by expressing an incoming spherical Hankel function $\xi_l^-(\rho)$ in terms of its Airy function asymptotic form, its phase is given by

$$\psi_l^{H^-} = \tan^{-1}\left(\frac{\mathrm{Bi}[\hat{y}]}{\mathrm{Ai}[\hat{y}]}\right) + \text{constant} \tag{5.7-22}$$

The difference $\psi_l^{A^-} - \psi_l^{H^-}$ is the phase accumulation in the lth spectral coefficient $a_l^-(\rho)$ for an Airy layer. We denote this phase of the spectral coefficient by the function $\vartheta_l^-(\rho) = \psi_l^{A^-}(\rho) - \psi_l^{H^-}(\rho)$. Taking the derivative $\partial\vartheta_l^- / \partial\rho$, we obtain

$$\frac{\partial\vartheta_l^-}{\partial\rho} = \frac{-1}{\pi K_{\rho_0}}\left(\frac{\tilde{y}}{\mathrm{Ai}[\tilde{y}]^2 + \mathrm{Bi}[\tilde{y}]^2} - \frac{\hat{y}}{\mathrm{Ai}[\hat{y}]^2 + \mathrm{Bi}[\hat{y}]^2}\right)\frac{1}{\hat{y}} \tag{5.7-23}$$

We note that $\partial \vartheta_l^- / \partial \rho$ rapidly approaches zero for increasing $\hat{y} > 0$.

We compare this expression with $\partial G[\rho, \nu] / \partial \rho$ given in Eq. (5.7-9). For negative $\hat{y}$, we replace the Airy functions in Eq. (5.7-23) with their asymptotic forms. Then, using Eq. (5.7-20), we obtain

$$\begin{gathered}\frac{\partial \vartheta_l^-}{\partial \rho} \to \frac{-1}{K_{\rho_0}}\left((-\tilde{y})^{3/2} - (-\hat{y})^{3/2}\right)\frac{1}{\hat{y}} = \\ \frac{\beta}{(1-\beta)K_{\rho_0}}\sqrt{-\hat{y}} \to \frac{-n'}{1-\beta}\sqrt{\rho^2 - \nu^2}\end{gathered} \tag{5.7-24}$$

whereas, from Eq. (5.7-9), $\partial G[\rho, \nu] / \partial \rho$ becomes

$$\frac{\partial G}{\partial \rho} = -\frac{d \log n}{d\rho} g(\hat{y}) \to -2K_\nu^2 \frac{d \log n}{d\rho}\sqrt{-\hat{y}} = \frac{-n'}{1-\beta}\sqrt{\rho^2 - \nu^2} \tag{5.7-25}$$

These asymptotic forms are identical for decreasing $\hat{y} < 0$.

Equation (5.7-23) for $\partial \vartheta_l^- / \partial \rho$ applies only to an Airy layer, but it is essentially exact and it applies without restriction on the value of $\hat{y}$. On the other hand, $\partial G[\rho, \nu] / \partial \rho$ obtained from Eq. (5.7-9) is a general form applying to any physical profile for $n(r)$, but it fails for increasing $\hat{y} > 0$. Clearly, we have a potential match made in heaven. Over the troublesome interval, say beginning at $\hat{y} > -2$, we can use the form for $\partial \vartheta_l^- / \partial \rho$ given in Eq. (5.7-23). The range $-2 \le \hat{y} \le 2$ corresponds to a spatial range of $4k^{-1}K_{\rho_0} \approx 60$ m. Approximating the index of refraction profile by a constant gradient n' should be fairly accurate in most circumstances, especially since the phase variability is rapidly dying out with increasing $\hat{y} > 0$.

If a single Airy layer is not sufficient, then we can form a concatenated series of Airy layers near a turning point. Any physical refractivity profile can be approximated by a series of Airy layers. In this case, β and $\tilde{y}$ would be discontinuous, according to Eqs. (5.7-18) and (5.7-20), across each boundary between Airy layers (see Section 4.7). Applying the continuity conditions to the wave functions and their derivatives across each boundary ties the Airy function solutions together for the different layers, which enables one to derive the phase in any layer. For a given spectral number, whenever one reaches downward through successive Airy layers to a radial distance $\rho < \rho^\dagger(\nu)$, $\tilde{y}$ will become positive there, and $\partial \vartheta_l^- / \partial \rho$ for that Airy layer rapidly approaches zero for increasing $\hat{y} > 0$.

Figure 5-7 shows two comparisons of $\partial \vartheta_l^- / \partial \rho$ and $\partial G[\rho, \nu] / \partial \rho$ versus $\hat{y}$. In Fig. 5-7(a), the refractivity profile corresponds to dry air at sea level, but in

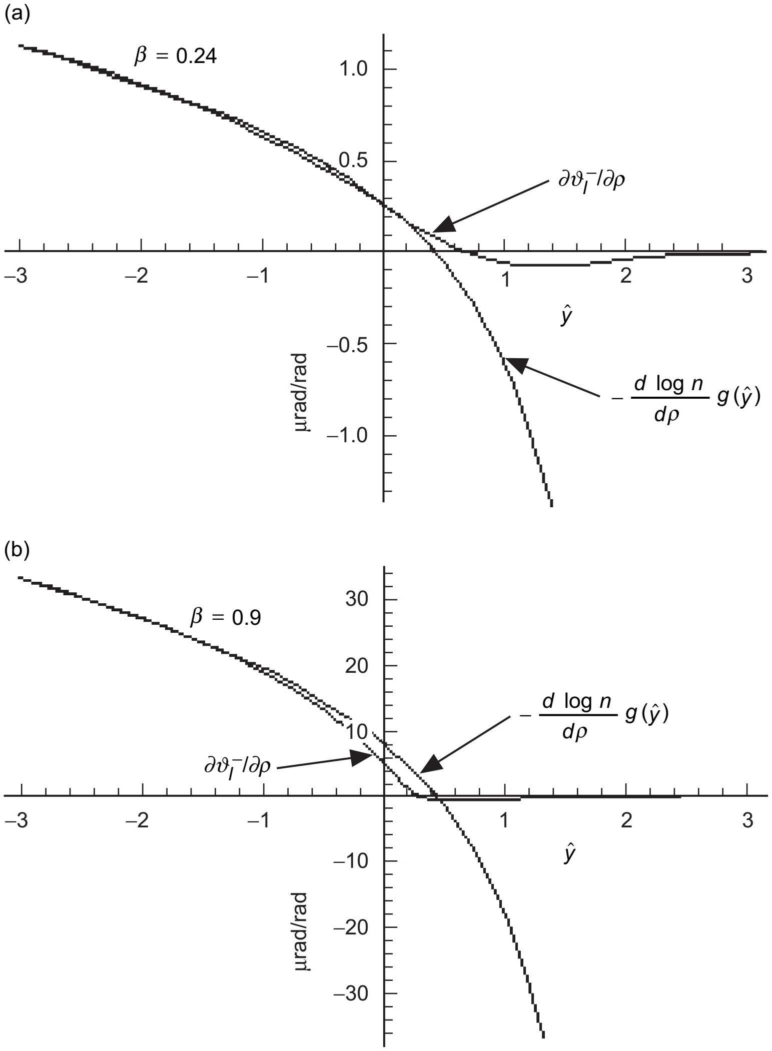

Fig. 5-7. Gradient of the phase of $a_l^-(\rho)$ in an Airy layer: (a) $\beta = 0.24$ and (b) $\beta = 0.9$. $\partial\vartheta_l^-/\partial\rho$ is the exact value; $-(d\log n/d\rho)g(\hat{y})$ is from modified Mie scattering theory.

Fig. 5-7(b), a rather hefty value of $\beta = 0.9$ has been used, hardly thin-atmosphere material.

5.7.3 Behavior of the WKB Solution at a Turning Point

The phase of a wave approaches a constant value as a function of ρ below a turning point. Its behavior can be quantified by examining the WKB solutions to the radial wave equation in Eq. (5.3-5), which are given in Eq. (5.3-10) with $f_l(u) = (n^2u^2 - l(l+1))/u^2$. The incoming and outgoing WKB solutions, $W_l^-(u)$ and $W_l^+(u)$, can be linearly combined to yield in the $f_l < 0$ regime where $\rho < \nu$ an exponentially damping solution for decreasing $\rho < \nu$, and also an exponentially increasing solution. Using the connection formulas [6] between the WKB solutions for these two regimes, $\rho < \nu$ and $\rho > \nu$, we have

$$\left.\begin{array}{ccc}
\underline{f_l(u)<0} & \underline{f_l(u_o)=0} & \underline{f_l(u)>0} \\
\dfrac{1}{2(-f_l)^{1/4}}\exp\left(-\int_u^{u_o}\sqrt{-f_l}\,du\right) & \rightarrow & \dfrac{1}{(f_l)^{1/4}}\cos\left(\int_{u_o}^{u}\sqrt{f_l}\,du-\dfrac{\pi}{4}\right) \\
\dfrac{\sin\left(\varphi+\dfrac{\pi}{4}\right)}{(-f_l)^{1/4}}\exp\left(\int_u^{u_o}\sqrt{-f_l}\,du\right) & \leftarrow & \dfrac{1}{(f_l)^{1/4}}\cos\left(\int_{u_o}^{u}\sqrt{f_l}\,du+\varphi\right)
\end{array}\right\} \quad (5.7\text{-}26)$$

where φ is an arbitrary phase that is not too close in value to $-\pi/4$.[8] For $f_l = u$ and $\varphi = +\pi/4$, these are the leading terms of the asymptotic forms for the Airy functions of the first and second kind.

It follows that one solution to the wave equation is exponentially increasing for decreasing $\rho < \nu$, and the other is exponentially damping to zero. The asymptotic form of the incoming wave, U_l^-, in the $\rho < \nu$ regime is a linear combination of these two exponential solutions. Therefore, the phase of U_l^- must approach a constant value with decreasing $\rho < \nu$. The Airy layer analysis just discussed shows that the phase of U_l^- *rapidly* approaches a constant; therefore, $\partial G/\partial\rho$ must rapidly approach zero. Expanding f_l in powers of $u - u_o$ and setting $n_o u_o = l$ leads to $f_l = -\hat{y}/K_{\rho_o}^2 + \mathrm{O}[\hat{y}/K_{\rho_o}^2]^2$. The exponential terms in the WKB solutions become $\exp(\pm 2\hat{y}^{3/2}/3)$. For $\hat{y} = 2$, the ratio of their amplitudes is about 100:1; for $\hat{y} = 3$, it is 2000:1.

---

[8] The arrow in each of these two connection formulas indicates the applicable direction of information transfer. For example, continuing the exponentially damping solution in the $f < 0$ regime into the $f > 0$ regime leads to a stable sinusoidal solution in that regime with “twice” the amplitude and a phase offset of $-\pi/4$. But the reverse cannot be guaranteed. Inaccuracy in the numerical computation of the solution to the wave equation starting in the $f > 0$ regime and integrating downward into the $f < 0$ regime, even with the phase set equal to $-\pi/4$ exactly, leads inevitably to a numerical solution that blows up for decreasing $\rho < \nu$.

5.7.4 Setting $G[\rho, \nu]$ for $\rho \le \rho^{\dagger}(\nu)$

In the discussions to follow, we have taken a simpler approach in view of Eq. (5.7-6) and also the very close agreement between $dG[\rho^{\dagger}(\nu),\nu]/d\nu$ and $\tilde{\alpha}(\nu,\nu)$. We let $G[\rho,\nu]$ run its course based on Eq. (5.7-2) for $\rho^{\dagger}(\nu) \le \rho < \infty$. It has a stationary value at $\rho = \rho^{\dagger}(\nu)$. Then we set $G[\rho,\nu] = G[\rho^{\dagger}(\nu),\nu] = G^{\dagger}(\nu)$ for $\rho \le \rho^{\dagger}(\nu)$, a constant value for a given value of ν. In summary, we modify Eq. (5.7-2) as follows:

$$G[\rho,\nu] = \begin{cases} \displaystyle\int_{\rho}^{\infty} \left(\frac{d\log n}{d\rho'}\right) g(\hat{y}')d\rho', & \rho \ge \rho^{\dagger}(\nu) \\ \displaystyle\int_{\rho^{\dagger}}^{\infty} \left(\frac{d\log n}{d\rho'}\right) g(\hat{y}')d\rho', & \rho \le \rho^{\dagger}(\nu) \end{cases} \tag{5.7-27}$$

Also, we have

$$\frac{\partial G[\rho,\nu]}{\partial \rho} = \begin{cases} -\left(\dfrac{d\log n}{d\rho'}\right) g(\hat{y}'), & \rho \ge \rho^{\dagger}(\nu) \\ 0, & \rho \le \rho^{\dagger}(\nu) \end{cases} \tag{5.7-28}$$

This arrangement, which involves some approximation (see Fig. 5-7), also simplifies and clarifies the strategy for matching the incoming and outgoing spectral coefficients to eliminate the Hankel function singularity at the origin. We discuss this further in Section 5.8.

5.8 Spectral Representation of an Electromagnetic Wave in a Spherical Stratified Medium

We will need to distinguish between an incoming region in the medium and an outgoing region. Figure 5-8 provides an example of the simplest topology for these regions. The boundary between these regions is given by the locus of points (r_*, θ_*), which defines the turning point for each ray, where for a spherical symmetric medium $E_{\theta}(r_*, \theta_*) = 0$. In geometric optics $\theta_* = \pi/2 - \tilde{\alpha}(\rho_*, \rho_*)$, which is obtained from Eq. (5.6-5). By "incoming" we mean the field at any point where the Poynting vector $\boldsymbol{S} = c(\boldsymbol{E} \times \boldsymbol{H})/4\pi$ for the wave is such that $\boldsymbol{S} \cdot \boldsymbol{r} < 0$. For the simple topology shown by Fig. 5-8, for example, the incoming region includes any point with a radial position r and an angular position θ that satisfies the condition $\theta_* < \theta < \pi$.

When the profile of the refractivity gradient has reversals in polarity, these regions may not be so simply connected. When a scattering surface is present,

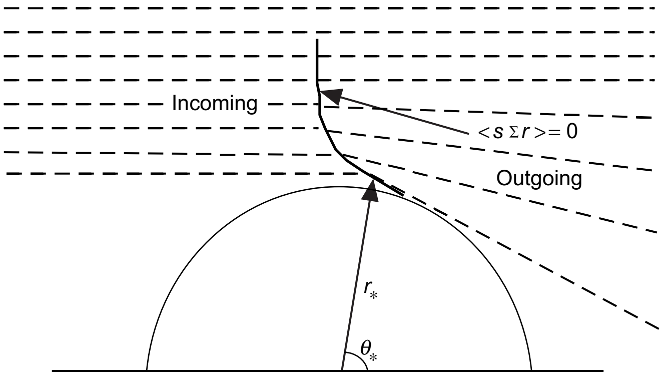

Fig. 5-8. Schematic of simple incoming and outgoing regions.

one could obtain both incoming and outgoing waves at the same point. Figure 5-9 sketches a more complicated refractivity profile that also produces coincident incoming and outgoing waves in certain regions.

We first develop the spectral coefficients for the pure refraction case, and we assume that no scattering surfaces are present in the medium. Scattering or diffraction occurs where sharp changes in gradient or discontinuities in the refractivity occur. We will deal with those cases later. In particular, we assume that $n(r)$ and its derivatives are continuous throughout the medium and that the simple topology of the kind shown in Fig. 5-8 applies.

Let us evaluate the electric field vector $\boldsymbol{E}(r,\theta)$ at a point within the refracting medium in terms of its incoming and outgoing spectral coefficients. We assume that the planar asymptotic boundary condition applies to the approaching wave and, therefore, a_l^- is obtained from Eq. (5.5-21). The proper functional form for a_l^+ is more problematical, and we defer that to later in this section. From Eqs. (5.3-6), (5.5-2), and (5.5-8), we have the following spectral representation for the in-plane ($\phi = 0$) radial and transverse components of the electric field for the TM wave:

$$\left.\begin{aligned} E_r &= \frac{E_o}{2\rho^2}\sum_{l=1}^{\infty} l(l+1)\left(a_l^-\xi_l^- + a_l^+\xi_l^+\right)\mathrm{P}_l^1(\cos\theta) \\ E_\theta &= \frac{E_o}{2\rho}\sum_{l=1}^{\infty}\left(a_l^-\xi_l'^- + a_l^+\xi_l'^+\right)\frac{\partial}{\partial\theta}\mathrm{P}_l^1(\cos\theta) \end{aligned}\right\} \tag{5.8-1a}$$

Because of the enormity of ρ and of l from where essentially all contributions to these summations originate, we can replace these summations by integrals, which are given by

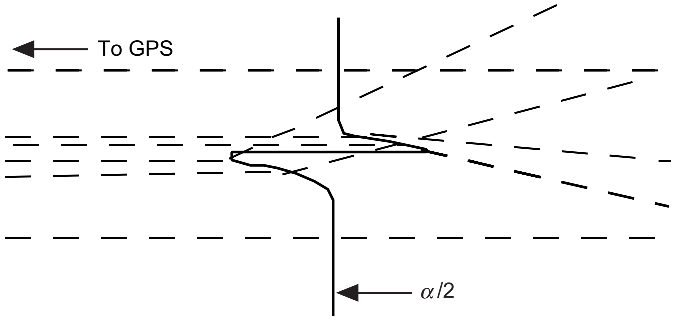

Fig. 5-9. Example of a topology with overlapping incoming and outgoing regions, from a sharp change in refractivity gradient.

$$\left.\begin{aligned} E_r &= \frac{E_o}{2\rho^2}\int_0^\infty \nu^2\left(a_l^- \xi_l^- + a_l^+ \xi_l^+\right) \mathrm{P}_l^1(\cos\theta)d\nu \\ E_\theta &= \frac{E_o}{2\rho}\int_0^\infty \left(a_l^- \xi_l'^- + a_l^+ \xi_l'^+\right) \mathrm{P}_l^{1\prime}(\cos\theta)d\nu \end{aligned}\right\} \tag{5.8-1b}$$

A similar set holds for the magnetic field. In the limit as n assumes a constant value throughout the medium, $a_l^+ \to a_l^- \to a_l$, and Eq. (5.8-1) reduces to the collimated form in Eq. (5.5-1) with $a_l = i^{l-1}(2l+1)/l(l+1)$, as it must. Also, using stationary phase arguments, we will show later that in the incoming region well away from a turning point only the $a_l^-(\rho)\xi_l^-(\rho)$ term contributes significantly to the scattering integral; in the outgoing region, only the $a_l^+\xi_l^+$ term contributes. Only for points very near a turning point must we include contributions from both spherical Hankel functions. This means that, except near a turning point, we may replace the terms $a_l^\pm\xi_l^\pm/2$ with $a_l^\pm\psi_l$ for computational purposes, which decays to zero rapidly with increasing $l > \rho$.

5.8.1 Behavior of $\partial G/\partial\nu$

The spectral representation for the electric field in Eq. (5.8-1b) involves integrals over spectral number. To evaluate these integrals using the stationary phase technique as an aid, we need to find those spectral neighborhoods where the phase accumulation of the integrands is stationary. In this regard, we study the variability of $G[\rho,\nu]$ with spectral number, $\partial G/\partial\nu$, in terms of the refractivity profile that determines it. We first look at $\partial G/\partial\nu$ for two different refractivity profiles. Both examples adhere to the thin-atmosphere assumptions. For Case A, n is exponentially distributed so that $d\alpha/dr$ is monotonic negative with altitude; therefore, no multipath or shadow zone situations arise. For this case, $\partial G/\partial\nu$ already has been shown in Fig. 5-4. In Case B, n has a

Gaussian distribution; multipath, shadow zones, and caustics are prominent features for this distribution. These two profiles for the index of refraction are given by

$$n = 1 + N_o \exp\left[-(\rho - \rho_o) / H\right] \tag{5.8-2a}$$

$$n = 1 + N_w \exp\left[-(\rho - \rho_w)^2 / 2H_w^2\right] \tag{5.8-2b}$$

Case B is useful for study of spherical shell structures embedded in an ambient profile such as that given by Case A. Case B could be used to describe the refractivity profile of a sporadic E-layer in the ionosphere or a marine layer in the lower troposphere. Case A can be used to describe the Earth's refractivity profile for dry air, and the values used for N_o and H in these examples correspond roughly to dry air refractivity ($N_o = 270 \times 10^{-6}$) and scale height ($k^{-1}H = 7\,\text{km}$) at sea level. For computational convenience, we now have written these refractivity profiles in terms of $\rho = krn(\rho)$, i.e., r is an implicit function of ρ.[9]

For the exponential refraction profile given by Case A, it can be shown using the thin-atmosphere assumption in the defining path integral for $\tilde{\alpha}(\rho, \nu)$, given in Eq. (5.6-2) [see also Appendix A, Eq. (A-30)], that $\tilde{\alpha}(\rho, \nu)$ is given by

---

[9] The extraction of n given a value of $u = kr$ through iteration of Eq. (5.8-2) is cumbersome because $\rho = un(\rho)$. However, this form for an exponential distribution in terms of ρ has some advantages. It results in the very simple form for $\tilde{\alpha}(\rho, \nu)$ given in Eq. (5.8-3), which closely agrees with the numerical integration version for $\tilde{\alpha}(\rho, \nu)$ given in Eq. (5.6-2). Provided $|un'/n| < 1$, there is a unique relationship between u and ρ. Equation (5.8-3) includes the effects of second-order ray path bending in the path integral in Eq. (5.6-2). When a positional exponential form is used instead, $n(u) = 1 + N_o \exp[-(u - u_o)/H_u]$, the form for $\tilde{\alpha}(u, \nu)$ requires a series in powers of (un'/n) to account for higher-order ray path bending. This has been discussed in Appendix A. For a given value of scale height $H_\rho = H$, the version in Eq. (5.8-2a) gives a smaller radial gradient than the positional exponential version (about 20 percent less for dry air at sea level). This is seen by noting that, for the two versions of the exponential distributions, one obtains the following for dry air at sea level:

$$H_u / H_\rho \doteq (d \log n / d \log \rho) \big/ (d \log n / d \log u) = d \log u / d \log \rho = 1 - \rho n' / n \approx 1.2$$

One can adjust the values of the parameters N_o and H in Eq. (5.8-2a) to attain a close, but not exact, match with the profile from the positional exponential form; also, the bending-angle profiles from the two versions can be matched rather closely.

For near-super-refractivity situations where $un'/n \to -1$, then the functional form $n(\rho)$ becomes inconvenient because $dn/d\rho = n'/(1 + un') \to \infty$. But the defining integral for $G[\rho, \nu]$ readily allows a change of variable to u.

$$\tilde{\alpha}(\rho,\nu) \doteq \left(n(\rho)-1\right)\sqrt{\frac{\pi\rho}{2H}}\left(1-\operatorname{erf}\left[\sqrt{\frac{\rho^2-\nu^2}{2\rho H}}\right]\right), \quad \nu<\rho \tag{5.8-3}$$

where $n(\rho)$ is given by Eq. (5.8-2a). This expression is very accurate when compared to the value from the path integral in Eq. (5.6-2). For the decreasing exponential distribution given in Eq. (5.8-2a), the difference is less than 1 percent for dry air. Equation (5.8-3) accounts for both the first- and second-order ray path bending effects when the refractivity profile in Eq. (5.8-2a) is used. For the dry air component of the Earth's atmosphere, the first-order bending term, $\left(\sqrt{2}-1\right)un'/n$, contributes less than 10 percent of the total. The second-order ray path bending effect for dry air at sea level amounts to roughly 1 percent of the total.

Figure 5-10 shows the variation of $\partial G/\partial\nu$ with ν while holding ρ fixed for Case A. It was obtained from the integral in Eq. (5.7-7). For $\nu<\rho$, we have already noted from Eqs. (5.6-2) and (5.7-8), and from Fig. 5-4, that $\partial G/\partial\nu \doteq \tilde{\alpha}(\rho,\nu)$, which holds very accurately for all values of ν nearly up to $\nu=\rho$. Numerical integrations of $\partial G/\partial\nu$ from Eq. (5.7-7) and $\tilde{\alpha}(\rho,\nu)$ from Eq. (5.6-2) show microradian-level agreement for both Cases A and B when the inequality $\nu-\rho <\sim -2K_\rho$ and the thin-atmosphere assumptions are satisfied.

The three curves for $\partial G/\partial\nu$ in Fig. 5-10 correspond to three different radial positions, which are defined, respectively, by $\rho-\rho_o=0, H/2, H$, and $\rho=un(\rho)$. The dashed curves in Figs. 5-10 and 5-11 mark the value of $\partial G/\partial\nu$ for $\nu=\rho_*+\hat{y}^\dagger K_{\rho_*}$ as a function of ρ_*, which is a stationary point for $G[\rho_*,\nu]$.

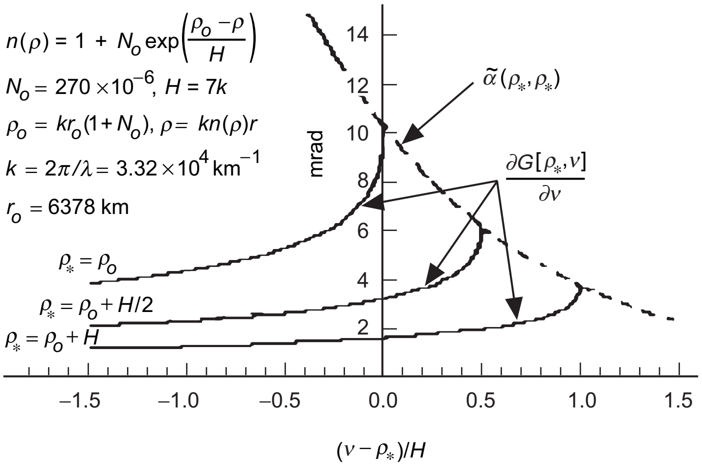

Fig. 5-10. $\partial G/\partial\nu$ **curves for an exponential refractivity profile. The dashed curve shows** $\partial G/\partial\nu$ **at** $\nu=\rho_*+\hat{y}^\dagger K_{\rho_*}$ **as** ρ_* **varies or, equivalently,** $\tilde{\alpha}(\rho_*,\rho_*)$**.**

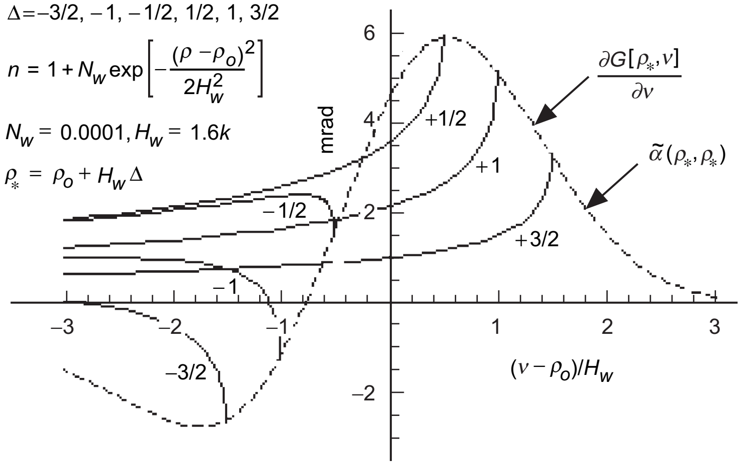

Fig. 5-11. $\partial G/\partial \nu$ curves for a Gaussian refractivity profile for different locations of its center. The dashed curve is the value of $\partial G/\partial \nu$ at $\nu = \rho_* + \hat{y}^\dagger K_{\rho_*}$ or, equivalently, $\tilde{\alpha}(\rho_*,\rho_*)$.

We have shown that at this stationary point $dG/d\nu = \partial G/\partial \nu \doteq \tilde{\alpha}(\rho,\rho)$ with high accuracy. Here, $\tilde{\alpha}(\rho,\rho)$ is given from either Eq. (5.6-2), or from Eq. (5.8-3) when Case A applies.

Figure 5-11 shows the resulting curves for $\partial G/\partial \nu$, obtained from the integral in Eq. (5.7-7) when the Gaussian refractivity profile in Eq. (5.8-2b) is used. If this profile also is applied in Eq. (5.6-2) to obtain $\tilde{\alpha}(\rho,\rho)$, a bipolar refractive bending-angle profile results, which is shown in Appendix E, Fig. E-1, and also as the dashed curve in Fig. 5-11. The bending-angle profile mimics the shape of $dn/d\rho$, but it is modified to reflect the geometry of a ray transecting a spherical shell. The intersection of the $\partial G/\partial \nu$ curve with the $\tilde{\alpha}(\rho,\rho)$ curve in Fig. 5-11 also occurs very near the point $\nu = \rho + \hat{y}^\dagger K_\rho$. The point where the polarity change occurs for $\partial G/\partial \nu$ at its initial break point depends on the location of the center of the Gaussian distribution relative to ρ_o. For $\rho_w < \rho_o$ the initial break is negatively directed, but for $\rho < \rho_w$ the slope of $n(\rho)$ becomes negative and $\partial G/\partial \nu$ will then break positive. Physically, this regime where the variability of $G[\rho,\nu]$ approaches zero, see Eqs. (5.7-26) through-(5.7-28), corresponds to the Gaussian layer being located below the level, $\rho_o = \nu$; the layer cannot be "sensed" by a ray with an impact parameter $\nu > \rho_o$. We will show later that there are no stationary phase points in spectral number for this regime.

5.8.2 Accuracy of the Osculating Parameter Technique

To check the accuracy of the spectral representation used in this section, as given in Eq. (5.8-1), we again use the Airy layer model for a refracting medium with spherical stratification. We embed this layer in an otherwise homogeneous medium. These analytic solutions can be compared with the osculating parameter and numerical solutions. We let

$$\left.\begin{array}{l} n^2 = n_A^2 + 2n_A \dfrac{dn}{d\tilde{\rho}}\left(\tilde{\rho} - \rho_A\right), \quad \dfrac{dn}{d\tilde{\rho}} = \left\{\begin{array}{l} \text{constant}, \ \tilde{\rho} \le \rho_A \\ 0, \ \tilde{\rho} > \rho_A \end{array}\right\} \\ \tilde{\rho} = kn_A r, \ \tilde{\rho}_A = \rho_A = kn_A r_A, \ n_A = \text{constant} \end{array}\right\} \tag{5.8-4}$$

Here $\tilde{\rho} = \rho_A$ marks the upper boundary of the Airy layer, and n_A is the value of the index of refraction there. From Sections 4.10 and 4.11, we know that the wave equations for this case are given by

$$\frac{d^2\left(\tilde{\rho}U_l\right)}{d\tilde{\rho}^2} + \left(\left(\frac{n}{n_A}\right)^2 - \frac{l(l+1)}{\tilde{\rho}^2}\right)\left(\tilde{\rho}U_l\right) = 0, \quad \tilde{\rho}V_l = -i\frac{d\left(\tilde{\rho}U_l\right)}{d\tilde{\rho}} \tag{5.8-5}$$

$U(\tilde{\rho})$ describes the field along the normal to the plane of propagation (the y-direction in Fig. 4-10). For a given value of l, $U(\tilde{\rho})$ also provides the radial spectral component of the electric field, and $V(\tilde{\rho})$ describes the tangential component parallel to the plane of stratification and in the plane of propagation (the θ-direction in Fig. 4-10).

This model has been discussed in Section 4.12, where a correspondence between spherical and Cartesian stratification was established, and also in Section 5.7 to obtain an asymptotic form for $G[\rho, \nu]$ valid for $\nu > \rho$. There the solutions to the wave equations in Eq. (5.8-5) are given to a good approximation by the Airy functions with their argument $\tilde{y}$ given by Eq. (4.12-5). Thus, in the medium described by Eq. (5.8-4) for $r \le r_A$, we have

$$\left.\begin{array}{l} \tilde{\rho}U_l \doteq \left\{\mathrm{Ai}[\tilde{y}], \mathrm{Bi}[\tilde{y}]\right\}, \quad \tilde{\rho}V_l \doteq i\left|1-\beta_A\right|^{1/3} K_{\tilde{\rho}_A}^{-1}\left\{\mathrm{Ai}'[\tilde{y}], \mathrm{Bi}'[\tilde{y}]\right\} n_A, \\ \tilde{\rho} = kn_A r, \ \beta_A = -\left(\dfrac{1}{n}\dfrac{dn}{d\tilde{\rho}}\tilde{\rho}\right)_A, \\ \tilde{y} = -\dfrac{1}{\left|1-\beta_A\right|^{2/3} K_{\tilde{\rho}_A}}\left(\left(1-\beta_A\right)\left(\tilde{\rho}-\tilde{\rho}_A\right) - \left(l - \tilde{\rho}_A\right)\right) \end{array}\right\} \tag{5.8-6}$$

For the region $r > r_A$, the solutions are the spherical Bessel functions of the first and second kinds, $\psi_l(\tilde{\rho}), \chi_l(\tilde{\rho})$. We note here that n_A is a constant in the Airy layer. Hence, $-\beta = (dn / d\tilde{\rho})\tilde{\rho} / n = (dn / dr)r / n$.

At the boundary $r = r_A$, we must match these two solution sets for each integer value of l to ensure the continuity of the tangential components of the electromagnetic field across the boundary. We first match the solutions when the $\mathrm{Ai}[\tilde{y}]$ solution applies in the region $r \le r_A$, that is, the solution that vanishes for decreasing $\tilde{\rho}$ with $\tilde{\rho} < l$. Upon noting from Eq. (5.8-6) that $\partial\tilde{y} / \partial\tilde{\rho} = -|1 - \beta_A|^{1/3} / K_{\tilde{\rho}_A}$ (with $\beta_A < 1$), we set

$$\left.\begin{aligned} &\mathrm{Ai}[\tilde{y}_A] = c_l \psi_l(\tilde{\rho}_A) + d_l \chi_l(\tilde{\rho}_A) \\ &-K_{\tilde{\rho}_A}^{-1}(1-\beta_A)^{1/3}\,\mathrm{Ai}'[\tilde{y}_A] = c_l \psi_l'(\tilde{\rho}_A) + d_l \chi_l'(\tilde{\rho}_A) \end{aligned}\right\} \tag{5.8-7}$$

Using the asymptotic forms for both the spherical Bessel functions and the Airy function for $-\tilde{y} >> 1$ and for $-\hat{y} >> 1$, we obtain values for the matching coefficients that are given by

$$\left.\begin{aligned} &c_l = \frac{|1-\beta_A|^{1/6}}{\sqrt{\pi K_{\tilde{\rho}_A}}}\cos\left(\tilde{X}_l - \hat{X}_l\right),\ d_l = -\frac{|1-\beta_A|^{1/6}}{\sqrt{\pi K_{\tilde{\rho}_A}}}\sin\left(\tilde{X}_l - \hat{X}_l\right), \\ &\tilde{X}_l = \frac{2}{3}(-\tilde{y}_A)^{3/2} + \frac{\pi}{4},\ \ \hat{X}_l = \frac{2}{3}(-\hat{y}_A)^{3/2} + \frac{\pi}{4} \end{aligned}\right\} \tag{5.8-8}$$

Here $\tilde{y}$ is given in Eq. (5.8-6), and $\hat{y}$ is given by Eq. (5.4-3). Their ratio $\hat{y} / \tilde{y}$ is equal to $|1 - \beta_A|^{2/3}$.

Similarly, for a $\mathrm{Bi}[\tilde{y}]$ solution in the region $r \le r_A$, that is, the solution that blows up for decreasing $\tilde{\rho}$ with $\tilde{\rho} < l$, we set

$$\left.\begin{aligned} &\mathrm{Bi}[\tilde{y}_A] = e_l \psi_l(\tilde{\rho}_A) + f_l \chi_l(\tilde{\rho}_A) \\ &-\frac{|1-\beta_A|^{1/3}}{K_{\tilde{\rho}_A}}\mathrm{Bi}'[\tilde{y}_A] = e_l \psi_l'(\tilde{\rho}_A) + f_l \chi_l'(\tilde{\rho}_A) \end{aligned}\right\} \tag{5.8-9}$$

When the asymptotic forms apply, that is, at a location well away from a turning point, we obtain

$$\left.\begin{aligned} e_l &= -\frac{|1-\beta_A|^{1/6}}{\sqrt{\pi K_{\tilde{\rho}_A}}}\sin\left(\tilde{X}_l-\hat{X}_l\right)=d_l \\ f_l &= -\frac{|1-\beta_A|^{1/6}}{\sqrt{\pi K_{\tilde{\rho}_A}}}\cos\left(\tilde{X}_l-\hat{X}_l\right)=-c_l \end{aligned}\right\} \qquad (5.8\text{-}10)$$

Referring to our discussion in Section 4.6 on incoming and outgoing waves in a Cartesian Airy layer, it follows in this case that outgoing and incoming waves at the boundary can be expressed in the form

$$\mathrm{Ai}[\tilde{y}_A]\mp i\,\mathrm{Bi}[\tilde{y}_A]=(c_l\mp id_l)\xi_l^{\pm}(\rho_A) \qquad (5.8\text{-}11)$$

The top sign applies to an outgoing wave, and the bottom sign to an incoming wave. Also, the complex coefficients $(c_l \mp id_l)$ provide the phase delay (modulo 2π) between the incoming and outgoing waves at the boundary due to the refracting medium below. This phase delay offset remains invariant for $r > r_A$ because the medium is taken to be homogeneous for $r \geq r_A$. From Eqs. (5.8-8) and (5.8-10), it follows that the ratio

$$\frac{c_l-id_l}{c_l+id_l}=\exp\left(2i\left(\tilde{X}_l-\hat{X}_l\right)\right) \qquad (5.8\text{-}12)$$

provides the round-trip phase delay between the incoming and outgoing wavelets of spectral number l at the boundary $r = r_A$. From Eqs. (5.8-6) and (5.8-8) and noting again that in the Airy layer $\hat{y}/\tilde{y} = |1-\beta_A|^{2/3}$, it follows that

$$\begin{aligned} \tilde{X}_l-\hat{X}_l &= \frac{2}{3}\left(\left(-\tilde{y}_A\right)^{3/2}-\left(-\hat{y}_A\right)^{3/2}\right) \\ &= \frac{2}{3}\cdot\frac{\beta_A}{1-\beta_A}\left(-\hat{y}_A\right)^{3/2} \doteq \frac{1}{3}\cdot\frac{\rho_A\beta_A}{1-\beta_A}\left(\frac{2(\rho_A-l)}{\rho_A}\right)^{3/2} \end{aligned} \qquad (5.8\text{-}13)$$

We return to this expression momentarily after discussing the form of $G[\rho,\nu]$ for this model of the refracting medium.

Now we use the osculating parameter technique in the spectral representation given in Eq. (5.8-1) to describe the wave in the refracting Airy medium where $r \leq r_A$. The basis functions are the spherical Hankel functions $\{\xi_l^+(\rho), \xi_l^-(\rho)\}$, where $\rho = knr$ and n now is variable and given by Eq. (5.8-4). For a given spectral number, the form for the radial term from Eq. (5.8-1) is given by

$$a_l^- \xi_l^- + a_l^+ \xi_l^+ = C_l \Big(\exp(-iG[\rho,\nu]) \xi_l^-(\rho) + \exp(iG[\rho,\nu]) \xi_l^+(\rho) \Big) \tag{5.8-14}$$

Here C_l is a spectral number-dependent complex factor that depends on boundary conditions, which we will discuss later in regard to turning points; it is not of interest here.

From Eq. (5.7-2), it follows that $G[\rho,\nu]$ for an Airy layer is given by

$$\left.\begin{aligned}
&G[\rho,\nu] \doteq \frac{\pi}{6}\left(\frac{1}{n}\frac{dn}{d\rho}\rho\right)_A \Big(\Gamma(\hat{y}) - \Gamma(\hat{y}_A)\Big), \quad \rho^\dagger(\nu) < \rho \le \rho_A, \\
&G[\rho,\nu] \to \frac{2}{3}\left(\frac{1}{n}\frac{dn}{d\rho}\rho\right)_A \Big((-\hat{y}_A)^{3/2} - (-\hat{y})^{3/2}\Big), \quad \tilde{y}_A, \hat{y} << -1, \\
&G[\rho,\nu] \equiv 0, \quad \rho \ge \rho_A
\end{aligned}\right\} \tag{5.8-15}$$

Here $\Gamma(\hat{y})/3$ is the integral of $g(\hat{y})$ given in Eq. (5.7-1). $\Gamma(\hat{y})$ has been discussed in Section 4.9 with regard to osculating parameters in a Cartesian-stratified medium, and it is given by Eq. (4.9-5). It is shown in Fig. 5-12. $\Gamma(\hat{y})$ has only the two roots shown in this figure, and it is monotonic elsewhere.

For a given value of l in both Eqs. (5.8-13) and (5.8-15), what is the value of $\hat{y}$ in Eq. (5.8-15), that is, what value for ρ must we use to match the round-trip phase delay $-2G[\rho,\nu]$ with the asymptotically exact value of this phase delay $2(\tilde{X}_l - \hat{X}_l)$, given from Eq. (5.8-13)? Noting that n is variable in Eq. (5.8-15), it follows from Eq. (5.8-4) that

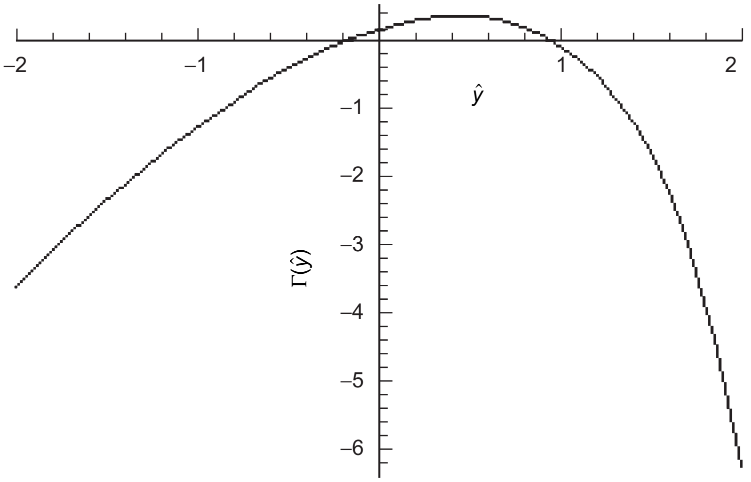

Fig. 5-12. Variation of $\Gamma(\hat{y})$ in the vicinity of a turning point.

$$\left(\frac{1}{n}\frac{dn}{d\rho}\rho\right)_A = -\frac{\beta_A}{1-\beta_A} \tag{5.8-16}$$

We see upon comparing Eq. (5.8-15) with Eq. (5.8-13) that $\hat{y}$ must be zero. However, the negative argument asymptotic forms for the Airy functions do not apply at $\hat{y}=0$; instead, we must set $\Gamma(\hat{y})=0$ in Eq. (5.8-15). This is discussed in Appendix I, Eq. (I-11), with regard to relating $dG[\rho^{\dagger}(\nu),\nu]/d\nu$ to $\tilde{\alpha}(\nu,\nu)$. The roots of $\Gamma(\hat{y})$ occur at $\hat{y} \doteq -0.2$ and $+0.9$, and $\Gamma(\hat{y})$ reaches a stationary value of almost zero at $\hat{y}=\hat{y}^{\dagger}$. It is nearly zero there compared to the value of $(-\hat{y}_A)^{3/2}$ when $-\hat{y}_A >> 1$ (see Fig. 5-12). Thus, we set $\rho=\rho^{\dagger}=\nu-K_{\rho}y^{\dagger}$ to force a near alignment of Eq. (5.8-15) with Eq. (5.8-13). The relative error of this choice is $\Gamma(\hat{y}^{\dagger})/\Gamma(\hat{y}_A) \approx 0.001$ for this example.

In Section 5.5, Eqs. (5.5-22) through (5.5-25), we discussed the spectral coefficients a_l^{+} for an outgoing wave in terms of $G[\rho,\nu]$. The equation for a_l^{+} involved a constant of integration $a_l^{+}[\rho_*,\rho_*]$. The question of the appropriate value of ρ_* to use in this constant of integration was left rather moot in that discussion. Here we set $\rho_* = \rho^{\dagger}$ and

$$a_l^{+}\left[\rho^{\dagger},\rho^{\dagger}\right] = i^{l-1}\frac{2l+1}{l(l+1)}\exp\left(-iG[\rho^{\dagger},\nu]\right) \tag{5.8-17}$$

This provides a rationale for setting $\rho=\rho^{\dagger}(\nu)$ in $2G[\rho,\nu]$ for the outgoing wave, at least when well away from a turning point so that $\hat{y}_A<0$. We will return later to this question of linking the incoming and outgoing spectral coefficients.

5.8.3 Numerical Comparisons

Although the close comparison between $2G[\rho^{\dagger},\nu]$ and $\left(c_l-id_l\right)/\left(c_l+id_l\right)$ at the boundary of the Airy layer is encouraging, we should compare the osculating parameter representation for the wave given in Eq. (5.8-14) with the exact solution obtained from integrating the wave equations in Eq. (5.8-5). Their level of agreement as a turning point is approached is of particular interest. Figure 5-13(a) shows the solution for $U_l(\rho)$, which is the solution to the wave equations in Eq. (5.8-5), and it also shows the osculating parameter solution from Eq. (5.8-14). They are virtually doppelgangers over the range shown for $\hat{y}$. In this example, $\nu=l+1/2=\rho_o=6400k$, $\rho_A=6432k$, $k=100\,\text{km}^{-1}$, $n'=1.56\times10^{-4}$, and $n_o=1$. The solution is closely approximated by $\text{Ai}[\tilde{y}]$. It yields a single-sided bending angle at

$\rho_* = \rho_o = 6400k$ of 10 mrad, and this medium has a moderate ray path curvature index β of about 0.1. The general procedure in Figs. 5-13 through 5-16 for comparing these solutions is as follows. For initial conditions, we set $U_l(\rho^\dagger) = \mathrm{Ai}[\tilde{y}^\dagger]$, and we also equate their derivatives at this point. This generates a numerical solution for $U_l(\rho)$ that exponentially damps to zero for decreasing ρ in the vicinity of the turning point at $\rho_o = \nu$ (but it blows up for $\rho << \rho_o$ because of limited numerical precision). Then at $\rho = \rho_A$, which in the example shown in Fig. 5-13 corresponds to a $\hat{y}$ value of about –50, we set $C_l(a_l^-(\rho)\xi_l^-(\rho) + a_l^+(\rho)\xi_l^+(\rho))$ equal to the numerical solution for $U_l(\rho)$ there, and we also equate their derivatives there. This sets the complex value of C_l in Eq. (5.8-14) and gives the osculating parameter solution for decreasing ρ.

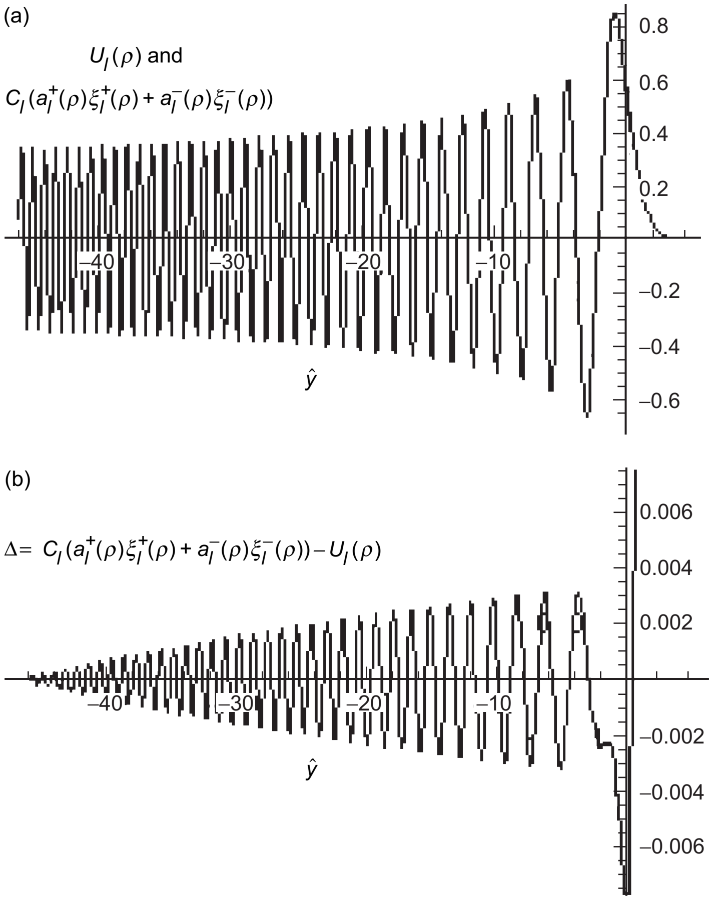

Fig. 5-13. Comparison of $U_l(\tilde{\rho})$ from a numerical integration of Eq. (5.8-5) in an Airy layer with the osculating parameter solution: (a) wave equation solutions and (b) the difference between the solutions.

Figure 5-13(b) shows the difference between $U_l(\tilde{\rho})$ and the osculating parameter form with the same initial conditions at the boundary $r = r_A$. Here $G[\rho, \nu]$ is obtained from Eq. (5.5-20), integrated on ρ over the Airy layer from ρ_A to ρ. In the osculating parameter solution for these two panels, $G[\rho, \rho_*]$ accumulates about 3 1/2 cycles between r_A and $r^\dagger$, where $r^\dagger = k^{-1}\rho^\dagger / n(\rho^\dagger)$. This accumulation of 3 1/2 cycles is required to keep the solution $C_l(a_l^- \xi_l^- + a_l^+ \xi_l^+)$ in Eq. (5.8-14) aligned in phase with the exact solution $U_l(\rho)$ over the entire Airy layer. Better than 1 percent numerical agreement holds between solutions except very near a turning point. As expected, for $\hat{y} >\sim -2$ the osculating parameter solution begins to deteriorate, but even at $\hat{y} = 0$ it still is moderately accurate for this example; the difference is 0.007. The differential equations in Eq. (5.8-5) become numerically unstable for $\hat{y} > 0$. Any small numerical errors in matching the boundary conditions or in the numerical integration will magnify greatly in the region $\hat{y} > 0$; that is, $\mathrm{Bi}[\tilde{y}]$ begins leaking into the numerical solution. See the discussion of the connection formula for the WKB solutions in Eq. (5.7-26). Matching boundary conditions closer to $\hat{y} = 0$, for example at $\hat{y} = -5$, improves the overall agreement, but the osculating parameter solution still deteriorates rapidly for $\hat{y} > 0$. But, the numerical solution for U_l also deteriorates for $\hat{y} > 0$ because of limited precision.

The wavenumber $k = 100\ \text{km}^{-1}$ used in Fig. 3-14 is more than 300 times smaller than the wavenumbers of the GPS navigation signals. The smaller value is used here to save computational time and to preserve computational accuracy—for given values of r_A and r_*, the number of cycles in the solution depends linearly on k. It is difficult to maintain coherency between solutions by matching both the solution and its derivative at the same point for highly oscillatory systems. The runoff error is roughly proportional to k. Small errors in the computation of U_l and $G[\rho, \nu]$ inevitably lead to runoff. An alternate matching strategy to reduce runoff is to pick two separate points and match solutions there, but not their derivatives.

Figure 5-14 shows another comparison between the numerical and osculating parameter solutions. Here a moderately strong refractivity gradient has been used, leading to single-sided bending-angle variations of more than 30 mrad over a tangency point altitude range of 8 km. Figure 5-14(a) shows the profile of the refractivity change, and Fig. 5-14(b) shows the resulting bending-angle profile. In the lowest layer, $\rho dn / d\rho = -0.8$, which gives a ray path curvature index of $\beta = 4/9$. But in the middle layer, $\rho dn / d\rho = +0.8$, which yields $\beta = -4$, a rather extreme negative ray path curvature. Figure 5-14(c) compares the two solutions, $U_l(\rho)$ and $a_l^-(\rho)\xi_l^-(\rho) + a_l^+(\rho)\xi_l^+(\rho)$. Here the

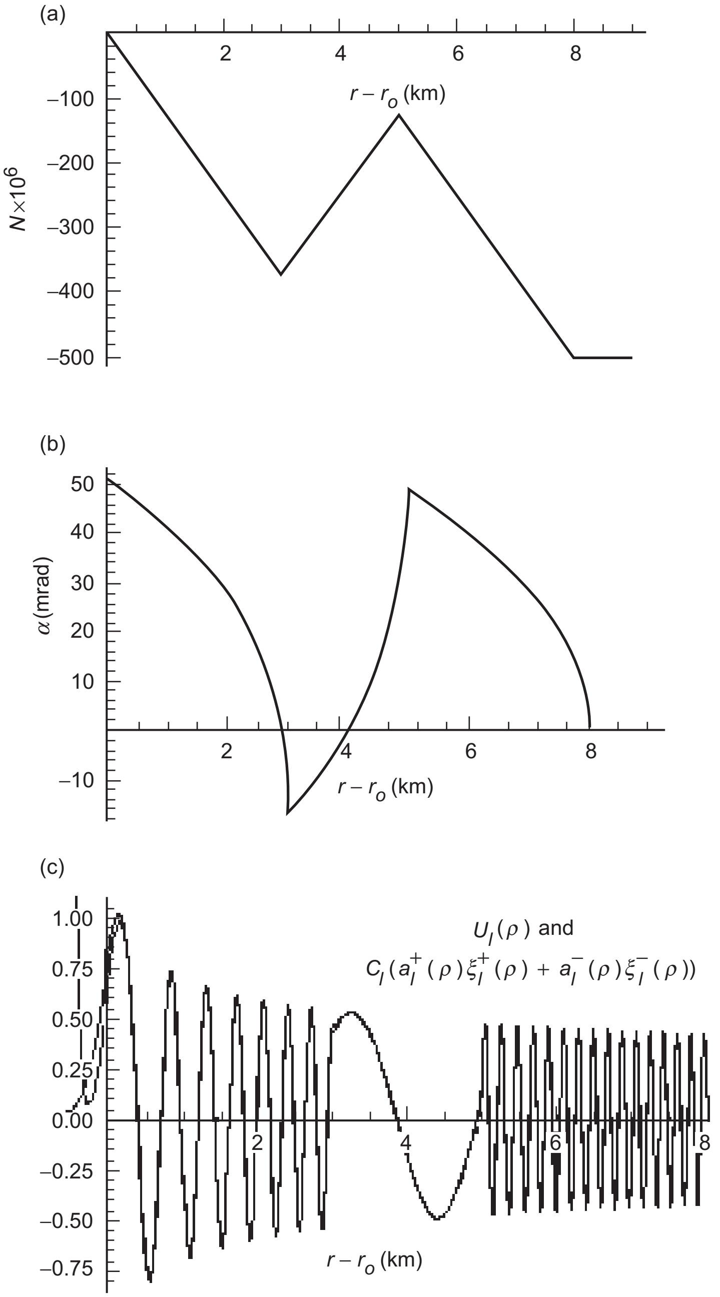

Fig. 5-14. Comparison of wave equation solutions in a strong refracting medium: (a) refractivity profile, (b) bending angle profile, and (c) wave equation solutions, $U_l(\rho)$ **and** $C_l(a_l^+(\rho)\xi_l^+(\rho) + a_l^-(\rho)\xi_l^-(\rho))$.

radial distance r, with a range of 8 km and with $k = 400\,\mathrm{km}^{-1}$, is used for the abscissa instead of $\hat{y}$. Per the discussion in Section 5.7 concerning Eqs. (5.7-25) and (5.7-26), by forcing the osculating parameter solution to follow the Airy layer solution for $\hat{y}$ values greater than ~ -2, roughly 1/2 km above the turning point for $k = 400\,\mathrm{km}^{-1}$ (~30 m for GPS wavelengths), one can greatly improve the solution below the turning point, until the numerical solution itself begins to fail.

Figure 5-15 compares the wave equation solutions for a severely refracting medium that includes a super-refracting layer, 1-km thick in the range $r_d < r < r_u$. The refractivity profile is shown in Fig. 5-15(a). Within the super-refracting layer, the ray path curvature index has a value of $\beta = 2$. Above the layer, $\beta = 0.4$, and below it, $\beta = 0.3$. These refractive gradients lead to enormous swings in the ray path bending angle. Figure 5-15(b) shows the resulting single-sided bending-angle profile versus tangency point radius, including the super-refracting zone $r^c < r_* < r_u$. For tangency points within this range, no rays can occur when spherical symmetry applies. Figure 5-15(c) shows the variation in impact parameter in the vicinity of this super-refracting layer. The impact parameter has a negative slope within the layer. Figure 5-15(d) compares the wave equation solutions. In this example, the turning point is well below the critical radius, i.e., $r_o < r^c$. Good agreement holds except near the turning point. A wavenumber value of $k = 1000\,\mathrm{km}^{-1}$ is used in Figs. 5-15 and 5-16. The wave equation solutions in Fig. 5-15(d) show a slight amplitude bulge and a slight reduction in frequency in the vicinity of the super-refracting layer, which is expected. Referring to the WKB solution connection formulas in Eq. (5.7-26), the amplitude and frequency factor expressed in length units is $f_l(\rho) \doteq -k^2 \hat{y} / K_\nu^2 \approx -46\hat{y}\ \mathrm{km}^{-2}$. When $\beta < 1$, $\partial\hat{y} / \partial r < 0$; but in a super-refracting medium where $\beta > 1$, then $\partial\hat{y} / \partial r > 0$. It follows that $\partial f_l / \partial r > 0$ for $r < r_d$; but within the super-refracting layer, $r_d < r < r_u$, $\partial f_l / \partial r < 0$. For a turning point below the critical tangency point, i.e., for $\nu < kn(r^c)r^c$, $f_l(\rho)$ remains positive for all $r > k^{-1}\nu / n(r)$, but it becomes less positive with increasing r within the super-refracting layer, which is reflected in the figure by the increasing amplitude ($\sim 1/\sqrt[4]{f_l}$) and decreasing frequency ($\sim \sqrt{f_l}$) within the layer. Above the layer, $\partial f_l / \partial r$ returns to positive territory. When $\nu < kn(r^c)r^c$, the lth spectral component of the wave effectively powers through the super-refracting layer, as shown in Fig. 5-15(d). The corresponding ray, with an impact parameter value $\rho_* = \nu \le kn(r^c)r^c = kn(r_u)r_u$, also powers through, although it is severely refracted as $\rho_* \to kn(r^c)r^c$ from below.

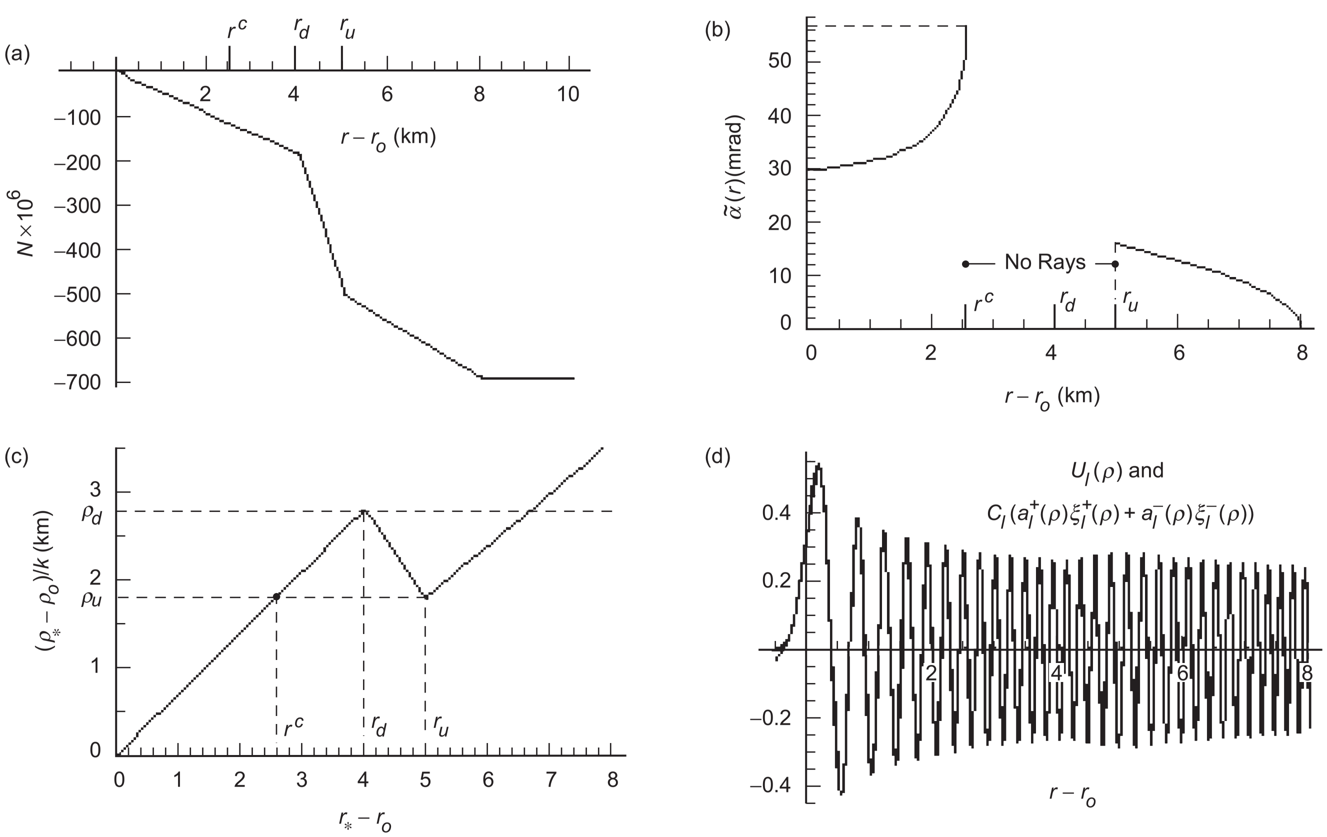

Fig. 5-15. Comparison of wave equation solutions in a severely refracting medium with a super-refracting layer: (a) refractivity profile, (b) bending angle profile, (c) impact parameter profile, and (d) wave equation solutions; spectral number $\nu = kn(r_o)r_o < kn(r^c)r^c$.

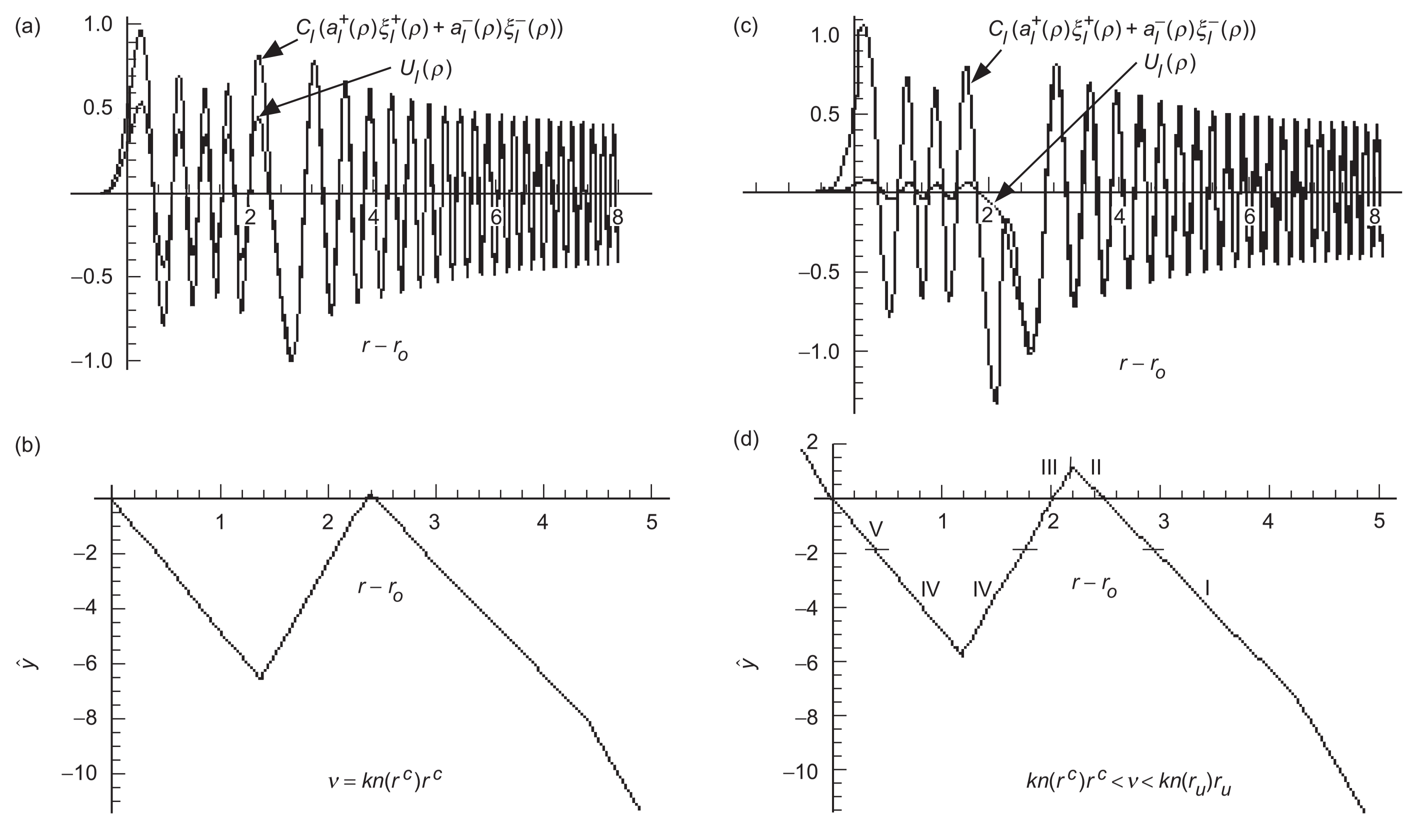

Fig. 5-16. Comparison of wave equation solutions with the spectral number located in the super-refracting zone: (a) wave equation solutions with $\nu = kn(r^c)r^c$, (b) profile for $\hat{y}$ for (a), (c) wave equation solutions with $kn(r^c)r^c < \nu < kn(r_u)r_u$, and (d) profile for $\hat{y}$ for (c).

As the ray path tangency point approaches the critical radius $r_* = r^c$, the bending angle approaches a limit, shown in Fig. 5-15(b), and the wave solution shows a marked transition from an oscillatory form to an exponential form in the vicinity of the layer. A delicate situation occurs when the turning point is such that $kn(r^c)r^c \le \nu \le kn(r_d)r_d$. Here $f_l(\rho)$ reverses sign at $kn(r)r = \nu$, with the lower root to the equality lying in the range $r^c < r < r_u$, and the upper root at $r > r_u$. In this case, we have two zones where $U_l(\rho)$ must be exponential-like: in that region in and above the super-refracting layer where $f_l < 0$, and below the turning point where $f_l < 0$ again. Inasmuch as there are no rays for tangency points in the range $r^c < r_* < r_u$, we expect the wave equation equations to give a damped amplitude for the field.

Lastly, Fig. 5-16 shows the case where the spectral number has been increased (actually, the refractivity profile was lowered in altitude relative to a fixed turning point) so that the spectral number lies in the range $kn(r^c)r^c \le \nu = kn(r_o)r_o \le kn(r_d)r_d$. This figure shows the wave equation solutions and the profile for $\hat{y}$. Figures 5-16(a) and 5-16(b) are for the case where $\nu = kn(r^c)r^c = kn(r_u)r_u$, the critical impact parameter value marking the boundaries of the zone corresponding to the altitude range $r^c < r_* < r_u$, within which no ray path tangency points may lie. Figures 5-16(c) and 5-16(d) are for the case where the spectral number lies within the critical range $kn(r_u)r_u < \nu < kn(r_d)r_d$, the equivalent of about 150 m in radial distance above r^c for $k = 1000\,\text{km}^{-1}$. Figures 5-16(a) and 5-16(c) were normalized so that the amplitudes of all of the wave equation solutions in Figs. 5-16(a) and 5-16(c) have the same asymptotic value with increasing r well above the atmosphere. Here the agreement between $U_l(\rho)$ and the osculating parameter solutions degrades significantly in the vicinity and below the super-refracting layer because $\hat{y}$ becomes positive over a limited interval about the upper boundary at $r = r_u$. It also becomes positive again below the turning point. Although the amplitudes of the two solutions diverge below the layer, their phases remain aligned right down to the turning point.

A super-refracting layer acts like a second turning point when the spectral number lies in the critical zone $kn(r^c)r^c \le \nu \le kn(r_d)r_d$. We note from Eq. (5.7-26) that the slightest hint of a positive value for $\hat{y}$ in the super-refractive zone ($\sqrt{-f_l} \doteq k\sqrt{\hat{y}} / K_\nu \approx 7\sqrt{\hat{y}}$) causes $U_l(\rho)$ to damp to near-zero below the lower critical point where $\hat{y} = 0$. The easiest way to see this is to consider the reverse sense of propagation. Consider a solution for $U_l(\rho)$ that is forced to damp to zero below the turning point at $\rho = \rho_o$. With these initial conditions on $U_l(\rho)$ and its derivative, the solution then is propagated outward.

When the region above the turning point where $f_l(\rho)$ first becomes negative is encountered, the solution becomes exponential-like. This causes the amplitude of $U_l(\rho)$, which still has an Airy function-like character (of the first kind) below this point, to be catapulted to an astronomical magnitude if $f_l(\rho)$ remains negative for a sufficient interval.[10] But we have normalized the asymptotic values of the outbound amplitudes to correspond to the amplitude of an incoming wave, which is essentially invariant over the narrow range of spectral numbers considered here. This forces the amplitude of $U_l(\rho)$ in the region below the lower point at which $f_l(\rho)=0$ to be greatly diminished when $\hat{y}_{\text{MAX}}=\hat{y}_u$ is positive. In Fig. 5-16(a), $\hat{y}_{\text{MAX}} \doteq 0$, and the amplitude of $U_l(\rho)$ below the layer is beginning to attenuate. But in Fig. 5-16(c), $\hat{y}_{\text{MAX}}$ is barely positive, 1.1, and $f_l(\rho)$ is negative only over a 40-m interval about $r=r_u$. Already for these slight intrusions the amplitude of $U_l(\rho)$ is an order of magnitude diminished below the layer. For GPS wavelengths, $\Delta\hat{y}=1$ corresponds to $\Delta r = 14\,\text{m}$ and $\sqrt{-f_l} \approx 70\sqrt{\hat{y}}$. Therefore, the cutoff in amplitude of $U_l(\rho)$ below a super-refracting layer for spectral numbers greater than the limiting value yielding $\hat{y}_{\text{MAX}}=0$ is extremely sharp.

The lower point for $r<r_u$ in the super-refracting layer where $\hat{y}=0$ is also the first point where the bending-angle integral for a hypothetical ray with an impact parameter value of $\rho_* = \nu$ would become complex, if such a ray were to exist. Here $kn(r)r$ becomes smaller than ρ_* for increasing r above this point until the upper point where $\hat{y}=0$ is reached at $r<r_u$.

A better approximation approach (but not used here) for the osculating parameter solution to obtain closer alignment with $U_l(\rho)$ in and below the super-refraction zone is to break the spherical medium into regimes. In Fig. 5-16(d), these regimes are designated by Roman numerals, and they have boundaries in the radial coordinate r at the points where $\hat{y} \approx -2$. In I and IV, the osculating parameter solution applies because $\hat{y}<-2$ throughout these regimes. In each of the tunneling regimes, II, III, and V, the refractivity profile is approximated by an Airy layer, which has a wave equation solution given by Eq. (5.8-6). Since $\hat{y}$ need not be too positive before the solution below the layer is essentially damped to zero, this Airy layer approximation should be valid. The coefficients of these different solutions are tied together by using the continuity conditions on the solutions and their derivatives across each boundary; these boundaries are marked in Fig. 5-16(d). The amplitude of the osculating parameter solution in IV then will damp to zero rapidly below the layer, which $U_l(\rho)$ also does, except for spectral numbers in the transition zone where $\hat{y}_{\mathrm{MAX}} \approx 0$. On the other hand, in region IV below the super-refraction zone, $G[\rho, \nu]$ contains valid phase information because $\hat{y} <\sim -2$.

---

[10] An easy refractivity model with which to see this amplification process is given by $n' = \text{constant} < -157\times10^{-6}\ \text{km}^{-1}$ in the super-refracting layer $r_d \le r \le r_u$, and $n' \equiv 0$ elsewhere. The wave equation solutions are: below the layer, $\text{Ai}[\hat{y}]$; within the layer, $a\text{Ai}[\tilde{y}]+b\text{Bi}[\tilde{y}]$; and above the layer, $c\text{Ai}[\hat{y}]+d\text{Bi}[\hat{y}]$. Equating these solutions and their derivatives across their respective boundaries, at $r=r_d$ and at $r=r_u$ where $\hat{y}=\hat{y}_{\text{max}}$, leads to an explicit evaluation of the coefficients c and d. It can be shown that the amplitude $|\,c^2+d^2\,|^{1/2} \to 2(\beta-1)^{1/6}\exp(2(\beta/(\beta-1))\hat{y}_{\text{max}}^{3/2}/3)$, when $\hat{y}_{\text{max}}>0$. The extreme case $n' \to -\infty$ with Δn finite is addressed in Chapter 3 (Mie scattering theory) and in Section 5.13.

In summary, Figs. 5-13 through 5-16 show good agreement between the exact and osculating parameter solutions over almost all regions except those in the immediate neighborhood of a turning point or in that delicate transition across the critical spectral number range $\nu \approx kn\left(r^c\right)r^c$, below a super-refracting layer. Here $\hat{y}_{\mathrm{MAX}} \approx 0$, but it is not yet positive enough to rapidly damp $U_l(\rho)$ to zero below the layer. In calculating the electric field from the integrals over spectral number that are given in Eq. (5.8-1b), Section 3.16 shows that the principal contribution to these integrals comes from a neighborhood in spectral number where the phasor in the integrand is varying the least. This is a stationary phase neighborhood, which may or may not be unique, depending on the refractivity profile. If the field is being evaluated at an incoming point well away from a turning point, then a stationary phase neighborhood will not be located near $\hat{y} = 0$, but rather in negative territory. Therefore, except for incoming positions near a turning point, we expect the accuracy of the osculating parameter technique applied to the spectral integrals in Eq. (5.8-1b) to be adequate. Moreover, near a turning point, one can use the Airy layer approximation to greatly improve the accuracy there, which is discussed in Section 5.11. The issue of outgoing points remains, and it is discussed later.

5.8.4 Comparison of Phase Delays in an Airy Layer from Wave Theory and Geometric Optics

According to geometric optics, the single-sided phase delay for an initially collimated incident ray with an impact parameter $\rho_* \le \rho_A$ is given by

$$\begin{aligned} ck\tau = k\int_{r_*}^{r_A} \frac{n^2 r\,dr}{\sqrt{n^2 r^2 - n_*^2 r_*^2}} &= -\int_{\rho_*}^{\rho_A} \frac{d\log n}{d\rho}\sqrt{\rho^2 - \rho_*^2}\,d\rho \\ &+ \sqrt{\rho_A^2 - \rho_*^2} + \rho_*\left(\tilde{\alpha}(\rho_*, \rho_*) - \tilde{\alpha}(\rho_A, \rho_*)\right) \end{aligned} \tag{5.8-18}$$

The second equality follows from integrating by parts and using Eq. (5.6-2) for the bending angle. Using Bouguer's law, we see that the bottom line simply equals $\rho_A \cos\theta_A \sec(\Delta\tilde{\alpha})$ through second order in $\Delta\tilde{\alpha} = \tilde{\alpha}(\rho_*, \rho_*) - \tilde{\alpha}(\rho_A, \rho_*)$. Therefore, the extra single-sided phase delay caused by the refractive gradient for a ray with an impact parameter $\rho_* \leq \rho_A$ is given by

$$ck\Delta\tau = -\int_{\rho_*}^{\rho_A} \frac{d\log n}{d\rho}\sqrt{\rho^2 - \rho_*^2}\,d\rho \doteq \frac{\beta_A \rho_*}{3(1-\beta_A)}\left(\frac{2(r_A - r_*)}{r_*}\right)^{3/2} \tag{5.8-19}$$

The approximate expression on the RHS applies to the Airy layer model, and it is accurate when thin-atmosphere conditions apply and $r_* / \lambda >> 1$ (see Appendix A). This expression also gives about 3 1/2 cycles for the conditions shown in Fig. 5-13, and it matches the phase delay expression given in Eq. (5.8-13).

Equation (5.8-13), which is an asymptotically exact result for an Airy layer, Eq. (5.8-15), which gives $G[\rho, \nu]$ from use of the osculating parameter technique, and Eq. (5.8-19), which is from geometric optics, all essentially agree on the phase induced by the refractive gradient on a wave passing through the Airy layer. We return to this model in Section 5.11, where calculating the field at a turning point is discussed.

Equation (5.8-19) provides us with further insight into the character of $G[\rho, \nu]$. When $\nu^* = \rho_*$, $G[\rho, \rho_*]$ provides the extra path delay for a ray with an impact parameter value of ρ_*, both from the curvature component of the ray that is induced by the refractive gradient and from the change in wave velocity along the ray in the medium.

5.8.5 Asymptotic Matching the Spectral Coefficients for Incoming and Outgoing Waves

Let (r_*, θ_*) mark a turning point and $\rho_* = kr_*n_*$ be the impact parameter associated with the ray passing the turning point. We know from Bouguer's law for a spherical symmetric medium that ρ_* is a constant when evaluated along that ray path.

When the planar asymptotic boundary conditions apply to the approaching wave, then the incoming spectral coefficient $a_l^-(\rho)$ is uniquely determined from Eq. (5.5-21). It is independent of the impact parameter ρ_* associated with the point (r, θ) at which $a_l^-(\rho)$ is evaluated because the asymptotic boundary conditions in Eq. (5.5-3) for a planar approaching wave are independent of impact parameter. Because the wave front surface is not symmetric about the turning-point boundary (the approaching waves are collimated prior to impacting the medium; the departing waves are dispersed), the outgoing coefficient depends on the value of ρ_*. For the outgoing wave, it follows from Eq. (5.5-23) that we can obtain $a_l^+[\rho, \rho_*]$ if we know the value of $a_l^+[\rho, \rho_*]$.

Consider first the symmetric problem mentioned earlier, where the electromagnetic wave is planar along the line $\theta = \pi / 2$, $\phi = 0$, i.e., along the x-axis in Fig. 4-10. From Bauer's identity in spherical coordinates, we have along the x-axis

$$1 = \sum_{l=1}^{\infty} i^l (2l+1) \left(\frac{\psi_l(\rho)}{\rho} \right) \mathrm{P}_l(0) \tag{5.8-20}$$

which holds for all values of ρ. As the wave propagates away from the line $\theta = \pi / 2$, which is along the x-axis, the cophasal normal path in the plane $\phi = 0$ will depend on its initial position ρ along the x-axis from which it started. Thus, for every value $\rho = \rho_*$, the spectral coefficients must have the form

$$a_l^{\pm}[\rho, \rho_*] = i^{l-1} \frac{2l+1}{l(l+1)} \exp\left(\pm i \left(G[\rho, v] - G[\rho_*, v] \right) \right) \tag{5.8-21}$$

Using these forms for the spectral coefficients in the scalar potentials given in Eq. (5.8-1), it is readily shown with the Helmholtz equation in Eq. (5.2-6) that the radial component of the electric field is invariant along the x-axis and is given by the RHS of Eq. (5.8-20).

To convert this symmetric form for the electromagnetic wave into a non-symmetric form, that is, the version where the wave is asymptotically collimated on the incoming side ($\pi > \theta > \theta_*$), we merely multiply both a_l^- and a_l^+ in Eq. (5.8-21) by $\exp(-iG[\rho_*, v])$ (thus preserving their equality at $\rho = \rho_*$). We will show later that this is equivalent to rotating clockwise each cophasal normal path by the angle $\tilde{\alpha}(\rho_*, \rho_*)$, where ρ_* is the impact parameter of the path. For this case, as $\rho \to \infty$

$$\left. \begin{aligned} a_l^- &\to i^{l-1} \frac{2l+1}{l(l+1)} \\ a_l^+ &\to i^{l-1} \frac{2l+1}{l(l+1)} \exp(-2iG[\rho_*, v]) \end{aligned} \right\}, \quad \rho \to \infty \tag{5.8-22}$$

The question arises as to what value to use for ρ_* in these expressions in either Eq. (5.8-21) or Eq. (5.8-22). Consider the variability of $a_l^-(\rho)$ with ρ for the collimated case when the spectral number is set to a fixed value v_o. At a point (r, θ) on the approaching side at large distances where $n \to 1$, we set $v_o = kr\sin\theta$; that is, v_o becomes the impact parameter for the cophasal normal passing through the point (r, θ). From Eq. (5.5-21), the evolution of $a_l^-(\rho)$

with ν while traveling along this particular ray path can be obtained by studying the behavior of $G[\rho,\nu]$ with ν fixed. Figure 5-6 shows an example of $G[\rho,\nu_o]$ versus ρ in the close vicinity of $\rho=\nu_o$. $G[\rho,\nu]$ has a stationary value at $\rho=\nu_o-\hat{y}^{\dagger}K_{\rho}$, where $\hat{y}^{\dagger}$ is given by Eq. (5.7-10). This point marks a stationary phase point for $a_l^-(\rho)$ [and for $a_l^+(\rho)$] with respect to ρ. We know that the forms for $G[\rho,\nu]$ given in Eq. (5.5-20) or Eq. (5.7-2) begin to fail for increasing $\hat{y}>0$, and that the correct form for $G[\rho,\nu]$ rapidly assumes a constant value. Figure 5-7 shows a comparison between the exact phase rate $\partial\vartheta_l^- / \partial\rho$ and $\partial G[\rho,\nu]/\partial\rho$ for an Airy layer.

Consistent with the approximation chosen in Eq. (5.7-27) for $G[\rho,\nu]$, we now set $a_l^+=a_l^-$ at the point where $\hat{y}=\hat{y}^{\dagger}$ to ensure no singularity at the origin from the Hankel functions and to attain a close match with the refractive bending angle. Note that this stationary phase point in ρ space varies with the value of ν_o. At this stationary point, $\rho^{\dagger}=\rho^{\dagger}(\nu)=\nu-K_{\rho^{\dagger}}y^{\dagger}$, we set

$$a_l^+\left[\rho^{\dagger},\rho^{\dagger}\right]=a_l^-\left(\rho^{\dagger}\right)=i^{l-1}\frac{2l+1}{l(l+1)}\exp\left(-iG\left[\rho^{\dagger},\nu\right]\right) \tag{5.8-23}$$

This is exactly the same form for $a_l^+[\rho_*,\rho_*]$ that we obtained in Eq. (5.8-17) at the boundary of an Airy layer to force alignment between the round-trip delay obtained from the osculating parameter technique with the round-trip delay from the Airy layer solution. Here $G[\rho,\nu]$ would include the delay from the Airy layer and from the overlying medium. Of course, our Airy layer can be made as thin as we please relative to the extent of the overlying medium. Thus, we asymptotically match the incoming and outgoing spectral coefficients.

From Eq. (5.5-23) it follows that $a_l^+(\rho)$ is given by

$$\begin{aligned} a_l^+(\rho) &= a_l^+\left[\rho^{\dagger},\rho^{\dagger}\right]\exp\left(-i\left(G\left[\rho^{\dagger},\nu\right]-G[\rho,\nu]\right)\right) \\ &= i^{l-1}\frac{2l+1}{l(l+1)}\exp\left(-i\left(2G\left[\rho^{\dagger}(\nu),\nu\right]-G[\rho,\nu]\right)\right) \end{aligned} \tag{5.8-24}$$

At the LEO, which is located at $(r_{\mathrm{L}},\theta_{\mathrm{L}})$ and assumed to be outside of the refracting medium where $n\equiv 1$, the second term in Eq. (5.8-24) is zero; that is, $G[\rho_{\mathrm{L}},\nu]\equiv 0$. It follows that

$$\left.\begin{aligned} a_l^+(\rho_{\mathrm{L}}) &= i^{l-1}\frac{2l+1}{l(l+1)}\exp\left(-i2G\left[\rho^{\dagger}(\nu),\nu\right]\right) \\ \rho^{\dagger} &= \nu-y^{\dagger}K_{\rho^{\dagger}} \end{aligned}\right\} \tag{5.8-25}$$

Thus, $-2G^{\dagger}(\nu) \equiv -2G[\rho^{\dagger}(\nu),\nu]$ is the two-way phase accumulation of the l th spectral coefficient from the stationary point $\rho^{\dagger} = kr^{\dagger}n(\rho^{\dagger})$ to outside of the refracting medium. *It corresponds in geometric optics to the extra phase accumulation induced by the refractivity gradient while traveling along a ray that has completely transected the atmosphere and that has an impact parameter value of* ν.

We will show later that the value of ν that yields a stationary phase in the wave theory spectral representation in Eq. (5.8-1) is essentially equal to the value of the impact parameter for the ray passing through the LEO provided that the inequality $\rho_* \mid d^2 n / d\rho_*^2 \mid << \tilde{\alpha}(\rho_*,\rho_*)$ is satisfied. The latter value is given from Bouguer's law by

$$\nu = \rho_* = kr_* n_* = kr_{\mathrm{L}} \sin\left(\theta_{\mathrm{L}} + \alpha_{\mathrm{L}}(\rho_*)\right) \tag{5.8-26}$$

where $\alpha_{\mathrm{L}}(\rho_*) = 2\tilde{\alpha}(\rho_*,\rho_*)$ is obtained from Eq. (5.6-5). When multipath situations occur, this value may not be unique; we will discuss that later. It follows that the stationary point for the spectral number in wave theory is given by

$$\nu = \nu^{\dagger} = \rho_* + \hat{y}^{\dagger} K_{\rho_*} \tag{5.8-27}$$

A continuing issue for outgoing points concerns the accuracy of the adopted form in Eq. (5.7-27) for $G[\rho,\nu]$ and, therefore, the accuracy of $-2G[\rho^{\dagger}(\nu),\nu]$ in representing the round-trip phase delay. Because of the failure of the osculating parameter technique for decreasing $\rho < \rho^{\dagger}$, this adopted form has some error. But the adopted form for $G[\rho,\nu]$ does have a stationary value at $\rho = \rho^{\dagger}$, and the correct form must rapidly approach a fixed value for $\rho < \rho^{\dagger}$ (see Fig. 5-7). In addition, we have already noted in Section 5.7 the close correspondence between $G[\rho^{\dagger}(\nu),\nu]$ and the component of the phase delay in the eikonal equation induced by the refractivity gradient for a ray with an impact parameter value of ν. Also noted there and in Appendix J is the high accuracy of the relationship, $dG[\rho_*^{\dagger}(\rho_*),\rho_*] / d\rho_* \doteq \tilde{\alpha}(\rho_*,\rho_*)$, provided that the curvature in the refractivity profile is moderate. In this section, the close comparison between $-2G[\rho^{\dagger}(\nu),\nu]$ and the exact solution for the round-trip phase delay in an Airy layer has been noted. Moreover, a byproduct of the numerical solutions presented in Figs. 5-13 through 5-16 (along with the second numerical solution for $U_l(\rho)$ with the boundary conditions generated from $\mathrm{Bi}[\tilde{y}^{\dagger}]$) is the exact value of the extra phase delay induced by the refractivity gradient of the medium. $G[\rho^{\dagger}(\nu),\nu]$, based on Eq. (5.7-27) and calculated from Eq. (5.7-2), may be directly compared to this numerical result for the different refractivity models assumed in these examples. The agreement is generally in the range of 0.5 to 0.1 percent when the curvature index β is not too close to unity. The computational imprecision in these results also is of the order of 0.1 percent. Section 6.5 compares the adopted form for $dG[\rho^{\dagger}(\nu),\nu]/d\nu$, a key spectral quantity in the recovery of the refractivity profile from the LEO amplitude and phase observations, with the exact form for an Airy layer. It gives the error as a function of the ray path curvature index.

An alternative rationale for picking the form given in Eq. (5.8-24) for a_l^{+} is based on probabilistic arguments derived from summing over all possible ray paths. The rationale is similar to the Feynman sum-over-histories technique in quantum electrodynamics to calculate the probability of a quantum event. On the incoming side, for an initial planar wave, the probability density distribution of impact parameter values for the rays is a flat curve; each value is equally likely to occur. Bouguer's law requires that the flat distribution be preserved after atmospheric encounter. Therefore, the values of ρ_* at a turning point are uniformly distributed. If we set the outgoing spectral coefficient to be the spatial average over all possible impact parameter values to be used in Eq. (5.8-22), we end up with an averaging integral to evaluate. The stationary phase value of this integral yields $\rho_* = \rho^{\dagger}(\nu)$. Therefore, the stationary value of $G[\rho,\nu]$ at $\rho = \rho^{\dagger}(\nu)$ should be adopted in Eq. (5.8-22).

5.9 Interpreting Wave Theory in a Refracting Medium Using the Stationary Phase Technique

We now return to the wave theory spectral representation in Eqs. (5.8-1a) and (5.8-1b) for the electric field at a point (r,θ) in the refracting medium. Before presenting numerical examples using this spectral representation, we apply stationary phase concepts to aid in the interpretation of those numerical results to compare with geometric optics. We follow Chapter 3 closely here; in particular, we refer to the material in Sections 3.10 through 3.13. The integrals in Eq. (5.8-1b) are characterized by a slowly varying factor multiplied by the sum of four phasors that are rapidly oscillating over most of the spectral number space. The main contributions to these integrals come from neighborhoods where any one of these phasors is varying the least. Our task now is to use the stationary phase technique on these integrals to identify the possible stationary phase neighborhoods for each phasor and to calculate the values for E_r and E_θ at a given point (r,θ).

5.9.1 Geometric Interpretation of the Phasors

We rewrite the asymptotic forms for the Hankel and Legendre functions in Eq. (5.8-1) in a phasor form that provides a useful geometric interpretation.

Except for a point (r,θ) located very near a turning point, we will show that the stationary phase neighborhoods in ν space are sufficiently below the value $\rho = krn(\rho)$ that the negative argument asymptotic forms for the Airy functions given in Eq. (3.8-7) can be used. In this case, from Eqs. (3.10-1) through (3.10-4), the spherical Hankel functions can be rewritten as

$$\left.\begin{aligned} \xi_l^{\pm}(\rho) &\sim \left(\frac{\rho}{D_\nu}\right)^{1/2} \exp\bigl(\pm i\bigl(D_\nu + \nu(\theta_\nu - \pi/2) - \pi/4\bigr)\bigr) \\ \xi_l^{\pm\prime}(\rho) &\sim \left(\frac{D_\nu}{\rho}\right)^{1/2} \exp\bigl(\pm i\bigl(D_\nu + \nu(\theta_\nu - \pi/2) - \pi/4\bigr)\bigr) \end{aligned}\right\} \tag{5.9-1}$$

where

$$D_\nu = \sqrt{\rho^2 - \nu^2}, \;\; \theta_\nu = \sin^{-1}\left(\frac{\nu}{\rho}\right), \quad \rho = krn(\rho), \quad \nu < \rho \tag{5.9-2}$$

Similarly, from Eq. (3.10-5), the asymptotic form for the Legendre polynomial $\mathrm{P}_l^1(\cos\theta)$ is given by

$$\mathrm{P}_l^1(\cos\theta) \sim -\sqrt{\frac{l}{2\pi\sin\theta}}\left(\exp\left[i\left(\nu\theta + \frac{\pi}{4}\right)\right] + \exp\left[-i\left(\nu\theta + \frac{\pi}{4}\right)\right]\right) \tag{5.9-3}$$

The geometric interpretation of θ_ν as the central angle to the point (ρ,θ_ν) and with D_ν as its tangential distance in phase units from a spherical caustic surface of radius ν has been given in Chapter 3, Eqs. (3.11-1) and (3.11-2), and in Figs. 3-14 and 3-15. Those figures are applicable to an outgoing wave, but the concepts are the same, whether incoming or outgoing. Figure 3-14 shows the geometric relationships given by Eq. (5.9-2). Two rays, originally collimated from the GPS direction, reach the point L located at (ρ,θ). The direct path is a straight path to the tangential point P_1 and then straight on to the point L. Along the retrograde path via P_2, the ray arrives tangentially at P_2, travels along the arc $\mathrm{P}_2\,\mathrm{P}_2'$, and then departs tangentially from P_2' going straight on to the point L. We note that, when it is assumed that the stationary phase value ν^* lies in the range $0 < \nu^* < \rho$, it follows that $0 < \theta_{\nu^*} < \pi/2$. As ν increases through its range of values in the spectral integrals in Eq. (5.8-1b), the radius of this caustic sphere expands, and its center descends.

The four phasors appearing in the integrals in Eq. (5.8-1b) result from the product of the spherical Hankel and Legendre functions in Eqs. (5.9-1) and (5.9-3) times the incoming and outgoing spectral coefficients given in

Eqs. (5.5-21) and (5.8-24), respectively. To further interpret these phasors geometrically, we let

$$\left.\begin{aligned}&\text{outgoing: } \theta = \theta_\nu + \Delta\theta_\nu \\ &\text{incoming: } \theta = \pi - \left(\theta_\nu + \Delta\theta_\nu\right)\end{aligned}\right\} \tag{5.9-4}$$

Because the stationary neighborhoods for ν will be close to $\nu^* = \rho \sin(\theta + \alpha)$, we would expect $\Delta\theta_\nu$ to be small in these neighborhoods. Figure 3-15 provides a geometric interpretation of $\Delta\theta_\nu$ in terms of the extra phase $\nu\Delta\theta_\nu$ along the $\theta = 0$ direction that results from the offset $\theta - \theta_\nu$ for an outgoing wave (and $\theta - \left(\pi - \theta_\nu\right)$ for an incoming wave).

5.9.2 Stationary Phase Conditions

We now insert the asymptotic forms in Eqs. (5.9-1) through-(5.9-3) into Eq. (5.8-1b), and we substitute the forms for the spectral coefficients a_l^- and a_l^+ given by Eqs. (5.5-21) and (5.8-24), respectively. After some manipulation of Eq. (5.8-1b), the spectral representation for $E_r(r,\theta)$ and $E_\theta(r,\theta)$ becomes

$$\left.\begin{aligned}&E_r = \\ &\frac{E_o}{\sqrt{2\pi\rho\sin\theta}} \int_0^\infty \left(\frac{\sin^3\theta_\nu}{\cos\theta_\nu}\right)^{\frac{1}{2}} \left(e^{i\Psi(+,+)} + e^{i\Psi(+,-)} + e^{i\Psi(-,+)} + e^{i\Psi(-,-)}\right) d\nu \\ &E_\theta = \\ &\frac{E_o}{\sqrt{2\pi\rho\sin\theta}} \int_0^\infty \left(\frac{\sin 2\theta_\nu}{2}\right)^{\frac{1}{2}} \left(e^{i\Psi(+,+)} + e^{i\Psi(+,-)} + e^{i\Psi(-,+)} + e^{i\Psi(-,-)}\right) d\nu\end{aligned}\right\} \tag{5.9-5}$$

where the four phases are given by

$$\left.\begin{aligned}\Psi(+,+) &= D_\nu + \nu\left(\theta_\nu + \theta\right) + \frac{\pi}{4} + G[\rho,\nu] - 2G\left[\rho^\dagger,\nu\right] \\ \Psi(+,-) &= D_\nu + \nu\left(\theta_\nu - \theta\right) - \frac{\pi}{4} + G[\rho,\nu] - 2G\left[\rho^\dagger,\nu\right] \\ \Psi(-,+) &= -D_\nu - \nu\left(\theta_\nu - \theta - \pi\right) + \frac{3\pi}{4} - G[\rho,\nu] \\ \Psi(-,-) &= -D_\nu - \nu\left(\theta_\nu + \theta - \pi\right) + \frac{\pi}{4} - G[\rho,\nu]\end{aligned}\right\} \tag{5.9-6}$$

Here (±,±) designates use of certain combinations of spherical Hankel functions and spherical harmonic asymptotic functions. For example in (+, –) the plus sign in the first argument designates use of the spherical Hankel function of the first kind ξ_l^+, and the minus sign in the second argument designates use of the negative exponential term in the asymptotic form for the Legendre polynomial. In the integrals in Eq. (5.9-5), θ_ν varies slowly with ν, but the phasor terms are rapidly varying except at stationary phase points. The principal contribution to these integrals comes from neighborhoods about stationary phase points. In the stationary phase technique, the phase of each phasor is expanded in a Taylor series through second degree about possible stationary phase values of ν. Thus, the first-degree term is zero, and the Taylor series contains only a zeroth-degree term and a quadratic term. Upon evaluating the slowly varying terms at a stationary phase point, the integral reduces to a Fresnel integral.

To see if a stationary phase point exists for the four phasors given in Eq. (5.9-6), we substitute Eq. (5.9-4) into Eq. (5.9-6) to obtain

$$\left.\begin{aligned}
\Psi(+,+) &= D_\nu + \nu\left(2\theta_\nu + \Delta\theta_\nu\right) + \frac{\pi}{4} + G[\rho,\nu] - 2G\left[\rho^\dagger,\nu\right] \\
\Psi(+,-) &= D_\nu - \nu\Delta\theta_\nu - \frac{\pi}{4} + G[\rho,\nu] - 2G\left[\rho^\dagger,\nu\right] \\
\Psi(-,+) &= -D_\nu - \nu\left(2\theta_\nu - 2\pi - \Delta\theta_\nu\right) + \frac{3\pi}{4} - G[\rho,\nu] \\
\Psi(-,-) &= -D_\nu + \nu\Delta\theta_\nu + \frac{\pi}{4} - G[\rho,\nu]
\end{aligned}\right\} \qquad (5.9\text{-}6')$$

Comparing the terms in Eq. (5.9-6′) with Fig. 3-14, we conclude that $(+,+)$ is associated with an outgoing wave from the far side of the scattering sphere—that is, it is associated with the retrograde path; $(-,-)$ is associated with the incoming wave on the near side, and so on. We can eliminate by inspection the phase terms $\Psi(+,+)$ and $\Psi(-,+)$, because these are associated with waves that travel around the far side of the sphere in Fig. 3-14 via point P_2. They will provide negligible contributions to the spectral integrals for the electric field when r_o / λ is large and the point L is located well into the first or second quadrants in θ. The term $2\nu\theta_\nu$ in their arguments results in very high rates of phase accumulation for essentially all values of ν.

5.9.3 Stationarity of $\Psi(\pm,\pm)$

Returning to Eq. (5.9-6), we take the partial derivative of the phase $\Psi(\pm,\pm)$ with respect to ν in each of these four phasor combinations that appear in Eq. (5.9-6) and attempt to set the resultant equal to zero. We conclude (remembering that $0<\theta_v \le \pi/2$ and that $0<\theta<\pi$) the following with regard to the possibility of achieving a stationary value for each of these phases:

$$\partial\Psi(+,+)/\partial v = 0:$$

no, if $\theta > \partial\left(2G\left[\rho_*^\dagger, v\right] - G[\rho, v]\right)/\partial v$,

$$\partial\Psi(+,-)/\partial v = 0:$$

yes, if $\theta < \pi/2 - \partial\left(2G\left[\rho_*^\dagger, v\right] - G[\rho, v]\right)/\partial v$,

$$\partial\Psi(-,+)/\partial v = 0:$$

no, if $\theta \ge 0$

$$\partial\Psi(-,-)/\partial v = 0:$$

yes, if $\theta > \pi/2 - \partial G\left[\rho_*^\dagger, v\right]/\partial v$.

As already mentioned, for an occultation from a LEO, we can effectively rule out the $(+,+)$ and $(-,+)$ combinations. These are contributions to the integrals in Eq. (5.9-5) that originate from the far side of the sphere (Fig. 3-14). They are negligible when θ lies well into the upper quadrants and when the ratio r_o/λ is very large, both of which are assumed here. The combination $(+,-)$ corresponds to an outgoing wave on the near side of the sphere where the spherical Hankel function $\xi_l^+(\rho)$ is used; the combination $(-,-)$ corresponds to an incoming wave on the near side where $\xi_l^-(\rho)$ applies.

5.9.4 Plane Waves

As an illustrative case, consider the stationary phase possibilities for a planar wave in a homogeneous medium. Here $n' \equiv 0$ and, therefore, $G[\rho, v] \equiv 0$. An appropriate spectral representation for this case is given from Bauer's identity (Section 5.3) in spherical coordinates:

$$\exp(i\rho\cos\theta) = \sum_{j=0}^{\infty} i^l (2l+1) \frac{\psi_l(\rho)}{\rho} \mathrm{P}_l(\cos\theta) \tag{5.9-7}$$

Here, expressing $i^l \psi_l \mathrm{P}_l$ in terms of phasors (with $\psi_l = (\xi_l^+ + \xi_l^-)/2$) leads to the same combinations $\Psi(\pm,\pm)$ given in Eq. (5.9-6) but with $G[\rho, v] \equiv 0$. Attempting to set $\partial\Psi(\pm,\pm)/\partial v = 0$ for the four possible sign combinations in the region $0<\theta<\pi$ produces the following conditions on θ_v:

$(+,+)$: $\theta_\nu=-\theta$; impossible
$(+,-)$: $\theta_\nu=\theta$; possible if $0<\theta<\pi/2$
$(-,+)$: $\theta_\nu=\theta+\pi$; impossible
$(-,-)$: $\theta_\nu=\pi-\theta$; possible if $\pi>\theta>\pi/2$

It follows that the $(+,-)$ case corresponds to a departing planar wave and that the $(-,-)$ case corresponds to an approaching wave. In either case, a stationary value for $\Psi(\pm,-)$ is achieved when the spectral number $\nu=\nu^*=\rho_*=\rho\sin\theta$ (see Eq. 5.9-6 with $G[\rho,\nu]\equiv 0$). For this value, $D_{\nu^*}=|D_{\rho_*}|=|\rho\cos\theta|$. The second derivative of $\Psi(\pm,-)$ is $\partial^2\Psi/\partial\nu^2=\pm D_{\nu^*}^{-1}$.

We can evaluate the summation in Bauer's identity using the stationary phase technique. Expanding $\Psi(\pm,-)$ in a Taylor series about the stationary phase point $\nu^*=\rho_*$ through the quadratic term yields

$$\left.\begin{aligned}&\Psi(\pm,-)\doteq D_{\nu^*}\pm\frac{1}{2D_{\nu^*}}\left(\nu-\nu^*\right)^2\mp\frac{\pi}{4},\\ &\nu^*=\rho_*=\rho\sin\theta,\ D_{\nu^*}=\left|\rho\cos\theta\right|\end{aligned}\right\}\tag{5.9-8}$$

Replacing the summation in Bauer's identity by an integral and using Eq. (5.9-8), we obtain

$$\begin{aligned}&\sum_{j=0}^{\infty}i^l(2l+1)\frac{\psi_l}{\rho}\mathrm{P}_l(\cos\theta)\doteq\sqrt{\frac{1}{2\pi}}\int_0^\infty D_\nu^{-1/2}\exp\left(\pm i\Psi(\pm,-)\right)d\nu\\ &\doteq\sqrt{\frac{\pm1}{2\pi iD_{\nu^*}}}\exp\left(\pm iD_{\nu^*}\right)\int_0^\infty\exp\left(\pm i\frac{(\nu-\rho_*)^2}{2D_{\nu^*}}\right)d\nu=\exp\left(\pm iD_{\nu^*}\right)\end{aligned}\tag{5.9-9}$$

By a change of variable $\pi s^2=(\nu-\rho_*)^2/D_{\nu^*}$, the integral in Eq. (5.9-9) is transformed into a complex Fresnel integral. Since $\rho_*>>1$, this is essentially a complete Fresnel integral equal to $(\pm 2\pi iD_{\nu^*})^{1/2}$. Thus, Eq. (5.9-9) reduces to $\exp(\pm iD_{\nu^*})=\exp(iD_{\rho_*})$, which equals the left side of Bauer's identity.

Note again that $2\psi_l=\xi_l^++\xi_l^-$. However, ξ_l^- appears in $\Psi(-,-)$, and ξ_l^+ appears in $\Psi(+,-)$. Therefore, only ξ_l^- contributes to the spectral sum in Eq. (5.9-9) for a position well within the incoming region, i.e., for an incoming wave. Only ξ_l^+ contributes for an outgoing wave. This is consistent with the asymptotic forms that ξ_l^+ and ξ_l^- assume when $\rho>>\nu$. Here

$\xi_l^{\pm} / \rho \to (\mp i)^{l+1} \exp(\pm i\rho) / \rho$. Thus, ξ_l^{+} / ρ corresponds to an outgoing spherical wave, and ξ_l^{-} / ρ corresponds to an incoming spherical wave.

5.9.5 The Electric Field for an Incoming Wave

We now evaluate the integrals in Eq. (5.9-5) for the electric field vector using the stationary phase technique. We first assume that the point (r,θ) is in the incoming region well away from a turning point, so that the negative argument asymptotic forms for the Airy functions apply. In an incoming region, $\pi > \theta > \pi / 2 - \tilde{\alpha}(\rho_*, \rho_*)$. If we set as a criterion for "well away" that the point (r,θ) must be such that $\hat{y} < -2$ at its stationary phase point, then by applying Bouguer's law in Eq. (5.6-3), one can show that a suitable criterion is $\theta > \pi / 2 - \tilde{\alpha}(\rho_*, \rho_*) + \sqrt{2} / K_{\rho_*}$. For GPS signals in the Earth's atmosphere, $\sqrt{2} / K_{\rho_*} \approx 3\,\text{mrad}$. In an incoming region well away from a turning point, only the phase ${}^{(i)}\Psi = \Psi(-,-)$ contributes significantly to the spectral integrals.

We denote the field in an incoming region by ${}^{(i)}\boldsymbol{E}(\rho,\theta)$, and we let ${}^{(i)}\Psi = \Psi(-,-)$. Thus, ${}^{(i)}\Psi$ is the spectral density function for the phase delay at the point (ρ,θ) for an incoming wave. It follows from Eqs. (5.9-5) and (5.9-6) for $\rho > \rho_*$ that

$$\left.\begin{aligned} {}^{(i)}E_r(\rho,\theta) &= \frac{E_o}{\sqrt{2\pi\rho\sin\theta}} \int_0^{\infty} \left(\frac{\sin^3\theta_\nu}{\cos\theta_\nu} \right)^{1/2} \exp\left(i\,{}^{(i)}\Psi(\rho,\theta,\nu)\right) d\nu, \\ {}^{(i)}E_\theta(\rho,\theta) &= \frac{E_o}{\sqrt{2\pi\rho\sin\theta}} \int_0^{\infty} \left(\sin\theta_\nu \cos\theta_\nu \right)^{1/2} \exp\left(i\,{}^{(i)}\Psi(\rho,\theta,\nu)\right) d\nu \end{aligned}\right\} \tag{5.9-10}$$

To evaluate these integrals using the stationary phase technique, we expand ${}^{(i)}\Psi$ in a Taylor's series through second order in spectral number about its stationary phase value. Using Eqs. (5.9-2) and (5.9-6), $\partial\,{}^{(i)}\Psi / \partial\nu$ becomes

$$\frac{\partial}{\partial\nu}\left({}^{(i)}\Psi\right) = -\left(\theta_\nu + \theta - \pi + \frac{\partial G}{\partial\nu}\right) = 0 \tag{5.9-11}$$

and the second derivative becomes

$$\frac{\partial^2}{\partial\nu^2}\left({}^{(i)}\Psi\right) = -\frac{1}{D_\nu} - \frac{\partial^2 G}{\partial\nu^2} \tag{5.9-12}$$

Let ν^* be a spectral number value that provides a stationary phase; that is, it satisfies the stationarity condition in Eq. (5.9-11). Then from Eqs. (5.9-2) and (5.9-11), one obtains

$$\left.\begin{aligned} \theta_{\nu^*} &= \pi - \theta - \left(\frac{\partial G[\rho,\nu]}{\partial \nu}\right)_{\nu=\nu^*} \\ \nu^* &= \rho \sin\theta_{\nu^*} \end{aligned}\right\} \tag{5.9-13}$$

We define $\delta(\rho,\theta,\nu)$ by

$$\left.\begin{aligned} \theta_\nu &= \pi - \theta - \delta \\ \delta &= \pi - \theta - \sin^{-1}\left(\frac{\nu}{\rho}\right) \\ \rho &= krn(\rho) \end{aligned}\right\} \tag{5.9-14}$$

where for a thin atmosphere $\delta^* = \delta(\rho,\theta,\nu^*)$ generally will be a small quantity. When ν assumes a value so that $\delta^* = \partial G / \partial \nu$, Eq. (5.9-14) shows that we have a stationary phase point. In our discussion in Section 3.12 on stationary phase processes in Mie scattering theory, we noted that δ^* should be very close in value to the refractive bending angle. Here δ^* should be close in value to the cumulative bending angle $\tilde{\alpha}(\rho,\rho_*)$ for a ray passing through the point (ρ,θ) with an impact parameter value of ρ_*. Here $\rho_* = \rho \sin\left[\theta + \tilde{\alpha}(\rho,\rho_*)\right]$. From Eq. (5.7-8), it follows that $\partial G[\rho,\nu] / \partial \nu = \tilde{\alpha}(\rho,\nu)$ to high accuracy provided that $\nu < \rho - {\sim}\, 2K_\nu$ (see Fig. 5-4). The differences between δ^* and $\tilde{\alpha}(\rho,\rho_*)$ and between ν^* and ρ_* can be obtained by expanding Eq. (5.9-14) in a power series for $G[\rho,\nu]$ about the point $\tilde{\nu}$ where $\partial G / \partial \nu = \tilde{\alpha}$, exactly. One obtains

$$\left.\begin{aligned} \nu^* - \rho_* &\doteq \left(\delta^* - \tilde{\alpha}\right)\rho\cos(\theta + \tilde{\alpha}) \\ \delta^* - \tilde{\alpha} &\doteq \left(\nu^* - \tilde{\nu}\right)\left(\frac{\partial^2 G[\rho,\nu]}{\partial \nu^2}\right)_{\nu=\nu^*} \end{aligned}\right\} \tag{5.9-15}$$

We expect that $\tilde{\nu}$ will be close to ρ_*. Upon setting $\partial^2 G / \partial \nu^2 = \partial \tilde{\alpha} / \partial \rho_*$, it follows that

$$\left.\begin{aligned} \nu^{*}-\rho_{*}&=D_{\rho_{*}}\frac{\partial\tilde{\alpha}(\rho,\rho_{*})}{\partial\rho_{*}}\left(1-D_{\rho_{*}}\frac{\partial\tilde{\alpha}(\rho,\rho_{*})}{\partial\rho_{*}}\right)^{-1}\\ \nu^{*}-\tilde{\nu}&=\left(\rho_{*}-\tilde{\nu}\right)\left(1-D_{\rho_{*}}\frac{\partial\tilde{\alpha}(\rho,\rho_{*})}{\partial\rho_{*}}\right)^{-1} \end{aligned}\right\} \tag{5.9-16}$$

It follows that

$$\delta^{*}-\tilde{\alpha}\doteq\left(\rho_{*}-\tilde{\nu}\right)\frac{\partial\tilde{\alpha}(\rho,\rho_{*})}{\partial\rho_{*}}\left(1-D_{\rho_{*}}\frac{\partial\tilde{\alpha}(\rho,\rho_{*})}{\partial\rho_{*}}\right)^{-1} \tag{5.9-17}$$

We note the defocusing factor showing up in these expressions for the offsets. It follows from Eqs. (5.9-14) and (5.9-15) that, if ν^{*} is near the value ρ_{*}, which is the value(s) of the impact parameter for the ray(s) passing through the point (r,θ), then δ^{*} will equal the corresponding value of $\tilde{\alpha}$ with close accuracy. If the ray system from the actual refractivity profile generates a caustic surface, when the position (r,θ) is such that ν^{*} lies near a contact point with that caustic, $1-(\partial\tilde{\alpha}/\partial\rho_{*})D_{\rho_{*}}\approx 0$. Equations (5.9-16) and (5.9-17) are not valid in that neighborhood.

Figure 5-17 shows the stationary phase solutions for the exponential refractivity profile in Eq. (5.8-2a) at the intersections of the $\partial G/\partial\nu$ and $\delta(\rho,\theta,\nu)$ curves [see Eqs. (5.7-7) and (5.9-14)]. The figure shows the

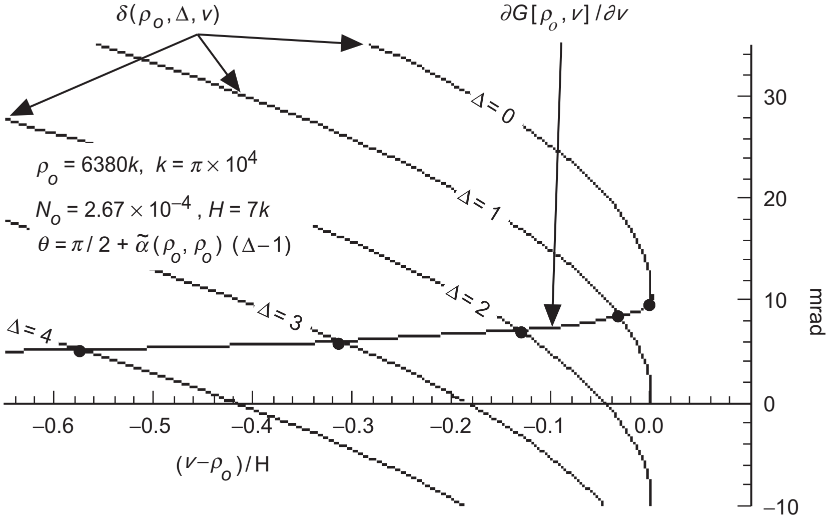

Fig. 5-17. Stationary phase solution ν^{*} to Eq. (5.9-13) for the Case A refractivity profile [Eq. (5.8-2a)].

stationary phase solution for four position points (r,θ), all at the same radial distance r_o and with θ increasing from the turning point at $\theta=\theta_*=\pi/2-\tilde{\alpha}(\rho_o,\rho_o)$ in four equally spaced increments up to $\theta=\pi/2+3\tilde{\alpha}(\rho_o,\rho_o)$. Even at $\theta=\pi/2$, which is very close to the turning point and where one might worry that either (1) the asymptotic form at negative arguments for the Airy functions might break down or (2) the approximations for the spectral coefficients given in Eq. (5.5-21) for a_l^- and Eq. (5.8-24) for a_l^+ might fail, the agreement is close. At $\theta=\pi/2$, the intersection point yields a stationary phase value that corresponds to an Airy function argument of $\hat{y}^*\approx-20$. This value for $\hat{y}^*$ also is corroborated by evaluating $K_\rho^{-1}(\rho_*-\rho)$ from Bouguer's law in Eq. (5.6-3). This justifies our use of the negative argument asymptotic forms for the Airy functions in the expressions for $\Psi(-,-)$ in Eq. (5.9-1) when θ is at least $\pi/2$ or greater. The intersection point for $\theta=\pi/2$ in Fig. 5-17 yields a value for $\partial G/\partial\nu$ of 8.056 mrad, which differs by only $\sim 5\ \mu$rad from the value for $\tilde{\alpha}(\rho_o,\rho_*)$, $\rho_*=\rho_o\cos\Delta$, predicted by ray theory in Eq. (5.6-2). A lower bound on θ already has been established from Bouguer's law, where we set $\hat{y}^*=-2$; this gave $\theta\geq\pi/2-\tilde{\alpha}(\rho_o,\rho_o)+\varepsilon$, $\varepsilon=\sqrt{2}K_{u_o}^{-1}\approx\tilde{\alpha}/3$. Thus, except for a very narrow range of θ values near the turning point, the stationary phase point ν^* should be very close to ρ_* when the curvature in the refractivity is relatively slight, i.e., when $K_{\rho_o}/(kH)$ is small. $K_{\rho_o}/(kH)$ essentially is the ratio of the Airy function transition scale (a change in ρ and/or ν corresponding to $\Delta\hat{y}=1$) to the refractivity scale height (in phase units), which for the example shown in Fig. 5-17 is about 0.002.

Even at the turning point at $\theta=\theta_*=\pi/2-\tilde{\alpha}(\rho_o,\rho_o)$, the intersection point in Fig. 5-17 (where $\hat{y}\cong0$ in this case) yields a value $\delta(\rho,\theta,\nu^*)=\partial G/\partial\nu|_{\nu^*}=9.894$ mrad; the ray theory value from Eq. (5.6-2) for $\tilde{\alpha}(\rho_o,\rho_o)$ is 10.110 mrad. We already have noted the levels of agreement between these quantities, which are shown in detail in Figs. 5-5 and 5-6. These figures show the close agreement between the wave-theoretic and geometric optics representations of bending angle under thin-atmosphere conditions except in the immediate vicinity of a turning point.

5.9.6 Evaluating the Electric Field Vector Using the Stationary Phase Technique

Using the stationary phase technique, we now evaluate the integrals in Eq. (5.9-10) for the electric field vector in the incoming region. We assume that the point (r,θ) is well into the incoming region so that the negative argument asymptotic forms for the Airy functions apply. We have just seen that the criterion $\theta > \pi/2 - 2\tilde{\alpha}(\rho_*,\rho_*)/3$ should suffice. Inserting into Eq. (5.9-10) the Taylor's series expansion through second-order terms for ${}^{(i)}\Psi(\rho,\theta,\nu) = \Psi(-,-)$ evaluated at the stationary phase point, and using Eqs. (5.9-11) through-(5.9-15), one obtains for $E_r(r,\theta)$ and $E_\theta(r,\theta)$

$$\left.\begin{aligned}
&{}^{(i)}E_{\left\{\begin{smallmatrix} r\\ \theta\end{smallmatrix}\right\}} \doteq E_o e^{i{}^{(i)}\Phi^*} \begin{Bmatrix}\sin\left({}^{(i)}\gamma^*\right)\\ \cos\left({}^{(i)}\gamma^*\right)\end{Bmatrix}\sqrt{\frac{-\sin\left({}^{(i)}\gamma^*\right)}{2\pi i D_{\nu^*}\sin\theta}}\int_0^\infty e^{-i\frac{(\nu-\nu^*)^2}{2\zeta D_{\nu^*}}}d\nu,\\
&{}^{(i)}\Phi^* = {}^{(i)}\Psi\left(\rho,\theta,\nu^*\right) - \frac{\pi}{4} = \left(-D_\nu + \nu\frac{\partial G}{\partial\nu} - G\right)_{\nu=\nu^*},\\
&\left(\frac{\partial^{(i)}\Psi}{\partial\nu}\right)_{\nu=\nu^*} = \sin^{-1}\left(\frac{\nu^*}{\rho}\right) - \left(\pi-\theta-\frac{\partial G}{\partial\nu}\right)_{\nu=\nu^*} = 0,\\
&{}^{(i)}\zeta = \left(1+{}^{(i)}D_\nu\frac{\partial^2 G}{\partial\nu^2}\right)^{-1}_{\nu=\nu^*},\quad G = G[\rho,\nu],\\
&{}^{(i)}\gamma^* = \theta + \left(\frac{\partial G}{\partial\nu}\right)_{\nu=\nu^*},\quad \pi > {}^{(i)}\gamma^* > \frac{\pi}{2},\\
&{}^{(i)}D_{\nu^*} = -\rho\cos\left({}^{(i)}\gamma^*\right) \ge 0,\quad \nu^* = \rho\sin\left({}^{(i)}\gamma^*\right)
\end{aligned}\right\}\text{(5.9-18)}$$

The integrals in Eq. (5.9-18) for ${}^{(i)}E_r$ and ${}^{(i)}E_\theta$ (upon noting that $-\nu^* \cong -\infty$) are readily transformed through a change of variable into the form $\int_{-\infty}^{\infty}\exp\left(-i\pi t^2/2\right)dt$, which is the complex conjugate of the complete Fresnel integral, with a value of $1-i = (-2i)^{1/2}$. Hence, the electric field for the incoming wave in Eq. (5.9-18) may be written as

$$\left.\begin{aligned}
&{}^{(i)}E_r \doteq E_o\sqrt{\frac{{}^{(i)}\zeta\sin\left({}^{(i)}\gamma^*\right)}{\sin\theta}}\sin\left({}^{(i)}\gamma^*\right)\exp\left(i{}^{(i)}\Phi^*\right)\\
&{}^{(i)}E_\theta \doteq E_o\sqrt{\frac{{}^{(i)}\zeta\sin\left({}^{(i)}\gamma^*\right)}{\sin\theta}}\cos\left({}^{(i)}\gamma^*\right)\exp\left(i{}^{(i)}\Phi^*\right)
\end{aligned}\right\}\text{(5.9-19)}$$

We recognize in Eqs. (5.9-18) and (5.9-19) the phase delay term ${}^{(i)}\Phi^*$, which here is largely a phase advance for the incoming wave because it is referenced to the $\theta = \pi/2$ line. Recalling the asymptotic relationships between $G[\rho,\nu]$ and $\partial G/\partial\nu$ and bending-angle quantities given by Eqs. (5.7-6) and

(5.7-8), respectively, we see that the equivalent form for ${}^{(i)}\Phi^*$ in geometric optics is

$$\left.\begin{aligned}{}^{(i)}\Phi^* &\doteq \rho\cos\big(\theta+\tilde{\alpha}(\rho,\rho_*)\big)+\rho_*\tilde{\alpha}(\rho,\rho_*)\\ &\quad+\int_{\rho_*}^{\rho}\tilde{\alpha}(\rho,\nu)d\nu+\int_{\rho}^{\infty}\tilde{\alpha}(\omega,\omega)d\omega\\ {}^{(i)}\gamma^* &\doteq \theta+\tilde{\alpha}(\rho,\rho_*)\end{aligned}\right\} \tag{5.9-20}$$

The leading term $\rho\cos\big(\theta+\tilde{\alpha}(\rho,\rho_*)\big)$ is the optical path delay (negative for this incoming case) from the tangent point on the spherical surface radius ρ_* to the point (ρ,θ). The second term is an arc-length term along a sphere of radius ρ_* due to refractive bending. The third and fourth terms—equal to $-G[\rho,\nu^*]$ in wave theory [see Eq. (5.7-6)]—account for the extra phase delay due to the refractive gradient-induced bending through the atmosphere that a ray of impact parameter value ρ_* from the GPS satellite (assumed to be at infinity) undergoes in reaching the incoming point (r,θ).

Equation (5.9-20) may be compared to the relationship with the eikonal equation given in Eq. (5.10-11). Here the spectral density function for the complete phase delay at (r,θ), ${}^{(i)}\Psi(\rho,\theta,\nu)$, has a close correspondence to the eikonal $\mathscr{S}(\rho)$ associated with the path delay along a ray. When ${}^{(i)}\Psi(\rho,\theta,\nu)$ is evaluated at a stationary phase point $\nu^*\doteq\rho_*$, then ${}^{(i)}\Psi(\rho,\theta,\rho_*)\Leftrightarrow\mathscr{S}(\rho)-\mathscr{S}(\rho_*)$.

We also recognize the defocusing factor ${}^{(i)}\zeta$ in Eq. (5.9-18), which has its analog in geometric optics to account for the dispersive effect of the refraction gradient on signal power (see Section 5.6). From Eq. (5.7-7), $\partial^2 G/\partial\nu^2$ is given by

$$\frac{\partial^2 G}{\partial\nu^2}\doteq 2\pi\int_{\rho}^{\infty}\frac{d\log n}{d\rho'}\big(\mathrm{Ai}[\hat{y}]\mathrm{Ai}'[\hat{y}]+\mathrm{Bi}[\hat{y}]\mathrm{Bi}'[\hat{y}]\big)d\rho' \tag{5.9-21}$$

Using the asymptotic forms for the Airy functions given in Eq. (3.8-10) when $\rho>\nu$, one obtains

$$\left.\frac{\partial^2 G}{\partial\nu^2}\doteq -\nu^2\int_{\rho}^{\infty}\frac{d\log n}{d\rho'}\frac{d\rho'}{\left(\rho'^2-\nu^2\right)^{3/2}}=\frac{\partial\tilde{\alpha}}{\partial\nu},\quad \tilde{\alpha}=\tilde{\alpha}(\rho,\nu)\right\} \tag{5.9-22}$$

The integral here can be integrated by parts to eliminate its near singularity. Figure 5-5 compares $\partial^2 G/\partial\nu^2$ and $\partial\tilde{\alpha}/\partial\nu$ for the exponential refractivity profile given in Eq. (5.8-2a). It follows that in terms of geometric optics quantities the defocusing factor can be written as

$$^{(i)}\zeta^{-1} \doteq \left(1-\rho\cos\left(\theta+\tilde{\alpha}(\rho,\nu)\right)\frac{\partial\tilde{\alpha}(\rho,\nu)}{\partial\nu}\right)_{\nu=\rho_*} \tag{5.9-23}$$

When $\partial\tilde{\alpha}/\partial\nu>0$, then $^{(i)}\zeta<1$ because $\pi>\theta+\tilde{\alpha}(\rho,\rho_*)>\pi/2$.

When the refractivity profile results in a unique stationary phase path from the GPS satellite to the point (r,θ) [e.g., Case A], then Eq. (5.9-19) shows that the refracted wave, which was planar before entering the atmosphere, is still nearly planar (for a thin atmosphere) at the point (r,θ). However, its Poynting vector $\boldsymbol{S}$ is pointed away from the original axis of propagation by an angular displacement $\tilde{\alpha}$. Its phase is delayed by an additional amount $({}^{(i)}\Phi^* - \rho\cos\theta)$. Its amplitude is modified by the factor $({}^{(i)}\zeta\sin(\theta+\tilde{\alpha})/\sin\theta)^{1/2}$, which may be significantly greater or less than unity depending on the magnitude of $\partial^2 G/\partial\nu^2$ at the stationary phase point.

If we have a multipath situation where, for example, three different total bending-angle values satisfy the boundary conditions, then Eq. (5.9-19) will appear in triplet form (or even in higher odd multiples for more complicated refractivity profiles). The Gaussian refractivity profile given in Eq. (5.8-2b) will produce triplets for a certain range of altitudes. The total field in this case would be obtained by vector addition of the field components from each contribution. We note again the failure of the stationary phase technique when the stationary phase points are too near each other or, alternatively, when they are too near the first contact points with the caustic surfaces for the complete ray system generated by varying the position of the point (r,θ). In wave theory, the accuracy of the stationary phase technique for evaluating the integrals in Eq. (5.9-10) depends on the magnitude of $\partial^{2\,(i)}\Psi/\partial\nu^2$ being sufficiently large. Caustics occur when stationary phase points in spectral number space also coincide, or nearly so, with $\partial^{2\,(i)}\Psi/\partial\nu^2=0$. The conditions for the validity of the stationary phase approach and the third-order approach leading to the Airy function of the first kind are discussed in Appendix D. Multipath scenarios and caustics are discussed more fully in Section 5.12.

Finally, we note the breakdown in accuracy of this osculating parameter approach if one attempts to use it exactly at a turning point. As we approach a turning point, $D_{\nu^*}\to 0$. Because $\partial^2 G[\rho,\nu]/\partial^2\nu$ is finite at $\nu=\rho$, we see from Eq. (5.9-18) that the defocusing factor ζ predicted by this technique approaches unity at a turning point. But from geometric optics [Eq. (5.6-16)], we know that $\zeta^{-1}\to 1+u_* n_*'/n_*$, which results from the singularity in $\partial\tilde{\alpha}(\rho,\nu)/\partial\nu$ as the turning point is approached, i.e.,

$D_\nu \partial\tilde{\alpha} / \partial\nu \rightarrow -(dn / d\rho)(\rho / n)$ as $D_\nu \rightarrow 0$. Turning points using an Airy layer approach are discussed in Section 5.11.

5.9.7 An Outgoing Electric Field

For a point in the outgoing region well away from a turning point, only the phase combination ${}^{(o)}\Psi = \Psi(+,-)$ in Eq. (5.9-6) contributes significantly to the scattering integrals for the electric field representation given in Eq. (5.9-5). For an outgoing region, $0 < \theta \leq \pi / 2 - \tilde{\alpha}(\rho_*, \rho_*)$, and we have

$$\left.\begin{aligned} {}^{(o)}E_r(\rho,\theta) &= \frac{E_o}{\sqrt{2\pi\rho\sin\theta}} \int_0^\infty \left(\frac{\sin^3\theta_\nu}{\cos\theta_\nu} \right)^{1/2} \exp\left(i{}^{(o)}\Psi(\rho,\theta,\nu)\right) d\nu \\ {}^{(o)}E_\theta(\rho,\theta) &= \frac{E_o}{\sqrt{2\pi\rho\sin\theta}} \int_0^\infty \left(\sin\theta_\nu \cos\theta_\nu\right)^{1/2} \exp\left(i{}^{(o)}\Psi(\rho,\theta,\nu)\right) d\nu \end{aligned}\right\} \tag{5.9-24}$$

Referring to Eq. (5.9-6), we see that ${}^{(o)}\Psi = \Psi(+,-)$ is obtained from ${}^{(i)}\Psi = \Psi(-,-)$ through the transformation

$${}^{(o)}\Psi = -{}^{(i)}\Psi, \quad G[\rho,\nu] \Rightarrow 2G\left[\rho^\dagger(\nu),\nu\right] - G[\rho,\nu]$$

${}^{(o)}\Psi$ is the spectral density function for the phase delay at the point (ρ,θ) for an outgoing wave. We need only apply this transformation to the incoming forms in Eq. (5.9-18) to obtain the stationary phase evaluation of the spectral integrals for an outgoing wave. Carrying through the stationary phase computations in Eq. (5.9-24) yields the electric field for the outgoing wave. It may be written as

$$\left.\begin{aligned} {}^{(o)}E_r &\doteq E_o \sin\left({}^{(o)}\gamma^*\right) \sqrt{\frac{{}^{(o)}\zeta \sin\left({}^{(o)}\gamma^*\right)}{\sin\theta}} \exp\left(i{}^{(o)}\Phi^*\right) \\ {}^{(o)}E_\theta &\doteq E_o \cos\left({}^{(o)}\gamma^*\right) \sqrt{\frac{{}^{(o)}\zeta \sin\left({}^{(o)}\gamma^*\right)}{\sin\theta}} \exp\left(i{}^{(o)}\Phi^*\right) \\ {}^{(o)}\gamma^* &= \theta + \left(2\frac{dG^\dagger}{d\nu} - \frac{\partial G}{\partial\nu} \right)_{\nu=\nu^*} \end{aligned}\right\} \tag{5.9-25}$$

where the outgoing phase ${}^{(o)}\Phi^*$ is given by

$$\left.\begin{aligned}
{}^{(o)}\Phi^* &= \left(D_\nu + \nu\left(2\frac{dG^\dagger}{d\nu} - \frac{\partial G}{\partial \nu}\right) - (2G^\dagger - G)\right)_{\nu=\nu^*} \\
&\doteq D_{\rho_*} + \rho_*\big(2\tilde{\alpha}(\rho_*,\rho_*) - \tilde{\alpha}(\rho,\rho_*)\big) \\
&\quad + 2\int_{\rho_*}^{\infty} \tilde{\alpha}(\omega,\omega)d\omega - \int_{\rho_*}^{\rho} \tilde{\alpha}(\rho,\omega)d\omega - \int_{\rho}^{\infty} \tilde{\alpha}(\omega,\omega)d\omega, \\
G^\dagger &= G\big[\rho^\dagger(\nu),\nu\big],\; G = G[\rho,\nu],\; D_{\rho_*} = \sqrt{\rho^2 - \rho_*^2}
\end{aligned}\right\} \tag{5.9-26}$$

The leading term D_{ρ_*} is the optical path delay from the tangent point on the spherical surface of radius ρ_* to the point (ρ,θ). The second term is an arc-length term along a sphere of radius ρ_* due to cumulative refractive bending $2\tilde{\alpha}(\rho_*,\rho_*) - \tilde{\alpha}(\rho,\rho_*)$ to the outgoing point (ρ,θ). The first and second terms combined reference the phase to the line $\theta = \pi/2$ for an incident-collimated wave originating from the direction $\theta = \pi$. The third, fourth, and fifth terms in wave theory account for the extra phase delay due to the refractive gradient-induced bending through the atmosphere that a ray of impact parameter value ρ_* from the GPS satellite (assumed to be at infinity) undergoes in reaching the outgoing point (ρ,θ).

The defocusing factor ${}^{(o)}\zeta$ in Eq. (5.9-25) also has its analog in geometric optics to account for the dispersive effect of the refraction gradient on signal power (see Section 5.6). It is given by

$$\left.\begin{aligned}
{}^{(o)}\zeta &= \left(1 - D_\nu\left(2\frac{d^2G[\rho^\dagger(\nu),\nu]}{d\nu^2} - \frac{\partial^2 G[\rho,\nu]}{\partial \nu^2}\right)\right)^{-1}\Bigg|_{\nu=\nu^*} \\
&\doteq \left(1 - D_{\rho_*}\left(2\frac{d}{d\rho_*}\big(\tilde{\alpha}(\rho_*,\rho_*)\big) - \frac{\partial}{\partial \rho_*}\big(\tilde{\alpha}(\rho,\rho_*)\big)\right)\right)^{-1}
\end{aligned}\right\} \tag{5.9-27}$$

Forms for $2d^2G[\rho^\dagger,\rho^\dagger]/d\nu^2 - \partial^2 G[\rho,\nu]/\partial\nu^2$ are given in Appendix J and Eq. (5.9-22).

As has already been shown for the incoming case, Eq. (5.9-25) shows the (small) deflections in angular displacement $2\tilde{\alpha}_* - \tilde{\alpha}$. Its phase is delayed by an additional amount, ${}^{(o)}\Phi^* - \rho\cos\theta$. Its amplitude is modified by the factor $(\zeta \sin(\theta + 2\tilde{\alpha}_* - \tilde{\alpha})/\sin\theta)^{1/2}$, and so on.

We have already commented in the incoming case about multipath and the possible non-uniqueness of these solutions, depending on the profile of the refractivity.

5.9.8 The Electric Field at the LEO

We assume that the LEO is well out of the refracting medium and receiving a signal from an outgoing wave. The equations given for the outgoing case also describe the field at the LEO except that they are somewhat simplified because $\tilde{\alpha}(\rho,\rho_*)\to 0$ as $\rho\to\infty$. They become

$$\left.\begin{aligned}
&E_r(\rho_{\mathrm{L}},\theta_{\mathrm{L}})\doteq E_o\sin\gamma^*\sqrt{\frac{\zeta\sin\gamma^*}{\sin\theta_{\mathrm{L}}}}\exp(i\Phi^*)\\
&E_\theta(\rho_{\mathrm{L}},\theta_{\mathrm{L}})\doteq E_o\cos\gamma^*\sqrt{\frac{\zeta\sin\gamma^*}{\sin\theta_{\mathrm{L}}}}\exp(i\Phi^*)\\
&\Phi^*=D_{\nu^*}+2\left(\nu\frac{dG^\dagger}{d\nu}-G^\dagger\right)_{\nu^*}\doteq D_{\rho_*}+2\rho_*\tilde{\alpha}_*+2\int_{\rho_*}^{\infty}\tilde{\alpha}(\nu,\nu)d\nu
\end{aligned}\right\}\qquad(5.9\text{-}28)$$

where

$$\left.\begin{aligned}
&D_{\nu^*}=\rho_L\cos\gamma^*\doteq D_{\rho_*}=\rho_L\cos(\theta+2\tilde{\alpha}_*),\\
&\zeta=\zeta(\nu^*,\rho_L)=\left(1-2D_{\nu^*}\frac{d^2G^\dagger}{d\nu^{*2}}\right)^{-1}\doteq\left(1-2D_{\rho_*}\frac{d\tilde{\alpha}_*}{d\rho_*}\right)^{-1},\\
&\gamma^*=\theta+\left(2\frac{dG^\dagger}{d\nu^*}\right)\doteq\theta+2\tilde{\alpha}_*,\ 0>\gamma^*<\frac{\pi}{2},\ \nu^*=\rho\sin^{(o)}\gamma^*,\\
&G^\dagger=G\left[\rho^\dagger(\nu^*),\nu^*\right],\ \tilde{\alpha}_*=\tilde{\alpha}(\rho_*,\rho_*),\ \rho_*=\rho_L\sin(\theta+2\tilde{\alpha}_*)
\end{aligned}\right\}\qquad(5.9\text{-}29)$$

Here it is understood that both $\tilde{\alpha}_*$ and the impact parameter ρ_* are implicit functions of the LEO position coordinates $(r_{\mathrm{L}},\theta_{\mathrm{L}})$ through the application of Bouguer's law and the total refractive bending angle given in Eq. (5.6-5).

5.10 Comparison of Geometric Optics and Wave Theory

Here we briefly review the scalar diffraction results applied to a thin phase screen model. These results then are compared with those from wave theory. Thin-screen models were discussed in Chapter 2, notably in Section 2.3. A thin phase screen model provides a proxy for the actual atmospheric medium through which the electromagnetic wave travels. A thin phase screen model mimics the transmission effects of the real atmosphere on a traversing electromagnetic wave. The closeness of this match is limited, of course, by limitations in the thin-screen model itself. However, it is surprising how accurate a description of certain electromagnetic processes can be achieved from the model in most situations when thin-atmosphere conditions apply. Thin-atmosphere conditions are defined in Chapter 2, Eqs. (2.2-8) and (2.2-9). Basically, thin-atmosphere conditions imply that the curvature of the ray path is much smaller than the curvature of the ambient equipotential surface, and that the length along the ray where refracting or bending occurs is small compared to the radius of curvature of the equipotential surface. Both of these conditions are related to the refractive gradient in the atmosphere. A somewhat strengthened thin-screen requirement for a perpendicularly mounted thin screen is that no caustics may occur in that screen. The condition for this is given in Eq. (2.3-13). Thin phase screen models offer considerable simplification in calculations of electromagnetic processes, including refractive bending and path delay, but also of other important properties, such as diffraction, multipath, caustics, and shadow zones. Chapter 2 discusses two alternate thin-screen models, a planar screen oriented perpendicularly to the LEO/GPS line near the point of tangency of the actual ray in the Earth's atmosphere and an impact parameter "screen," actually the post-encounter impact parameter space curve generated by varying the impact parameter $\rho_* = ka$.

In Chapter 3, we discussed rainbow caustic effects that would be difficult, but not impossible, for a thin-screen model to predict. Processes at turning points also would be difficult for a thin-screen model, as well as super-refractivity situations. Also, the thin planar screen model will encounter difficulty when caustics occur in the screen, i.e., when $1 + a\alpha d\alpha / da = 0$. For an exponentially distributed refractivity, this is equivalent to requiring $\beta < (2\pi)^{-1/2} \approx 0.4$, where β is the ray path curvature parameter given in Eq. (2.2-9) as part of the thin-atmosphere definition. This threshold $\beta = (2\pi)^{-1/2}$ is exceeded across some marine layer boundaries in the lower troposphere, but rarely is exceeded at higher altitudes.

5.10.1 Comparison of Wave Theory with Geometric Optics

We now compare stationary phase terms in spectral number from wave theory with phase terms from geometric optics. In ray theory, the phase at the point $(r_{\mathrm{L}}, \theta_{\mathrm{L}})$ relative to the phase at the line $\theta = \pi / 2$ for a collimated incident wave traveling along the direction $\theta = 0$ is given by [see Eqs. (A-55) through (A-57)]

$$\varphi = \rho_{\mathrm{L}} \cos\left(\theta_{\mathrm{L}} + \alpha_{\mathrm{L}}\right) + \rho_* \alpha_{\mathrm{L}} + \int_{\rho_*}^{\infty} \alpha_{\mathrm{L}}(\omega) d\omega \tag{5.10-1}$$

In wave theory, a stationary value of the spectral density function for the phase delay at the LEO, Φ_{L}^*, referenced to the line $\theta = \pi / 2$, is given from Eq. (5.9-28) by

$$\left.\begin{aligned}&\Phi_{\mathrm{L}}^{*}=\left(\sqrt{\rho_{\mathrm{L}}^{2}-\nu^{2}}+2\nu\frac{dG^{\dagger}}{d\nu}-2G^{\dagger}\right)\bigg|_{\nu=\nu^{*}}\\&\left(\theta_{\nu}-\theta_{\mathrm{L}}-2\frac{dG^{\dagger}}{d\nu}\right)\bigg|_{\nu=\nu^{*}}=0,\\&\theta_{\nu}=\sin^{-1}\left(\frac{\nu}{\rho_{\mathrm{L}}}\right),\quad G^{\dagger}(\nu)=G\left[\rho^{\dagger}(\nu),\nu\right]\end{aligned}\right\}\tag{5.10-2}$$

The second line is the stationary phase condition that the spectral number must satisfy. We have seen in Section 5.7, Eqs. (5.7-4) and (5.7-14) (see also Appendix J), that

$$\left.\begin{aligned}&2\frac{dG^{\dagger}(\nu)}{d\nu}=\alpha_{\mathrm{L}}(\nu)+\mathrm{O}\left[\rho\frac{d^{2}n}{d\rho^{2}}\bigg|_{\rho=\nu}\right]\\&2G^{\dagger}(\nu)\doteq-\int_{\nu}^{\infty}\alpha_{\mathrm{L}}(\omega)d\omega\end{aligned}\right\}\tag{5.10-3}$$

This means that the term $\rho(d^2n/d\rho^2)$ must be much smaller than α_{L} to maintain close agreement between spectral number in wave theory and impact parameter in ray theory. This translates into a scale height in distance (i.e., not a scale height in impact parameter) for an exponential refractivity profile that must be greater than about 1 km. This scale height limit already is super-refractive in the lower troposphere, i.e., $\beta > 1$; rays won't exist for a certain critical altitude range of tangency points lying in and below the super-refractive layer. (See Section 6.4.) If this stationary phase condition in Eq. (5.10-2) can be satisfied, and if the curvature condition is met, i.e., $\rho_* \mid d^2n/d\rho^2 \mid_* << \alpha_{\mathrm{L}}(\rho_*)$, then $\nu^* \doteq \rho_{\mathrm{L}}\sin(\theta_{\mathrm{L}}+\alpha_{\mathrm{L}}(\nu^*))$, and it follows that the stationary value for the spectral density function is given by

$$\Phi_{\mathrm{L}}^{*}\doteq\rho_{\mathrm{L}}\cos\left(\theta_{\mathrm{L}}+\alpha_{\mathrm{L}}(\nu^{*})\right)+\nu^{*}\alpha_{\mathrm{L}}(\nu^{*})+\int_{\nu^{*}}^{\infty}\alpha_{\mathrm{L}}(\omega)d\omega\tag{5.10-4}$$

The spectral number ν^* will be close to ρ_* if the inequality $\rho_* \mid d^2n/d\rho^2 \mid_* << \alpha_{\mathrm{L}}(\rho_*)$ holds; then the stationary value of phase delay spectral density function in Eq. (5.10-4) is essentially identical to the phase delay or eikonal function from geometric optics in Eq. (5.10-1). Therefore, when a stationary phase value for the spectral number exists, then the two systems give stationary values for the phase delay that are essentially the same when the impact parameter in ray theory is set equal to that spectral number in wave theory.

Concerning the correspondence with the thin-screen models, we have seen in Chapter 2, Eq. (2.3-12), that the phase delay evaluated at the point $(\rho_*, \theta_{\rho_*})$ on the impact parameter space curve (with $\theta_{\rho_*} = \pi/2 - \alpha_{\mathrm{L}}(\rho_*)$) is given by

$$\varphi_{\rho_*} = \rho_* \alpha_{\mathrm{L}} + \int_{\rho_*}^{\infty} \alpha_{\mathrm{L}}(\omega) d\omega \tag{5.10-5}$$

The difference between this impact parameter phase delay and the stationary value of the spectral density function Φ_{L}^{*} is simply due to the geometric delay (see Fig. 5-18) between the LEO and the point $(r_{\rho_*}, \theta_{\rho_*})$ on the impact parameter space curve, that is, $\rho_{\mathrm{L}} \cos(\theta_{\mathrm{L}} + \alpha_{\mathrm{L}})$.

Regarding the planar thin-screen model mounted perpendicularly to the LEO/GPS line, the Fresnel phase function in Chapter 2, Eq. (2.5-1) is given by

$$\Phi(h, h_{\mathrm{LG}}) = \frac{\pi}{\lambda D}(h - h_{\mathrm{LG}})^2 + \int_{h}^{\infty} \alpha_{\mathrm{L}}(\omega) \, d\omega \tag{5.10-6}$$

where h and D are in phase units. Referring to Eq. (5.10-4), the first term, $\rho_{\mathrm{L}} \cos(\theta + \alpha_{\mathrm{L}})$, is the optical distance from the LEO to the tangent point on a sphere of radius ρ_*, which is the impact parameter of the ray passing through the point $(\rho_{\mathrm{L}}, \theta_{\mathrm{L}})$. The second term is the optical distance $\rho_* \alpha_{\mathrm{L}}$ along the circumference of a sphere of radius ρ_* from $\theta = \pi/2 - \alpha_{\mathrm{L}}$ to $\theta = \pi/2$. The sum of these two terms is given by

$$\rho_{\mathrm{L}} \cos(\theta_{\mathrm{L}} + \alpha_{\mathrm{L}}) + \rho_* \alpha_{\mathrm{L}} = \rho_{\mathrm{L}} \cos\theta_{\mathrm{L}} \sec\alpha_{\mathrm{L}} - \alpha_{\mathrm{L}}^3 \rho_{\mathrm{L}} \sin\frac{\theta_{\mathrm{L}}}{3} + \rho_{\mathrm{L}} \, \mathrm{O}\left[\alpha_{\mathrm{L}}^4\right] \tag{5.10-7}$$

Thus, through second order in α_{L}, the first two terms in the stationary phase value for the spectral density function in Eq. (5.10-4) sum to the phase accumulation along the ray asymptote from the LEO to the line $\theta = \pi/2$.

The planar thin-screen distance D was rather loosely defined as the perpendicular distance from the LEO to the thin screen; see Fig. 5-18. In this figure, $h = \rho_{\mathrm{L}} \sin(\theta_{\mathrm{L}} + \alpha_{\mathrm{L}}) \sec\alpha_{\mathrm{L}} - \rho_o$ and $h_{\mathrm{LG}} = \rho_{\mathrm{L}} \sin\theta_{\mathrm{L}} - \rho_o$, where ρ_o provides the reference altitude. The impact parameter space curve is defined by the point $(\rho_*, \theta_{\rho_*})$ as ρ_* varies. Here $\theta_{\rho_*} = \pi/2 - \alpha_{\mathrm{L}}(\rho_*)$. If in Eq. (5.10-6) we now set $D = D_S = \rho_{\mathrm{L}} \cos\theta_{\mathrm{L}}$, it follows upon comparison with Eq. (5.10-4) that through second order in α_{L} we have matched the geometric components of the phase delay in the two systems. This is about as close an agreement as we should expect because the version of the scalar diffraction integral that we have

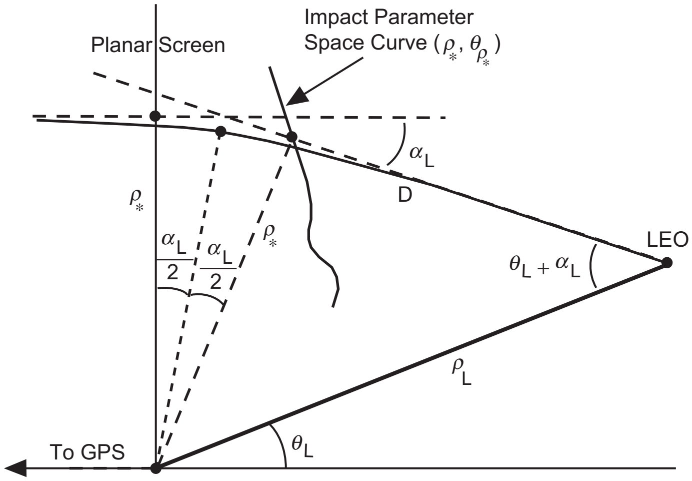
Impact Parameter
Space Curve (ρ_*, θ_{ρ_*})
Planar Screen
α_L
D
ρ_*
$\frac{\alpha_\mathrm{L}}{2}$
$\frac{\alpha_\mathrm{L}}{2}$
ρ_*
LEO
$\theta_\mathrm{L} + \alpha_\mathrm{L}$
ρ_L
θ_L
To GPS

Fig. 5-18. Geometric relationships between ray path and phase screens for collimated incident rays.

used in Chapter 2 (the Rayleigh–Sommerfeld is typical) is accurate only through second order in α_L.

Next to be reconciled are the phase delays in the two systems induced by the refractivity gradient, which are the integral terms in Eqs. (5.10-4) and (5.10-6). We also have not been too specific about the orientation of the thin screen. For convenience here, we place it along the line $\theta = \pi / 2$. Comparing these terms requires

$$\int_{h_S^*}^{\infty} \alpha_\mathrm{L}(h_S')\,dh_S' = \int_{\rho_*}^{\infty} \alpha_\mathrm{L}(\rho_*')\,d\rho_*' \tag{5.10-8}$$

This must hold for all values of h_LG, the altitude of the LEO/GPS line in the planar thin-screen model above the reference plane, or, equivalently, for all locations $(r_\mathrm{L}, \theta_\mathrm{L})$ of the LEO during the occultation. This condition may or may not be feasible, depending on whether or not h is a single-valued function of ρ_*. Differentiating with respect to ρ_* yields

$$\alpha_\mathrm{L}(h)\frac{dh}{d\rho_*} = \alpha_\mathrm{L}(\rho_*) \tag{5.10-9}$$

If no caustics occur in the screen, then at every altitude we can equate the bending angle in the thin screen at a thin-screen altitude h to the atmospheric bending angle $\alpha_\mathrm{L}(\rho_*)$. If we place the thin screen along the line $\theta = \pi / 2$, then it follows that

$$h = \rho_* \sec\alpha_{\mathrm{L}} - \rho_{\mathrm{L}} \sin\theta_o = \rho_* \sec\alpha_{\mathrm{L}} - \rho_o \tag{5.10-10}$$

In a medium with large refractive gradients, thin-screen caustics where $dh / d\rho_* = 0$ can arise. The perpendicularly mounted thin screen is not suitable for these situations.

5.10.2 Duality between Systems

It follows from the previous discussions that when stationary values of the spectral density function exist with respect to spectral number, and when super-refractivity situations are avoided, then we have a kind of duality between the stationary phase processes over spectral number in wave theory and over impact parameter in geometric optics. For thin-atmosphere conditions away from turning points, rainbow caustics, etc., we may establish a correspondence between wave theory and geometric optics when stationary phase values in each system are assumed. For wave theory applied to a spherical refracting medium on one hand, and for the scalar diffraction integral applied to a thin-screen proxy for this refracting medium on the other hand, Table 5-1 shows the correspondence between these systems when stationary phase values are assigned in each system. Table 5-1 shows this correspondence at a LEO position. Here $G^\dagger = G^\dagger(\nu) \equiv G[\rho^\dagger(\nu), \nu]$, and $\rho^\dagger(\nu) = \nu - \hat{y}^\dagger K_{\rho^\dagger}$.

In summary, a thin phase screen model combined with scalar diffraction theory gives results that closely match those from wave theory applied to a spherical geometry when (1) caustics do not occur in the thin screen, $dh / d\rho_* \neq 0$, which is related to the thin-atmosphere conditions cited earlier, (2) the observer is relatively far from the refraction zone, and (3) certain LEO rainbow caustic and reflection locations are avoided.

On the other hand, there are situations where wave theory and wave/optics approaches give disparate results. One example is when no stationary spectral numbers occur; this corresponds to super-refractivity in geometric optics or to transition across a shadow boundary. Another example is a caustic contact point where second-order geometric optics predicts infinity for the amplitude of the ray and it errs in predicting the exact location of maximum flaring. Wave theory accurately addresses these cases. Although addressed later, one also can make a close correspondence between wave theory and geometric optics results when reflections occur.

Table 5-1. Duality between systems at the LEO.

	Electrodynamics in a Spherical Medium	⇔	Geometric Optics/Scalar Diffraction
Variational Parameter:	Spectral Number, ν		Impact Parameter, $kn_* r_* = \rho_*$
Atmospheric Phase Delay	$-\left(2G^\dagger\right)_{\nu=\nu^*} = -2G[\rho^\dagger(\nu^*),\nu^*]$	⇔	$\varphi(\rho_*)$, Thin Screen Phase
Stationary Phase Condition	$\left(\sin^{-1}\left(\dfrac{\nu}{\rho}\right) - \theta - 2\dfrac{dG^\dagger}{d\nu}\right)_{\nu=\nu^*}$	$=0=$	$\left(\alpha_L(\rho_*) + \dfrac{d\varphi}{d\rho_*}\right)$
Stationary Point	$\nu^* = \rho_L \sin\left(\theta_L + 2\dfrac{dG^\dagger}{d\nu}\right)_{\nu=\nu^*}$	⇔	$\rho_* = \rho_L \sin\gamma_L$
Gradient	$2\left(\dfrac{dG^\dagger}{d\nu}\right)_{\nu=\nu^*}$	⇔	$\alpha_L = 2\tilde{\alpha}(\rho_*,\rho_*)$, Bending Angle
Stationary Phase at LEO	$\left(D_\nu + 2\nu\dfrac{dG^\dagger}{d\nu} - 2G^\dagger\right)_{\nu=\nu^*}$	⇔	$\rho_L\cos\gamma_L + \rho_*\alpha_L + \int_{\rho_*}^{\infty}\alpha_L(\nu)d\nu$
Defocusing ζ	$\left(1 - 2D_\nu\dfrac{d^2G^\dagger}{d\nu^2}\right)^{-1}_{\nu=\nu^*}$	⇔	$\left(1 - \rho_L\cos\gamma_L\dfrac{d\alpha_L}{d\rho_*}\right)^{-1}$
Caustic $\zeta\to\infty$	$\left(1 - 2D_\nu\dfrac{d^2G^\dagger}{d\nu^2}\right) = 0$	⇔	$\left(1 - \rho_L\cos\gamma_L\dfrac{d\alpha_L}{d\rho_*}\right) = 0$

5.10.3 Amendments to Account for Wave-Front Curvature from the Finite Distance of the Emitting GPS Satellite

Almost all of the discussion in this monograph has assumed an infinite distance for the emitting GPS satellite. The wave-front curvature effects from an emitting GPS satellite at a finite distance can be accommodated as follows. From geometric optics, see Appendix A, Eq. (A-55), the phase delay along a ray, now referenced to the emitting GPS satellite, is given by

$$\varphi = \sqrt{\rho_{\mathrm{L}}^2 - \rho_*^2} + \sqrt{\rho_{\mathrm{G}}^2 - \rho_*^2} + \rho_* \alpha_{\mathrm{L}}(\rho_*) + \int_{\rho_*}^{\infty} \alpha_{\mathrm{L}}(\omega) d\omega \qquad (5.10\text{-}11)$$

Here it is assumed the emitter and the receiver are well out of any refracting medium. Otherwise, we would have to break the terms involving α_{L} into separate parts, one for δ_{L}, the ray path deflection angle at the LEO, and one for δ_{G}, the ray path deflection angle at the GPS, with $\alpha_{\mathrm{L}} = \delta_{\mathrm{L}} + \delta_{\mathrm{G}}$; see Fig. A-3.

This form for the phase delay in Eq. (5.10-11) is the eikonal function $\mathscr{S}(\boldsymbol{r})$ in geometric optics. The eikonal equation is $|\nabla \mathscr{S}| = n$, and a constant value for $\mathscr{S}$ defines the geometric optics equivalent of a surface of constant phase delay of the electromagnetic wave (essentially a wave-front or cophasal surface).

The main change in wave theory for a finite GPS distance is in the asymptotic form that the incoming spectral coefficients assume for large radial distances out of the atmosphere. This difference between collimated and spherical incident waves was briefly discussed in Section 5.5, Eqs. (5.5-3a) and (5.5-3b). When one accounts for wave-front curvature, the spectral density function $\Psi(+,-)$ for an outgoing wave at the LEO [see Eq. (5.9-6)] is amended to the form (always with $\theta_{\mathrm{G}} \equiv \pi$)

$$\left.\begin{aligned} \Psi &= \sqrt{\rho_{\mathrm{G}}^2 - \nu^2} + \sqrt{\rho_{\mathrm{L}}^2 - \nu^2} + \nu\left(\theta_\nu^{\mathrm{G}} + \theta_\nu^{\mathrm{L}} - \theta_{\mathrm{L}}\right) - 2G^\dagger(\nu) - \frac{\pi}{4} \\ \theta_\nu^{\mathrm{G}} &= \sin^{-1}\left(\frac{\nu}{\rho_{\mathrm{G}}}\right) \\ \theta_\nu^{\mathrm{L}} &= \sin^{-1}\left(\frac{\nu}{\rho_{\mathrm{L}}}\right) \end{aligned}\right\} \qquad (5.10\text{-}12)$$

Then the stationary value of $\Psi(+,-)$, if one exists, is obtained by setting $\partial\Psi(+,-)/\partial\nu = 0$. This yields

$$\frac{\partial\Psi}{\partial\nu} = \left(\theta_\nu^{\mathrm{G}} + \theta_\nu^{\mathrm{L}} - \theta_{\mathrm{L}}\right) - 2\frac{dG^\dagger}{d\nu} = 0 \qquad (5.10\text{-}13)$$

Letting $\Phi_{\mathrm{L}}^{*}=\Psi(+,-)|_{\nu=\nu^{*}}+\pi/4$ and using Eq. (5.10-3), we obtain

$$\begin{aligned}\Phi_{\mathrm{L}}^{*}&=\sqrt{\rho_{\mathrm{G}}^{2}-\nu^{*2}}+\sqrt{\rho_{\mathrm{L}}^{2}-\nu^{*2}}+2\left(\nu\frac{dG^{\dagger}}{d\nu}\right)_{\nu^{*}}-2G^{\dagger}(\nu^{*})\\&\to\sqrt{\rho_{\mathrm{G}}^{2}-\rho_{*}^{2}}+\sqrt{\rho_{\mathrm{L}}^{2}-\rho_{*}^{2}}+\rho_{*}\alpha_{\mathrm{L}}(\rho_{*})+\int_{\rho_{*}}^{\infty}\alpha_{\mathrm{L}}(\omega)d\omega\end{aligned}\tag{5.10-14}$$

The lower line is obtained by letting $\nu^{*}\to\rho_{*}$, and it is in agreement with the eikonal form in Eq. (5.10-11) given from geometric optics.

5.11 The Electric Field at a Turning Point

At a turning point, $r=r_{*}$ and $\theta=\theta_{*}$. We have discussed in Section 5.8 the breakdown in accuracy of the representation of the field by osculating parameters when the field is evaluated in the immediate neighborhood of a turning point. When certain scale factors permit, we can accurately approximate the medium by a spherical Airy layer in the neighborhood of a turning point. We have seen in Sections 4.7 and 4.8 for a Cartesian stratified medium that the osculating parameter approach works well at a turning point when the Airy functions are used as basis functions. For the boundary $r=r_{A}$ between the Airy layer below and the medium above, Section 5.8 uses the continuity conditions from electrodynamics to match the osculating parameter solution for $r\geq r_{A}$ to the Airy solution for $r\leq r_{A}$.

The Airy layer approximation works well when the effect of curvature in the refractivity profile is sufficiently small over the width of the layer. Two key scale factors can permit this approximation. The first is related to n''/n'. For an exponential medium, this factor becomes H^{-1}, where H is the scale height (here in length units). In this case, we want the width of the Airy layer Δr to be small enough that, in the power series expansion of the exponential representation of the medium, the quadratic and higher-order terms in $\Delta r/H$ are negligible, i.e., $\Delta r/H<<1$. On the other hand, we don't want the boundary $r=r_{A}$ of the Airy layer to be chosen so close to the turning point radius that the accuracy of the osculating parameter approach has begun to deteriorate, which occurs when $\hat{y}>\sim -2$. Using Eq. (5.4-3) to express $\Delta\hat{y}$ in terms of Δr over the width of the Airy layer, we have

$$\Delta\hat{y}=-\frac{kH}{K_{\rho_{A}}}\frac{\Delta r}{H}\tag{5.11-1}$$

Thus, the two dimensionless factors permitting an Airy layer approximation are kH and $K_{\rho_{A}}=\left(kn_{A}r_{A}/2\right)^{1/3}$; the latter is related to r_{A}/λ. When H

corresponds to the Earth's dry air conditions ($H \approx 7\,\text{km}$) and for GPS wavelengths, $kH / K_{\rho_A} \approx 500$. In this case, we could set $\Delta r / H \sim 0.01$, achieving better than 0.01 percent accuracy in the representation of the refractivity by an Airy layer, with a boundary above which the osculating parameter approach also is sufficiently accurate. We also want to keep $\Delta\hat{y}$ small enough that phase runoff in the Airy function approximate solution, given in Eq. (5.8-6), as compared to the exact solution is negligible. This also is related to the size of n'' / n'.

In matching the solution in the Airy layer involving the Airy function of the first kind with the osculating parameters/spherical Hankel functions that hold above the layer, we apply the continuity conditions from electrodynamics. This results in the matching coefficients c_l and d_l given in Eq. (5.8-8). We may multiply these coefficients by any complex factor that we wish [for example, $i^l(2l+1)/l(l+1)$], provided that we apply that factor to both coefficients or, equivalently, to both the incoming and outgoing components of the field. Also, at the boundary the outgoing phase term $2G\left[\rho^{\dagger}, \nu\right] - G\left[\rho_A, \nu\right]$, which is given in Eq. (5.8-24), must equal the exact value of the round-trip phase delay through the Airy layer. This fixes $\rho^{\dagger}$ at the Airy layer boundary per Eq. (5.8-15). For a given value for l, the asymptotically exact value for the round-trip phase delay through an Airy layer is given by Eqs. (5.8-12) and (5.8-13). Fortunately, we need not explicitly apply this condition; we need only the representation by the Airy function of the first kind at the turning point. But in practice the numerical integration of these wave equations has a stability problem below the turning point. The slightest phase error in the initial conditions at the boundary $r = r_A$ results in a blowup below the turning point or, equivalently, to a leakage of the Airy function of the second kind into the numerical solution. See the discussion of the WKB solutions and Eq. (5.7-26).

Near a turning point, we start with the integral version of the spectral representation for the field given in Eq. (5.8-1b). Because we are evaluating the field near a turning point, we do not have unrestricted use of the negative argument asymptotic form for the Airy function. But we still can use the negative exponential form for the Legendre function, which generally is applicable for large spectral numbers and for $0 < \theta < \pi$.

We replace the form $a_l^- \xi_l^- + a_l^+ \xi_l^+$ in Eq. (5.8-1) with $\text{Ai}[\tilde{y}]$ times a spectral number-dependent coefficient. When the negative argument asymptotic forms hold at the boundary of the Airy layer, we have from Eq. (5.8-8) the connecting relationship between the solution below the boundary and the solutions above the boundary. This is given by

$$\left.\begin{aligned} 2\left(\mathrm{Ai}[\tilde{y}]\right)_A &= \frac{(1+\varepsilon)^{1/6}}{\sqrt{\pi K_A}}\left(\xi_l^{+} e^{+i\left(\tilde{\mathrm{X}}_l-\hat{\mathrm{X}}_l\right)}+\xi_l^{-} e^{-i\left(\tilde{\mathrm{X}}_l-\hat{\mathrm{X}}_l\right)}\right)_A \\ \tilde{X}_l &= \frac{2}{3}\left(-\tilde{y}_A\right)^{3/2}+\frac{\pi}{4} \\ \hat{X}_l &= \frac{2}{3}\left(-\hat{y}_A\right)^{3/2}+\frac{\pi}{4} \end{aligned}\right\} \tag{5.11-2}$$

Here $\tilde{y}$ is given by Eq. (5.8-6), and $\tilde{y}=\hat{y}|1-\beta|^{-2/3}$. We also have seen in Section 5.8 that

$$\left(\tilde{X}_l-\hat{X}_l\right)_A = G[\rho_A,\nu]-G\left[\rho^{\dagger},\nu\right] \tag{5.11-3}$$

where $\rho^{\dagger}$ in this case is adjusted to force this equality to hold, which is a value very close to ν. In general, it follows from Eq. (5.8-8) that we may set

$$\left(a_l^{-}\xi_l^{-}+a_l^{+}\xi_l^{+}\right)_A = C_l\,\frac{2\sqrt{\pi K_{\rho_A}}}{|1-\beta|^{1/6}}\,\mathrm{Ai}\left[\tilde{y}_A\right] \tag{5.11-4}$$

where C_l is chosen to account for the asymptotic boundary conditions on the wave. For an initially collimated wave, we use the asymptotic boundary conditions as $r \to \infty$ for a planar incoming wave. For this case, $a_l^{-}\left(\rho_A\right)$ is given by Eq. (5.5-21), and $a_l^{+}\left(\rho_A\right)$ is given by Eq. (5.8-24). It then follows from Eqs. (5.11-2) and (5.11-3) that C_l is given by

$$\left.\begin{aligned} C_l &= i^{l-1}\,\frac{2l+1}{l(l+1)}\exp\left(-iG^{\dagger}(\nu)\right) \\ G^{\dagger}(\nu) &= G\left[\rho^{\dagger}(\nu),\nu\right] \end{aligned}\right\} \tag{5.11-5}$$

We now have the replacement form at the boundary of the Airy layer for an originally collimated incoming wave. It is given by

$$\left(a_l^{-}\xi_l^{-}+a_l^{+}\xi_l^{+}\right)_A = \frac{2\sqrt{\pi K_{\rho_A}}}{|1-\beta|^{1/6}}\,i^{l-1}\,\frac{2l+1}{l(l+1)}\exp\left(-iG^{\dagger}(\nu)\right)\left(\mathrm{Ai}[\tilde{y}]\right)_A \tag{5.11-6}$$

We can use this form on the RHS to evaluate the field at any point within the Airy layer. For a given spectral number and radial position, $\tilde{y}$ is obtained from Eq. (5.8-6). Upon using the spectral form in Eq. (5.8-1b), we obtain

$$\left.\begin{aligned}
&E_r(\tilde{\rho},\theta)=\frac{|1-\beta|^{-1/6}}{K_{\rho_*}}\frac{E_o}{\sqrt{\sin\theta}}\int_0^\infty\left(\frac{\nu}{\rho}\right)^{3/2}\mathrm{Ai}[\tilde{y}]e^{i\left(\nu\left(\frac{\pi}{2}-\theta-G^\dagger(\nu)\right)\right)}d\nu,\\
&E_\theta(\tilde{\rho},\theta)=\frac{|1-\beta|^{-1/6}}{K_{\rho_*}^2}\frac{iE_o}{\sqrt{\sin\theta}}\int_0^\infty\left(\frac{\nu}{\rho}\right)^{1/2}\mathrm{Ai}'[\tilde{y}]e^{i\left(\nu\left(\frac{\pi}{2}-\theta-G^\dagger(\nu)\right)\right)}d\nu,\\
&\tilde{y}=-\frac{1}{K_{\rho_*}|1-\beta|^{2/3}}\left((1-\beta)(\tilde{\rho}-\rho_*)-(l-\rho_*)\right),\\
&\tilde{\rho}=kn_*r,\ \ \beta=-\left(\frac{1}{n}\frac{dn}{d\tilde{\rho}}\tilde{\rho}\right)_{\rho_*},\ \ K_{\rho_*}=\left(\frac{\rho_*}{2}\right)^{1/3},\ \ \tilde{\rho}\le\tilde{\rho}_A
\end{aligned}\right\}\quad(5.11\text{-}7)$$

The constant gradient of the refractivity in the Airy layer, $n'=dn/d\tilde{\rho}$, is set by the actual values of $n(\rho)$ at the turning point r_* and at the boundary at $r=r_A$. Thus, the gradient of the refractivity will be discontinuous at the boundary, but refractivity itself will be continuous.

5.11.1 Fourier Transform of the Airy Function

We have seen in previous sections on stationary phase processes that, near a turning point and at the stationary phase value in spectral number, $dG\left[\rho^\dagger(\rho_*),\rho_*\right]/d\rho_*\doteq\tilde{\alpha}(\rho_*,\rho_*)$ with very high accuracy for thin-atmosphere conditions. But for now let us consider the integrals in Eq. (5.11-7) as Fourier transforms. When throughout the medium $n(\rho)=\text{constant}$, then $G[\rho,\nu]\equiv 0$ or at most a constant; it can be removed from the integrands in Eq. (5.11-7). From [8], we have the integral representation for the Airy function:

$$\mathrm{Ai}[\hat{y}]=\frac{(3a)^{1/3}}{2\pi}\int_{-\infty}^{\infty}\exp\left(i\left(at^3+(3a)^{1/3}\hat{y}t\right)\right)dt \tag{5.11-8}$$

where a is any positive constant. It is easy to show that this integral form satisfies the differential equation for the Airy function $\mathrm{Ai}''=\hat{y}\,\mathrm{Ai}$. Using the Dirac delta function,

$$\delta(\omega)=\frac{1}{2\pi}\int_{-\infty}^{\infty}\exp(i\omega t)dt \tag{5.11-9}$$

it follows from Eqs. (5.11-8) and (5.11-9) that the Fourier transform of $\mathrm{Ai}[\hat{y}]$ is given by

$$\int_{-\infty}^{\infty}\mathrm{Ai}[\hat{y}]\exp(i\omega\hat{y})d\hat{y}=\exp\left(\frac{-i\omega^3}{3}\right) \tag{5.11-10}$$

If we set $\omega = K_\rho(\pi/2-\theta)$ and we use the approximation $\nu \doteq \rho + K_\rho \hat{y} + \hat{y}^2/60K_\rho$ [see Eq. (5.4-3)], then we obtain

$$\int_{-\infty}^{\infty} \mathrm{Ai}[\hat{y}] e^{i\nu(\pi/2-\theta)} d\hat{y} = e^{i\rho\left(\pi/2-\theta-(\pi/2-\theta)^3/3!+(\pi/2-\theta)^5/5!\right)} \doteq e^{i\rho\cos\theta} \tag{5.11-11}$$

Thus, the Fourier transform of the Airy function of the first kind, at least near a turning point, is the phasor associated with the optical path length along the ray measured from the turning point, hardly a surprising result.

We can carry the Fourier transform approach a bit further and apply it to the radial component of the electric field in Eq. (5.11-1) for the case of the homogeneous medium where $G[\rho,\nu] \equiv 0$. Again using the Dirac delta function and its derivatives, it can be shown upon expanding the term $(l/\rho)^{3/2}$ in powers of $\hat{y}$ that

$$\frac{1}{\sqrt{\sin\theta}} \int_{-\infty}^{\infty} \left(\frac{l}{\rho}\right)^{3/2} \mathrm{Ai}(\hat{y}) e^{i\nu(\pi/2-\theta)} d\hat{y} \doteq \sin\theta e^{i\rho\cos\theta} \tag{5.11-12}$$

which we already know from physical considerations to be true.

Returning to the stratified case in Eq. (5.11-7), we now evaluate the radial component of the field at the turning point $E_r(\rho_*,\theta_*)$, where $\theta_* = \pi/2 - \tilde{\alpha}(\rho_*,\rho_*)$. We expand $G[\rho^\dagger,\nu]$ in powers of spectral number about the given value ρ_* where $(dG[\rho^\dagger(\nu),\nu]/d\nu)_{\rho_*} \doteq \tilde{\alpha}(\rho_*,\rho_*)$. We also make a change of variable in the integration from ν to $\tilde{y}$ using Eq. (5.11-7). We obtain

$$\left.\begin{aligned}
&E_r(\rho_*,\theta_*) \doteq E_o \sqrt{\frac{1-\beta}{\cos\tilde{\alpha}_*}} e^{i\Phi_{\rho_*}} \int_{-\infty}^{\infty} \mathrm{Ai}[\tilde{y}] \exp\left(-\frac{i}{2}\frac{d\tilde{\alpha}_*}{d\rho_*}(\nu-\rho_*)^2\right) d\tilde{y},\\
&\Phi_{\rho_*} = \rho_*\tilde{\alpha}_* - G\left[\rho^\dagger(\rho_*),\rho_*\right],\ \ \rho_* = kr_*n(\rho_*),\\
&\theta_* = \frac{\pi}{2} - \tilde{\alpha}_*,\ \ \frac{d\tilde{\alpha}}{d\rho} = \frac{d\tilde{\alpha}(\rho,\rho)}{d\rho},\ \ \tilde{\alpha}_* = \tilde{\alpha}(\rho_*,\rho_*),\\
&\nu \doteq \rho_* + \tilde{y}(1-\beta)^{2/3} K_{\rho_*},\ \ \beta = -\left(\frac{1}{n}\frac{dn}{d\tilde{\rho}}\tilde{\rho}\right)_{\rho_*},\ \ \tilde{\rho} = kn_*r
\end{aligned}\right\} \tag{5.11-13}$$

We note the phase term Φ_{ρ_*}. It may be written as

$$\Phi_{\rho_*} = \rho_*\tilde{\alpha}(\rho_*,\rho_*) - G\left[\rho^\dagger(\rho_*),\rho_*\right] = \rho_*\tilde{\alpha}(\rho_*,\rho_*) + \int_{\rho_*}^{\infty} \tilde{\alpha}(\omega,\omega)d\omega \tag{5.11-14}$$

The first term is simply an optical path length along the circular arc of radius ρ_* measured from the reference point $(\theta = \pi/2)$ to the angular position $\theta = \pi/2 - \tilde{\alpha}_*$. The second term, from Eq. (5.7-6), is the phase retardation induced by the gradient in the refractivity that the ray incurs in traveling through the atmosphere to the tangency point at r_*.

The quadratic term in the integral in Eq. (5.11-13) involving $d^2G/dv^2 = d\tilde{\alpha}/dv$ is related to the defocusing of the incident collimated wave resulting from the gradient of the refractivity.

5.11.2 Fresnel Transform of the Airy Function

To obtain the Fresnel transform of the Airy function, we again use the integral form for the Airy function given by Eq. (5.11-8). We obtain

$$\int_{-\infty}^{\infty} \mathrm{Ai}[\tilde{y}]\exp\left(i\left(\sigma\tilde{y}+\tau\tilde{y}^2\right)\right)d\tilde{y} = \frac{1}{2\pi}\int_{-\infty}^{\infty} e^{iz^3/3}\left(\int_{-\infty}^{\infty} e^{i\left((z+\sigma)\tilde{y}+\tau\tilde{y}^2\right)}d\tilde{y}\right)dz \qquad (5.11\text{-}15)$$

Here σ and τ are constants. From Eq. (5.11-13), it follows for our case that

$$\tau = -\frac{1}{2}K_{\rho_*}^2(1-\beta)^{4/3}\frac{d\tilde{\alpha}}{d\rho_*} \qquad (5.11\text{-}16)$$

Equation (5.11-15) is a more general version of the Fresnel transform; the latter is obtained by setting $\sigma = 0$. Upon completing the square in the inner integral of Eq. (5.11-15), one can write it in terms of the complete Fresnel integral. Then with a change of variable and the use again of the integral form for the Airy function given in Eq. (5.11-8), one finally obtains

$$\int_{-\infty}^{\infty} \mathrm{Ai}[\tilde{y}]\exp\left(i\left(\sigma\tilde{y}+\tau\tilde{y}^2\right)\right)d\tilde{y} = \sqrt{\frac{\pi}{|\tau|}}\,\mathrm{Ai}[b]\exp(ic) \qquad (5.11\text{-}17)$$

where

$$\left.\begin{aligned} b &= -\frac{1+8\sigma\tau}{16\tau^2} \\ c &= \pm\frac{\pi}{4}+\frac{1}{192\tau^3}-\frac{(1+4\sigma\tau)^2}{64\tau^3} \end{aligned}\right\} \qquad (5.11\text{-}18)$$

Here $+\pi/4$ is used in the expression for c when $\tau > 0$, and $-\pi/4$ is used when $\tau < 0$. Thus, the Fresnel transform of the Airy function yields an Airy function again but with offsets in phase and argument and with a modified amplitude. We note the defocusing term $\sqrt{|\tau|}$ appearing in the denominator of Eq. (5.11-17).

Using the Fresnel transform of the Airy function, the value of the integral in Eq. (5.11-13) becomes

$$E_r(\rho_*,\theta_*)=\frac{E_o|1-\beta|^{1/2}}{\sqrt{\cos\tilde{\alpha}_*}}\sqrt{\frac{\pi}{|\tau|}}\,\mathrm{Ai}[b]\exp\left(i\left(\Phi_{\rho_*}+c\right)\right) \tag{5.11-19}$$

We note that, for thin-atmosphere conditions, $\tau \ll 1$. For an exponential atmosphere,

$$\tau=-\frac{1}{4}\left(\frac{\pi K_{\rho_*}}{kH}\right)^{1/2}\beta(1-\beta)^{4/3} \tag{5.11-20}$$

For GPS signals with dry air at sea level, $\tau\sim 10^{-3}$. In this case, Eq. (5.11-17) essentially collapses to unity as $\tau\to 0$ and for $\sigma=0$. In this case, Eq. (5.11-19) reduces to the form

$$E_r(\rho_*,\theta_*)=\frac{E_o|1-\beta|^{1/2}}{\sqrt{\cos\tilde{\alpha}_*}}\exp\left(i\Phi_{\rho_*}\right) \tag{5.11-21}$$

We see the defocusing factor $|1-\beta|^{1/2}$ appearing here. Squaring this factor yields the defocusing in signal power, which essentially agrees with Eq. (5.6-16), the prediction from geometric optics for the defocusing at a turning point.

For E_θ, one can use the Fresnel transform of $\mathrm{Ai}'[\hat{y}]$ to derive similar results. E_θ should be essentially zero at a turning point. Also, the integral of $\mathrm{Ai}'[\hat{y}]$ over the real axis is zero.

5.12 Caustics and Multipath

Whether or not there is a unique ray, or possibly no ray, arriving at the point (r,θ) depends on the nature of the profile of $n(\rho)$, which may or may not result in caustics for the ray system and consequent multiple ray paths within the multipath zone. We have discussed caustics and their effects in Chapters 2 and 3, and they arise again here. These chapters also show examples of the converse of a multipath zone: the shadow zone, which in second-order geometric optics is a zone devoid of rays in the limit and extreme defocusing in actuality. A shadow zone based on geometric optics has an analog in wave theory. In shadow zones, wave theory using the spectral integrals in Eqs. (5.8-1) or (5.9-24) predicts much-diminished amplitudes for the field, but not zero. Also, wave theory accounts for diffraction. Using the stationary phase technique, it is readily shown that, in a strict shadow zone in geometric optics, the wave theory spectral integrals have no stationary phase points in spectral number; thus, a small but non-zero fluctuating amplitude results. In the thin-screen model, geometric optics predicts no rays within a shadow zone, but the scalar diffraction integral from a thin screen yields a small but non-zero amplitude in this zone. The scalar diffraction integral applied to a thin screen integrates the path delay phasor over impact parameter space in the thin screen. Section 5.10 discussed the close correspondence between stationary phase values of spectral number in wave theory and stationary phase values of impact parameter in the scalar diffraction/thin screen. Under most conditions, the scalar diffraction/thin-screen model generates essentially the same values for the electromagnetic field at a point well away from the screen, including diffraction effects, that are obtained from wave theory using the spectral technique described here.

We have already shown a specific example without caustics in Fig. 5-10 for a monotonic profile for the refractivity, the exponential profile given in Eq. (5.8-2a). In that example, for a given position (r_o,θ), the stationary phase condition on wavenumber in Eq. (5.9-11) is satisfied uniquely at the intersection of the δ and $\partial G / \partial \nu$ curves versus ν. These curves are generated from Eqs. (5.9-14) and (5.7-7), respectively, for several values of θ, and they apply to an incoming region. The curve for $\partial G / \partial \nu$ (and implicitly the δ curve) in Fig. 5-10 uses a refraction profile that corresponds closely to the physical conditions for the dry air component of the Earth's atmosphere with r_o corresponding to sea level. The value of ν at the intersection point of the $\partial G / \partial \nu$ and δ curves is essentially the impact parameter at the Earth's surface. Fixing (r_o,θ) to a different pair of values would cause displacements of the δ curve (see Eq. (5.9-14)) and the $\partial G / \partial \nu$ curve (see Eq. (5.7-7)) and, therefore, to an intersection at a different bending angle $\tilde{\alpha}(\rho_o,\nu)$, which yields a different ν value.

5.12.1 A Numerical Example of Multipath and Caustics

As a simple first example, we consider the refractivity profile from Eq. (5.8-2b), where $n(\rho)$ has a non-super-refracting Gaussian distribution. A more realistic case, to be considered later, embeds this distribution in a background distribution corresponding to the near-exponential form for dry air. This dry air distribution causes significant defocusing, which has the effect of greatly compressing the bending angle spread from the multiple rays.

In the case of a Gaussian refractivity profile, $d\tilde{\alpha} / d\rho$ is not monotonic, and, therefore, caustics and multipath arise for certain positions (r,θ). We use the refractivity profile given by Eq. (5.8-2b) to obtain the electric field at the LEO. When this Gaussian profile is used in Eq. (5.6-5), a bipolar bending-angle profile results, $\tilde{\alpha}(\rho_*,\rho_*)$ (see Appendix E). The total refractive bending angle at the LEO is $\alpha_{\mathrm{L}}(\rho_*) = 2\tilde{\alpha}(\rho_*,\rho_*)$.

Now, we use this Gaussian profile for $n(\rho)$ in the integral expression for $2dG^{\dagger}(\nu)/d\nu = 2dG[\rho^{\dagger}(\nu),\nu]/d\nu$ given by Eqs. (5.7-7) and (5.7-13), and we generate the curve in Fig. 5-19 by varying ν. In this example, a particular set of values, $N_{\mathrm{w}} = 0.0001$, $H_{\mathrm{w}} = 1.6k$, and $\rho_w = \rho_o$, has been used. H_{w} is the $1-\sigma$ width of the Gaussian refractivity distribution. Here, $\rho_o \approx 2\times 10^8$, which corresponds to near sea level for a GPS wavelength. The peak refractivity is N_{w}, which is about 40 percent of the refractivity from dry air there.

We know from our earlier discussion that this $2dG^{\dagger}(\nu)/d\nu$ curve coincides with $2\tilde{\alpha}(\rho_*,\rho_*)$ to very high accuracy. From the stationarity condition on $\Psi(+,-)$ [see Eq. (5.9-6)] for an outgoing wave, we have, upon setting $\partial\Psi/\partial\nu = 0$, the relationships

$$\left.\begin{aligned}\delta &= \theta_{\nu} - \theta_{\mathrm{L}} = \sin^{-1}\left(\frac{\nu}{\rho_{\mathrm{L}}}\right) - \theta_{\mathrm{L}} \\ \delta^{*} &= \theta_{\nu^{*}} - \theta_{\mathrm{L}} = 2\left(\frac{dG^{\dagger}(\nu)}{d\nu}\right)_{\nu^{*}}\end{aligned}\right\} \tag{5.12-1}$$

where ν^{*} denotes a stationary value of the spectral number. By varying ν while fixing $\rho_{\mathrm{L}} = kr_{\mathrm{L}} = 1.1kr_o$ and θ_{L} to specific orbital values, we generate the δ curves in Fig. 5-19 for three specific orbital values of θ_{L}. The intersections of the δ and $2dG[\rho^{\dagger}(\nu),\nu]/d\nu$ curves correspond to the δ^{*} and ν^{*} values given in Eq. (5.12-1), which are stationary phase values for $\Psi(+,-)$, i.e., $\partial\Psi/\partial\nu = 0$ at these points. The two particular δ curves tangent to the $2dG^{\dagger}/d\nu$ curve bound the range of θ_{L} values where the effects of multipath are evident. In this example, that range is about 17 mrad between the upper and lower caustic contacts for a typical LEO orbit. An intermediate value for θ_{L} yields a δ curve with three intersections with the $2dG^{\dagger}/d\nu$ curve and, therefore, three stationary phase points for $\Psi(+,-)$ in ν space. Within these two bounding δ curves, three rays with different bending angles from the GPS satellite will concurrently converge to the LEO. Outside of this zone, there is only a single ray and its corresponding bending angle.

The upper and lower δ curves, corresponding to tangency points on the $2dG^{\dagger}/d\nu$ curve with bending-angle values of 12.42 and –5.68 mrad, respectively, define the first contact points with the upper and lower caustic surfaces bounding this region. The θ_{L} values corresponding to these upper and lower tangency points are positions for the LEO where episodes of intense flaring can occur. Each tangency point is near the point of maximum observed amplitude. At these points, the tangency condition $2d^2G/d\nu^2 = \partial\delta/\partial\nu$ must

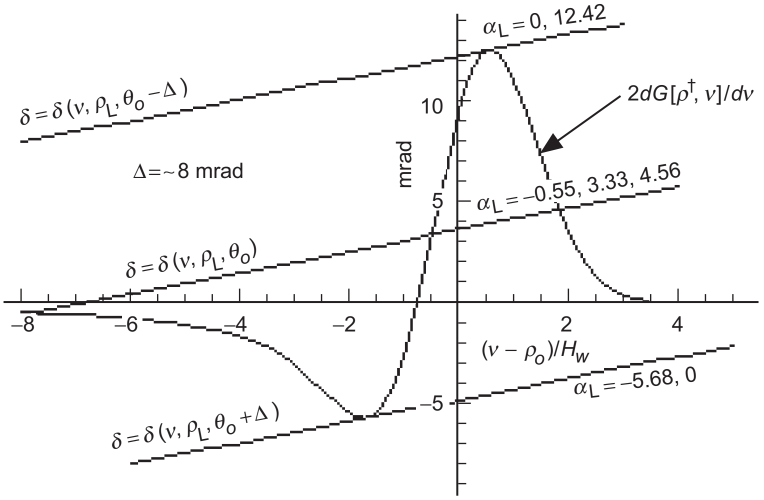

Fig. 5-19. Wave theory multipath zone in spectral number for a Gaussian refractivity profile. The phasor $\exp(i\Psi(+,-))$ in the spectral integral is stationary at an intersection of the δ and $2dG^\dagger/d\nu$ curves, which gives the bending angle $2\tilde{\alpha}$ of the corresponding ray. Tangent points are caustic contacts where $\partial\Psi/\partial\nu = \partial^2\Psi/\partial^2\nu = 0$.

hold. From Eq. (5.12-1), we have $\partial\delta/\partial\nu = 1/D_\nu$, where $D_\nu = \sqrt{\rho_L^2 - \nu^2}$. The defocusing factor at the LEO for a tangency point is given by $\zeta^{-1} = 1 - 2D_\nu d^2G/d\nu^2 = 0$ (see Eq. (5.9-29)), which defines a caustic contact point. Setting $\nu = \nu^* = \rho_*$, we conclude that a condition for no caustics is given by $2d^2G^\dagger/d\nu^2 \doteq 2d\tilde{\alpha}/d\rho_* < 1/D_{\rho_*}$ for all ρ_* values. Therefore, the gradient of the bending angle can be positive, but not too positive, less than about $0.3\ \text{mrad/km}$ for a GPS wavelength and with $r_\text{L} \approx 1.1 r_o$. We also note that, in cases where the refractivity gradient is continuous, the number of multipath rays is odd, except at a caustic contact point.

If these stationary phase points are adequately separated in wavenumber (see Appendix D for an "adequacy" index), then geometric optics as an approximate technique should suffice, which treats them as corresponding to separate rays. Geometric optics can be used with Eq. (5.6-5) to generate the ray for the impact parameter value $\rho_* = \rho_*(\nu^\dagger)$ corresponding to each of these intersection points. The phasors for three rays can be combined as vectors, i.e., taking into account their relative phases and amplitudes to obtain the aggregate electric field at the point $(r_\text{L}, \theta_\text{L})$. However, near the caustic limits, two of these points will merge, and geometric optics will become inadequate for stationary phase points in spectral number that are in the neighborhood of the caustic contact point. In wave theory, the second-order stationary phase technique for evaluating the integrals in Eq. (5.8-1b) over spectral number also becomes inadequate for the same reason. These spectral integrals should be directly evaluated, or a third-order stationary phase technique can be used, such as that described in Appendix D and discussed later in this chapter.

A caustic contact historically is associated with laser-like rays, for example, a rainbow spectral component from a water drop. Whether or not that kind of flaring in signal amplitude actually occurs at a caustic depends on the curvature of the $2dG^{\dagger}/d\nu$ curve; that is, it depends on the magnitude of $\partial^3\Psi(+,-)/\partial\nu^3$ at the caustic contact point $\nu=\nu^*$, where $\partial\Psi(+,-)/\partial\nu=\partial^2\Psi(+,-)/\partial\nu^2=0$. If the magnitude of $\partial^3\Psi(+,-)/\partial\nu^3$ is relatively small at the caustic point, then a broader neighborhood of spectral numbers about the stationary phase point contributes constructively to the spectral integral evaluation. This results in a larger amplitude. In other words, the spectral width about a stationary phase point across which phase coherence in the integrand is preserved depends inversely on $\partial^3\Psi(+,-)/\partial\nu^3$ when both $\partial\Psi(+,-)/\partial\nu$ and $\partial^2\Psi(+,-)/\partial\nu^2$ are at or near zero. We will show later that the amplitude of the flaring at a caustic contact point is proportional to $(\partial^3\Psi(+,-)/\partial\nu^3)^{-1/3}$. If the amplitudes of the new rays created at a caustic contact point are relatively strong, then signal flaring is to be expected even if interference is present from a pre-existing ray. If the amplitudes of the new rays are relatively weak, then the pre-existing ray will be dominant and the signal flaring, such as it is, will show up on the envelope of the resulting interference fringes. The Gaussian refractivity profile used in this section yields the latter scenario. Section 5.13 and Chapter 6 provide examples of the former scenario with very strong nascent rays.

Figure 5-20 shows the relationship between LEO orbital angle θ_{L} and impact parameter ρ_* from geometric optics for the same Gaussian refractivity profile and orbit model used in Fig. 5-19. This impact parameter diagram is obtained directly from Bouguer's law, $\theta_{\mathrm{L}}=\sin^{-1}(\rho_*/\rho_{\mathrm{L}})-2\tilde{\alpha}(\rho_*,\rho_*)$. Once the refractivity profile is specified, $\tilde{\alpha}(\rho_*,\rho_*)$ is obtained from Eq. (5.6-5). For $-12.2\le\theta_{\mathrm{L}}-\theta_o\le 4.8$, a triplet of impact parameter values and bending angles simultaneously satisfies the boundary conditions provided by the position $(r_{\mathrm{L}},\theta_{\mathrm{L}})$ of the LEO. Significant multipath occurs within this zone. Caustic contacts lie at the points where $d\theta_{\mathrm{L}}/d\rho_*=0$. These points correspond to episodes of signal flaring, and they mark the boundaries of the multipath zone, in this example at $\theta_{\mathrm{L}}-\theta_o=4.8$ and at $\theta_{\mathrm{L}}-\theta_o=-12.2$. Above $\theta_{\mathrm{L}}-\theta_o=4.8$, the rays labeled (a) and (b) are non-existent in a second-order geometric optics context. Only the ray labeled (m) exists. Similarly, rays (m) and (a) do not exist below $\theta_{\mathrm{L}}-\theta_o=-12.2$; only (b) rays exist.

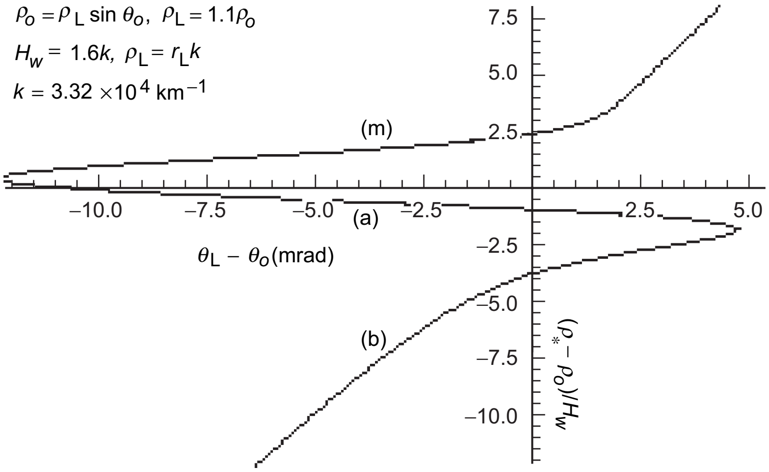

Fig. 5-20. Impact parameter diagram from geometric optics. This figure shows ρ_* versus LEO orbit angle θ_L in the neighborhood of the same refracting layer described in Fig. 5-19. Labels (m), (a), and (b) identify the corresponding rays: main, anomalous, and branching.

For the occulted GPS satellite lying in the orbit plane of the LEO and setting , θ_L decreases with time at a rate of roughly 1 mrad/s. Therefore, events unfold in Fig. 5-20 from right to left for a setting occultation. Above $\theta_L - \theta_o = 4.8$, only one stationary phase value in spectral number is realized. There is a unique value for any given orbit angle above this limit. This unique sequence of stationary phase values in spectral number versus θ_L above this limit corresponds in geometric optics to the impact parameter branch (m) in the figure, which defines the tangency points or impact parameter values generated by the (m) family of stationary phase paths, the (m) rays. When $\theta_L - \theta_o$ drops below 4.8 mrad, the first contact with a caustic is made. This results in flaring of the signal and the onset of interference from the triplet of competing stationary phase points in spectral number. In geometric optics, this corresponds to the existence of three competing ray systems, (m), (a), and (b); a member from each family passes through the position of the LEO. See Fig. 2-3 for a ray diagram. Ray (a) is the anomalous ray, and although it is a path of stationary phase, it can be shown that this path provides a local maximum in phase delay. Paths (m) and (b) provide local minima. This multipath episode continues until the lower caustic contact point is reached at $\theta_L - \theta_o = -12.2$. Below this point, a single stationary phase value in spectral number resumes, corresponding to the lower main ray (b) and the resumption of a smooth signal.

Figure 5-21(a) shows the signal amplitude $|\boldsymbol{E}(r_L, \theta_L)|$ at the LEO versus orbit angle $\theta_L - \theta_o$ for the same models used in Figs. 5-19 and 5-20. This figure

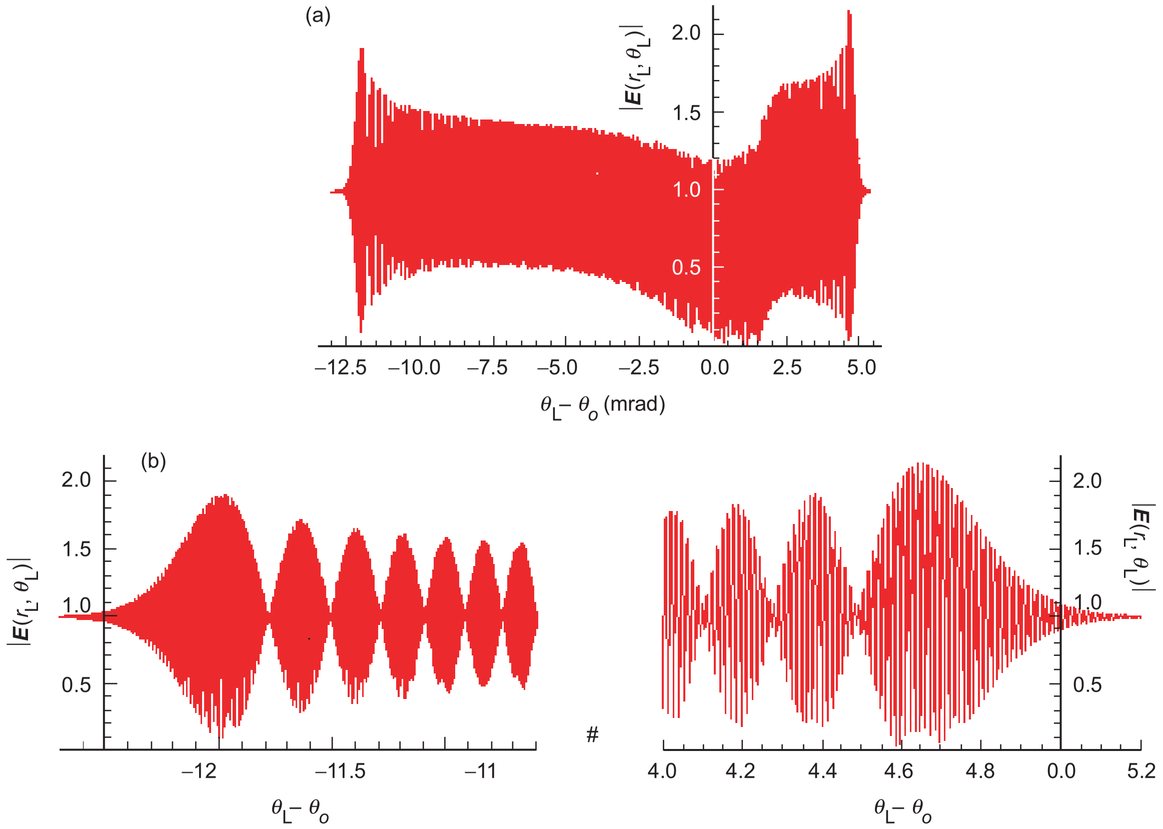

Fig. 5-21. Amplitude of the field at the LEO versus orbit angle for the same orbit model and Gaussian refractivity profile used in Figs. 5-19 and 5-20: (a) amplitude over the entire multipath zone and (b) amplitude in the vicinity of the upper and lower caustic contact points.

was obtained from a numerical integration of the spectral integral for E_r given in Eq. (5.8-1b) or, equivalently, Eq. (5.9-10). The numerical integration was aided by the stationary phase technique to isolate stationary phase neighborhoods, thereby reducing the computational burden[11] (see Section 2.6). The spectral coefficient $a_l^{\dagger}(\rho)$ used in the integration is given in Eq. (5.8-25), and $G^{\dagger}(\nu)=G[\rho^{\dagger}(\nu),\nu]$ is given from Eq. (5.7-2), using the refractivity profile given in Eq. (5.8-2b) and the parameter values used for Figs. 5-19 and 5-20. Figure 5-21(a) shows the smooth and nearly constant signal amplitude outside of the multipath zone, and it clearly shows the abrupt onset of a multipath episode at the upper caustic contact point at about $\theta_{\mathrm{L}}-\theta_o \approx 4.8$, continuing until the lower contact point at $\theta_{\mathrm{L}}-\theta_o \approx -12.0$. This figure demonstrates the violent interference from a triplet set of stationary phase points that can result from a non-monotonic refractivity profile if the refractive gradient is even moderate in magnitude. Caustic flaring at the contact points is almost immediately overwhelmed by phase interference among the three full-fledged stationary phase paths. In this example, inspection of the gradients in bending angle in the middle of the multipath zone in Fig. 5-20 shows that none of the paths is overly defocused relative to its competitors. Defocusing is evident in the neighborhood of $\theta_{\mathrm{L}}-\theta_o=0$ because of the steep gradients in bending angle on all three rays there. Above $\theta_{\mathrm{L}}-\theta_o=5$, the principal contribution to $E(r_{\mathrm{L}},\theta_{\mathrm{L}})$ comes from the main ray (m) without interference from the (a) and (b) rays (see Fig. 5-20). Below this point, three mutually interfering ray paths contribute to the spectral integrals. Contact with the lower caustic occurs at $\theta_{\mathrm{L}}-\theta_o \approx -12.2$. Abrupt termination of the scintillation episode follows. Below this only the (b) ray remains to contribute to $E(r_{\mathrm{L}},\theta_{\mathrm{L}})$.

Figure 5-21(b) is a blowup of the neighborhoods around the upper and lower caustic contact points to show the fast and slow fringes in amplitude of the field at the LEO. The high-frequency fringes from interference between rays are resolved at the upper contact point; at the lower point, their spacing is less than the resolution of the figure. The lower contact point shows somewhat less flaring than the upper point. Figure 5-20 shows that $d^2\theta_{\mathrm{L}}/d\rho_*^2$ is somewhat larger at the lower point than at the upper point. It will be shown that $d^2\theta_{\mathrm{L}}/d\rho_*^2=\partial^3\Psi(+,-)/\partial\nu^3$ when $\nu=\rho_*$. It follows that when $d^2\theta_{\mathrm{L}}/d\rho_*^2$ is larger, the near-tangency condition between the $2dG^{\dagger}(\nu)/d\nu$ curve and the δ

---

[11] Here one uses the stationary phase technique to find all spectral numbers that yield a stationary value in $\Psi(+,-)$, in this example a maximum of three. Then in Eq. (5.9-24) it is necessary only to carry out a numerical integration over a suitable neighborhood around each of these spectral numbers, taking care to properly phase-connect these separate converged integration intervals.

curve near a caustic contact point runs over a shorter interval in spectral number. Therefore, a smaller contribution to the spectral integral for $E(r_{\mathrm{L}},\theta_{\mathrm{L}})$ comes from the spectral neighborhood around the lower caustic point in Fig. 5-21(b) than from the neighborhood around the upper caustic point. The peak amplitudes near caustic contacts are slightly offset, 0.1 to 0.2 mrad, from the geometric optics predictions for caustic contact (i.e., where $\zeta \to \infty$).

Figure 5-22 shows the difference in phase near the upper caustic point between the complete field at the LEO and the field from only the (m) ray. The spikes of large phase acceleration in this figure correspond to orbit angles in Fig. 5-21(b) where the complete field is almost totally annihilated through mutual interference between the three rays. The frequency of the phase fringes in Fig. 22 scales with impact parameter separation of the rays, which in turn scales roughly linearly with the $1-\sigma$ width of the Gaussian refractivity profile. Fast fringes are from interference between the main ray (m) and the nascent rays (a) and (b). Slow modulation or banding results from interference between the (a) and (b) rays as their impact parameters begin to separate near the caustic point.

5.12.2 A Geometric Optics Interpretation of Multipath

Geometric optics can accurately predict many of the fringe features for multipath situations, such as those shown in Figs. 5-21 and 5-23. One must take into account the amplitudes of the competing rays and their phase interference as the orbit angle or, equivalently, time evolves. A notable exception is the failure of geometric optics to accurately predict the field in the immediate

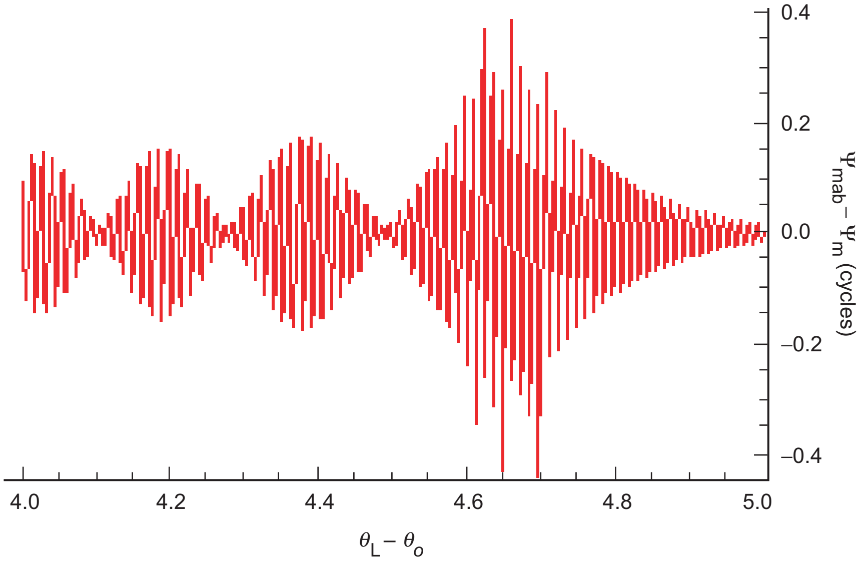

Fig. 5-22. Phase difference near the upper caustic, expressed in cycles of the complete field at the LEO minus the field of the (m) ray.

vicinity of a caustic contact. Second-order geometric optics predicts an infinite amplitude at such places, whereas wave theory gives the correct values.

We now apply geometric optics to see how well it does at predicting the fringe amplitudes and frequencies shown in Fig. 5-21. Starting with Bouguer's law, and given our specific refractivity and orbit models, the impact parameter curve for each competing ray system can be calculated. From the impact parameter diagram in Fig. 5-20, one can determine the defocusing of any ray versus orbit angle and also the interference frequencies between any two rays. To interpret the fringes, we need the relative phase changes and amplitudes of these competing rays evaluated at the LEO.

For the phase change or excess Doppler, we start with the stationary value of the spectral density of the phase at the LEO. From Eqs. (5.9-6) and (5.12-1), it is given by

$$\left.\begin{aligned}&\Psi^*(+,-)=D_{\nu^*}+\nu^*\left(\theta_{\nu^*}-\theta_{\mathrm{L}}\right)-2G^{\dagger}\left(\nu^*\right)-\frac{\pi}{4},\\&D_{\nu^*}=\sqrt{\rho_{\mathrm{L}}^2-\nu^{*2}},\quad \nu^*=\rho_{\mathrm{L}}\sin\theta_{\nu^*}\end{aligned}\right\}\tag{5.12-2}$$

where $G^{\dagger}(\nu)=G[\rho^{\dagger}(\nu),\nu]$ is given in Eq. (5.7-2) with $\rho^{\dagger}=\nu-\hat{y}^{\dagger}K_{\rho^{\dagger}}$. Here we evaluate $\Psi(+,-)$ at a stationary value $\Psi^*(+,-)$ with respect to spectral number. That spectral number ν^* is allowed to assume the value of the impact parameter ρ_* at a given epoch for a specific ray, either (m), (a), or (b) as shown in Fig. 5-20. We know from spectral theory that ν^* will be very close to ρ_* for that ray, away from super-refracting conditions. Now we differentiate $\Psi^*(+,-)$ with respect to time. Both the orbital position of the LEO and the impact parameter change as time evolves.[12] Since we are interested only in the difference in phase between rays, we can neglect the Doppler term from the observed GPS satellite. Thus, we have

---

[12] We also should include the obliquity effect resulting from the GPS satellites generally not lying in the LEO orbit plane. This correction factor is discussed in Chapter 6. It can reduce Doppler values by up to about 35 percent for inclination angles up to 30 deg. Here we assume that the occulted GPS satellite lies in the orbit plane of the LEO. This assumption essentially impacts only the scale factor between LEO orbit angle change and elapsed time.

$$\begin{aligned}\frac{d\Psi^*}{dt} &= \frac{\partial\Psi^*}{\partial\rho_{\text{L}}}\dot{\rho}_{\text{L}} + \frac{\partial\Psi^*}{\partial\theta_{\text{L}}}\dot{\theta}_{\text{L}} + \frac{\partial\Psi^*}{\partial\nu}\dot{\rho}_* \\ &= \frac{D_{\rho_*}}{\rho_{\text{L}}}\dot{\rho}_{\text{L}} - \rho_*\dot{\theta}_{\text{L}} + \dot{\rho}_*\left(\theta_\nu - \theta_{\text{L}} - 2\frac{dG^\dagger}{d\nu}\right)_{\nu^*=\rho_*}\end{aligned} \tag{5.12-3}$$

But, at a stationary phase point in spectral number, $\theta_\nu - \theta_{\text{L}} - 2dG^\dagger / d\nu = 0$, and for a circular orbit $\dot{\rho}_L \equiv 0$. It follows in this case that

$$\frac{d\Psi^*}{dt} = -\rho_*\dot{\theta}_{\text{L}} \quad \text{or} \quad \frac{d\Psi^*}{d\theta_{\text{L}}} = -\rho_* \tag{5.12-4}$$

Thus, $d(\Delta\Psi_*) / d\theta_L = -\Delta\rho_*$, where $\Delta\rho_*$ is the difference in impact parameter values between any two of the three rays, (m), (a), or (b), at a given epoch or orbit angle, and $\Delta\Psi_*$ is the difference in phase at the LEO between these two rays. These impact parameter differences can be read directly from Fig. 5-20. The high-frequency fringes in Fig. 5-21(b) near $\theta_{\text{L}} - \theta_o = 5$ result from interference between the combined but relatively weak[13] (a) and (b) rays with the strong (m) ray. At $\theta_{\text{L}} - \theta_o = 4.8$, the difference in altitudes of the impact parameters between the (m) ray and the nascent (a) and (b) rays is 16.3 km. Thus, the frequency of the fringes resulting from phase interference between these two ray systems is given by $(2\pi)^{-1} d(\Psi_{*\text{m}} - \Psi_{*\text{ab}}) / d\theta_{\text{L}} = 16.3 / \lambda$, or about 82 cycles/mrad. Although difficult to measure precisely in Fig. 5-21(b), the high-frequency fringe rate is indeed about 80 cycles/mrad. At the lower caustic contact point near $\theta_{\text{L}} - \theta_o = -12$, the high-frequency fringes are caused by interference between the (b) ray and the dying (m) and (a) rays (or nascent rays for a rising occultation). Figure 5-20 shows a much wider separation in impact parameter values there between the (b) ray and the (m) or (a) ray. The high-frequency fringe rate is around 180 cycles/mrad. We deal with fringe frequency compression from defocusing later.

The low-frequency modulation in Fig. 5-21(b) comes from interference between the (a) and (b) rays near the upper caustic contact point at $\theta_{\text{L}} - \theta_o = 4.8$, and between the (m) and (a) rays near the lower contact at $\theta_{\text{L}} - \theta_o = -12$. These ray pairs have narrowly different impact parameter values at these locations in this figure, but they have about the same amplitude initially. For the right-hand side of Fig. 5-21(b) near $\theta_{\mathrm{L}} - \theta_o = 4$, $(2\pi)^{-1} d(\Psi_{\mathrm{a}}^* - \Psi_{\mathrm{b}}^*) / d\theta_{\mathrm{L}}$ is about 5 cycles/mrad, but this modulation frequency is accelerating rapidly with decreasing θ_{L}. We can infer this acceleration from Fig. 5-20, which shows the impact parameter values of these two rays separating rapidly with decreasing θ_{L} as they move away from the caustic contact point where these rays were created. At the lower caustic point, the low frequency and weakening modulation results from interference between the (m) and (a) rays, which are dying out completely below $\theta_{\mathrm{L}} - \theta_o = -12$.

---

[13] Caustic rays are renowned for beaming like searchlights at their nascence, but in this example the (a) and (b) rays are relatively dim (a combined amplitude of 1.14 compared to the (m) ray amplitude of 1.0). This is because of the relatively large magnitude of $d^2\theta_{\text{L}} / d\rho_*^2$ at the caustic contact point. The upper Gaussian wing of the refractivity profile leads to a rapid falloff in the gradient of the bending angle with increasing altitude and, therefore, to a main ray (m) not significantly defocused here.

5.12.3 Amplitude Variability from Geometric Optics

Except in the immediate neighborhood of the caustic points, the amplitude variability shown in Fig. 5-21 can be predicted using geometric optics. In this approach, one adds up the complex amplitudes of the three rays taking into account their respective defocusing. The amplitude of the slow modulation in this figure can be obtained from the defocusing factor $\zeta^{-1} = 1 - 2D_{\rho_*} d\tilde{\alpha}_* / d\rho_*$ for each ray. The slow modulation peaks and valleys in amplitude shown in Fig. 5-21(b) are accurately predicted from the four combinations $|\zeta_{\mathrm{m}}^{1/2} \pm \zeta_{\mathrm{b}}^{1/2} \pm |\zeta_{\mathrm{a}}|^{1/2}|$. ($\zeta_{\mathrm{a}}$ is negative, a hallmark of an anomalous ray; the path delay along this ray is a local maximum.) For example, in Fig. 5-21(b) at $\theta_{\mathrm{L}} - \theta_o = 4.2$, the (m) ray is still not significantly defocused; its amplitude is unity. For the (a) and (b) rays, we have $|\zeta_{\mathrm{a}}|^{1/2} = 0.382$ and $\zeta_{\mathrm{b}}^{1/2} = 0.461$. The four combinations yield $1 \pm 0.461 \pm 0.382 =$ 1.843, 0.157, 1.079, and 0.921. The corresponding peak values of the envelope in Fig. 5-21(b) are about 1.84 and 0.16 for the points of maximum amplitude difference, and 1.08 and 0.93 for the nodes. This is very close agreement, considering that the envelope isn't well defined in that figure.

At the upper caustic contact point in Fig. 5-21(b), $\zeta_{\mathrm{ab}} \to \infty$; therefore, the agreement cited above must break down as we near such a point. From geometric optics, this occurs at $\theta_{\mathrm{L}} - \theta_o = 4.77$, but the peak amplitude from wave theory in Fig. 5-21(b) occurs at $\theta_{\mathrm{L}} - \theta_o = 4.65$. At the lower caustic point, $\zeta_{\mathrm{am}} \to \infty$ at $\theta_{\mathrm{L}} - \theta_o = -12.18$, but the peak amplitude from wave theory occurs at $\theta_{\mathrm{L}} - \theta_o = -11.98$.

5.12.4 Third-Order Theory

The small offsets in location of the peak and the major discrepancy in amplitude prediction from geometric optics can be reconciled through use of a third-order stationary phase technique. Here, to evaluate the spectral integrals in

Eq. (5.9-10), we expand $\Psi(+,-)$ in spectral number about the caustic contact point where $\partial^2\Psi(+,-)/\partial\nu^2=0$, retaining third-order terms. We obtain

$$\left.\begin{aligned}&\Psi(+,-)\doteq\Psi\big|_{\nu_{\mathscr{C}}}+\left(\nu-\nu_{\mathscr{C}}\right)\frac{\partial\Psi}{\partial\nu}\bigg|_{\nu_{\mathscr{C}}}+\frac{\left(\nu-\nu_{\mathscr{C}}\right)^3}{3!}\frac{\partial^3\Psi}{\partial\nu^3}\bigg|_{\nu_{\mathscr{C}}}\\&\frac{\partial^2\Psi}{\partial\nu^2}\bigg|_{\nu_{\mathscr{C}}}=0\end{aligned}\right\}\tag{5.12-5}$$

Here $\nu_{\mathscr{C}}$ is the value of the spectral number at the caustic contact point. It satisfies the tangency condition between the $2dG^\dagger/d\nu$ and δ curves shown in Fig. 5-19, and we know that its value is close in value to $\rho_{\mathscr{C}}$, which is the impact parameter value at the caustic contact point. Therefore, for the purpose of evaluating the amplitude of the field at the LEO, we set $\nu_{\mathscr{C}}=\rho_{\mathscr{C}}$. The partial derivatives $\partial\Psi(+,-)/\partial\nu$ and $\partial^3\Psi(+,-)/\partial\nu^3$ are evaluated at that point. We obtain

$$\left.\begin{aligned}&\frac{\partial\Psi}{\partial\nu}\bigg|_{\nu=\rho_{\mathscr{C}}}\hat{=}\,\Psi'_{\mathscr{C}}=\theta_{\rho_{\mathscr{C}}}-\theta_{\mathrm{L}}-2\tilde{\alpha}_{\mathscr{C}},\\&\frac{\partial^2\Psi}{\partial\nu^2}\bigg|_{\nu=\rho_{\mathscr{C}}}\hat{=}\,\Psi''_{\mathscr{C}}=\frac{d\theta_{\mathrm{L}}}{d\rho_*}\bigg|_{\rho_*=\rho_{\mathscr{C}}}=\left(\frac{1}{D_{\rho_*}}-2\frac{d\tilde{\alpha}}{d\rho_*}\right)_{\rho_{\mathscr{C}}}=0,\\&\frac{\partial^3\Psi}{\partial\nu^3}\bigg|_{\nu=\rho_{\mathscr{C}}}\hat{=}\,\Psi'''_{\mathscr{C}}=\frac{d^2\theta_{\mathrm{L}}}{d\rho_*^2}\bigg|_{\rho_*=\rho_{\mathscr{C}}}=\left(\frac{\rho_*}{D_{\rho_*}^3}-2\frac{d^2\tilde{\alpha}}{d\rho_*^2}\right)_{\rho_{\mathscr{C}}},\\&\tilde{\alpha}_{\mathscr{C}}=\tilde{\alpha}(\rho_{\mathscr{C}},\rho_{\mathscr{C}}),\ 2\tilde{\alpha}=\alpha_{\mathrm{L}}\end{aligned}\right\}\tag{5.12-6}$$

Here the relationships, $\Psi''=d\theta_L/d\rho_*$ and $\Psi'''=d^2\theta_L/d\rho_*^2$, follow from Bouguer's law in Eq. (5.12-5). Differentiating that expression successively with respect to $\rho_{\mathscr{C}}$ yields the relationships given in Eq. (5.12-6). Since we seek only the modulation amplitude near the caustic contact point (but not the phase), we can simplify the spectral integrals in Eq. (5.9-10) by placing the slowly varying quantities, i.e., $(\sin^3\theta_\nu/\cos\theta_\nu)^{1/2}$ and $\left(\sin\theta_\nu\cos\theta_\nu\right)^{1/2}$, outside of the integrals and setting them equal to their values at the caustic contact point. When the radial and angular components of the field are combined, Eq. (5.9-10) yields the field at the LEO from the nascent rays near the caustic contact in the form

$$E_{\mathscr{C}}(r_{\mathrm{L}},\theta_{\mathrm{L}}) \doteq E_o\left(\frac{\tan\theta_{\mathscr{C}}}{2\pi\rho_{\mathrm{L}}\sin\theta_{\mathrm{L}}}\right)^{\frac{1}{2}} e^{i\Psi_{\nu_{\mathscr{C}}}}\int_0^{\infty} e^{i\left((\nu-\nu_{\mathscr{C}})\Psi'_{\nu_{\mathscr{C}}}+\frac{1}{3!}(\nu-\nu_{\mathscr{C}})^3\Psi'''_{\nu_{\mathscr{C}}}\right)}d\nu \qquad (5.12\text{-}7)$$

Here $\sin\theta_{\mathscr{C}} = \rho_{\mathscr{C}} / \rho_{\mathrm{L}}$, where $\rho_{\mathscr{C}}$ is the impact parameter at the caustic contact point. The subscript "$\mathscr{C}$" on $E_{\mathscr{C}}(r_{\mathrm{L}},\theta_{\mathrm{L}})$ is to remind us that it represents the nascent field only. The Taylor series expansion in Eq. (5.12-7) is not intended to span the spectral number range needed to include the stationary point corresponding to the main ray. Making a change of integration variable to $(\nu-\nu_{\mathscr{C}}) = \mathrm{sign}[\Psi'''_{\nu_{\mathscr{C}}}](2/|\Psi'''_{\nu_{\mathscr{C}}}|)^{1/3}t$, and noting that $\nu_{\mathscr{C}} \doteq \rho_{\mathscr{C}}$ is a very large number, we obtain for the amplitude of the nascent field at the LEO

$$\begin{gathered}\left|\boldsymbol{E}_{\mathscr{C}}(r_{\mathrm{L}},\theta_{\mathrm{L}})\right| \doteq E_o\left(\frac{2\pi\tan\theta_{\mathscr{C}}}{\rho_{\mathrm{L}}\sin\theta_{\mathrm{L}}}\right)^{\frac{1}{2}}\left(\frac{2}{\left|\Psi'''_{\mathscr{C}}\right|}\right)^{\frac{1}{3}}\frac{1}{2\pi}\int_{-\infty}^{\infty}\exp\left(i(zt+t^3/3)\right)dt = \\ E_o\left(\frac{2\pi\tan\theta_{\mathscr{C}}}{\rho_{\mathrm{L}}\sin\theta_{\mathrm{L}}}\right)^{\frac{1}{2}}\left(\frac{2}{\left|\Psi'''_{\mathscr{C}}\right|}\right)^{\frac{1}{3}}\mathrm{Ai}[z] = E_o\left(\frac{2\pi\tan\theta_{\mathscr{C}}}{\rho_{\mathrm{L}}\sin\theta_{\mathrm{L}}}\right)^{\frac{1}{2}}\left(\frac{1}{2}\left|\frac{d^2\theta_{\mathrm{L}}}{d\rho_{\mathscr{C}}^2}\right|\right)^{-\frac{1}{3}}\mathrm{Ai}[z]\end{gathered} \qquad (5.12\text{-}8)$$

where z is given by

$$\begin{aligned} z &= \Psi'_{\mathscr{C}}\left(\frac{2}{\left|\Psi'''_{\mathscr{C}}\right|}\right)^{\frac{1}{3}}\mathrm{sign}\left[\Psi'''_{\mathscr{C}}\right] \\ &= \left(\theta_{\rho_{\mathscr{C}}}-\theta_{\mathrm{L}}-2\tilde{\alpha}_{\mathscr{C}}\right)\left(\frac{1}{2}\left|\frac{d^2\theta_{\mathrm{L}}}{d\rho_{\mathscr{C}}^2}\right|\right)^{-\frac{1}{3}}\mathrm{sign}\left[\frac{d^2\theta_{\mathrm{L}}}{d\rho_{\mathscr{C}}^2}\right]\end{aligned} \qquad (5.12\text{-}9)$$

In Eq. (5.12-8), the integral form for the Airy function given in Eq. (5.11-8) has been used.

Equation (5.12-8) tells us a few things. First, near a caustic contact, the profile of the signal flaring envelope with orbit angle closely follows the shape of the Airy function of the first kind (first established by George Airy). Figure 5-23 provides a comparison of this third-order prediction of amplitude at the LEO from the nascent (a) and (b) rays with their actual combined amplitude from wave theory for the same case shown in the right side of Fig. 5-21(b). Here the contribution from the main ray (m) is removed. The shape of the third-order curve follows the absolute value of the Airy function. The agreement is very close in the neighborhood of the caustic contact point. Third-order theory predicts zero amplitude at the nodes, which actually occurs only when the (a) and (b) rays have identical amplitudes and opposite phase. In Fig. 5-23, we see

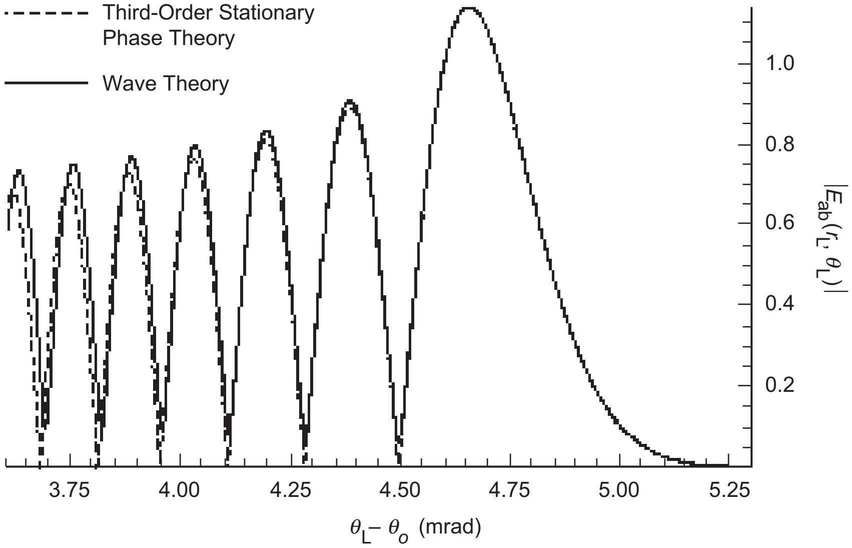

Fig. 5-23. Comparison of the amplitude of the field at the LEO from only the nascent rays (a) and (b) based on wave theory versus third-order stationary phase theory. Refractivity and orbit models are the same as those used in Figs. 5-19 through 5-22.

slight differences from the wave theory and also a gradual phase misalignment building up as θ_L recedes from the caustic contact. The accuracy of third-order theory with decreasing θ_L depends on the degree of symmetry in the θ_L versus ρ_* curve for these two nascent rays about the caustic point. If $|d^3\theta_L / d\rho_*^3|_{\mathscr{C}}$ and the higher derivatives are relatively small, then the defocusing for the two nascent rays will remain roughly equal in magnitude as the impact parameters of the nascent rays move away from the caustic contact point. When close symmetry holds, these rays will continue with decreasing θ_L to mostly null each other at the nodes of the secondary lobes, and they will double each other's amplitude at the peaks. The Airy function approximation will be valid in this case over a wider range of θ_L values. Second-order geometric optics predicts an infinite amplitude at the caustic contact point at $\theta_L - \theta_o = 4.77$, which is 0.13 mrad greater than the actual location of the peak. But the accuracy of geometric optics improves rapidly away from the caustic contact point. Even at the first node, it accurately predicts its amplitude and location.

The second conclusion from Eq. (5.12-8) is that the amplitude of the nascent field at the LEO is proportional $(|d^2\theta_L / d\rho_*^2|_{\mathscr{C}})^{-1/3}$, a quantity that is readily obtained from Bouguer's law and the bending-angle equation if the refractivity profile is given. We see that caustic flaring comes in two flavors. When $|d^2\theta_L / d\rho_*^2|_{\mathscr{C}}$ is small enough, we will have strong flaring near a caustic contact, on which high-frequency fringes from interference with the main ray will cause a minor modulation. Here there is a wider range of spectral numbers associated with the nascent rays that coherently contribute to the spectral integral. An example of this is shown in Section 5.13, Figs. 5-31 and 5-32. Rainbow caustics have a similar form. However, when $|d^2\theta_{\mathrm{L}} / d\rho_*^2|_{\mathcal{C}}$ is larger, as is the case in Fig. 5-20, then there is a narrower range of spectral numbers contributing coherently to the spectral integral. In this case, the amplitude of the nascent field will be smaller; interference fringes from the main ray will become the dominant feature, with the nascent field providing the envelope of the amplitude fringes. Two examples of relatively weak caustics are shown in Fig. 5-21.

The third conclusion concerns the location of maximum amplitude. Neither $\Psi''_{\mathcal{C}}$ nor $\Psi'''_{\mathcal{C}}$ is variable; their values are set at the caustic contact point. But, z is a variable, and it depends on the value of θ_{L}. We now adjust θ_{L} to achieve the maximum value for $\left|\boldsymbol{E}_{\mathcal{C}}(r_{\mathrm{L}},\theta_{\mathrm{L}})\right|$ given in Eq. (5.12-8). The value $z=0$ corresponds to the stationary phase point ($\theta_{\rho_{\mathcal{C}}} - \theta_{\mathrm{L}\mathcal{C}} - 2\tilde{\alpha}_{\mathcal{C}} = 0$ in the second-order stationary phase formulation) also occurring at the caustic point where $1-2D_{\mathcal{C}}\tilde{\alpha}_{\mathcal{C}}=0$, which is the prediction from geometric optics concerning maximum amplitude (i.e., infinity). This condition yields a determination of $\theta_{\mathrm{L}\mathcal{C}}$, which is at $\theta_o + 4.77$ for the upper caustic contact point, and at $\theta_o - 12.18$ for the lower point. But, we see that the Airy function achieves greater values away from the stationary phase point at the caustic, which has a value of $\mathrm{Ai}[0]=0.355$. The maximum value of $\mathrm{Ai}[z]$ nearest to $z=0$ is 0.536, and it occurs at $z=-1.019$. If we let $\hat{\theta}_{\mathrm{L}}$ be the value of θ_{L} where $z=-1.019$, then the offset between the geometric optics prediction of the location $\theta_{\mathrm{L}\mathcal{C}}$ of maximum amplitude and the third-order stationary phase prediction, $\hat{\theta}_{\mathrm{L}}$, is given by

$$\hat{\theta}_{\mathrm{L}} - \theta_{\mathrm{L}\mathcal{C}} = 1.019\left(\frac{1}{2}\left|\frac{d^2\theta_{\mathrm{L}}}{d\rho_*^2}\right|\right)_{\mathcal{C}}^{-(1/3)} \mathrm{sign}\left[\frac{d^2\theta_{\mathrm{L}}}{d\rho_*^2}\right]_{\mathcal{C}} \tag{5.12-10}$$

This expression predicts offsets in Fig. 5-21 for the upper caustic point at $\theta_{\mathrm{L}} - \theta_o = 4.77$ of $\hat{\theta}_{\mathrm{L}} - \theta_{\mathrm{L}\mathcal{C}} = -0.13$ mrad, or $\hat{\theta}_{\mathrm{L}} - \theta_o = -4.64$. At the lower caustic point at $\theta_{\mathrm{L}} - \theta_o = -12.18$, the offset is +0.16 mrad, or $\hat{\theta}_{\mathrm{L}} - \theta_o = -12.02$. Figure 5-21(b) shows that these predictions are very close to the actual offsets obtained from wave theory.

The maximum amplitudes predicted by Eq. (5.12-8) for the nascent field at the LEO are 1.09 near $\theta_{\mathrm{L}} - \theta_o = 4.8$ and 0.90 near $\theta_{\mathrm{L}} - \theta_o = -12$. The actual values are 1.14 and 0.91. Because the amplitudes of the nascent fields are comparable to the main ray, the (m) ray at the upper caustic and the (b) ray at the lower caustic, there will be high-frequency fringes of comparable amplitude superimposed on this nascent radiation. Thus, it is the envelope of the field at the caustic points that we should examine. Setting the field amplitude of the main ray to unity, Eq. (5.12-10) predicts the peaks in the envelope to be 2.09 maximum and –0.09 minimum near $\theta_{\mathrm{L}} - \theta_o = 4.7$, and 1.90 and +0.10 near $\theta_{\mathrm{L}} - \theta_o = -12$. Since we are displaying amplitudes here, the negative minimum peak near $\theta_{\mathrm{L}} - \theta_o = 4.8$ is "reflected" about the θ_{L} axis and becomes +0.09. These compare very closely, if not perfectly, with the actual peaks in the lobe nearest the caustic contact points.

An index to characterize the two flavors of caustic flaring, strong and weak, can be formulated. We take the ratio $E_{\mathscr{C}}(r_{\mathrm{L}}, \theta_{\mathrm{L}}) / E_o \zeta_{\mathrm{m}}^{1/2}$, which is the ratio of the amplitude of the field at the LEO from the nascent (a) and (b) rays at the caustic point $\theta_{\mathrm{L}} = \theta_{\mathrm{L}\mathscr{C}}$ divided by the field from the main ray (m) at the same orbit angle. It follows from Eqs. (5.12-6) and (5.12-8) that this ratio is given by

$$\left\{ \mathscr{R} = \frac{E_{\mathscr{C}}}{E_o \zeta_{\mathrm{m}}^{1/2}} = \sqrt{2\pi}\,\mathrm{Ai}[-1.02] \left| \frac{d\theta_{\mathrm{L}}}{d\rho_*} \right|_{\mathrm{m}}^{1/2} \left| \frac{1}{2} \frac{d^2\theta_{\mathrm{L}}}{d\rho_*^2} \right|_{\mathscr{C}}^{-(1/3)} \right. \qquad (5.12\text{-}11)$$

If $\left| d^2\theta_{\mathrm{L}} / d\rho_*^2 \right|_{\mathscr{C}} >> 5 \left| d\theta_{\mathrm{L}} / d\rho_* \right|_{\mathrm{m}}^{3/2}$, then $\mathscr{R} << 1$, and vice versa.

Even the fine structure in the minimum envelope in Fig. 5-21(b) at $\theta_{\mathrm{L}} - \theta_o = 4.7$ is predicted well by Eq. (5.12-8). As θ_{L} is moved away from its maximum amplitude point at $\hat{\theta}_{\mathrm{L}}$, z varies and $\mathrm{Ai}[z]$ diminishes. If we adjust z so that the amplitude of the nascent field at the LEO is unity, this will mark a pair of points along the θ_{L} axis where the nascent field and the main field from the (m) ray can completely cancel each other. Setting $E_{\mathscr{C}}(r_{\mathrm{L}}, \theta_{\mathrm{L}}) = 1$ yields z values of –1.40 and –0.58. This yields $\theta_{\mathrm{L}} - \hat{\theta}_{\mathrm{L}} = +0.05, -0.06$, or $\theta_{\mathrm{L}} - \theta_o = 4.69, 4.58$, which corresponds almost exactly with the θ_{L} values where cancellation is almost complete.

The first node in the envelope nearest the peak corresponds in Eq. (5.12-8) to the first zero of $\mathrm{Ai}[z]$, which occurs at $z = -2.34$. This yields $\theta_{\mathrm{L}} - \hat{\theta}_{\mathrm{L}} = -0.16$, or $\theta_{\mathrm{L}} = \theta_o + 4.48$, which is very close to the location of the actual node in Fig. 5-21(b), $\theta_{\mathrm{L}} = \theta_o + 4.49$. Here third-order theory predicts zero for the nodal amplitude, but we see a slight departure from this value. The accuracy of the third-order theory deteriorates the further away from the caustic point one applies it. Actually, third-order theory does well for several lobes at predicting amplitude peaks and nodes, but eventually it falls out of phase with wave theory results.

The defocusing factors of the (a) and (b) rays at the first node at $\theta_{\mathrm{L}} = \theta_o + 4.49$ are given by $|\zeta_{\mathrm{a}}|^{1/2} = 0.462$ and $\zeta_{\mathrm{b}}^{1/2} = 0.526$. This node marks the point where the (a) and (b) rays first become 180 deg out of phase. The difference of these defocusing factors is 0.06, which is very close to the actual nodal amplitude at $\theta_{\mathrm{L}} = \theta_o + 4.49$.

One also can predict the location of the first node from geometric optics. We know from Eq. (5.12-2) that at $\theta_{\mathrm{L}} = \theta_{\mathrm{L}\mathscr{C}}$ the phase function difference $\Psi_{\mathrm{a}}^* - \Psi_{\mathrm{b}}^* = 0$ because, according to geometric optics, the (a) and (b) rays are merged at that caustic contact point. We now adjust θ_{L} away from the caustic point until the phase difference is $\Psi_{\mathrm{a}}^* - \Psi_{\mathrm{b}}^* = \pi$, exactly. The expressions for Ψ^* in Eq. (5.12-2) can be used for this calculation, although care in taking the difference must be exercised because of the enormity of Ψ^* itself. When this program is undertaken for the example shown in Fig. 5-21(b), one obtains $\theta_{\mathrm{L}} = \theta_o + 4.56$ for the location of the node where the (a) and (b) rays have exactly opposite phase, a somewhat less accurate result than the third-order stationary phase prediction, but still a rather good prediction.

An alternate approach is to use the third-order expansion for Ψ^* around the caustic contact point $(\rho_{\mathscr{C}}, \theta_{\mathrm{L}\mathscr{C}})$ in the impact parameter diagram (see Fig. 5-24). We use this expansion to calculate the separation distance $\rho_{\mathrm{a}} - \rho_{\mathrm{b}}$ and the

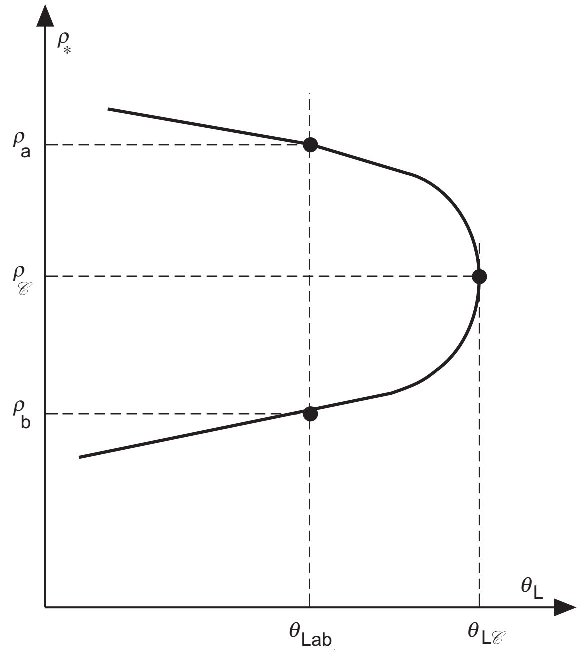

Fig. 5-24. Quadratic behavior of ρ_* for nascent rays near caustic.

change in orbit angle $\theta_{\mathrm{La}} - \theta_{\mathrm{Lb}}$ required to achieve exactly π rad phase difference between the (a) and (b) rays at the LEO since their nascence. At the caustic contact point $\theta_{\mathrm{L}} = \theta_{\mathrm{L}\mathscr{C}}$, and from Eqs. (5.12-5) and (5.12-6), it follows that $\Psi'_{\mathscr{C}} = 0$ and $\Psi''_{\mathscr{C}} = \left(d\theta_{\mathrm{L}} / d\rho_*\right)_{\mathscr{C}} = 0$. Therefore, we may write the difference in phase between rays (a) and (b) in terms of the third-order expansion as

$$\begin{aligned} \Psi_{\mathrm{a}} - \Psi_{\mathrm{b}} &\doteq \frac{1}{3!}\left(\frac{d^2\theta_{\mathrm{L}}}{d\rho_*^2}\right)_{\mathscr{C}} \left(\left(\rho_{\mathrm{a}} - \rho_{\mathscr{C}}\right)^3 - \left(\rho_{\mathrm{b}} - \rho_{\mathscr{C}}\right)^3\right) \\ &= \frac{1}{24}\left(\frac{d^2\theta_{\mathrm{L}}}{d\rho_*^2}\right)_{\mathscr{C}} \left(\rho_{\mathrm{a}} - \rho_{\mathrm{b}}\right)^3 = \pi \end{aligned} \tag{5.12-12}$$

It follows that the separation distance in impact parameters of the (a) and (b) rays at their first null since nascence, $\Delta\rho_{*\mathrm{ab}}$, is given by

$$\Delta\rho_{*\mathrm{ab}} = \left(\rho_{\mathrm{a}} - \rho_{\mathrm{b}}\right)\Big|_{\Delta\Psi_{\mathrm{ab}} = \pi} = (24\pi)^{1/3} \left|\frac{d^2\theta_{\mathrm{L}}}{d\rho_*^2}\right|_{\mathscr{C}}^{-(1/3)} \operatorname{sign}\left[\frac{d^2\theta_{\mathrm{L}}}{d\rho_*^2}\right]_{\mathscr{C}} \tag{5.12-13}$$

For $\Delta\theta_{\mathrm{L}} = \left(\theta_{\mathrm{L}} - \theta_{\mathrm{L}\mathscr{C}}\right)\Big|_{\Delta\Psi_{\mathrm{ab}} = \pi}$, we obtain

$$\begin{aligned} \Delta\theta_{\mathrm{L}} &\doteq \frac{1}{2}\left(\frac{d^2\theta_{\mathrm{L}}}{d\rho_*^2}\right)_{\mathscr{C}} \left(\rho_{\mathrm{a}} - \rho_{\mathscr{C}}\right)^2 \doteq \frac{1}{2}\left(\frac{d^2\theta_{\mathrm{L}}}{d\rho_*^2}\right)_{\mathscr{C}} \left(\rho_{\mathrm{b}} - \rho_{\mathscr{C}}\right)^2 \\ &\doteq \frac{1}{8}\left(\frac{d^2\theta_{\mathrm{L}}}{d\rho_*^2}\right)_{\mathscr{C}} \left(\rho_{\mathrm{a}} - \rho_{\mathrm{b}}\right)^2 = \frac{1}{2}(3\pi)^{2/3} \left|\frac{d^2\theta_{\mathrm{L}}}{d\rho_*^2}\right|_{\mathscr{C}}^{1/3} \operatorname{sign}\left[\frac{d^2\theta_{\mathrm{L}}}{d\rho_*^2}\right]_{\mathscr{C}} \end{aligned} \tag{5.12-14}$$

We can compare the coefficients in Eqs. (5.12-9) and (5.12-14) for predicting the location of the first node. The coefficient in Eq. (5.12-9) for $\Delta\theta_{\mathrm{L}} = \theta_{\mathrm{L}} - \theta_{\mathrm{L}\mathscr{C}}$ is 2.34, which corresponds to the first zero of the Airy function Ai[z]. Equation (5.12-9) predicts the location of the node at $\theta_{\mathrm{L}} = \theta_o + 4.48$, which is very close to the actual first node shown in Fig. 5-23. Equation (5.12-14) gives a coefficient of $(3\pi)^{2/3} / 2 = 2.23$, and it predicts the location at $\theta_{\mathrm{L}} = \theta_o + 4.50$.

We recall that the semi-minor axis of the first Fresnel zone in second-order geometric optics is the separation distance of the impact parameters for two rays that arrive at the LEO exactly π rad out of phase. Thus, at a point where $\Psi'' \neq 0$, one obtains

$$\Psi_{\mathrm{a}} - \Psi_{\mathrm{b}} \doteq \frac{1}{2}\Psi''\left(\rho_{\mathrm{a}} - \rho_{\mathrm{b}}\right)^2 = \pi \tag{5.12-15}$$

or

$$
\begin{aligned}
k\mathscr{F} &= \left(\rho_\mathrm{a} - \rho_\mathrm{b}\right)_{\Delta\Psi=\pi} = \left(\frac{2\pi}{|\Psi''|}\right)^{1/2} = \left|\frac{1}{2\pi}\frac{d\theta_\mathrm{L}}{d\rho_*}\right|^{-(1/2)} \\
&= \left(\frac{2\pi D_{\rho_*}}{\left|1-2D_{\rho_*}\tilde{\alpha}'_*\right|}\right)^{1/2} = \left(2\pi D_{\rho_*}|\zeta_*|\right)^{1/2}
\end{aligned}
\tag{5.12-16}
$$

At any rate, $\mathscr{F}$ is infinite at the caustic point. For comparison, for the example given in Fig. 5-21 at the upper caustic point at $\theta_\mathrm{L} = \theta_o + 4.47$, $k^{-1}\Delta\rho_{*\mathrm{ab}}$ in Eq. (5.12-13) has a value of 880 m. In a vacuum, $\mathscr{F}$ is about 750 m at the LEO radial distance of $r_\mathrm{L} = 1.1r_o$, whereas at sea level for a defocusing dry air medium, $\mathscr{F}$ is about 250 m. We show in the next section that the defocusing medium significantly compresses the separation distance between the impact parameters of caustic rays (see Fig. 5-26). At sea level for dry air $k^{-1}\Delta\rho_\mathrm{ab}$ is reduced to about 290 m. The offset $\Delta\theta_\mathrm{L}$ between the primary peak amplitude at the upper caustic point and the first node is about 0.29 mrad in Fig. 5-21 and about 0.80 mrad in a defocusing dry air medium (see Fig. 5-26). (This corresponds to roughly 300 ms and 800 ms of elapsed time, respectively, plenty of time for a phase-locked loop GPS receiver to decide that it has got the right stuff!).

From these and previous discussions, we conclude that even at the first node after the caustic point, second-order ray optics does a good job at predicting the field amplitude, but it gives a somewhat less accurate prediction of the phase. This agreement with wave theory results improves as the impact parameters for the nascent rays recede further from the caustic point.

In summary, geometric optics works well for predicting the amplitude of the field in multipath conditions provided that (1) the separation in altitudes between impact parameters of the competing rays exceeds a certain minimum distance and (2) caustic contact neighborhoods are avoided. Condition (1) is equivalent to the requirement in spectral theory that the stationary points in spectral number be sufficiently separated. When this is satisfied, the spectral integrals, one for each stationary phase point, do not significantly co-mingle; that is, the spectral neighborhood providing significant contributions to the spectral integral from one ray does not overlap the spectral neighborhood for the other ray. This is equivalent to saying that the two rays corresponding to these two spectral integrals are separated adequately in impact parameter altitude. An accuracy index based on this separation concept can be derived from second- and third-order stationary phase theory. This has been given in Appendix D. One can derive from that discussion an accuracy-dependent index for minimum separation altitudes of the impact parameters (or spectral numbers in wave theory) for which second-order ray theory will be adequate. For a given accuracy, it can be shown that this index is proportional to $\left(d\theta_{\mathrm{L}} / d\rho_*\right)^{-1/2}$, or to the first Fresnel zone. From the agreements in amplitude fringes and modulations discussed above, we also can infer that the relative phases between rays are handled accurately by geometric optics away from caustic neighborhoods. Getting absolute phase from ray theory to agree closely with the phase from wave theory is somewhat more challenging because of the extreme sensitivity of absolute phase to boundary conditions; this results from the fact that $r_o / \lambda >> 1$. But, even the phases between the two systems can be aligned by renormalization.

5.12.5 Reduction of Multipath Spectral Width by Defocusing

The frequencies of the high-frequency interference fringes shown in Figs. 5-21 and 5-22 have a temporal equivalent in the range from 80 to 180 Hz. These high frequencies result from using a solitary Gaussian refraction model in these figures without the presence of a defocusing background medium. These frequencies exceed by an order of magnitude the actual maximum bandwidth (~10 to 15 Hz) of transient signatures in the excess Doppler observed by a LEO sounding the Earth's atmosphere. This disparity in the fringe frequency bandwidth appearing in Figs. 5-21 and 5-22 versus realistic bandwidths is largely due to the defocusing coming from the gradient of the dry air refractivity, which was omitted in these early figures. In a background medium that is defocusing, the impact parameter spread between multipath rays is greatly compressed. We present now a simple expression that accounts for the defocusing, and from which the qualitative aspects of the interference fringes from a Gaussian model with dry air added can be inferred.

From Bouguer's law given in Eq. (5.6-5), we have

$$\left.\begin{aligned} \theta_{\mathrm{L}} - \theta_o &= \sin^{-1}\left(\frac{\rho_*}{\rho_{\mathrm{L}}}\right) - \sin^{-1}\left(\frac{\rho_o}{\rho_{\mathrm{L}}}\right) - 2\left(\tilde{\alpha}(\rho_*,\rho_*) - \tilde{\alpha}(\rho_o,\rho_o)\right) \\ &\doteq D_{\rho_o}^{-1}(\rho_* - \rho_o) - 2\left(\tilde{\alpha}(\rho_*,\rho_*) - \tilde{\alpha}(\rho_o,\rho_o)\right) \\ D_{\rho_o} &= \rho_{\mathrm{L}} \cos\left(\theta_o + 2\tilde{\alpha}(\rho_o,\rho_o)\right) \end{aligned}\right\} \qquad (5.12\text{-}17)$$

It follows that the shape of the θ_{L} versus ρ_* curve, such as that shown in Fig. 5-20, is essentially determined by the shape of $\tilde{\alpha}(\rho_*,\rho_*)$.

Suppose that $\tilde{\alpha}(\rho_*,\rho_*)$ is composed of two parts. The first part is from a refractivity gradient for a local medium arising from, for example, a localized water vapor layer. The second part is from a smooth background refractivity gradient arising from, for example, dry air. We write $\tilde{\alpha} = \tilde{\alpha}_{\mathrm{W}} + \tilde{\alpha}_{\mathrm{A}}$.[14] We expect that the rapid variations and the caustic points in $\theta_{\mathrm{L}}(\rho_*)$ come from rapid variations in $\tilde{\alpha}_{\mathrm{W}}$. On the other hand, $\tilde{\alpha}_{\mathrm{A}}$ is relatively slowly varying, with a monotonic negative gradient. Therefore, over a sufficiently narrow range of impact parameter values, the linear expression $\tilde{\alpha}_{\mathrm{A}} \doteq \tilde{\alpha}_{\mathrm{A}o} + \tilde{\alpha}'_{\mathrm{A}}(\rho_* - \rho_o)$ will suffice. Because of the non-linearity in $\tilde{\alpha}_{\mathrm{W}}$ versus ρ_*, we have to keep the full expression. In Eq. (5.12-17), we substitute $\tilde{\alpha}_{\mathrm{W}} + \tilde{\alpha}_{\mathrm{A}}$ for $\tilde{\alpha}$, and we hold θ_{L} fixed while varying ρ_*. This gives us an expression for the breadth $\Delta\rho_*$, or the altitude difference at any given epoch between impact parameter values associated with any two competing rays arriving at the LEO. Upon expanding Eq. (5.12-17) through first degree in $\Delta\rho_*$, we have

$$\Delta\rho_*\big|_{\Delta\theta_{\mathrm{L}}=0} = \rho_{*2} - \rho_{*1} = \frac{2D_{\rho_o}\left(\tilde{\alpha}_{\mathrm{W}2} - \tilde{\alpha}_{\mathrm{W}1}\right)}{1 - 2D_{\rho_o}\tilde{\alpha}'_{\mathrm{A}}} \tag{5.12-18}$$

Here $\tilde{\alpha}_{\mathrm{W}2} - \tilde{\alpha}_{\mathrm{W}1}$ is the difference in one-way bending angles resulting from the local intrusive medium at a given orbit angle θ_{L} between multipath rays no. 1 and no. 2. At sea level, the defocusing factor from dry air is $\zeta_{\mathrm{A}}^{-1} = 1 - 2D_{\rho_o}\tilde{\alpha}'_{\mathrm{A}} \approx 10$. It follows that, given the change in bending angle $(\tilde{\alpha}_{\mathrm{W}2} - \tilde{\alpha}_{\mathrm{W}1})$, $\Delta\rho_*$ and, therefore, from Eq. (5.12-4) the multipath Doppler spread $\Delta(d\Psi_* / dt)/2\pi$ will be reduced by about a factor of ten relative to the spread that would be realized without the background refractivity.

5.12.6 Combined Water Vapor and Dry Air Refractivity Model

Figure 5-25 shows $dG^\dagger(\nu)/d\nu$ (or in a geometric optics context, $\tilde{\alpha}(\nu)$) where Cases A and B for the refractivity profile have been combined into the form

$$n - 1 = N_o \exp\left(\frac{\rho_o - \rho}{H}\right) + N_w \exp\left(-\frac{(\rho - \rho_w)^2}{2H_w^2}\right) \tag{5.12-19}$$

The curves for $dG^\dagger / d\nu$ are for different altitudes of the center of the Gaussian distribution near ρ_o; the center is given by ρ_w. Here $N_w = 0.2N_o$ and

---

[14] Strictly speaking, we should write $\tilde{\alpha}_{\mathrm{W}} = \tilde{\alpha}_{\mathrm{W+A}} - \tilde{\alpha}_{\mathrm{A}}$. In other words, expressing $\tilde{\alpha}_{\mathrm{W}}$ and $\tilde{\alpha}_{\mathrm{A}}$ as separate integrals in Eq. (5.6-5) is not strictly legitimate because of their non-linear dependence on refractivity. Two rays with the same impact parameter value, one in a medium of W+A and one in a medium of W only, follow different paths. However, for a thin atmosphere, Eq. (5.12-18) is fairly accurate.

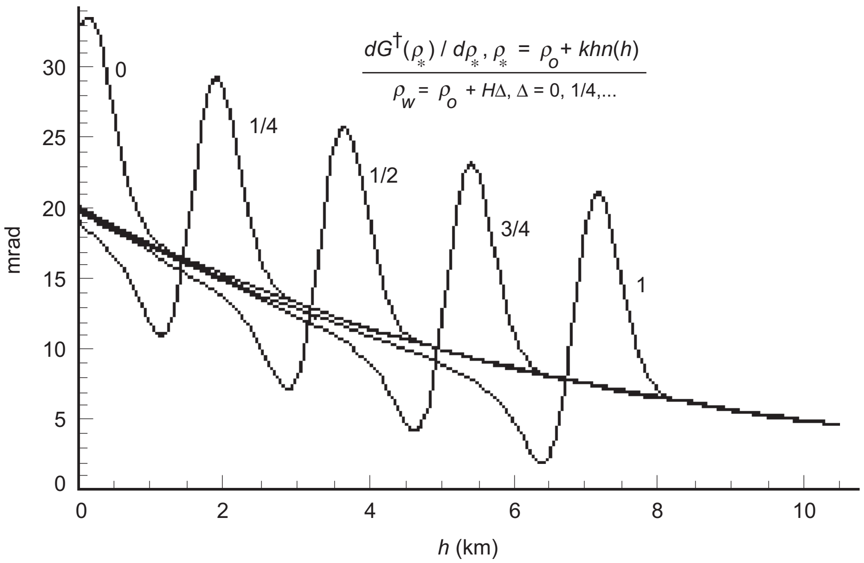

Fig. 5-25. Bending angle by a refractivity profile from dry air plus a narrow Gaussian marine layer that is located at different altitudes above sea level.

$H_w = 0.05H$. The values chosen for the dry air component are $H = 7k$, $N_o = 270\times10^{-6}$, and $\rho_o = 6378(1+N_o)k$. These yield a refractivity profile at sea level that closely matches the dry air profile for a standard atmosphere. This dry air profile yields a two-sided bending angle at sea level of 20.4 mrad. A marine layer with substantial water vapor that is several hundred meters thick could have a refractivity profile similar to the Gaussian one used in this example. The value used for N_w in this example could correspond to a peak water vapor number density of about 1 percent of the local density of dry air. This composite moist refractivity profile yields a narrow (~1-km) transient with a peak $|n'\rho|$ value of 0.8. This bending-angle profile also results in two caustics.

Figure 5-26 is an impact parameter diagram showing the relationship between impact parameter ρ_* and the LEO orbit angle θ_{L}. This curve results from the combined exponential distribution for dry air plus the Gaussian distribution located in the lower troposphere, given in Eq. (5.12-19). Here $k^{-1}\rho_w = 1.75\,\mathrm{km}$ and ρ_o is the impact parameter of a ray with a tangency point at sea level. Also, $\theta_{\mathrm{L}o} = \sin^{-1}(\rho_o/\rho_{\mathrm{L}}) - 2\tilde{\alpha}(\rho_o,\rho_o)$, which is the orbit angle of the LEO at the refracted shadow boundary. For a setting occultation, θ_{L} decreases with time at a rate of roughly 1 mrad/s. This figure shows the extensive range ($\Delta\theta_{\mathrm{L}} \sim 20\,\mathrm{mrad}$, or about 1400 km of LEO orbital motion) or duration (~20 s) of multipath at the LEO compared to the half-width H_w

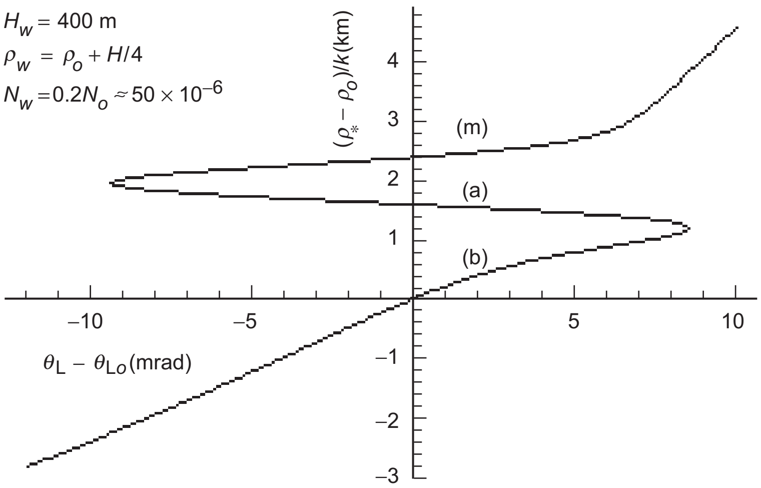

Fig. 5-26. Impact parameter diagram with defocusing. The LEO orbit radius is $\rho_L = 1.1\rho_o$. This figure shows ρ_* versus θ_L in the multipath zone from a narrow Gaussian refractivity profile from a marine layer, plus a more slowly varying dry air exponential distribution with $N_0 = 260 \times 10^{-6}$, $hk^{-1} = 7$ km.

(350 m) of the layer. Scintillation in amplitude and phase at the LEO first occurs at ray path tangency altitudes that are about 3 km above the altitude of the layer itself or about 10 s earlier.

Whereas Figs. 5-19 through 5-23 use a solitary Gaussian refractivity distribution and include no defocusing effects from dry air, Fig. 5-26 includes defocusing effects arising from the background refractivity due to dry air, which manifests itself in the much narrower impact parameter separations for the multiple rays. This defocused scenario produces maximum high-frequency fringes of around 15 Hz, much closer to a realistic case. Over most of the multipath zone, the bandwidth of the interference spectrum is less than 10 Hz for that example. Defocusing from the dry air refractivity profile compresses the bandwidth of the interference spectrum, but defocusing does not compress the duration of the multipath episode. In Appendix E, it is shown that the scale for $\left(\tilde{\alpha}_{\mathrm{W}2} - \tilde{\alpha}_{\mathrm{W}1}\right)$ for any two competing rays within the multipath zone depends nearly linearly on H_{W}, the $1-\sigma$ width of the Gaussian distribution, and it depends only weakly on the peak refractivity value N_{W}. The width of the multipath zone in orbit angle or in elapsed time—for example, the difference in θ_{L} between the upper and lower caustic points—depends on $H_{\mathrm{W}}^{-3/2}$; it depends linearly on N_{W}. As we already have noted in Eq. (5.12-18), the fringe frequency scales, fast and slow, are compressed by defocusing from the slowly varying negative refractivity gradient from the background medium, dry air in this case. This compression ratio from dry air near sea level is about ten to one.

The excess Doppler difference between rays is $\dot{\theta}_{\mathrm{L}}\Delta\rho_* / 2\pi \approx 5\Delta r_*$ Hz, where the difference in tangency points between rays, Δr_*, is in kilometers. Therefore, the fast fringe frequency between the main ray (m) and the nascent rays (a) and (b) shown in Fig. 5-26 is about 15 Hz at the midpoint in the multipath zone. This may be compared to the fast fringe frequency range of 80 to 180 Hz in Fig. 5-20, which does not include any defocusing from an ambient medium. A simple rule of thumb to convert an impact parameter diagram from ρ_* versus θ_{L} into a Doppler spread versus elapsed time is as follows: Multiply the ordinate in kilometers by the factor $5\dot{\theta}_{\mathrm{L}}$ to obtain hertz, and divide the abscissa in milliradians by $\dot{\theta}_{\mathrm{L}}$ to obtain seconds. Here $\dot{\theta}_{\mathrm{L}}$ is the rate of change of the subtending angle between the emitting GPS satellite and the LEO in the plane of propagation, typically $0.6 \text{ to } 1.0$ mrad/s, mostly depending on an obliquity factor between the LEO orbit and propagation planes.

Figure 5-27 shows the signal amplitude $|\boldsymbol{E}(r_{\mathrm{L}},\theta_{\mathrm{L}})|$ at the LEO versus orbit angle $\theta_{\mathrm{L}} - \theta_{\mathrm{L}o}$ during entry into the multipath zone for the same refractivity and orbit model used in Fig. 5-26. Knife-edge diffraction effects from the Earth's limb are ignored in these figures. This figure was obtained from a numerical integration of the spectral integral in Eq. (5.9-10). Above $\theta_{\mathrm{L}} - \theta_{\mathrm{L}o} \approx 8.5$, the main ray (m) provides the principal contribution to $\boldsymbol{E}(r_{\mathrm{L}},\theta_{\mathrm{L}})$, without interference from the (a) and (b) rays. For the $\theta_{\mathrm{L}} - \theta_{\mathrm{L}o}$ range shown here, the main ray impact parameter is located 2 to 4 km above sea level. Because of defocusing from the dry air refractivity gradient there, the amplitude of the (m) ray

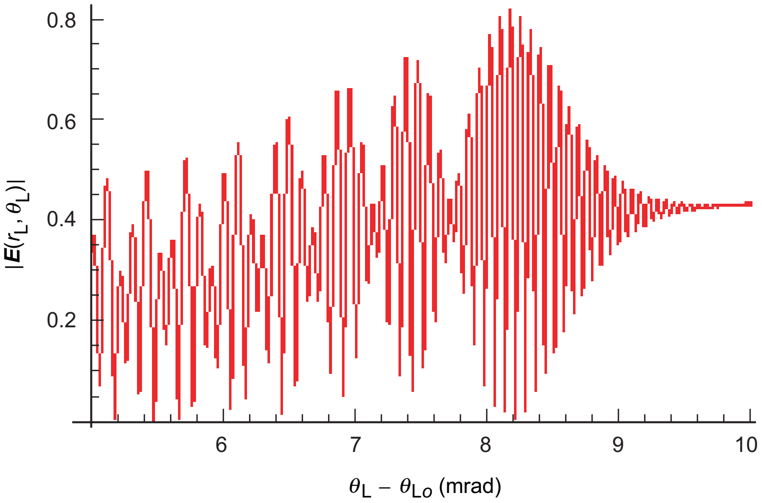

Fig. 5-27. Amplitude of the field at the LEO versus orbit angle near entry into the multipath zone for the defocused case using the same refractivity and orbit models used in Fig. 5-26. The equivalent elapsed time shown in this figure is about 5 s.

has been reduced to about 0.4 from its vacuum value of unity. The contact with the caustic surface where $d\theta_{\mathrm{L}} / d\rho_* = 0$ occurs at $\theta_{\mathrm{L}} - \theta_{\mathrm{L}o} \approx 8.54$, but the actual maximum flaring from wave theory occurs at $\theta_{\mathrm{L}} - \theta_{\mathrm{L}o} \approx 8.17$. Geometric optics predicts infinite amplitude at the caustic contact point, but the actual value for the field contribution from the nascent rays (a) and (b) is 0.407. We have already noted that these differences between geometric optics and wave theory predictions can be reconciled using third-order stationary phase theory. The fast fringe frequency near maximum flaring is about 13 Hz, which is due to the 2.6-km separation between the impact parameter of the (a) and (b) rays at their nascence and the impact parameter of the (m) ray. This rate reduces to a minimum of about 10 Hz near $\theta_{\mathrm{L}} - \theta_{\mathrm{L}o} = 4$. The slow modulation of the envelope, initially at roughly 1 Hz, is due to interference between the (a) and (b) rays. The node at $\theta_{\mathrm{L}} - \theta_{\mathrm{L}o} = 7.8$ marks the first occasion where the (a) and (b) rays are π radians out of phase since their nascence. As the impact parameter separation distance between the (b) ray and the other two increases, the fast frequency gradually increases to a maximum of about 20 Hz near the lower caustic contact at $\theta_{\mathrm{L}} - \theta_{\mathrm{L}o} = -9.4$.

An additional consequence follows from Figs. 5-26 and 5-27. Multipath from a relatively narrow refracting feature low down in the atmosphere, given a sufficient gradient, can be felt by the LEO for nominal ray path tangency points far above (this height difference scales roughly as $H_{\mathrm{w}}^{-3/2}$). For a setting occultation, flaring of the observed signal at some otherwise benign point is a harbinger of things to come. We will return to this case later in connection with the effect of an embedded reflecting surface on the electric field at the LEO.

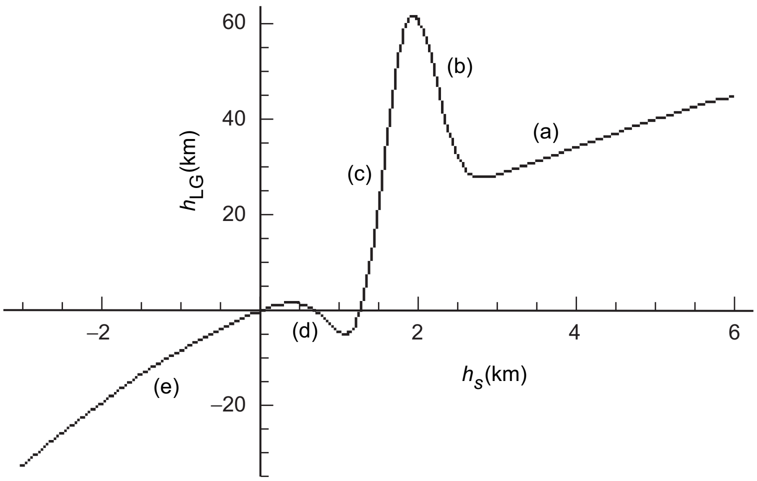

Fig. 5-28. Impact parameter diagram in the thin phase screen for the same refractivity profile used in Fig. 5-26, except that $N_w = -0.2N_o$.

Finally, Fig. 5-28 shows in the thin phase screen the impact parameter altitude h_S versus h_{LG} using the same Gaussian-plus-dry-air refractivity profile used in Fig. 5-26, except that $N_w = -0.2N_o$, an unlikely scenario in the lower troposphere. We have discussed the thin screen phase model in Section 5.10. This refractivity profile results in four caustics, five separate ray systems, and also a quasi-shadow zone around $h_S = 1.5\,\mathrm{km}$ as a result of local defocusing there. Figure 5-29 shows the amplitude of the field at the LEO that results from the refractivity profile used to produce Fig. 5-28. Multiplying the abscissa by 3 gives the altitude h_{LG} in Fig. 5-28. The steep gradient in h_S versus h_{LG} in the thin screen, or equivalently in the θ_L versus ρ_* curve, results in the shadow zone. These rays in this example don't concurrently interfere with each other as quintuplets, but only as triplets. But, it would be easy enough to adjust the local refractivity gradient so that the lower caustic point at the nascence of the (d) and (e) rays in Fig. 5-28, for example, is raised to an altitude in h_{LG} that is higher than the caustic point at the nascence of the (b) and (c) rays. This would create a quintuplet multipath episode.

5.13 Spectral Coefficients in a Spherical Refracting Medium with an Embedded Discontinuity

The case where the refractivity is discontinuous at $r = r_o$ in a large, homogeneous, spherical symmetric medium was discussed in Chapter 3. Mie scattering [1,2] forms the basis of that discussion. It employed the stationary

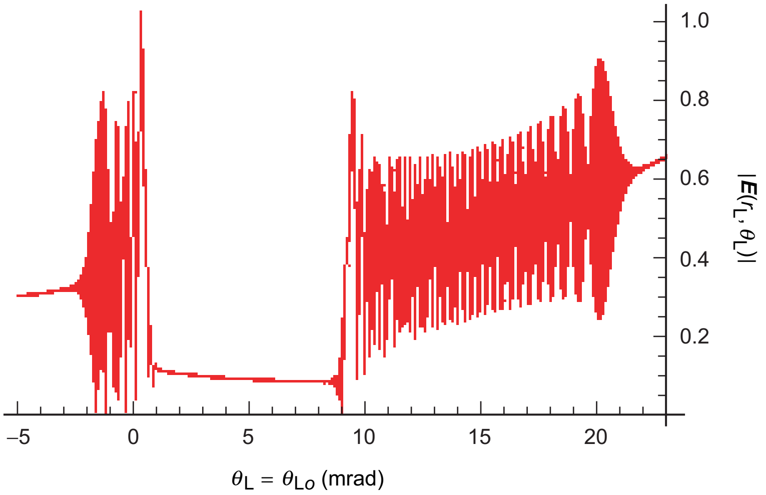

Fig. 5-29. Amplitude of the field at the LEO for the refractivity and orbit model used in Fig.5-28. Double reversal in the polarity of the bending-angle gradient causes four caustics and two multipath zones.

phase technique for interpretation and to aid the numerical evaluation of the scattering integrals. All of the scattering equations carry over to the case of a scattering sphere in a spherical symmetric stratified medium if we replace the spectral coefficients for an incident planar wave in those equations in Chapter 3, $i^{l-1}(2l+1)/(l(l+1))$, by the spectral coefficients $a_l^-(\rho)$ for an incoming wave. From Eq. (5.5-21), these spectral coefficients are given by

$$a_l^-(\rho) = i^{l-1}\frac{2l+1}{l(l+1)}\exp\left(-iG[\rho,\nu]\right) \tag{5.13-1}$$

These coefficients are applicable to an initially planar wave that has been subsequently refracted and retarded by the overlying spherical stratified medium before striking the scattering surface.

Let us now consider the spectral coefficients for the outgoing wave, $a_l^+(\rho)$. From Eq. (5.8-24), we have

$$a_l^+(\rho) = i^{l-1}\frac{2l+1}{l(l+1)}\exp\left(-i\left(2G\left[\rho^\dagger(\nu),\nu\right]-G[\rho,\nu]\right)\right) \tag{5.13-2}$$

Here the actual functional form of $a_l^+(\rho)$ will depend in part on the physical properties assumed for the refracting and perhaps scattering atmosphere, and also in part on the impact parameter(s) associated with the ray(s). Suppose that the scattering surface is located at $r = r_o$. For $\rho^\dagger > \rho_o$, these coefficients in Eq. (5.13-2) are still applicable. What happens when $\rho^\dagger \le \rho_o$? That depends on the medium lying below.

5.13.1 A Medium with a Discontinuity in its Refractive Gradient

We consider a spherical shell with $n(\rho)$ variable for $\rho \ge \rho_o$ and with $dn/d\rho \equiv 0$ for $\rho < \rho_o$. For this case Eqs. (5.5-18) and (5.5-22) show that both a_l^- and a_l^+ are constant with ρ when $\rho < \rho_o$. They also must be equal there to avoid the Hankel function singularity at the origin. Recall that the definition of the spherical Bessel function of the first kind is $\psi_l = \left(\xi_l^+ + \xi_l^-\right)/2$, which is well-behaved at the origin. It follows in this case that $a_l^+(\rho_o) = a_l^-(\rho_o)$. This also follows from the defining integral for $G[\rho,\nu]$ given in Eq. (5.5-20), or by its Airy function form given in Eq. (5.7-2), which we use here. Thus, $G\left[\rho^\dagger,\nu\right] = G[\rho_o,\nu]$, $\rho^\dagger \le \rho_o$. It follows that the spectral coefficients for the incoming wave are given by

$$a_l^-(\rho) = \begin{cases} i^{l-1}\dfrac{2l+1}{l(l+1)}\exp\left(-iG[\rho,\nu]\right), & \rho \ge \rho_o \\ i^{l-1}\dfrac{2l+1}{l(l+1)}\exp\left(-iG[\rho_o,\nu]\right), & \rho \le \rho_o \end{cases} \tag{5.13-3a}$$

At the LEO, $G[\rho_L,\nu]\equiv 0$, and the spectral coefficients for the outgoing wave are given by

$$a_l^+(\rho_\mathrm{L}) = \begin{cases} i^{l-1}\dfrac{2l+1}{l(l+1)}\exp\left(-i2G\left[\rho^\dagger,\nu\right]\right), & \rho^\dagger \ge \rho_o \\ i^{l-1}\dfrac{2l+1}{l(l+1)}\exp\left(-i2G[\rho_o,\nu]\right), & \rho^\dagger \le \rho_o \end{cases} \tag{5.13-3b}$$

For a given value of $\nu = l+1/2$ such that $\rho^\dagger(\nu)\le\rho_o$, $-2G[\rho_o,\nu]$ is the total phase delay incurred by the lth spectral coefficient of an initially plane wave as a result of that wave passing completely through an intervening refracting shell with an inner boundary at $r = r_o$. When the stationary phase technique is applied to the spectral integrals, it yields a stationary phase value for ν that corresponds in geometric optics to a ray with an impact parameter $\rho_* \doteq \nu^* \le \rho_o$.

The total field at the LEO consists of both the incoming and outgoing radial components, as given by Eq. (5.13-3a) for $\rho = \rho_\mathrm{L}$ and Eq. (5.13-3b), respectively. But, we have already seen from our discussion in Section 5.9 of the stationary phase technique that, at the LEO, for an occultation, only the outgoing components contribute to the scattering integrals given in Eq. (5.9-5). Because the LEO is so far away from a turning point, only the outgoing components yield stationary phase neighborhoods in spectral number. So, we can ignore the incoming components at the LEO for an occultation geometry.

We also note the relative ease with which this spectral technique using osculating parameters can deal with a discontinuity in the gradient of the refractivity at $r = r_o$. Such a discontinuity might correspond to a discontinuity in scale height of the atmosphere, for example, at the boundary of a marine layer, or in the lapse rate of the troposphere, for example, at the tropopause. From Eq. (5.5-20), it follows that $G[\rho,\nu]$ is continuous with ρ, even though n' is discontinuous at $r = r_o$. Also, $dG\left[\rho^\dagger(\nu),\nu\right]/d\nu$ is continuous. It follows that, using the stationary phase technique to evaluate the field from the integrals in Eq. (5.9-5), the same stationary phase point in spectral number is obtained as that obtained from the ambient medium without the discontinuity in n'. We know that, for a given the position $\left(r_\mathrm{L},\theta_\mathrm{L}\right)$ of the LEO, the stationary phase point ν^* is near the impact parameter ρ_*. But the second derivative

$d^2G[\rho^\dagger,\nu]/d\nu^2$ is discontinuous at $\nu^* = \rho_o$. This means that, when using the stationary phase technique, it is necessary to break the integral for the field over spectral number into two parts: one part for $\nu > \rho_o - \hat{y}^\dagger K_{\rho_o}$, and a second part for $\nu < \rho_o - \hat{y}^\dagger K_{\rho_o}$. When the impact parameter is close to ρ_o, these two parts when summed interfere in phase, resulting in fringes in the amplitude and phase of the field.

We choose the simple model in Eq. (5.13-4) with which to compare wave theory scattering results with Fresnel diffraction from a thin-screen model. Here we assume that $n' \equiv 0$ for $r < r_o$. For $r \ge r_o$, we assume that $n = n(\rho)$, which is arbitrary other than satisfying the thin-atmosphere conditions. As a specific example, we assume that n follows an exponential law for $r > r_o$ and is a constant for $r < r_o$; thus,

$$\left.\begin{aligned} n^+ &= 1 + N_o \exp\left(-\frac{\rho-\rho_o}{H}\right), \ \rho \ge \rho_o \\ n^- &= 1 + N_o, \ \rho \le \rho_o \end{aligned}\right\} \tag{5.13-4}$$

Figure 5-30 shows the $2dG^\pm/d\nu$ curves from Eq. (5.7-7) and certain δ curves from Eq. (5.12-1) for this particular refraction profile. From Eq. (5.7-7), it follows that $dG^\pm/d\nu$ is defined by

$$\left.\begin{aligned} &\frac{dG^+}{d\nu} = -\pi K_{\rho^\dagger}\int_{\rho^\dagger}^{\infty}\frac{d\log n}{d\rho}\left(\mathrm{Ai}[\hat{y}]^2 + \mathrm{Bi}[\hat{y}]^2\right)d\rho, \ \rho^\dagger \ge \rho_o \\ &\frac{dG^-}{d\nu} = -\pi K_{\rho_o}\int_{\rho_o}^{\infty}\frac{d\log n}{d\rho}\left(\mathrm{Ai}[\hat{y}]^2 + \mathrm{Bi}[\hat{y}]^2\right)d\rho, \ \rho^\dagger \le \rho_o \\ &\frac{dG^+}{d\nu} = \frac{dG[\rho^\dagger(\nu),\nu]}{d\nu}, \ \frac{dG^-}{d\nu} = \frac{\partial G[\rho_o,\nu]}{\partial\nu}, \ \hat{y} \doteq K_\rho^{-1}(\nu-\rho) \end{aligned}\right\} \tag{5.13-5}$$

When $\nu^* - \rho_o < -\sim 2K_{\rho_o}$, we may replace the Airy functions in these integral expressions for $2dG^-/d\nu$ with their respective asymptotic forms. From Eq. (5.7-8), we obtain

$$\frac{dG^-}{d\nu} \doteq -\nu\int_{\rho_o}^{\infty}\frac{d\log n}{d\rho}\frac{d\rho}{\sqrt{\rho^2-\nu^2}} = \tilde{\alpha}(\rho_o,\nu), \ \rho^\dagger \le \rho_o - K_{\rho^\dagger}\hat{y}^\dagger \tag{5.13-6}$$

Using the refractivity profile given in Eq. (5.13-4), an explicit form $\tilde{\alpha}(\rho_o,\nu)$ is given in Eq. (5.8-3). Here $\tilde{\alpha}(\rho_o,\nu)$ is the cumulative bending on a ray at

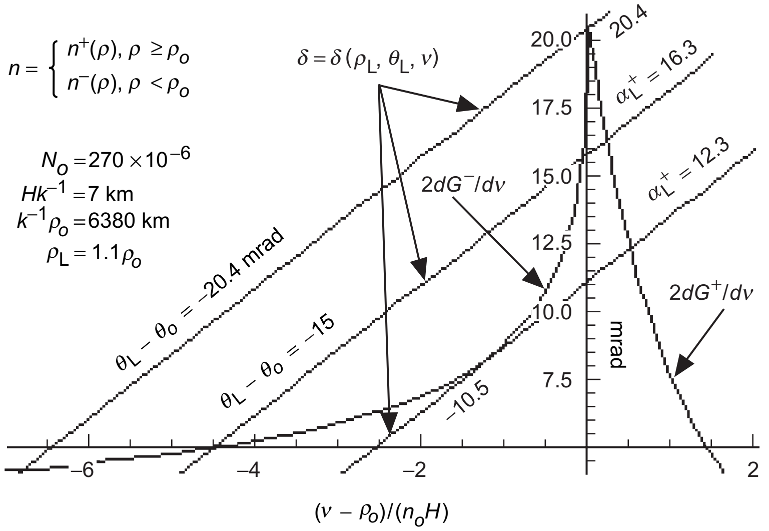

Fig. 5-30. Stationary phase curves for a spherical shell with a discontinuity in *dn/dρ* **at** r_o **per Eq. (5.13-4). Stationary phase points occur at the intersections of the** δ **and** $2dG^{\pm}/d\nu$ **curves.**

$\rho = \rho_o$ with an impact parameter value of $\nu \le \rho_o$. It corresponds to $\alpha^-(\nu)/2$ given in Section 2.3, Eq. (2.3-10). As was discussed in Section 5.7, the small difference between $dG^-/d\nu$ and $\tilde{\alpha}(\rho_o,\nu)$ shows up only in the immediate vicinity of a turning point.

We may write the integral form as $dG^{\pm}/d\nu$

$$2\frac{dG^+}{d\nu} \doteq -2\nu\int_{\nu}^{\infty}\frac{d\log n}{d\rho}\frac{d\rho}{\sqrt{\rho^2-\nu^2}} = 2\tilde{\alpha}(\nu,\nu), \quad \rho^{\dagger} > \rho_o \qquad (5.13\text{-}7)$$

Here $2\tilde{\alpha}(\nu,\nu) = \alpha_{\mathrm{L}}^{+}(\nu)$ corresponds to $\alpha^{+}(\nu)$ in Eq. (2.3-11), the bending angle for a transecting ray through the upper medium with a value ν for its impact parameter such that $\nu \ge \rho_o$. This ray completely transects the atmosphere unperturbed by the discontinuity lying below.

The δ curves in Fig. 5-30 are obtained from Eq. (5.12-1), and they depend uniquely on the LEO angular position θ_{L} as a parameter when the orbital radius r_{L} is fixed. From Bouguer's law in Eq. (5.6-5), this dependence may be recast in terms of bending angle, except that in this example bending angle is not unique over a certain range of angular positions. For that reason, we have chosen $\alpha_{\mathrm{L}}^{+}(\rho_*)$, the bending angle in the upper regime, as the parameter. It is unique. By expanding Eq. (5.12-1) in powers of $(\nu - \rho_*)$, and upon noting that

$\partial\theta_\nu / \partial\nu = D_\nu^{-1}$, it follows that over a sufficiently narrow range of spectral numbers $\delta \doteq \alpha_{\mathrm{L}}^{+}(\rho_*^{+}) + (\nu - \rho_*^{+}) / D_{\rho_*}$. The point of first contact with the caustic surface is located at the point of tangency of the $2dG^{-} / d\nu$ curve with the δ curve for $\alpha_{\mathrm{L}}^{+} = 12.3\,\mathrm{mrad}$, or for $\theta_{\mathrm{L}} - \theta_o = -10.5$ mrad for this example. For LEO angular positions from this value down to $\theta_{\mathrm{L}} = \theta_o - 20.4$, there are three stationary phase points in spectral number and, therefore, three bending angles. For orbital angles outside of $-20.4 \le \theta_{\mathrm{L}} - \theta_o \le -10.5\,\mathrm{mrad}$, i.e., for δ curves above the uppermost curve or below the lowest one in Fig. 5-30, there is just one intersection point, or one stationary phase point and only one value for the bending angle. The LEO-observed phase and amplitude in this region between the caustic contact point and the cusp in bending angles are marked by strong multipath interference effects and by diffraction in the transition regions. In a wave theory context, fringes in the observed amplitude and phase result from interference among the spectral components for spectral numbers in the immediate neighborhood of ρ_o when the impact parameter is nearby. In geometric optics, these fringes come from interference among multiple rays.

At the point of tangency of the δ curve with the $2dG^{-} / d\nu$ curve, the condition $2d^2G^{-} / d\nu^2 = \partial\delta / \partial\nu$ must hold. The geometric optics equivalent is $d\alpha_{\mathrm{L}}^{-} / d\nu = \partial\delta / \partial\nu = D_\nu^{-1}$, which is equivalent to the condition that the defocusing factor ζ must be infinite. This wave theory tangency condition in Fig. 5-30 is equivalent to the geometric optics condition on the impact parameter (for a circular LEO orbit) $d\rho_* / d\theta_{\mathrm{L}} \to \infty$, which is shown in Fig. 5-31. At this tangency point, flaring in the observed signal will be evident,

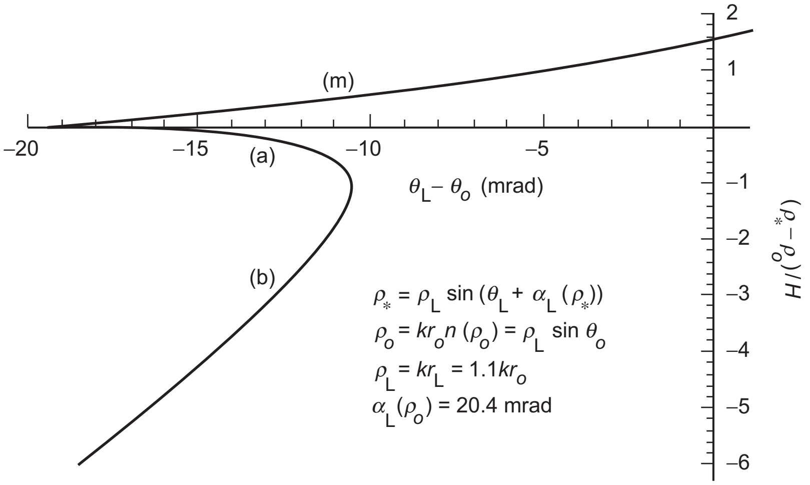

Fig. 5-31. Impact parameter diagram for the refracting shell described in Fig. 5-30. Boundary encountered at $\theta_{\mathrm{L}} - \theta_o = -20.4$.

although the actual maximum in flaring occurs at a point slightly offset from the tangency point. This offset has been discussed in Section 5.12 using third-order stationary phase theory.

Figure 5-32 shows the amplitude of the field at the LEO in the vicinity of the first contact with the caustic ($\theta_{\mathrm{L}} - \theta_o = -10.5\ \mathrm{mrad}$) using the same conditions used in Fig. 5-30. The flaring is quite prominent in this example. Figures 5-32 through 5-34 were obtained from a numerical integration of the spectral integrals in Eq. (5.9-24) aided by the stationary phase technique to isolate the contributing stationary phase neighborhoods in spectral number. At $\theta_{\mathrm{L}} - \theta_o = -10.5\ \mathrm{mrad}$, a pair of powerful rays, (a) and (b) in Fig. 5-31, are created. In this example, their individual amplitudes are roughly six times the amplitude of the original (m) ray at this orbital position. Therefore, their contributions to the field at the LEO largely overwhelm the contribution from the (m) ray by an order of magnitude. Third-order stationary phase theory is needed at the caustic point in Fig. 5-32 to accurately predict the amplitude and location of the peak. Second-order geometric optics predicts an infinite amplitude at the caustic point, whereas Fig. 5-32 shows that wave theory yields a peak amplitude of about 5.3. In Section 5.12, it is shown that the peak amplitude associated with a caustic is proportional to $(d^2\theta_{\mathrm{L}} / d\rho_*^2)^{-1/3}$, evaluated near the caustic contact point where $d\theta_{\mathrm{L}} / d\rho_* = 0$. This curvature term is readily obtained from Bouguer's law in Eq. (5.12-5) and the bending profile, which is given in Eq. (5.6-5) in terms of the refractivity profile. Equation (5.12-13) provides a ratio for the amplitudes of the nascent rays compared with the amplitude of the main ray, expressed in terms of the first

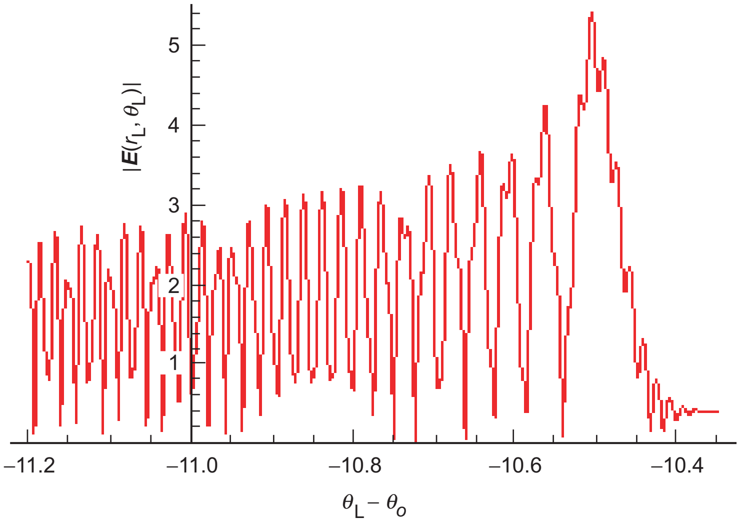

Fig. 5-32. Amplitude of the field at the LEO near the caustic contact using the same refractivity and orbit models used in Fig. 5-30.

and second derivatives of the curve, θ_{L} versus ρ_* as shown in Fig. 5-31. For the specific exponential shell model in Eq. (5.13-4), which we are using in this section, Eq. (5.12-13) yields a flaring from the nascent rays alone that is 12.3 times the amplitude of the (m) ray. This yields a maximum amplitude of 5.3 from all three rays combined, very close to the actual peak amplitude shown in Fig. 5-32 near the caustic contact. The amplitude of the main ray (m) is normalized to unity outside the medium, but defocusing at $\theta_{\mathrm{L}} - \theta_o = -10.5$ mrad has reduced it to 0.4.

These new rays (a) and (b) begin to mutually interfere with each other, as is evidenced by the onset of fringes for $\theta_{\mathrm{L}} - \theta_o \le -10.5$ mrad. As discussed in Section 5.12, Eq. (5.12-4), the frequency of these fringes can be obtained by multiplying the difference in impact parameter values in kilometers by $5\dot{\theta}_{\mathrm{L}}$. At $\theta_{\mathrm{L}} = \theta_o - 10.6$ mrad for rays (a) and (b), that frequency already has grown to about 40 Hz (with $\dot{\theta}_{\mathrm{L}} = -1$ mrad/s). Figure 5-31 shows that the impact parameter values for the (a) and (b) rays promptly separate with decreasing θ_{L}, and their defocusing factors begin to steeply decrease from initially infinite values. This rapid separation in impact parameter values leads to a rapidly increasing fringe frequency with decreasing θ_{L}. This interference initially results principally from the mutual interference between the (a) and (b) rays with a smaller modulation from the weaker (m) ray. Later, as shown in Fig. 5-33, as the (a) ray becomes defocused, the high-frequency interference is between the (b) and (m) rays with a weaker modulation of much lower frequency from interference between the (m) and (a) rays.

Figure 5-33 shows the amplitude of the field near the end of the interference zone. Here the (m) and (b) rays are well separated and the anomalous ray (a) has become a minor contributor because of its defocusing (see Fig. 5-31). The impact parameter differences read from Fig. 5-31 at the end of the interference zone predict very high fringe frequencies here. At $\theta_{\mathrm{L}} - \theta_o = -19$, the frequency of the high-frequency fringes between the (m) and (b) rays is about 250 cycles/mrad. The low-frequency modulation in Fig. 5-33 comes from interference between the (m) and (a) rays, which have narrowly different impact parameter values in this figure. Here $d(\Psi_{*\mathrm{a}} - \Psi_{*\mathrm{m}})/d\theta_{\mathrm{L}}$ is about 5 cycles/mrad at $\theta_{\mathrm{L}} - \theta_o = -17$, about 2 cycles/mrad at $\theta_{\mathrm{L}} - \theta_o = -19$, and zero at $\theta_{\mathrm{L}} - \theta_o = -20.4$, the end of the multipath zone.

As also was discussed in Section 5.12, the amplitude of the slow modulation in Fig. 5-33 can be obtained from the defocusing factor $\zeta^{-1} = 1 - D_{\rho_*} d\alpha_{\mathrm{L}} / d\rho_*$ for each ray. The modulation peaks and valleys are accurately predicted from the four combinations $\left| |\zeta_{\mathrm{a}}|^{1/2} \pm |\zeta_{\mathrm{b}}|^{1/2} \pm |\zeta_{\mathrm{m}}|^{1/2} \right|$. The slow modulation ($\Delta\theta_{\mathrm{L}} \sim 0.2$ mrad per cycle at $\theta_{\mathrm{L}} - \theta_o = -17$) results from interference between the narrowly separated (m) and (a) rays. The (a) ray

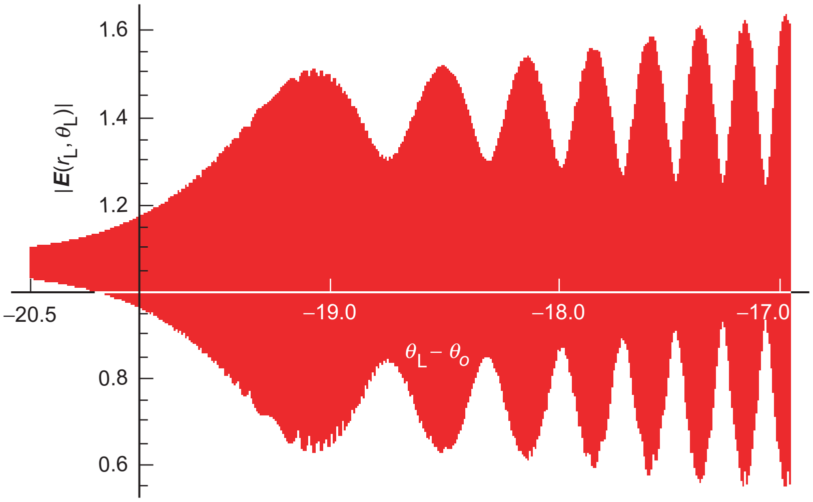

Fig. 5-33. Continuation of Fig. 5-32 to the lower boundary of the interference zone at $\theta_L - \theta_o = -20.4$.

becomes very defocused with decreasing θ_L. At $\theta_L - \theta_o = -17$, the amplitude contributions from the three rays based on their defocusing factors have the ratios b:m:a ~1:1/3:1/5. At $\theta_L - \theta_o = -19$, these ratios are ~1:1/3:1/11. For $\theta_L - \theta_o < -20.4$, they are 1:0:0.

The mean amplitude of the field for the range of $\theta_L - \theta_o$ values shown in Fig. 5-33 is about 1.1. This is about a factor of three greater than the amplitude of the (m) ray here because of the lens-like property of the refracting shell given by Eq. (5.13-4).

Figure 5-34 shows a section of the de-trended phase of the complete field $\Delta\Phi^*_{\text{mba}}$ at the LEO, expressed in cycles for the range $-11.35 \le \theta_L - \theta_o \le -10.85$. It may be compared to the amplitude fringes shown in Fig. 5-32, which cover most of this region. This figure shows the bursts of rapid acceleration in phase that correspond to local neighborhoods where substantial destructive interference occurs, principally between the newly created (a) and (b) rays. These points correspond to the troughs in amplitude in Fig. 5-32. Phase changes of 1/2 cycle occur over a change in θ_L of less than $2\ \mu\text{rad}$, or less than 2 ms of elapsed time. For a more realistic refractivity model with multipath impact parameter separations that are 1/4 the size of those in Fig. 5-31, the elapsed time for a 1/2-cycle change from these brief bursts would be closer to 5 ms, which is still a significant operational problem for a closed-loop receiver.

Finally, Fig. 5-35 provides a much more benign scenario. It shows the amplitude of the field at the LEO from the spectral integral in Eq. (5.8-1b) for the case where the gradient of the refractivity has a discontinuity of the opposite

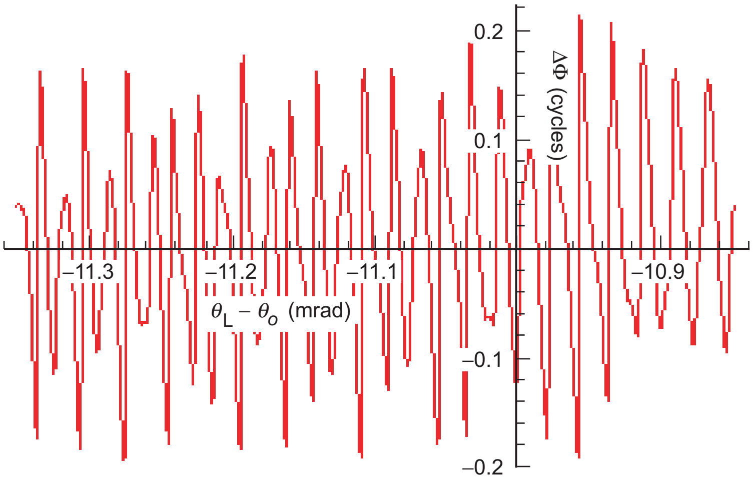

Fig. 5-34. De-trended phase at the LEO near onset of multipath. Figures 5-30 through 5-34 use the same refractivity and orbit models.

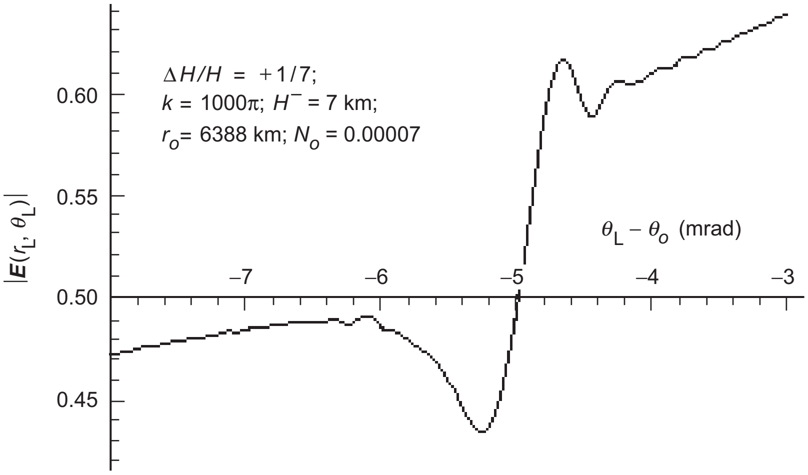

Fig. 5-35. Amplitude at the LEO from a discontinuity in scale height.

polarity to that used in Fig. 5-32 (and also significantly smaller). The index of refraction for this case is given by

$$\left.\begin{aligned} n^{+} &= 1 + N_o \exp[-(\rho - \rho_o)/H^{+}], \quad \rho > \rho_o \\ n^{-} &= 1 + N_o \exp[-(\rho - \rho_o)/H^{-}], \quad \rho \le \rho_o \end{aligned}\right\} \qquad (5.13\text{-}8)$$

Here $\Delta H = H^{+} - H^{-} > 0$. This profile results in a mild shadow zone in the neighborhood $-6 \le \theta_{\mathrm{L}} - \theta_{o} \le -5\,\mathrm{mrad}$ with minor diffraction effects. The bending-angle profile for this example is given in Section 2.3 by the Case B scenario, in particular Eq. (2.3-21). See also Section 2.4. In this case, ΔH is positive. When the tangency point of the ray descends through the surface of the discontinuity, the ray experiences an increased bending rate because of the increased gradient in refractivity in the lower layer. The amplitude profile closely follows the square root of the defocusing function except in the immediate vicinity of the shadow zone. One can compare Fig. 5-35 with Fig. 2-10 from the thin-screen/scalar diffraction approach. Figure 2-10 applies to a discontinuity in the lapse rate at the tropopause of $\Delta(dT/dr) = -7\,\mathrm{K/km}$, whereas Fig. 5-35 applies to a discontinuity in scale height of $\Delta H = +1\,\mathrm{km}$. There is a rough correspondence between these two quantities in terms of their perturbations on bending angle, which is given by $\Delta H / H \leftrightarrow -H\Delta(dT/dr)$. When this becomes an equality, the perturbations on the bending angle are about the same, and the resulting diffraction pattern is about the same. Here $\Delta H = +1\,\mathrm{km}$ is equivalent to a lapse rate discontinuity of 4 to 5 K/km.

5.13.2 A Transparent Sphere Embedded in a Refracting Medium

For a transparent sphere with a discontinuity in $n(\rho)$ at $\rho = \rho_o$ and $n' = 0$ inside, the spectral coefficients evaluated at the scattering sphere for the total scattering, including the scattering effects of multiple internal reflections, are obtained by modifying the discussion in Section 3.5, Eqs. (3.5-11) and (3.5-15b), to account for the phase delay $-G\left[\rho_o^{+}, \nu\right]$ in the incident wave induced by the refractivity gradient in the overlying medium. The term $b_l^{(0)}$ is called the zeroth-degree reflection coefficient because it applies only to an external reflection from the sphere; $b_l^{(j)}$ is the *j*th-degree reflection coefficient; it applies to a wave that has undergone $j-1$ internal reflections within the sphere. Thus, $j=1$ corresponds to a wave entering and exiting the sphere without undergoing any internal reflections, $j=2$ corresponds to a wave with one internal reflection, and so on. Summing these coefficients over degree yields the total or aggregate scattering coefficient S_l, which is given by

$$S_l = \sum_{j=0}^{\infty} b_l^{(j)} = -a_l^{-}\left(\rho_o^{+}\right)\left(\frac{\tilde{\mathcal{W}}_l + \mathcal{W}_l^{-}}{\mathcal{W}_l + \mathcal{W}_l^{+}}\right) \tag{5.13-9}$$

where $\tilde{\mathcal{W}}_l$ is the complex conjugate of $\mathcal{W}_l$. Here

$$a_l^-\left(\rho_o^+\right)=i^{l-1}\frac{2l+1}{l(l+1)}\exp\left(-iG\left[\rho_o^+,\nu\right]\right),\quad \rho_o^+=n_o^+u_o \tag{5.13-10}$$

and

$$\left.\begin{aligned}\mathcal{W}_l&=\xi_l^+\left(n_o^+u_o\right)\xi_l^{-\prime}\left(n_o^-u_o\right)-\left(n_o^--n_o^+\right)\xi_l^{+\prime}\left(n_o^+u_o\right)\xi_l^-\left(n_o^-u_o\right)\\ \mathcal{W}_l^\pm&=\xi_l^\pm\left(n_o^+u_o\right)\xi_l^{\pm\prime}\left(n_o^-u_o\right)-\left(n_o^--n_o^+\right)\xi_l^{\pm\prime}\left(n_o^+u_o\right)\xi_l^\pm\left(n_o^-u_o\right)\end{aligned}\right\} \tag{5.13-11}$$

Here n_o^+ is the index of refraction on the outer side of the boundary at $r=r_o$; n_o^- is the value on the inner side. For a transparent sphere, $n(\rho)$ is constant and real for $\rho<\rho_o$. Upon propagating the aggregate scattering coefficients upward through the refracting medium to the LEO, one obtains

$$S_l(\rho_{\mathrm{L}})=-i^{l-1}\frac{2l+1}{l(l+1)}\left(\frac{\tilde{\mathcal{W}}_l+\mathcal{W}_l^-}{\mathcal{W}_l+\mathcal{W}_l^+}\right)\exp\left(-i2G\left[\rho_o^+,\nu\right]\right) \tag{5.13-12}$$

Once again, we see that the scattering coefficients are phase delayed relative to their vacuum counterparts by an amount $-2G\left[\rho_o^+,\nu\right]$. The total outgoing field is obtained by adding these scattering coefficients, given by Eqs. (5.13-10) and (5.13-12), to the spectral coefficients in Eq. (5.13-3) for the direct field. This combination then is used in the spectral integrals in Eq. (5.8-1b).

Rainbow caustics through a refracting atmosphere with a sharp transparent boundary underneath can be obtained from this approach.

5.14 The Scattered Field from a Perfectly Reflecting Sphere Embedded in a Refracting Medium

Continuing the subject of embedded discontinuities begun in Section 5.13, we now consider a perfectly reflecting sphere embedded in a refracting medium. This example has some application to grazing, near-specular reflections from the ocean [9,10], especially at very shallow angles of incidence where the reflected signal is essentially linearly polarized. The transmitted GPS signals are right-hand circularly polarized (RHCP). Therefore, for grazing angles, roughly half the original power is potentially available from reflected signals, especially if the sea surface is smooth.

The spectral coefficients $b_l^{(0)}$ for a very large, perfectly reflecting sphere in a homogeneous medium are given in Chapter 3, Eq. (3.17-1). Those coefficients were obtained from the more general case of a transparent sphere with a finite discontinuity in the refractivity at its boundary $\rho=\rho_o$. By letting $n\to\infty$ at $\rho=\rho_o^-$, one obtains in the limit the reflection coefficients for a perfectly reflecting sphere. Therefore, in the case of a reflecting sphere in a non-homogenous medium, $G[\rho,\nu]$ is defined only for $\rho \geq \rho_o$. There is essentially infinite phase windup in the spectral coefficients traveling inward across that boundary. If we modify the scattering equation in Eq. (3.17-1) to account for the sphere being embedded in a stratified refracting medium, we have the following for the reflection coefficients at the boundary:

$$b_l^{(0)}(\rho_o) = -\frac{1}{2}\left(a_l^{+}(\rho_o) + a_l^{-}(\rho_o)\frac{\xi_l'^{-}(\rho_o)}{\xi_l'^{+}(\rho_o)} \right), \quad \rho_o = kn_o r_o \qquad (5.14\text{-}1)$$

At the boundary, the spectral coefficients are

$$a_l^{+}(\rho_o) = a_l^{-}(\rho_o) = i^{l-1}\frac{2l+1}{l(l+1)}\exp\left(-iG[\rho_o,\nu]\right) \qquad (5.14\text{-}2)$$

These apply to an initially planar incoming wave. The modification to this equation to account for an initially spherical incoming wave is found in Section 5.3, Eqs. (5.5-3a) and (5.5-3b). We recall from Chapter 3 that the superscript "(0)" on $b_l^{(0)}$ denotes the zeroth-degree reflection coefficient—that is, the coefficient for the ray with only a surface reflection, i.e., no internal reflections within the sphere. This is the only non-zero term for a perfectly reflecting sphere. To obtain $b_l^{(0)}(\rho)$ for $\rho > \rho_o$, we use arguments that are similar to those used in Section 5.8 to propagate the outgoing spectral coefficients through the medium. We define $b_l^{(0)}(\rho_{\mathrm{L}})$ as the reflection coefficient at the LEO. Assuming that the LEO is out of the medium so that $G[\rho_{\mathrm{L}},\nu] \equiv 0$, we obtain

$$b_l^{(0)}(\rho_{\mathrm{L}}) = b_l^{(0)}(\rho_o)\exp\left(-iG[\rho_o,\nu]\right) \qquad (5.14\text{-}3)$$

It follows from Eqs. (5.8-24) and (5.13-1) that the reflection coefficients at the LEO for a perfect spherical reflector in a stratified medium are given by

$$b_l^{(0)}(\rho_{\mathrm{L}}) = -\frac{1}{2} i^{l-1}\frac{2l+1}{l(l+1)}\left(1 + \frac{\xi_l'^{-}(\rho_o)}{\xi_l'^{+}(\rho_o)} \right)\exp\left(-i2G[\rho_o,\nu]\right) \qquad (5.14\text{-}4)$$

In other words, for the stratified medium, the reflection coefficient of spectral number l at the LEO is delayed in phase by an amount $-2G\left[\rho_o,\nu\right]$ as compared to the pure vacuum case discussed in Chapter 3.

The total field at the LEO is obtained from the spectral integrals in Eq. (5.8-1b), which are composed of the reflection coefficients in Eq. (5.14-4) plus the spectral coefficients for the incident field. For a collimated approaching wave, the spectral coefficients for the incident field are given by

$$\left.\begin{aligned}
a_l^-(\rho_{\mathrm{L}}) &= i^{l-1}\frac{2l+1}{l(l+1)}\exp\left(-iG[\rho_{\mathrm{L}},\nu]\right),\\
a_l^+(\rho_{\mathrm{L}}) &= i^{l-1}\frac{2l+1}{l(l+1)}\exp\left(-i2G\left[\rho^\dagger,\nu\right]\right),\ \ \rho^\dagger \ge \rho_o\\
a_l^+(\rho_{\mathrm{L}}) &= i^{l-1}\frac{2l+1}{l(l+1)}\exp\left(-i2G[\rho_o,\nu]\right),\ \ \rho^\dagger \le \rho_o
\end{aligned}\right\} \tag{5.14-5}$$

Referring to Fig. 5-36, we see that for LEO orbital positions above the shadow boundary there are two paths, a direct path with an impact parameter $\rho_d \ge \rho_o = kr_o n(r_o)$ and a reflected path with an impact parameter $\rho_{\mathrm{r}} \le \rho_o$. For regimes where the stationary phase condition in spectral number, $\nu^* \doteq \rho_d \le \rho_o$, would have held in the absence of the reflecting sphere, there are no stationary phase points for ν. Here one obtains a diffracted knife-edge decay in amplitude as the GPS satellite becomes occulted by the reflecting sphere.

From Section 5.9, we know that at the LEO the incoming coefficients $a_l^-(\rho_{\mathrm{L}})$ for the direct ray (d) may be ignored because they provide no stationary phase points in spectral number. The sum of the reflection and outgoing direct coefficients gives the total field at the LEO. They may be recombined into the form

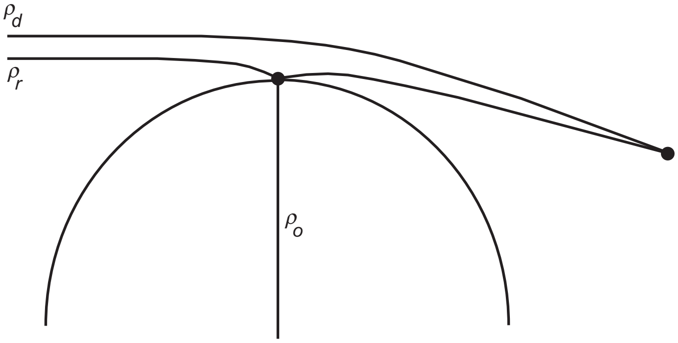

Fig. 5-36. Direct and reflected paths for a sphere of radius r_o embedded in a medium with a monotonic refractive gradient.

$$\left.\begin{array}{l} b_l^{(0)}(\rho_{\mathrm{L}})+\dfrac{1}{2}a_l^{+}(\rho_{\mathrm{L}})= \\ \left\{\begin{array}{l} i^{l+1}\dfrac{1}{2}\dfrac{2l+1}{l(l+1)}\left(\left(1+\dfrac{\xi_l^{-'}(\rho_o)}{\xi_l^{+'}(\rho_o)}\right)e^{-i2G[\rho_o,\nu]}-e^{-i2G\left[\rho^{\dagger},\nu\right]}\right),\ \rho^{\dagger}>\rho_o, \\ \dfrac{1}{2}i^{l+1}\dfrac{2l+1}{l(l+1)}\dfrac{\xi_l^{-'}(\rho_o)}{\xi_l^{+'}(\rho_o)}e^{-i2G[\rho_o,\nu]},\ \rho^{\dagger}<\rho_o \end{array}\right\} \end{array}\right\} \qquad (5.14\text{-}6)$$

Consider the regime $\rho^{\dagger}(\nu)>\rho_o$, the middle line in Eq. (5.14-6). For $\nu>\rho_o$, $\xi_l^{-'}(\rho_o)/\xi_l^{+'}(\rho_o)\to -1$ rapidly because of the runoff of $\mathrm{Bi}[\hat{y}]$ for $\hat{y}\doteq K_{\rho_o}^{-1}(\nu-\rho_o)>0$. Consequently, $b_l^{(0)}(\rho_o)\to 0$ for increasing $\nu>\rho_o$. Already at $\hat{y}=+3$, $|\xi_l^{-}(\rho_o)/\xi_l^{+}(\rho_o)+1|=0.001$. This leaves only the term $i^{l-1}(2l+1)/l(l+1)\exp(-i2G[\rho^{\dagger},\nu])/2$ in this regime where $\rho^{\dagger}(\nu)>\rho_o$. This is just the spectral coefficient for a direct ray, but applied to a spectral integral that has a lower cutoff at $\rho^{\dagger}(\nu)>\rho_o$. For $\rho_d >> \rho_o$, there will be a stationary phase point ν^* well above the cutoff. Assuming that the overlying medium has a monotonic refractivity gradient, i.e., no multipath, there will be only the one stationary phase point near $\nu=\rho_d$. It follows that when $\rho_d >> \rho_o$ this integral yields the field from the direct path, unencumbered by the reflection barrier; the lower cutoff at $\rho^{\dagger}(\nu)>\rho_o$ has no effect on the value of the integral. This is the field for a wave that has traveled through a refracting medium without influence from the reflecting surface below.

On the other hand, for a LEO orbital position that is lower than that shown in Fig. 5-36, for which the direct ray has an impact parameter value $\rho_d\approx\rho_o$, the stationary phase point ν^* will be near ρ_o. Here the lower cutoff in the spectral integral near $\nu=\rho_o$ does affect the calculation of the field at the LEO. It yields the knife-edge diffraction pattern that the wave from the direct ray will exhibit as the GPS satellite appears to approach the limb of the reflecting sphere and becomes eclipsed. If the LEO is located so that $\rho_d \leq\sim \rho_o$, then no stationary phase contributions occur for any value of ν; the LEO is in the refracted shadow. We will show these properties later using stationary phase theory.

The spectral coefficients on the lower line in Eq. (5.14-6) where $\rho^{\dagger}(\nu)>\rho_o$ provide the principal contribution to the reflected field at the LEO. Referring to Fig. 5-36, if the orbital position of the LEO is such that $\rho_d>\rho_o$, then there is also a reflected ray with an impact parameter value $\rho_r<\rho_o$. There will be a stationary phase point in spectral number, $\nu=\nu^*$, near $\nu=\rho_r$, and the spectral integral over a neighborhood about this point provides the principal contribution to the reflected field. For spectral numbers $\nu < \rho_o$, $\xi_l^{-'} / \xi_l^{+'} \to -i\exp\left(-4i(-\hat{y})^{3/2} / 3\right)$, which also winds up rapidly with decreasing $\nu < \rho_o$. Therefore, for near-grazing reflections, only spectral numbers very near but below ρ_o contribute significantly to the spectral integrals for the reflecting part, but they do so only when the reflected ray exists with $\rho_r \le \rho_o$. Figure 5-38, which we discuss later, shows the impact parameter diagram for both the direct and reflected rays for a reflecting surface embedded in a refracting medium. It shows the narrow separation between ρ_r and ρ_o for near-grazing conditions.

Applying the spectral coefficients for the outgoing part of the wave given in Eq. (5.14-6) to the spectral integrals in Eq. (5.8-1b), one obtains

$$\left.\begin{aligned} E_r^+(r_{\mathrm{L}},\theta_{\mathrm{L}}) &= \frac{E_o}{\rho_{\mathrm{L}}^2}\int_0^\infty \nu^2\left(\frac{a_l^+(\rho_{\mathrm{L}})}{2} + b_l^{(0)}(\rho_{\mathrm{L}})\right)\xi_l^+(\rho_{\mathrm{L}})\mathrm{P}_l^1(\cos\theta_{\mathrm{L}})d\nu \\ E_\theta^+(r_{\mathrm{L}},\theta_{\mathrm{L}}) &= \frac{E_o}{\rho_{\mathrm{L}}}\int_0^\infty \left(\frac{a_l^+(\rho_{\mathrm{L}})}{2} + b_l^{(0)}(\rho_{\mathrm{L}})\right)\xi_l^{+'}(\rho_{\mathrm{L}})\frac{\partial}{\partial\theta}\mathrm{P}_l^1(\cos\theta_{\mathrm{L}})d\nu \end{aligned}\right\} \quad (5.14\text{-}7)$$

Here the forms for the spectral coefficients for the direct and reflected waves are given in Eqs. (5.14-5) and (5.14-6). The spectral coefficient for the incoming part for the direct wave at the LEO, $a_l^-(\rho_{\mathrm{L}})$, is excluded, because the LEO is located well into the outgoing region.

Asymptotic forms can be used everywhere in these integrals except in the reflection coefficients for spectral numbers near $\nu = \rho_o$. However, the Airy functions may be used in place of the spherical Hankel functions, $\xi_l^{-'} / \xi_l^{+'} \doteq (\mathrm{Ai}'[\hat{y}] + i\,\mathrm{Bi}'[\hat{y}]) / (\mathrm{Ai}'[\hat{y}] - i\,\mathrm{Bi}'[\hat{y}])$.

We now consider the stationary phase points in spectral number in the phasor form of the integrands in Eq. (5.14-7). For an outgoing wave, these phasor forms are given by Eqs. (5.9-6) and (5.9-24) but are augmented here by the inclusion of the reflection coefficients. We note that $\left|\xi_l^- / \xi_l^+\right| = 1$ for real values of l and ρ. Therefore, we may write this ratio in phasor form:

$$\left.\frac{\xi_l^-}{\xi_l^+} = \exp(i2\Omega), \quad \Omega = \tan^{-1}\left(\frac{\mathrm{Bi}'[\hat{y}]}{\mathrm{Ai}'[\hat{y}]}\right)\right\} \quad (5.14\text{-}8)$$

Let $I(\rho_{\mathrm{L}},\theta_{\mathrm{L}})$ denote the part of the field at the LEO for a perfectly reflecting sphere that is due to the ratio $\xi_l^-(\rho_o) / \xi_l^+(\rho_o)$. It follows from Eqs. (5.14-6) through (5.14-8) that Eq. (5.9-24) for this part becomes

$$\left.\begin{aligned}
&I_r(r_\mathrm{L},\theta_\mathrm{L})=\frac{E_o}{\sqrt{2\pi\rho\sin\theta_\mathrm{L}}}\int_0^\infty\left(\frac{\sin^3\theta_\nu}{\cos\theta_\nu}\right)^{1/2}e^{i\left(2\Omega+\Psi_o(+,-)\right)}d\nu,\\
&I_\theta(r_\mathrm{L},\theta_\mathrm{L})=\frac{E_o}{\sqrt{2\pi\rho\sin\theta_\mathrm{L}}}\int_0^\infty\left(\sin\theta_\nu\cos\theta_\nu\right)^{1/2}e^{i\left(2\Omega+\Psi_o(+,-)\right)}d\nu,\\
&\Psi_o(+,-)=D_\nu+\nu(\theta_\nu-\theta_\mathrm{L})-2G[\rho_o,\nu]-\frac{\pi}{4},\\
&D_\nu=\sqrt{\rho_\mathrm{L}^2-\nu^2},\quad\theta_\nu=\sin^{-1}\left(\frac{\nu}{\rho_\mathrm{L}}\right),\\
&\Omega=\tan^{-1}\left(\frac{\mathrm{Bi}'[\hat{y}]}{\mathrm{Ai}'[\hat{y}]}\right),\ \hat{y}\doteq K_{\rho_o}^{-1}\left(\nu-\rho_o\right)
\end{aligned}\right\}\qquad(5.14\text{-}9)$$

The total direct and reflected field at the LEO is given by

$$\left.\begin{aligned}
E_r(r_\mathrm{L},\theta_\mathrm{L})&=I_r(r_\mathrm{L},\theta_\mathrm{L})+J_r(r_\mathrm{L},\theta_\mathrm{L})\\
E_\theta(r_\mathrm{L},\theta_\mathrm{L})&=I_\theta(r_\mathrm{L},\theta_\mathrm{L})+J_\theta(r_\mathrm{L},\theta_\mathrm{L})
\end{aligned}\right\}\qquad(5.14\text{-}10)$$

where from Eq. (5.14-6) we have

$$\left.\begin{aligned}
&J_r\left(r_\mathrm{L},\theta_\mathrm{L}\right)=\frac{E_o}{\sqrt{2\pi\rho\sin\theta_\mathrm{L}}}\int_{\nu_o^\dagger}^\infty\left(\frac{\sin^3\theta_\nu}{\cos\theta_\nu}\right)^{1/2}\left(e^{i\Psi^\dagger(+,-)}-e^{i\Psi_o(+,-)}\right)d\nu,\\
&J_\theta\left(r_\mathrm{L},\theta_\mathrm{L}\right)=\frac{E_o}{\sqrt{2\pi\rho\sin\theta_\mathrm{L}}}\int_{\nu_o^\dagger}^\infty\left(\frac{\sin2\theta_\nu}{2}\right)^{1/2}\left(e^{i\Psi^\dagger(+,-)}-e^{i\Psi_o(+,-)}\right)d\nu,\\
&\Psi^\dagger(+,-)=D_\nu+\nu\left(\theta_\nu-\theta_\mathrm{L}\right)-2G\left[\rho^\dagger(\nu),\nu\right]-\frac{\pi}{4},\\
&\Psi_o(+,-)=D_\nu+\nu\left(\theta_\nu-\theta_\mathrm{L}\right)-2G[\rho_o,\nu]-\frac{\pi}{4},\\
&\nu_o^\dagger\doteq\rho_o+\hat{y}^\dagger K_{\rho_o},\ \rho^\dagger(\nu)\doteq\nu-\hat{y}^\dagger K_{\rho_o}
\end{aligned}\right\}\qquad(5.14\text{-}11)$$

The contribution from the $\Psi_o(+,-)$ term to these *J* integrals mostly will be negligible when $\nu>\rho_o$. Moreover, because $2\Omega\rightarrow\pi$ rapidly for $\nu>\rho_o$, this region in the *I* integral given in Eq. (5.14-9) will essentially completely cancel this $\Psi_o(+,-)$ term in the *J* integral. But the $\Psi^\dagger(+,-)$ part of the *J* integrals in Eq. (5.14-11) accounts for the direct field at the LEO. When $\rho_d>>\rho_o$, this field is undisturbed by the reflecting surface and the stationary phase point in this integral $\nu^*>>\rho_o$; but when $\rho_d\approx\rho_o$, $\nu^*\approx\rho_o$ and *J* yields a knife-edge diffraction pattern.

5.14.1 Stationary Phase Analysis

Let us now examine the possible stationary phase neighborhoods for the reflection integrals I_r and I_θ given in Eq. (5.14-9). We seek the zero points for $\partial\left(2\Omega+\Psi_o\right)/\partial\nu$. From Eqs. (5.14-8) and (5.14-9), it follows that the stationary phase condition is given by

$$\left.\begin{array}{l}\dfrac{\partial}{\partial\nu}\left(2\Omega+\Psi_o\right)\doteq-\dfrac{2\hat{y}}{\pi\,\mathrm{M}[\hat{y}]K_{\rho_o}}+\theta_\nu-\theta_{\mathrm{L}}-2\dfrac{\partial G[\rho_o,\nu]}{\partial\nu},\\ \mathrm{M}[\hat{y}]=\mathrm{Ai}'^2[\hat{y}]+\mathrm{Bi}'^2[\hat{y}],\quad \hat{y}\doteq K_{\rho_o}^{-1}(\nu-\rho_o)\end{array}\right\}\qquad(5.14\text{-}12)$$

We assume here that the overlying medium has a monotonic refractivity gradient. Therefore, the direct ray system is unique (no multipath). One can show in this case that, for LEO orbital angular positions such that $\theta_{\mathrm{L}}+2\tilde{\alpha}(\rho_o,\rho_o)\geq\theta_{\rho_o}\doteq\theta_o+N_o\tan\theta_o$, where $\theta_o=\sin^{-1}(r_o/r_{\mathrm{L}})$, there is a single negative stationary phase point, i.e., $\hat{y}^*<0$. Otherwise, that point lies in positive territory, and the stationary phase contribution from there will largely cancel the $\Psi_o(+,-)$ contribution in the J integral. The latter situation corresponds to the LEO lying in the refracted shadow of the reflecting sphere. The LEO orbital position $\theta_{\mathrm{L}o}=\theta_{\rho_o}-2\tilde{\alpha}(\rho_o,\rho_o)$ marks the shadow boundary, the beginning (for the setting case) of the eclipse of the GPS satellite by the reflecting sphere. Thus, except in the immediate vicinity of this shadow boundary, the stationary phase value for the spectral number will be less than ρ_o, that is, $\nu^*\doteq\rho_o+K_{\rho_o}\hat{y}^*$ with $\hat{y}^*<0$, when $\theta_{\mathrm{L}}+2\tilde{\alpha}(\rho_o,\rho_o)\geq\theta_{\rho_o}$.

For the J integral, essentially only the $\Psi^\dagger(+,-)$ term contributes to the field when combined with the I integral. Except in the interval $\nu^\dagger\leq\nu\leq\sim\nu^\dagger+3K_{\rho_o}\sim$, the $\Psi_o(+,-)$ term in the J integral rapidly winds up, contributing negligibly to the integral. It follows that, to calculate the total field at the LEO using the stationary phase technique, one needs only the contribution to the I integrals in Eq. (5.14-9) from the stationary phase neighborhood provided by the condition in Eq. (5.14-12), plus the $\exp(i\Psi^\dagger(+,-))$ contribution from the J integral in Eq. (5.14-11). For $\rho_d>>\rho_o$, the latter integral gives essentially the direct field at the LEO unperturbed by the reflecting sphere but refracted by the overlying medium. The spectral treatment for this direct ray has been previously discussed in Section 5.9, and its stationary phase solution is presented there. Note the lower limit ρ_o in spectral number for the integration in Eq. (5.14-11). If the LEO orbital position is such that the impact parameter for a ray unperturbed by the reflecting surface is less than ρ_o, i.e., $\rho_d<\rho_o$, then this J integral will not contribute significantly to the field. Moreover, if $\theta_{\mathrm{L}} < \theta_{\rho_o} - 2\tilde{\alpha}(\rho_o,\rho_o)$, the I integrals also have no stationary phase points for negative values of $\hat{y}$, and the contribution from the positive stationary phase points in $\hat{y}$ will be essentially completely canceled by the $\exp(i\Psi_o(+,-))$ term in the J integral. For orbital positions well into this region, it will be dark.

If $\hat{y}$ is sufficiently negative, i.e., $\hat{y} <\sim -2$, we may use the negative argument asymptotic forms in $\mathrm{M}[\hat{y}]$. In this case, $\pi\mathrm{M}[\hat{y}] \to (-\hat{y})^{1/2}(1-7/(32\hat{y}^3)+\cdots)$. It follows that $2\Omega + \Psi_o(+,-)$ in the I integrals is given by

$$\left.\begin{aligned}
&2\Omega + \Psi_o(+,-) = -\frac{4}{3}(-\hat{y})^{3/2} - \frac{\pi}{2} + \Psi_o(+,-)\\
&\text{or}\\
&2\Omega + \Psi_o(+,-) = 2\left(\nu\left(\frac{\pi}{2} - \theta_\nu^o\right) - \sqrt{\rho_o^2 - \nu^2}\right)\\
&+\sqrt{\rho_{\mathrm{L}}^2 - \nu^2} + \nu\left(\theta_\nu - \theta_{\mathrm{L}}\right) - 2G[\rho_o,\nu] - \frac{3\pi}{4},\\
&\theta_\nu = \sin^{-1}\left(\frac{\nu}{\rho_{\mathrm{L}}}\right),\ \theta_\nu^o = \sin^{-1}\left(\frac{\nu}{\rho_o}\right),\\
&\frac{2}{3}(-\hat{y})^{3/2} = \sqrt{\rho_o^2 - \nu^2} - \nu\cos^{-1}\left(\frac{\nu}{\rho_o}\right),\quad \nu \le \rho_o
\end{aligned}\right\} \tag{5.14-13}$$

Although the power series expression for $\hat{y}$ in terms of spectral number ν and ρ_o for the reflecting sphere, which is given in Eq. (5.14-12), is adequate, its exact form is given in Eq. (5.14-13) for $\hat{y} < 0$. See Eq. (5.4-3) for further discussion. The exact form is useful in a later discussion showing the correspondence between stationary phase in spectral number and the law of reflection.

It follows upon setting $\partial G[\rho_o,\nu]/\partial\nu = \tilde{\alpha}(\rho_o,\nu)$ and $\partial\left(2\Omega + \Psi_o\right)/\partial\nu = 0$ that the stationary phase point for $\hat{y}^* < 0$ is given by the condition

$$2\theta_{\nu^*}^o - \theta_{\nu^*} + \theta_{\mathrm{L}} + 2\tilde{\alpha}\left(\rho_o,\nu^*\right) = \pi \tag{5.14-14a}$$

or

$$\hat{y}^* \doteq -\frac{1}{4}K_{\rho_o}^2\left(\theta_{\mathrm{L}} + 2\tilde{\alpha}(\rho_o,\nu^*) - \theta_{\nu^*}\right)^2 \tag{5.14-14b}$$

To obtain an explicit value for ν^* in terms of θ_L, we note that for near-grazing reflections $\theta_\mathrm{L} + 2\tilde{\alpha}\left(\rho_o, \nu^*\right)$ will be close in value to θ_o, as shown in Fig. 5-37. We expand θ_{ν^*} in a Taylor series expansion about θ_{ρ_o}. Here θ_{ρ_o} and θ_L^A are defined by

$$\left.\begin{aligned}
\theta_{\rho_o} &= \sin^{-1}\left(\frac{\rho_o}{\rho_\mathrm{L}}\right) \doteq \theta_o + N_o \tan\theta_o \\
\theta_o &= \sin^{-1}\left(\frac{r_o}{r_\mathrm{L}}\right) \\
\theta_\mathrm{L}^A &= \theta_\mathrm{L} + 2\tilde{\alpha}\left(\rho_o, \nu^*\right)
\end{aligned}\right\} \tag{5.14-15}$$

The angle θ_L^A is the apparent orbit angle for the LEO. Because of the incoming and outgoing bending, $\tilde{\alpha}\left(\rho_o, \nu^*\right)$ on each leg, our coordinate frame will have been effectively rotated clockwise by $2\tilde{\alpha}\left(\rho_o, \nu^*\right)$ (see Fig. 5-36). Thus, the angles of incidence and reflection will be less by an amount $\tilde{\alpha}\left(\rho_o, \nu^*\right)$ than they would be for the case of a reflecting sphere in a homogeneous medium.

We rewrite Eq. (5.14-14a) as $2\theta_{\nu^*}^o - \left(\theta_{\nu^*} - \theta_{\rho_o}\right) + \left(\theta_\mathrm{L}^A - \theta_{\rho_o}\right) = \pi$. Expanding θ_{ν^*} about θ_{ρ_o} in powers of $\nu^* - \rho_o$, we obtain

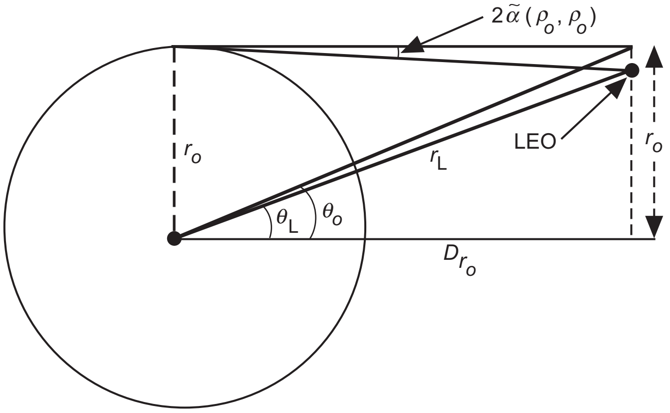

Fig. 5-37. Geometry for the LEO near the shadow boundary of a reflecting sphere embedded in a refracting medium.

$$\theta_{\nu^*} = \theta_{\rho_o} + \frac{\nu^* - \rho_o}{\sqrt{\rho_{\mathrm{L}}^2 - \rho_o^2}} + \cdots \; = \theta_{\rho_o} + \left(\sin\theta^o_{\nu^*} - 1 \right) \tan\theta_{\rho_o} + \cdots \tag{5.14-16}$$

Noting that for near-grazing reflections $\theta^o_{\nu^*} \approx \pi/2$, it follows from Eq. (5.14-14) that $2\Omega + \Psi_o(+,-)$ has a stationary value in spectral number when $\nu = \nu^*$ or $\hat{y} = \hat{y}^*$, which are given by the conditions

$$\left.\begin{aligned}
\theta^o_{\nu^*} &= \frac{\pi}{2} - \frac{\theta^A_{\mathrm{L}} - \theta_{\rho_o}}{2} - \frac{\left(\theta^A_{\mathrm{L}} - \theta_{\rho_o}\right)^2}{16} \tan\theta_{\rho_o} + \cdots \\
\nu^* &= \rho_o \sin\theta^o_{\nu^*} = \rho_o \left(1 - \frac{\left(\theta^A_{\mathrm{L}} - \theta_{\rho_o}\right)^2}{8} + \cdots \right) \\
\hat{y}^* &= -\frac{K^2_{\rho_o}}{4} \left(\theta^A_{\mathrm{L}} - \theta_{\rho_o}\right)^2 + \cdots
\end{aligned}\right\} \tag{5.14-17}$$

Because $\theta^A_{\mathrm{L}} = \theta_{\mathrm{L}} + 2\tilde{\alpha}\left(\rho_o, \nu^*\right)$, an iteration is required in Eq. (5.14-17) to determine ν^* once a specific form for $2\tilde{\alpha}(\rho_o, \nu)$ is given. For the specific exponential refractivity profile used in the numerical examples here for dry air, $2\tilde{\alpha}(\rho_o, \nu)$ for the reflected ray is given accurately by Eq. (5.8-3). It can be shown that in this case

$$\left.\begin{aligned}
&2\tilde{\alpha}\left(\rho_o, \nu^*\right) = 2\tilde{\alpha}_o - \frac{\beta}{1+\beta} \left(\theta_{\mathrm{L}} + 2\tilde{\alpha}_o - \theta_{\rho_o} \right) \\
&\times \left(1 + \frac{\rho_o}{24H(1+\beta)^3} \left(\theta_{\mathrm{L}} + 2\tilde{\alpha}_o - \theta_{\rho_o} \right)^2 + \cdots \right), \\
&\tilde{\alpha}_o = \tilde{\alpha}(\rho_o, \rho_o), \quad \beta = \frac{N_o \rho_o}{H}
\end{aligned}\right\} \tag{5.14-18}$$

This expression is accurate to 1 percent for near-grazing reflections, i.e., $\left| \theta_{\mathrm{L}} + 2\tilde{\alpha}_o - \theta_{\rho_o} \right| < 0.05$. It follows for this case that

$$\nu^* \doteq \rho_o \left(1 - \frac{1}{8} \left(\frac{\theta_{\mathrm{L}} + 2\tilde{\alpha}_o - \theta_{\rho_o}}{1+\beta} \right)^2 \right) \tag{5.14-19}$$

Figure 5-38 shows the impact parameter diagram for this reflection case. This figure uses the same refractivity model for the overlying medium as that used in Figs. 5-30 through 5-34. A circular LEO orbit was used with $r_{\mathrm{L}} = 1.1 r_o$.

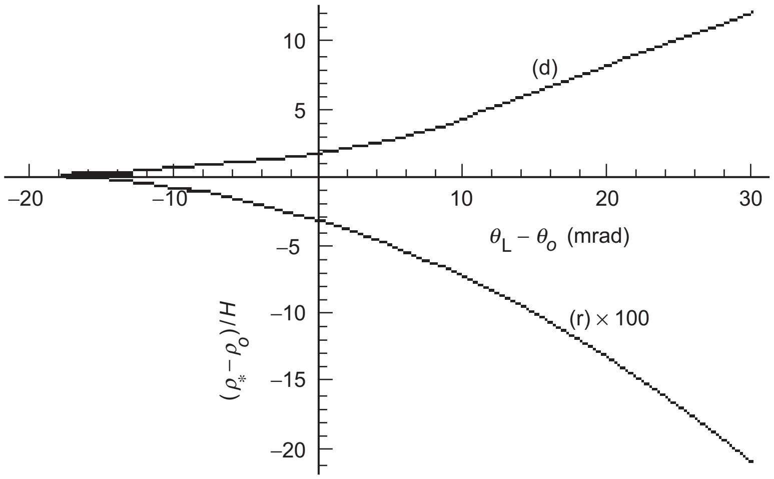

Fig. 5-38. Impact parameter diagram for a reflecting sphere embedded in a refracting medium versus orbit angle near grazing. The direct curve (d) is identical to the (m) curve in Fig. 5-31.

Therefore, the (d) curve in Fig. 5-38 for the direct ray is identical to the (m) curve in Fig. 5-31. The impact parameters for the (d) and (r) rays merge at $\theta_{\mathrm{L}} - \theta_{\rho_o} = -20.4$, the grazing point. Divide the impact parameter value given in Fig. 5-38 for the reflected ray (r) by 100 to obtain the correct value. The reflected ray is very defocused for near-grazing conditions. At $\theta_{\mathrm{L}} - \theta_{\rho_o} = 0$, it is about an order of magnitude more defocused than the (d) ray. This can be calculated by recalling from geometric optics that for a circular LEO orbit the defocusing factor is given by $\zeta = \left|D_{\rho_*}\left(d\theta_{\mathrm{L}} / d\rho_*\right)\right|^{-1}$. If we set $\nu^* = \rho_*$ in the stationary phase condition given in Eq. (5.14-14a), then we can form the derivative $d\theta_{\mathrm{L}} / d\rho_*$ while still satisfying the stationary phase condition as θ_{L} and ρ_* vary. For the defocusing factor ζ_{r} for the (r) ray, we obtain

$$\zeta_{\mathrm{r}}^{-1} = D_{\rho_*}\left|\frac{d\theta_{\mathrm{L}}}{d\rho_*}\right|_r^{-1} = \frac{2\cos\theta_{\rho_*}}{\sin\left(\left(\theta_{\mathrm{L}}^A - \theta_{\rho_*}\right)/2\right)\sin\theta_{\rho_o}} - 1 + 2D_{\rho_*}\frac{\partial\tilde{\alpha}(\rho_o,\rho_*)}{\partial\rho_*} \qquad (5.14\text{-}20\text{a})$$

For near-grazing reflections, the term $\left(\theta_{\mathrm{L}}^A - \theta_{\rho_*}\right)$ is small. Also, $\theta_{\rho_*} - \theta_{\rho_o} \doteq -\left(\theta_{\mathrm{L}}^A - \theta_{\rho_o}\right)^2 / 8D\rho_o$, which is a very small term. Expanding about $\left(\theta_{\mathrm{L}}^A - \theta_{\rho_o}\right)$ yields

$$\zeta_{\mathrm{r}}^{-1} \doteq \frac{4\cot\theta_{\rho_o}}{\theta_{\mathrm{L}} + 2\tilde{\alpha}(\rho_o,\rho_*) - \theta_{\rho_o}} - \left(1 - 2D_{\rho_o}\frac{\partial\tilde{\alpha}(\rho_o,\rho_*)}{\partial\rho_*}\right) \tag{5.14-20b}$$

The first term on the RHS is dominant for near-grazing reflections. At $\theta_{\mathrm{L}} - \theta_o = 0$ for the case shown in Fig. 5-38, the values of the first and second terms are about 120 and 20, respectively. Thus, Eq. (5.14-20) predicts about 0.08 for the amplitude $E_o\zeta_{\mathrm{r}}^{1/2}$ of the reflected ray at $\theta_{\mathrm{L}} - \theta_o = 0$. The amplitude of the (d) ray there is about 0.6, which decreases to less than 0.4 at the grazing point at $\theta_{\mathrm{L}} - \theta_o = -20.4$ mrad.

Figure 5-39 shows the impact parameter diagram for the reflected and direct rays for $\theta_o - 2\tilde{\alpha}(\rho_o,\rho_o) \le \theta_{\mathrm{L}} \le \pi$, which covers the entire range of LEO orbit angles for which a reflected ray exists, from the shadow boundary to a vertical reflection. Here Eq. (5.14-14a) has been used to solve for ρ_{r} using the same refractivity for the overlying medium and orbit models that are used in Fig. 5-30.

We note that $\left(\theta_{\mathrm{L}}^A - \theta_{\rho_o}\right)K_{\rho_o}$ has a scale invariance provided that third- and higher-order terms in $\left(\theta_{\mathrm{L}}^A - \theta_{\rho_o}\right)$ given for $\hat{y}^*$ in Eq. (5.14-17) can be ignored. The stationary phase points for a reflecting sphere of another radius $\tilde{\rho}_o$ is obtained from our problem merely by applying the scale factor $(\tilde{\rho}_o / \rho_o)^{1/3}$ to the results obtained here for $\left(\theta_{\mathrm{L}}^A - \theta_{\rho_o}\right)K_{\rho_o}$. One of the practical aspects of this is that the a priori value for $\tilde{\rho}_o$—for example, in the case of the topography of the ocean surface—is uncertain to some extent in an actual observation

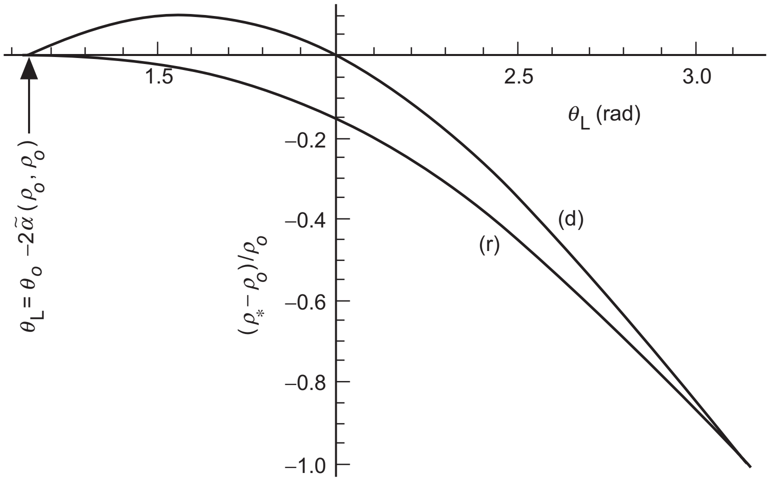

Fig. 5-39. Large scale version of the impact parameter diagram over the entire LEO orbit above the grazing point.

sequence of reflected and direct signals. This is particular true for near-grazing conditions. This scale-invariance property may be useful.

For $\hat{y} < 0$, we can determine from the I integrals in Eq. (5.14-9), using the stationary phase technique, the contribution from the stationary phase point to the field at the LEO from the reflecting sphere. We need the second derivative $\partial^2 \left(2\Omega + \Psi_o \right) / \partial \nu^2$ evaluated at the stationary phase point, given by either Eq. (5.14-14) or Eq. (5.14-17). This is given by

$$\left(D_\nu \frac{\partial^2 (2\Omega + \Psi)}{\partial \nu^2} \right)_{\nu^*} = \left(\frac{-2D_\nu}{\rho_o \cos \theta_\nu^o} + 1 - 2D_\nu \frac{\partial^2 G}{\partial \nu^2} \right)_{\nu^*} \tag{5.14-21a}$$

Replacing $\left(\partial^2 G / \partial \nu^2 \right)_{\nu^*}$ with $\partial \tilde{\alpha} / \partial \rho_*$ and also $\theta_{\nu^*}^o$ with its expansion in terms of $\left(\theta_{\mathrm{L}}^A - \theta_{\rho_o} \right)$, which is given in Eq. (5.14-27), we obtain

$$\left(\frac{\partial^2 (2\Omega + \Psi)}{D_\nu \partial \nu^2} \right)_{\nu^*} \doteq \frac{-4 \cot \theta_{\rho_*}}{\theta_{\mathrm{L}} + 2\tilde{\alpha}(\rho_o, \rho_*) - \theta_{\rho_*}} + 1 - 2D_{\rho_*} \frac{\partial \tilde{\alpha}(\rho_o, \rho_*)}{\partial \rho_*} \tag{5.14-21b}$$

which is the same as the defocusing factor from geometric optics given in Eq. (5.14-20b). For orbital positions near but above the shadow boundary ($\hat{y}^* < 0$), it follows from the stationary phase technique that the field at the LEO from the reflecting sphere is given by

$$\begin{aligned} I &\doteq \frac{E_o \exp\left(i\Phi^* \right)}{\sqrt{-2\pi i \rho_{\mathrm{L}} \cos \theta_{\rho_o}}} \int_0^\infty \exp\left(i \frac{1}{2} \left. \frac{\partial^2 \left(2\Omega + \Psi_o \right)}{\partial \nu^2} \right|_{\nu^*} \left(\nu - \nu^* \right)^2 \right) d\nu \\ &\doteq \frac{E_o \exp\left(i\Phi^* \right)}{\sqrt{-2\pi i \rho_{\mathrm{L}} \cos \theta_{\rho_o}}} \left(\frac{1}{\pi} \left| \frac{\partial^2 \left(2\Omega + \Psi_o \right)}{\partial \nu^2} \right|_{\nu^*} \right)^{-1/2} \int_{-\infty}^{\infty} \exp\left(-i \frac{\pi}{2} x^2 \right) dx \end{aligned} \tag{5.14-22a}$$

or

$$I\left(\rho_{\mathrm{L}}, \theta_{\mathrm{L}} \right) \doteq E_o \exp\left(i\Phi^* \right) \sqrt{\zeta_{\mathrm{r}}^*} \tag{5.14-22b}$$

where

$$\left.\begin{aligned}
\left(\zeta_r^*\right)^{-(1/2)} &= \left(D_\nu \left| \frac{\partial^2 \left(2\Omega + \Psi_o\right)}{\partial \nu^2} \right| \right)_{\nu^*}^{1/2} \\
&\doteq \sqrt{\left| \frac{4\cot\theta_{\rho_*}}{\theta_\mathrm{L} + 2\tilde{\alpha}(\rho_o,\rho_*) - \theta_{\rho_*}} - \left(1 - 2D_{\rho_*}\frac{\partial\tilde{\alpha}(\rho_o,\rho_*)}{\partial\rho_*}\right) \right|}, \\
\Phi^* &= \left(2\Omega + \Psi_o - \pi/4\right)^* \\
&= -\pi + \sqrt{\rho_\mathrm{L}^2 - \nu^{*2}} - 2\sqrt{\rho_o^2 - \nu^{*2}} + 2\left(\nu^*\tilde{\alpha}\left(\rho_o,\nu^*\right) - G\left[\rho_o,\nu^*\right]\right)
\end{aligned}\right\} \qquad (5.14\text{-}23)$$

and also

$$\left.\begin{aligned}
&\theta_{\rho_o} = \sin^{-1}\left(\frac{\rho_o}{\rho_\mathrm{L}}\right) \doteq \theta_o + N_o \tan\theta_o, \quad \theta_o = \sin^{-1}\left(\frac{r_o}{r_\mathrm{L}}\right), \\
&\theta_\mathrm{L}^A = \theta_\mathrm{L} + 2\tilde{\alpha}\left(\rho_o,\nu^*\right), \quad \nu^* = \rho_o\left(1 - \frac{\left(\theta_\mathrm{L}^A - \theta_{\rho_o}\right)^2}{8} + \cdots\right), \\
&\rho_o = kn_o r_o, \quad \rho_\mathrm{L} = kr_\mathrm{L}, \quad D_{\rho_o} = \sqrt{\rho_\mathrm{L}^2 - \rho_o^2}
\end{aligned}\right\} \qquad (5.14\text{-}24)$$

The stationary phase term Φ^* in Eq. (5.14-23) gives the stationary value of the phase at the LEO from the reflecting sphere relative to the phase of the field (neither refracted nor reflected) at the centerline at $\theta = \pi/2$ in Fig. 5-43(a). The π term gives the phase reversal from the reflection. The term $\sqrt{\rho_\mathrm{L}^2 - \nu^{*2}} - 2\sqrt{\rho_o^2 - \nu^{*2}}$ accounts for the difference in optical path length relative to the centerline in Fig. 5-43(a). The first term, $\sqrt{\rho_\mathrm{L}^2 - \nu^{*2}}$, gives the length along a straight line from the tangent point on the circle of radius ν^* centered at the origin to the LEO. The second term, $-2\sqrt{\rho_o^2 - \nu^{*2}}$, subtracts the length ($\sqrt{\rho_o^2 - \nu^{*2}}$) between that tangent point and the reflection point along this straight line, and it also subtracts the distance ($\sqrt{\rho_o^2 - \nu^{*2}}$) that the reflection point has moved counterclockwise from the centerline. The third term, $2\nu^*\tilde{\alpha}\left(\rho_o,\nu^*\right)$, accounts for the extra path length along an arc of radius ν^* resulting from the refractive bending. The fourth term, $-2G\left[\rho_o,\nu^*\right]$, accounts for the extra round-trip delay from infinity down to a radius ν^* resulting from the refractive gradient in the overlying medium. These third and fourth terms may be rewritten in the form $2\left(\nu^*\tilde{\alpha}\left(\rho_o,\nu^*\right)-G\left[\rho_o,\nu^*\right]\right)$ $\doteq 2\left(\rho_o\tilde{\alpha}\left(\rho_o,\nu^*\right)-G[\rho_o,\rho_o]\right)$.

The form of the amplitude signature $\sqrt{\zeta_{\mathrm{r}}}$ given in Eq. (5.14-23) is dominated by the $\left(\theta_{\mathrm{L}}^A-\theta_{\rho_o}\right)^{-1}$ term for near-grazing reflections. This dominance continues with increasing θ_{L} until the term $\left(1-2D_{\rho_{\mathrm{r}}}\partial\tilde{\alpha}/\partial\nu\right)$ in $\partial^2\left(2\Omega+\Psi_o\right)/\partial\nu^2$ given in Eq. (5.14-21) becomes dominant. Equating these two terms yields a threshold of $\theta_{\mathrm{L}}^A-\theta_{\rho_o}\approx 4\zeta^*\cot\theta_{\rho_o}$, or when θ_{L} becomes about a quarter of a radian greater than $\theta_o-2\tilde{\alpha}(\rho_o,\rho_o)$. Here the impact parameter of the direct ray is well above the atmosphere. For impact parameters above this threshold, $\zeta_{\mathrm{r}}^{-1}\to 1-2D_\nu\partial\tilde{\alpha}(\rho_o,\nu)/\partial\nu$ is the defocusing factor at the reflecting surface for a ray with an impact parameter value of ν. In this case, the amplitude of the reflected signal at the LEO reduces to $|I|\to E_o\zeta_{\mathrm{r}}^{1/2}$, the same form that the amplitude of the direct ray has except that the defocusing factor is based on the bending angle $\tilde{\alpha}\left(\rho_o,\nu^*\right)$ for the reflected ray rather than $\tilde{\alpha}(\rho_*,\rho_*)$ for the direct ray. However, polarization effects from reflections at these steeper angles must be considered. The GPS receiver onboard the LEO is configured for RHCP.

5.14.2 Results from Wave Theory

Figures 5-40 through 5-42 show the amplitude of the field at the LEO from a GPS satellite that is being occulted by a perfectly reflecting sphere embedded in a refracting atmosphere. Figure 5-40 shows the amplitude $E^{(\mathrm{d})}$ from the direct ray only. This corresponds to the (d) ray in the impact parameter diagram shown in Fig. 5-38. Figure 5-41 shows the amplitude $E^{(\mathrm{r})}$ from the reflected ray (r) only, and Fig. 5-42 shows the amplitude of the complete field. These figures show the transition over about 25 mrad in orbit angle, or roughly 1/2 minute in time, as the LEO moves into the shadow. Here an exponential profile [Eq. (5.8-2a)] has been used for the overlying medium with $N_o=270\times10^{-6}$, $k^{-1}H=7\,\mathrm{km}$, $r_o=6378\,\mathrm{km}$, and $k=3.31\times10^4\,\mathrm{km}^{-1}$. Also, $r_{\mathrm{L}}=1.1r_o$ and $\theta_o=\sin^{-1}\left(r_o/r_{\mathrm{L}}\right)$. From Eq. (5.6-5) or Eq. (5.8-3), one can show that $2\tilde{\alpha}(\rho_o,\rho_o)=20.4\,\mathrm{mrad}$ for these parameter values. Figures 5-40 through 5-42 were obtained from a numerical integration of Eq. (5.8-1b) aided by the stationary phase technique. The impact parameter diagram in Fig. 5-38 effectively provides those stationary phase points in spectral number for a given value of θ_{L}.

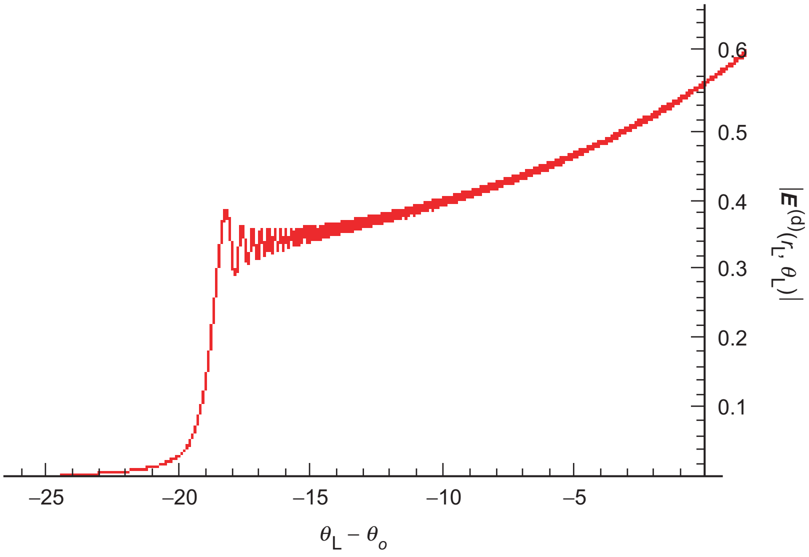

Fig. 5-40. A perfectly reflecting sphere embedded in a refracting medium. Wave theory prediction of the amplitude $|E^{(d)}(r_L, \theta_L)|$ of the field at the LEO from the direct ray only.

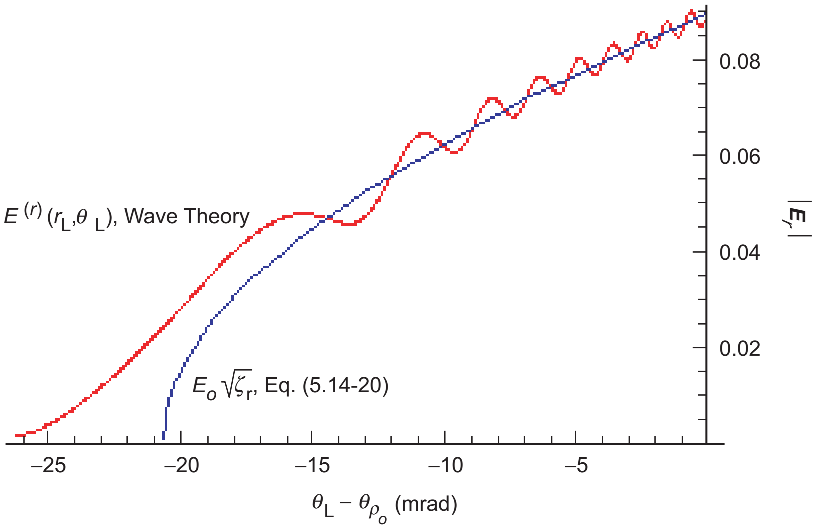

Fig. 5-41. Amplitude of the field at the LEO from a perfectly reflecting sphere embedded in a refracting medium, reflected ray (r) only.

The mean amplitude in Fig. 5-40 shows a rapid decay for θ_{L} values such that $\rho_d < \rho_o$, or $\theta_{\mathrm{L}} - \theta_o < -2\tilde{\alpha}(\rho_o, \rho_o)$. This is the penumbra region. The GPS satellite being eclipsed by the reflecting sphere causes the knife-edge diffraction pattern in Fig. 5-40. For $\rho_d > \rho_o$, Fig. 5-41 clearly shows the $\sqrt{\zeta_{\mathrm{r}}}$ signature in the mean amplitude for the reflected wave that is predicted from the stationary phase technique in Eq. (5.14-23). This agrees with the geometric optics prediction in Eq. (5.14-20) for LEO orbit angles above the shadow boundary, $\theta_{\mathrm{L}} > \theta_o - 2\tilde{\alpha}(\rho_o, \rho_o)$.

Figure 5-42, which gives the wave theory prediction of the total field at the LEO over the same near-grazing orbit angles shown in Figs. 5-40 and 5-41, shows the fringes from interference between the direct and reflected rays. Very high fringe frequencies develop as the separation in altitude between the impact parameters of the reflected and direct rays increases with increasing θ_{L}. The single-sided amplitude of the interference fringes here nearly equals the amplitude of the reflected ray (r) in Fig. 5-41. The fringe amplitude would be significantly reduced for an imperfectly reflecting sphere. The fringe frequency here ranges from about 60 Hz at $\theta_{\mathrm{L}} - \theta_{\rho_o} = 0$, about 20 s before eclipse for the setting case, to zero at $\theta_{\mathrm{L}} - \theta_o = -2\tilde{\alpha}(\rho_o, \rho_o) = -20.4$ mrad, at the refracted shadow boundary.

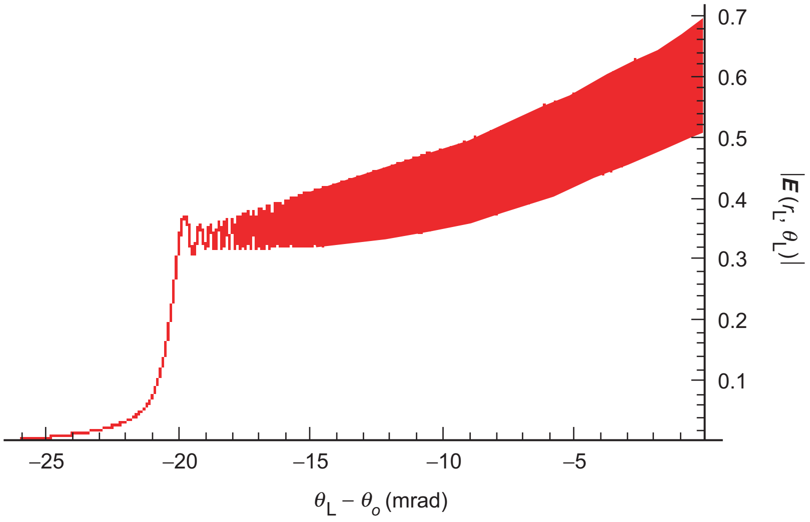

Fig. 5-42. Amplitude of the complete field $(d)+(r)$ at the LEO from a perfectly reflecting sphere embedded in a refracting medium, the direct ray from Fig. 5-40 plus the reflected ray from Fig. 5-41.

5.14.3 Law of Reflection

Chapter 3 provides a geometric optics interpretation of the stationary phase point for a reflecting sphere in a homogeneous medium. There it was shown for a point $(r_{\mathrm{L}}, \theta_{\mathrm{L}})$ sufficiently away from the shadow boundary (so that the negative argument asymptotic terms for the Airy functions are valid) that, when the spectral number assumes its stationary phase point, the condition for stationarity in spectral number becomes identical with the law of reflection in geometric optics. We also can similarly interpret the stationary phase results for a reflecting sphere embedded in a refracting medium. Referring to Figs. 5-43(a) and 5-43(b), which are representations in spectral number space, we have two concentric circles in each figure. The outer circle corresponds to the reflecting sphere, and it has a fixed radius ρ_o in spectral number space. The inner one of variable radius is a circle of radius ν, the spectral number. In Fig. 5-43(a), $\nu = \nu^*$, the stationary phase value. In Fig. 5-43(b), the provisional reflection point has been moved clockwise; here $\nu < \nu^*$, and the angle of incidence i is greater than the angle of reflection $r = \theta_\nu^o$. Noting the triangle ABC in Fig. 5-43(b), we see that the sum of the interior angles of this triangle satisfies the relationship

$$i + r - \theta_\nu + \theta_{\mathrm{L}}^A = \pi \tag{5.14-25}$$

for any provisional point of reflection on the circle of radius ρ_o in spectral number. But, at the actual reflection point where $i = r$, Eq. (5.14-25) becomes the same relationship given in Eq. (5.14-14a) for the stationary phase condition on the spectral number. We conclude that $\theta_{\nu^*}^o$, which always equals the angle of reflection r by construction, also equals the angle of incidence i when the spectral number assumes its stationary phase value, thus establishing the law of reflection. It follows that

$$i = r = \theta_{\nu^*}^o \doteq \frac{\pi}{2} - \frac{\theta_o^A - \theta_{\rho*}}{2} \tag{5.14-26}$$

Lastly, we see in Fig. 5-43(a) that the position of the reflection point on the reflecting sphere is located at a point counterclockwise relative to the midpoint. This rotation, ε, is given by

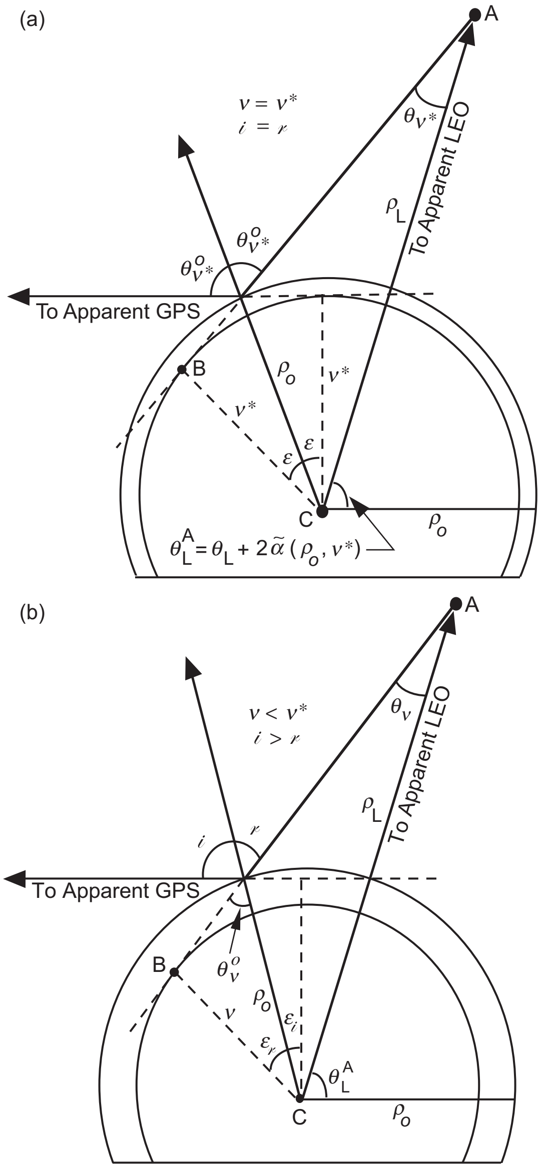
(a)
A
$\nu = \nu^*$
$i = r$
θ_{ν^*}
To Apparent LEO
ρ_L
$\theta^o_{\nu^*}$
$\theta^o_{\nu^*}$
To Apparent GPS
B
ρ_o
ν^*
ν^*
ε
ε
C
ρ_o
$\theta^A_L = \theta_L + 2\tilde{\alpha}(\rho_o, \nu^*)$
(b)
A
$\nu < \nu^*$
$i > r$
θ_ν
To Apparent LEO
ρ_L
i
r
To Apparent GPS
θ^o_ν
B
ρ_o
ν
ε_i
ε_r
θ^A_L
C
ρ_o

Fig. 5-43. The law of reflection; the geometry in spectral number space for a reflecting sphere embedded in a refracting medium. The outer circle describes a reflecting sphere of radius r_o, which maps in spectral number space into a fixed circle of radius ρ_o. The inner circle has a variable radius value, ν: (a) the radius of the inner circle is the stationary phase value, ν^*, which gives $i = r$, the law of reflection, and (b) $\nu < \nu^*$, a non-stationary phase value, which gives $i > r$.

$$\left.\begin{aligned}\varepsilon=\frac{\pi}{2}-\theta^{o}_{\nu^*}&=\frac{\theta_{\mathrm{L}}^{A}-\theta_{\rho_o}}{2}+\frac{\left(\theta_{\mathrm{L}}^{A}-\theta_{\rho_o}\right)^2}{16}\tan\theta_{\rho_o}+\cdots\\ &\doteq\frac{\theta_{\mathrm{L}}-\theta_o}{2}+\tilde{\alpha}\left(\rho_o,\nu^*\right)-\frac{1}{2}N_o\tan\theta_o\end{aligned}\right\}\tag{5.14-27}$$

For the exponential refractivity model given in Eq. (5.8-2) and from the resulting bending-angle expression given in Eq. (5.8-3), we have

$$\varepsilon\doteq\frac{\theta_{\mathrm{L}}-\theta_o}{2}+\tilde{\alpha}(\rho_o,\rho_o)-\frac{N_o\rho_o}{2H}\left(\theta_{\mathrm{L}}-\theta_o\right)-\frac{1}{2}N_o\tan\theta_o\tag{5.14-28}$$

Thus, the refractive bending (for a negative refractivity gradient, i.e., $\tilde{\alpha}\left(\rho_o,\nu^*\right)>0$) acts to increase the counterclockwise rotation of the reflection point. This is qualitatively indicated in Fig. 5-36. For sea-level conditions and for $\theta_{\mathrm{L}}-\theta_o=10\,\mathrm{mrad}$, the third and fourth terms on the RHS of Eq. (5.14-28) provide a correction of about 10 percent.

For a backward reflection case, that is, when $\theta_{\mathrm{L}}>\pi/2$, the incoming spectral coefficients $a_l^-(\rho_{\mathrm{L}})$ also would have to be taken into account. When $\theta_{\mathrm{L}}>>\pi/2$, this geometry would correspond more closely to a near-vertical reflection geometry than to the near-grazing one discussed here.

References

[1] C. Chapman and J. Orcutt, "The Computation of Body Wave Synthetic Seismograms in Laterally Homogeneous Media," *Reviews of Geophysics*, vol. 23, no. 2, pp. 105–163, 1985.

[2] G. Mie, "Beiträge zur Optik Truber Medien Speziell Kolliodaler Metallösungen," *Annales de Physique* (Leipzig), vol. 25, pp. 377–452, 1908.

[3] M. Born and E. Wolf, *Principles of Optics: Electromagnetic Theory of Propagation, Interference, and Diffraction of Light,* 6th ed., New York, New York: Pergamon Press, 1980.

[4] J. Jackson, *Classical Electrodynamics,* 2nd ed., Oxford, United Kingdom: J. Wiley & Sons, Inc., 1975.

[5] T. Eckersley and G. Millington, "Application of the Phase Integral Method to the Analysis of the Diffraction and Reflection of Wireless Waves Round the Earth." *Philos. Trans*., vol. 237, pp. 273–309, 1938.

[6] J. Mathews and R. Walker, *Mathematical Methods of Physics*, Menlo Park, California: The Benjamin/Cummings Publishing Co., 1970.

[7] M. Levy, *Parabolic Equation Methods for Electromagnetic Wave Propagation*, London, United Kingdom: The Institution for Electrical Engineers, 2000.

[8] M. Abramowitz and I. Stegun, eds., *Handbook of Mathematical Functions With Formulas, Graphs, and Mathematical Tables,* U.S. Department of Commerce, National Bureau of Standards, U.S. Government Printing Office, Washington, D.C., 1964.

[9] A. Pavelyev, A. Zakharov, A. Kucherjavenkov, E. Molotov, I. Siderenko, I. Kucherjavenkova, and D. Pavelyev, "Propagation of Radio Waves Reflected from Earth's Surface at Grazing Angles between a Low-Orbit Space Station and a Geostationary Satellite," *Journal of Communications Technology and Electronics*, vol. 42, no. 1, pp. 51–57, 1997.

[10] G. Beyerle, K. Hocke, J. Wickert, T. Schmidt, C. Marquardt, and Ch. Reigber, "GPS Radio Occultations with CHAMP: A Radio Holographic Analysis of GPS Signal Propagation in the Troposphere and Surface Reflections," *Journal of Geophysical Research*, vol. 107, no. D24, 10.1029/ 2001JD001402, 2002.